A study of AGN and their Environments

in the Far–Infrared

Jose Manuel Cao Orjales

Submitted to the University of Hertfordshire in partial fulfilment

of the requirements of the degree of Doctor of Philosophy

August 2014

Abstract

My Ph.D. has been composed of work involving the use of far–IR and submm observations of AGN. During this time it has focused on the interplay between AGN and their host galaxies and cluster environments. Understanding the role of AGN, and how they affect the evolution of both their host galaxies and surrounding environments, is a pressing concern in cosmological models of the universe, affecting as they do the chemical makeup, star formation rate, and morphology of their host galaxies.

In Chapter 2, we focus on attempting to determine whether there is an inherent physical difference between Broad Absorption Line Quasars and non–BAL QSOs using *Herschel* observations taken at 250, 350 and 500 μm as part of the H–ATLAS (Eales et al. 2010) survey. BAL QSOs have been considered the most visible form of AGN feedback, and therefore are a prime starting point for understanding how galaxy evolution may be affected by the presence of an AGN. By using matched samples of 50 BAL and 329 non–BAL QSOs, we create weighted stacks at each wavelength, finding similar far–IR flux–densities for each sample within the errors. By SED modelling using a simple modified black body (Hildebrand 1983) fit to Mrk 231 and IZw1, we derive likely upper and lower limits for the BAL and non–BAL QSOs in each wavelength, again finding they are consistent within the errors. A bevy of statistical tests run on either population similarly finds no evidence to reject the null hypothesis they are drawn from the same parent population. These results would imply that HiBAL QSOs can be unified with ordinary QSOs within a simple orientation dependent scheme. We cannot make the same distinction for LoBALs or FeLoBALs, which the literature suggests may well be a separate evolutionary phase.

In Chapter 3, we determine whether the presence of an AGN correlates to an overdensity of star–forming galaxies in the FIR, as has been found at shorter wavelengths (Falder et al. 2010). For the SHAGs study, 171 AGN were observed and selected at $z \sim 1$. By using observations at 250 μm, we are able to trace close to the peak of the grey–body SED created by reprocessing by dust of radiation from young O and B stars. Following data reduction, we determine number counts and correct for completeness within a 1 Mpc radius of the central AGN. We find an overdensity on the

order of around 0.4 sources per AGN, implying a degree of activity already significantly lower than at higher redshifts. This overdensity appears to be somewhat different between RL AGN and RQQ within 1 Mpc. A correlation is found between radio luminosity and star formation overdensity, consistent with a stronger dependence found by Falder et al. (2010) at 3.6 μm, and there also appears to be a correlation between stellar mass and star formation overdensity for radio–loud QSOs. The galaxies in the environs of the AGN have LIRG–level luminosities, and are likely the progenitors of modern day S0 galaxies, whose population increases steadily from $z \sim 1$ to the present day (Postman et al. 2005; Smith et al. 2005).

Our work with SCUBA–2, presented in Chapter 4, follows on from a prior sample of X–ray–absorbed QSOs (Stevens et al. 2005). This new sample is composed of more highly–absorbed X–ray QSOs and covers a larger area than the initial sample, so is ideal for an analysis of source counts around AGN at high–redshift. Data from the JCMT have been reduced, and completeness corrections and flux corrections applied to catalogues to determine the number counts around AGN. A comparison background, created using data from the Cosmology Legacy Survey has been used to derive comparison counts. The AGN have been investigated, yet none are detected above 3 σ at 850 μm, in contrast to the original sample. This may suggest that star formation in their host galaxies has been suppressed. Upon stacking in redshift and BAL classification, no difference in flux–density is apparent and the sources studied here have a similar stacked submm output to an unabsorbed QSO sample created for the original X–ray absorbed QSOs. However, over half of the sources here are BAL QSOs in contrast to the original absorbed QSO sample which contained only 1 BAL QSO. From the work in Chapter 2, one might expect BAL and non–BAL QSOs to have similar flux–densities. We argue that the sources studied in this thesis have likely undergone rapid evolution owing to a strong outflow, and as such star formation has been suppressed sufficiently that the submm emission is below the confusion noise. BAL winds may still be present, but essentially, the show is already over. A similar mechanism may already have occurred in unabsorbed QSOs if all QSOs pass through an X–ray–absorbed phase. With regard to source counts, we find that there is tentative evidence for an overdensity of sources around these AGN. The SFRs of the companion sources have been calculated using several greybody analogues, all of which imply a high degree of activity, suggesting these fields will evolve to become some of the most massive regions at the present epoch, in keeping with current theories of SMGs and high–redshift clusters.

Acknowledgements

Doing a PhD in Astrophysics and working alongside some of the greatest minds in the world has always been a major dream of mine. The past three and a half years have been a rollercoaster ride, with many great memories that I will cherish for the rest of my life. I would not have reached this point without the love and support of many people, too many to list all of them here!

Firstly, I would like to extend a heartfelt thank you to my supervisors Jason Stevens and Matt Jarvis. Thank you for giving me the opportunity to pursue my dream and for allowing me access to some truly fantastic data. You have allowed me to visit some of the world's most cutting–edge facilities in the course of my PhD, the memories of which I will never forget. Jason, your ability to find time to talk verges on superhuman; without your support, encouragement and seemingly endless patience in our discussions, I'm not sure I would have made it this far. Matt, thank you for reminding me to take things in stride, not let myself get too overwhelmed by the task at hand and treat things with a bit of humour.

To my parents Manuel and Lourdes, I can never repay the huge debt I owe to both of you. Since the first time I expressed an interest

in astronomy, you have done nothing but nurture my curiosity and provide everything I could ever need. I am truly blessed to have parents like you. *Gracias mama y papa, sin tu amor y confianza en mi no seria la persona que soy hoy. Te quiero mucho y espero que te he hecho orgulloso de mi.*

I also cannot forget to mention my godparents and cousin Melissa. You all have a very special place in my heart for all the belief and support you have provided over the years.

Finally, to my friends...thank you for the chilled pub nights, epic nights out, film nights, video game sessions, ping pong buffet visits, random holidays, silly jokes and inappropriate banter. Without you 'orrible lot, the low points would have been truly abysmal and the high points mediocre. You helped to remind me that there was more to life than the latest AGN paper or seemingly endless debugging errors!

Jose Manuel Cao Orjales

Hertford, 2014

Contents

List of Figures

List of Tables

Chapter 1

Introduction

1.1 Active Galactic Nuclei

1.1.1 A History

One of the earliest observations of the phenomena now known as Active Galactic Nuclei (AGN) was actually carried out as as part of an attempt to answer the question of whether spirals were gaseous objects akin to the Orion nebula, or very distant collections of unresolved stars (Fath 1909). Fath found that for the majority of the 'spiral nebulae' observed, a continuous spectrum with stellar absorption lines was visible. In the case of NGC 1068 however, the spectrum showed both bright and broad emission lines, an interesting find. It was not until over 30 years later that a systemic study of sources showing these nuclear emission lines was performed by Carl Seyfert (Seyfert 1943). The 6 observed sources had highly luminous nuclei, brighter than the total stellar light of the host galaxy and their spectra showed high–excitation broad emission lines (leading to the

term “Seyfert Galaxies” for galaxies showing these features). This study by itself however would not be sufficient to launch AGN as a major topic in astronomy.

With the advent and development of radio astronomy in the 40s, 50s and 60s, large catalogues of radio loud sources (see Section 1.1.5 for further details) were compiled during some of the first radio surveys of the sky. Radio sources in this period were separated into Class I and Class II sources. Class I sources were generally found in the plane of the galaxy, whilst Class II were isotropic and likely extra–galactic in nature. Cyg A was the first of these sources confirmed to be extra–galactic (Baade & Minkowski, 1954). Using the redshifts of several emission lines, their results indicated that the galaxy was at a distance of 31 Mpc, well outside the extent of our galaxy. Of equally great interest was that this distance implied a tremendous luminosity in the radio for this galaxy; the term radio galaxy (RG) was used to describe these objects.

The 3C (Edge et al. 1959) and 3R (Bennett 1962) catalogues contained hundreds of sources with resolved optical companions, but also present were compact radio sources with unresolved companions. The first step in associating compact radio sources with optical counterparts came with a lunar occultation of 3C 273. Hazard, Mackey & Shimmins (1963) were able to associate the source with a 13th magnitude star with a faint wisp (later found to be a jet) oriented away from the star. Optical spectra observed by Schmidt (1963) had four emission lines, however all had their wavelengths boosted by about 16 per cent and indicated the object was at a redshift of $z = 0.16$. Concurrently with this work, Matthews & Sandage (1962) had been able to associate 3C 48 with what looked like a star. Follow–up spectroscopy of 3C 48 (Greenstein & Matthew 1963) showed that it too had a peculiar spectrum, with its wavelengths shifted even further with a

redshift of $z = 0.37$.

The idea these objects might still be found within the Milky Way was arguably put to rest following a detailed analysis by Greenstein & Schmidt (1964) of 3C 48 and 3C 273. They considered explanations of the redshift involving (1) rapid motion of objects in or near the Milky Way, (2) gravitational redshifts, and (3) cosmological redshifts. If these sources were indeed found within the galaxy and were a result of gravitational redshift, the observed widths of the emission lines required the line emitting gas to be confined to a small radius around the massive object producing the redshift, but this was unlikely when considering the emission line profiles. On the other hand, the only remaining alternative was that the redshift was cosmological in nature and the sources were galaxies. This would be in keeping with the observed luminosities however this scenario required that these sources be moving at appreciable fractions of the speed of light. Further discoveries of this type of source led to the term Quasi–Stellar Radio Source or Quasar being created to describe these compact radio sources. However, not all quasars appeared to have radio emission (Sandage 1965); indeed only a small fraction of the overall population present radio emission (Sramek & Weedman 1980; Condon et al. 1981). This led to the coinage of the term Quasi–Stellar Object (QSO); objects with both detected and non–detected radio emission that appeared stellar in the optical.

As to the physical nature of these sources, as early as 1959 it had been inferred using a virial argument that if material in the nucleus were to be gravitationally bound and prevent disintegration of the source, it would require an object of extreme mass, of the order $10^{9} M_{\odot}$ (Woltjer 1959). The possibility that the centres of active galaxies were violent, explosive regions led to a wealth of possible ideas

as to their source. For example, Burbidge (1961) suggested that a chain reaction of supernovae (SN) was possible in a dense star cluster in a galactic nucleus. Shock waves from one SN would propagate and compress nearby stars, causing them to explode. Hoyle & Fowler (1963) discussed the idea of a supermassive star (up to $\sim 10^8\,\mathrm{M}_\odot$) as a source of gravitational and thermonuclear energy. Models appeared able to reproduce the observed broad emission lines, with magnetic fields around the star likely giving rise to the observed jets in M87. The currently held view of black hole driven accretion was also suggested as a possible mechanism (Salpeter 1964; Zel'dovich & Novikov 1965; Lynden-Bell 1969, 1978). This proved controversial however owing to the still theoretical nature of these objects at the time and required astronomy to come to terms with the idea that objects with masses several billion times the mass of the sun could exist in regions smaller than the solar system, whilst still outshining their entire host galaxy, a difficult task. Whilst nowadays black holes and their accretion disks are held to be responsible for quasars, it was only through the combined efforts of multiple authors over two decades in various fields that led to this acceptance. For example, the discovery and study of stellar mass black holes within the galaxy, such as Cygnus X–1 (Webster & Murdin 1972), to accept sources of very high mass with very small sizes. Combining optical, infrared, and ultraviolet observations, Malkan (1983) was able to fit the continua of a number of quasars with accretion disc models. High central velocity dispersion in nearby galaxies further implied the existence of an unseen but massive object (Dressler & Richstone 1988; Kormendy 1988). The distinction between stellar mass black holes and the monsters residing at the centres of galaxies required a new term, giving rise to the super–massive black hole (SMBH).

Further study of these peculiar objects yielded more clues as to their physical structure. Greenstein & Schmidt (1964) had already observed an absorption line present in the spectrum of 3C 48. With the study of 3C 191 (Burbidge, Lynds & Burbidge 1966), a spectrum rife with absorption lines was discovered. Other sources were also discovered with strong absorption lines. The determined redshifts however in many cases left lines without identifications, often with the redshift derived from absorption lower than that derived from emission lines. The common interpretation today is that intervening material at the derived absorption redshift overlay absorption spectra on the spectrum of the quasar itself, and this is believed to be responsible for the Lyman–Alpha forest visible in the spectra of high–redshift quasars (the effect is due to electrons in neutral hydrogen in the line of sight at different redshifts transitioning from the first excited state or above to the ground state). A different form of absorption was found in the spectrum of PHL 5200 by Lynds (1967a). The spectrum differed in that broad absorption bands on the short wavelength sides of several species such as C IV ($\lambda\,1550\,$Å), Lyman α ($\lambda\,1216\,$Å) were visible, akin to a P–Cygni profile. Lynds argued this was the result of an expanding shell of gas around the central object. This gave rise to the term Broad Absorption Line Quasars (BAL QSOs in this thesis), and is discussed in greater detail in Section 1.1.3.

1.1.2 The Unified Model

Whilst it is now commonly accepted that AGN have a SMBH at their core, it is still a point of contention as to how such a variety in their properties arises. Why are some AGN highly obscured and others shine brightly in X–ray or have

strange absorption features in their spectra (see Section 1.1.4)? Why do some sources have strong radio emission whilst others do not (see Section 1.1.5)? The observed characteristics of an AGN likely depend on both innate properties such as the availability of gas, the accretion mode etc., as well as external factors such as orientation and the observed wavelength.

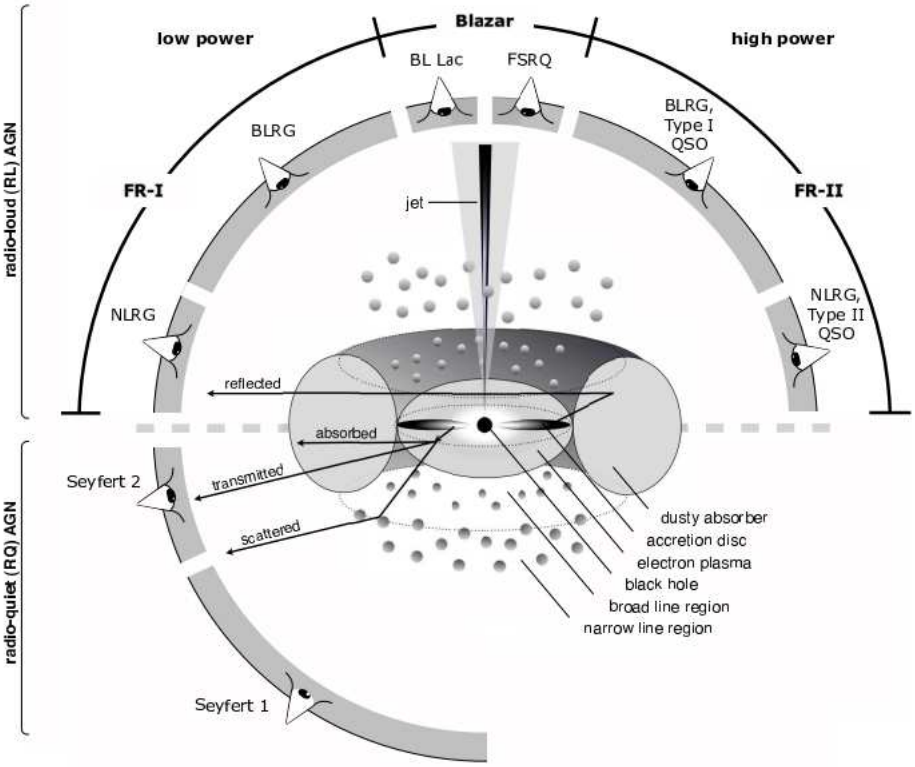

Figure 1.1: A diagram showing the structures and orientations responsible for various observed AGN types, and characteristics of each (Beckmann & Shrader 2012).

The most widely accepted model is that proposed by Antonucci (Antonucci 1993, see Urry & Padovani 1995 for further discussion on the unified model). Its simple premise that different AGN are merely a consequence of orientation is one of its greatest strengths, as it allows easy testing against available data (see Fig.

1.1). This model consists of a central black hole surrounded by material in the process of accretion, itself composed of several parts which are responsible for various observed properties. A thin hot accretion disc (~ 1 parsec in scale) close to the black hole itself is responsible for most of the emission and flat continuum observed at near–infrared (NIR), ultra–violet (UV) and X-ray wavelengths. Broad line clouds close to the black hole also naturally explain the broad observed emission lines due to the high velocities at which the material is moving. A torus of cold dusty material, which is surrounded by clouds responsible for narrow optical lines is found further out (out to ~ 100 parsecs). This torus serves to obscure the continuum, and gives rise to the varying emission line properties for different quasars. In those sources where the accretion disc is visible (i.e. an inclined view), broad permitted and forbidden lines and continuum characteristic of 'Type 1 AGN' such as Seyfert Type 1s, Quasars or Broad Line Radio Galaxies (if the source has radio emission; see Section 1.1.5) are seen. On the other hand, when an observer is oriented such that their line of sight intersects the torus, the AGN is classified as Type 2, such as Seyfert Type–2s and Narrow Line Radio Galaxies. With Type 2 AGN, both permitted and forbidden lines are visible as in Type 1 sources, but these lines are narrower, indicative of lower velocities. This orientation interpretation appears valid; for example, spectropolarimetry of NGC 1068, which shows a Type 2 spectrum overall presents Type 1 emission when polarised light is observed (Antonucci & Miller 1985). These hybrid features were attributed to electrons above and below the disc scattering continuum and broad–line photons into the line of sight. As data have improved, the need for a more geometrically complex model of the absorbing torus has arisen. For example, when observed in the infrared, Seyfert 2 galaxies exhibit a 10 μm silicate emission

feature. In Seyfert 1s, this emission is observed in the form of broad flat–topped peaks shifted toward long wavelengths. Furthermore, interferometric studies of NGC 1068 suggest that dust temperatures as different as $\sim 800\,\mathrm{K}$ and $\sim 300\,\mathrm{K}$ are in close proximity (Jaffe et al., 2004). These results are in utter contrast to smooth density torus models which predict $10\,\mu$m emission in Type 1 AGN and strong absorption in Type 2 sources. A solution to this problem would be if the torus is clumpy (Nikutta, Elitzur & Lacy 2009). The flat topped peaks are a natural consequence of self–absorption by clouds at various distances which allow the flux from the wings of emission peaks to escape. Inteferometric results can also be reproduced by a clumpy torus model, where the temperature differences arise from the hot (facing towards the accretion disk) and cold sides of individual clouds at various distances. The unified model offers a relatively thorough explanation of how the observed emission lines present in AGN spectra are produced, yet offers no explanation as to what determines whether an AGN is radio–loud or radio–quiet, and does not consider the possibility of evolution over time. Furthermore, whilst it includes jets as outflows, it does not include other forms, such as the equatorial winds found in BAL QSOs.

1.1.3 Outflows

Outflows from Active Galactic Nuclei (AGN) appear to be a common feature of QSOs, with 60% having outflows (Ganguly & Brotherton, 2008). Their pervasiveness might even mean that mass ejection is required for mass accretion onto a SMBH, such as removing angular momentum from inflowing material (Konigl & Kartje 1994). The role of said outflows has become an important feature of

contemporary models of the formation and evolution of galaxies over cosmic time (Croton et al., 2006; Ganguly & Brotherton, 2008), being required in theoretical attempts to understand galaxy 'downsizing'. In semi–analytic models of galaxy assembly (Granato et al., 2004), AGN activity removes dense gas from the centres of galaxies, heating up the surrounding Intergalactic Medium (IGM) and at the same time enriching the IGM with metals. This view is supported by recent results (e.g. Gabel et al. 2006) which show outflows with high metallicities which could serve to enrich the IGM. Due to the IGM's low density however, it cannot cool efficiently and so cannot fall back onto the galaxy to fuel star formation (see Section 1.2.1 for further discussion on proposed mechanisms).

Indicators for the intrinsic origin of an absorption line system possibly due to outflows are (1) velocity width, (2) partial coverage, (3) time variability, and (4) high metallicity. Generally, velocity width has been used in the past to identify absorbers due to various shortcomings and assumptions required with the other methods (e.g. partial coverage requires proximity to the source). Those with the greatest velocity dispersions are termed 'Broad Absorption Lines', or BALs (e.g Weymann et al. 1991). These have Full–Width Half–Maximum (FWHM) values greater than $2000\,\mathrm{kms}^{-1}$ and are believed to be evidence of high velocity outflows (see next paragraph). Those with very narrow absorption lines, such that they cleanly intersect the C IV doublet are known as 'Narrow Absorption Lines', (NALs e.g Hamann & Ferland 1999). These have FWHM of less than $500\,\mathrm{kms}^{-1}$. Unlike BALs, they can be due to cosmologically intervening clouds or galaxies unrelated to the QSO, as well as clouds associated with or ejected from the QSO itself. Finally the last type are known as Mini-BALs. These are intrinsic absorbers whose velocity widths are between 500 and $2000\,\mathrm{kms}^{-1}$ (e.g.

Hamann et al. 1997, Churchill et al. 1999) and are also thought to form in BAL winds, possibly from turbulence. In this thesis, we shall concentrate on the first of these, BAL QSOs.

The existence of BAL QSOs has been known for some time (Lynds, 1967a,b), having been discovered shortly after it was realised QSOs were a separate type of radio source. A possible mechanism for the launch and outflow of the material present in BAL QSOs is the accretion–disk wind model (see Figure 1.2) where the wind is launched from the disc and driven by UV line pressure (Murray et al. 1995; Proga, Stone & Kallmann 2000; Luo et al. 2013). However, a 'shielding' gas is also invoked; if the ionisation state of gas is too high, the line–driving becomes less efficient. This shielding material prevents the gas being overionised by the emitted UV and X–ray emission. From recent work, X–ray absorption variability has been detected on timescales of a few years (Miller et al. 2006; Chartas et al. 2009), implying that the shielding gas may not be a fixed structure and is likely susceptible to rotational and outflow/inflow motions. Indeed, absorption line variability is detected by Vivek et al. (2014) in a sample of 22 LoBAL QSOs. Their team attributes the differences to continuum variations and the transit of material across the line of sight. The discovery and investigation of radio–loud BAL QSOs (e.g. Becker et al. 1997, Bruni et al. 2012) has complicated matters further, with both a two component wind (equatorial and polar outflows, e.g Bourguet & Hutsémekers 2010(@) and separate evolutionary phases being invoked (Montenegro-Montes et al. 2008, 2009). Whilst the geometry is still under investigation within the field, the results presented in this thesis argue for an 'orientation effect', in that the various observed properties of BAL QSOs can all be attributed merely to the orientation of the observer. This would mean that

simply because an AGN may not have an absorption feature in its spectrum, one cannot discount the possibility that a BAL wind is still present.

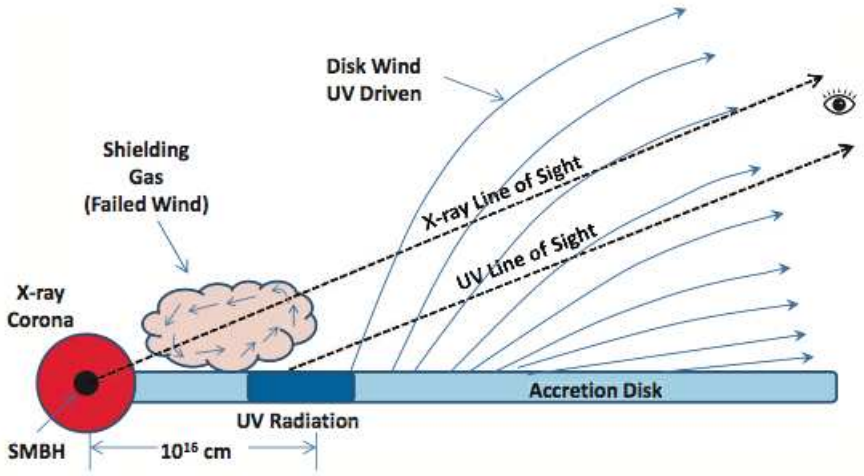

Figure 1.2: A diagram of the disk-wind scenario for BAL QSO outflows (Luo et al. 2013). Material is ejected from the accretion disc and driven out by UV radiation from the disk. BAL QSOs are observed when the line of sight intersects the outflowing wind. The shielding gas prevents overionisation of the material, thereby ensuring a relatively efficient carrier mechanism.

Broad Absorption Lines arise from resonance line absorption in gas outflowing with velocities of up to 0.1c (Weymann et al. 1991; Arav et al. 2001; Hall et al. 2002; Reichard et al. 2003b). One of the spectra from the sample in Chapter 2 is shown in Figure 1.3, which clearly shows some of the strongest features.

BAL QSOs can be further split up based on their absorption features into three distinct subclasses. The first of these are HiBAL QSOs. These contain absorption in Ly α, N V (λ1240 Å), Si IV (λ1394 Å) and C IV (λ1549 Å). These are the most prevalent, making up around 85% of the BAL population. LoBALs contain all of the previously mentioned absorption features seen in HiBALs, but also contain absorption features in Mg II (λ2796, 2803 Å) and other low ionisation species such as Al II (λ1671 Å) and Al III (λ1855, 1863 Å). These comprise around

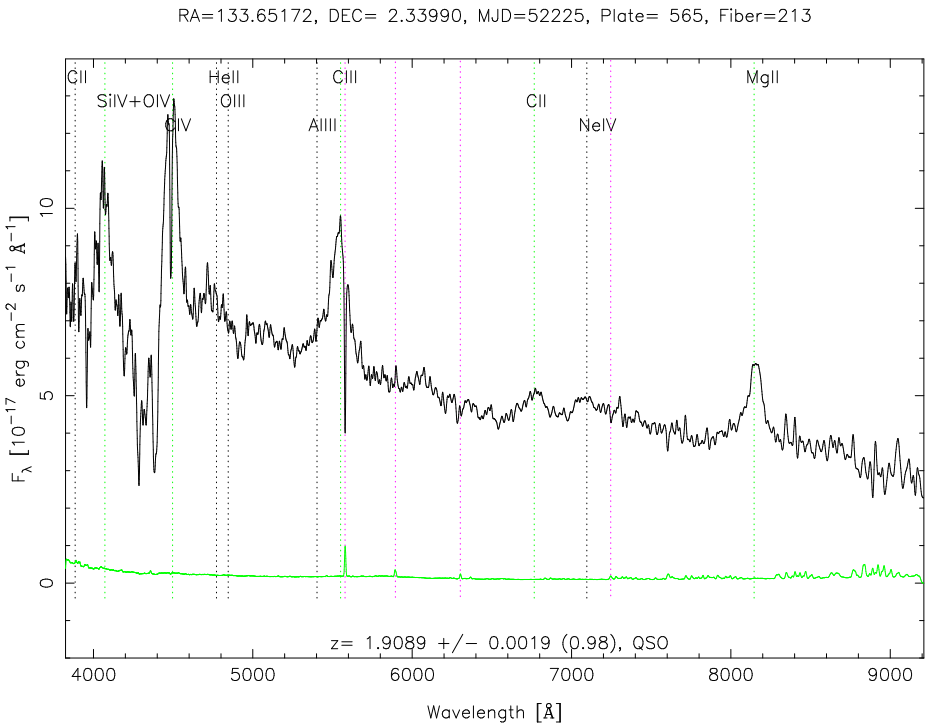

Figure 1.3: The observed spectrum of SDSS085436.41+022023.5, the highest flux emitting BAL QSO in the sample found in Chapter 2 at 250 μm. Clearly visible is the P-Cygni profile of C IV, along with the CIII and MgII emission peaks. The dotted green lines relate to features fit by the SDSS pipeline whilst dotted magenta lines correspond to night sky lines. Dotted black lines are found where a line might be expected but is not found. The green line is merely the error on the number of counts as deduced by the SDSS.

15% (Sprayberry & Foltz 1992 estimated 17%). The third and final class are FeLoBALs, which show the absorption features of LoBALs, but as well as this show absorption features arising from metastable excited levels of iron.

As a subclass of AGN, BAL QSOs until recently were quoted as making up around 10-15% in QSO surveys (Weymann et al. 1991; Tolea et al. 2002; Reichard et al. 2003b). However, Trump et al. (2006) quoted a much higher BAL QSO population; an observed fraction within the 3rd Data Release of the Sloan Digital Sky Survey (Schneider et al., 2005) of 26%.

$$\mathrm{BI} = \int_{3000}^{25000} (1 - \frac{\mathrm{f(V)}}{0.9})\mathrm{C}\,\mathrm{dV} \tag{1.1}$$

The argument put forward by Trump et al. (2006) is that the definition of BAL QSOs, the 'Balnicity index' or 'BI' in equation 1.1 is not a valuable method to use, instead opting for the use of the 'Absorption Index' or 'AI' in equation 1.2.

$$\mathrm{AI} = \int_{0}^{29000} [1 - \mathrm{f(V)}]\mathrm{C}'\,\mathrm{dV} \tag{1.2}$$

In both the BI and AI, f(V) is the normalised flux as a function of velocity displacement blueward from the line centre (e.g. from C IV, λ1549 Å). The value of C is set to be zero, becoming 1.0 when the quantity in brackets has been continuously positive over an interval of 2000 kms^{-1}. However, the BI only counts as absorption those troughs dipping 10% or more below the estimated continuum. This limit should ensure the exclusion of non–BALs where the continuum has been estimated too highly. In the case of the AI, contiguous troughs which exceed the minimum depth (10%) are considered as with the BI, but only need to be continuously positive over an interval of 1000 kms^{-1} for C' to be taken as

1.0. This then means that narrower features which can often be attributed to absorption close to the QSO (but perhaps unrelated to the BAL wind) lead to a positive AI.

The AI then is therefore designed to be less strict than the BI, so it is to be expected that a larger number of QSOs will be classified as BAL QSOs, objects which using the BI would be excluded from a sample. In an attempt to rectify the problem, Knigge et al. (2008) attempted to determine the *intrinsic* BAL QSO fraction as well as the *observed* fraction, using approaches designed to be stricter than the AI, but more complete than the 'classic' definition of a BAL QSO from the BI. After correcting for bias, they give the *intrinsic* fraction as 0.17 $\pm$ 0.01(statistical error) $\pm$ 0.03(systematic error), having an upper limit of $\sim$ 0.23. It also appeared the AI led to a bi–modal distribution, indicating there was significant contamination from non–BAL QSO sources. However, the question of definition remains a fundamental problem when studying the properties of BAL QSOs. More recently, other classification schemes (e.g. Scaringi et al. 2009) have used a combination of simple metrics, neural networks and visual inspection. Perhaps somewhat unsurprisingly, Scaringi et al. (2009) find that the raw BAL QSO fraction (12.5%) appears to have a dependence on signal-to-noise, increasing from 9% in low signal-to-noise data, up to 15% and that furthermore, no single existing metric produces clean and robust BAL QSO classifications, requiring a variety of complementary metrics.

Until relatively recently, it was thought that broad–absorption features and radio loudness were mutually exclusive (e.g Stocke et al. 1992). However with the advent of the FIRST radio survey, the existence of radio–loud BALs were confirmed (e.g. Becker et al. 1997, 2000; Gregg et al 2000; Gregg, Becker & de

Vries 2006; Brotherton et al. 2006). BAL QSOs in general also appear to be self-absorbed in soft x-rays (Green & Mathur, 1996; Gallagher et al., 2002, 2006; Gibson et al., 2009). This observed X–ray deficiency is found to correlate with the absorption strength and velocity of the C IV BAL (Gallagher et al. 2006; Gibson et al. 2009) strengthening the argument that a shielding gas is present and that furthermore, this has a direct effect on the observed emission found in BAL spectra. Using current X–ray observatories, the X–ray absorption column density around these objects can be constrained up to $\sim 5 \times 10^{23}\,\mathrm{cm}^{-2}$. Above this level, even hard X–rays are absorbed, leading to the X–ray spectrum being dominated by a scattered component. Multi–wavelength data can ameleoriate the loss of data in this regime by allowing an estimate of the X–ray weakness and allows a comparison between BAL QSOs and non–BAL QSOs (e.g. Gallagher et al. 2007). This indicates that in the general case, this weakness is entirely due to absorption. Indeed, X-ray weaker sources have higher energy photons (Gallagher et al. 2006).

Of course, that is the general case in X–rays but what of other wavelengths, and does orientation fully explain the observed properties of BAL QSOs relative to non–BAL QSOs? Work continues in trying to find the overall multiband statistical properties of QSOs exhibiting BAL flows (e.g Miller et al. 2009) and how this may affect the geometries close to the accretion disk. Relative to the QSO population at large, they are found to be redder than non-BAL QSOs (Brotherton et al., 2001; Scaringi et al., 2009). Sprayberry & Foltz (1992) compared the composite spectra of BAL QSOs to those without broad absorption lines, finding that LoBAL QSOs have significantly redder continua consistent with a line of sight dust hypothesis. In that work, they argued that the spectral shape of LoBAL

QSOs was similar to that of HiBAL QSOs when reddened by an SMC–type extinction law with E(B–V) ~ 1. Furthermore, whilst X–ray variability is observed, this is not extreme when compared to non–BAL QSOs (Saez et al. 2012). Broad absorption line variability has also been detected at optical wavelengths by (Hall et al, 2011). There they find that the QSO FBGS J1408+3054, previously an FeLoBAL for 20 years, has become a LoBAL and MgII absorption is far weaker than during previous observations. This would suggest that some structure in the BAL wind has been removed from the line of sight. This all strengthens the argument for BAL QSOs being an orientation effect, with BAL QSOs drawn from the same parent population as non–BAL QSOs (Reichard et al., 2003b).

An alternative explanation is that the different species (HiBAL, LoBAL and FeLoBAL) may be separate stages in an evolutionary phase. For example, even when intrinsic X–ray absorption is taken into account, LoBAL QSOs remain X–ray weak, with work by Streblyanska et al. (2010) suggesting that LoBALs and HiBALs may be physically different objects. An example of a mechanism that could cause intrinsic X–ray weakness is wind quenching of the accretion-disk corona, as proposed by Proga, Stone & Kallmann (2000), where the coronal X–ray emission is suppressed when the failed disc wind falls into the corona and makes it "too dense, too opaque, and consequently too cold". The study performed by (Gregg, Becker & de Vries, 2006) on eight BAL QSOs finds a strong anti–correlation between radio loudness and absorption feature strength, which can be relatively easily explained if an evolutionary phase is invoked. In this scenario, the BAL–producing material prevents the development of strong radio jets and lobes (their entire sample were FRII, see Section 1.1.5 for an overview of radio morphology). Composite Spectral Energy Distribution (SED, see Section

1.3.2 for an explanation of this term) work by Gallagher et al. (2007) using data ranging from from X-ray to radio wavelengths finds similarities between HiBAL and non–BAL QSOs but differences when LoBAL QSOs are considered. As noted by others, Gallagher et al. (2007) find UV/Optical photometry that indicates stronger reddening and X–ray weakness in LoBAL QSOs. It should be noted however that their team were unable to create a LoBAL composite owing to a lack of sources and there were insufficient detections for a comparison of FIR or submm photometry for the LoBAL QSO sample. One should also be wary of these conclusions since the absorbed nature of BAL QSOs means that X-ray data will be limited in quality, so these findings cannot be taken as conclusive.

1.1.4 Obscured QSOs

Obscured AGN have enjoyed particular attention for several decades due to a belief that a major portion of the power from accretion onto black holes is absorbed by circumnuclear matter (Fabian1999 1999; Nulsen & Fabian 2000). Indeed, it is expected that they are major contributors to the cosmic X–ray background (XRB, Gilli, Comastri & Hasinger 2007; Cowie, Barger & Hasinger 2012), with energies above 1 keV being made up of the summed emission from point sources (below 1 keV the Galaxy dominates the X–ray intensity). Whilst the majority of X–ray point sources detected with photon energies between 2–8 keV are moderately obscured, an additional heavily obscured population is required, with around 50 per cent of the XRB being missed at energies above 8 keV (Worsley et al. 2004, 2005). Fig. 1.4 shows the XRB spectrum from 0.2 to 400 keV as collated from various instruments by Gilli (2004). Population synthesis models

(e.g. Gilli, Comastri & Hasinger 2007; Ueda et al. 2014) including both Type 1 and Type 2 AGN, Compton–thick and Compton–thin sources, have attempted to describe the observed redshift and luminosity distributions of these sources, as well as their source counts and the overall shape of the XRB. From Ueda et al. (2014), the absorption column density plays a role in the placement of an AGN within the XRB, with the model spectra of the most obscured AGN ($N_H = 25.5$) peaking at energies of around 40–50 keV. The properties of these obscured AGN also appear to vary with redshift. Low luminosity sources (log L_X 42–44 erg s^{-1}) in both the soft X–ray (0.5–2 keV) and hard (2–10 keV) bands peak at $z \sim 0.7$–1.0. In contrast, higher luminosity sources ($L_X > 44$ erg s^{-1}) within these bands appear to peak at redshifts of around 2–2.5, and their co–moving space density declines rapidly to the present day by almost two orders of magnitude (Gilli, Comastri & Hasinger, 2007). In comparison, the co–moving space density of low luminosity sources increases by less than a factor of 10 from $z = 0$ to $z \sim 0.7$–1.0 and decreases thereafter. By understanding these interdependences between obscured fractions, redshift and luminosity, the connection between AGN activity and formation of the host galaxy can be determined.

Of particular relevance to this thesis is the extensive work performed on a sample of X–ray absorbed QSOs in the submm (Page, Mittaz & Carrera 2001; Page et al. 2004; Stevens et al. 2005) and how they relate to the unobscured fraction of X–ray sources. In an initial sample of 8 sources, it was found that the four with redshifts $z > 1.5$ were detected as Ultra Luminous Infrared Galaxies (ULIRGs, defined as galaxies with infrared luminosities $> 10^{12}$ $L_\odot$) whilst those below were not. A larger sample of 20 absorbed sources were also observed and compared to a sample of unabsorbed QSOs. A correlation between far–infrared

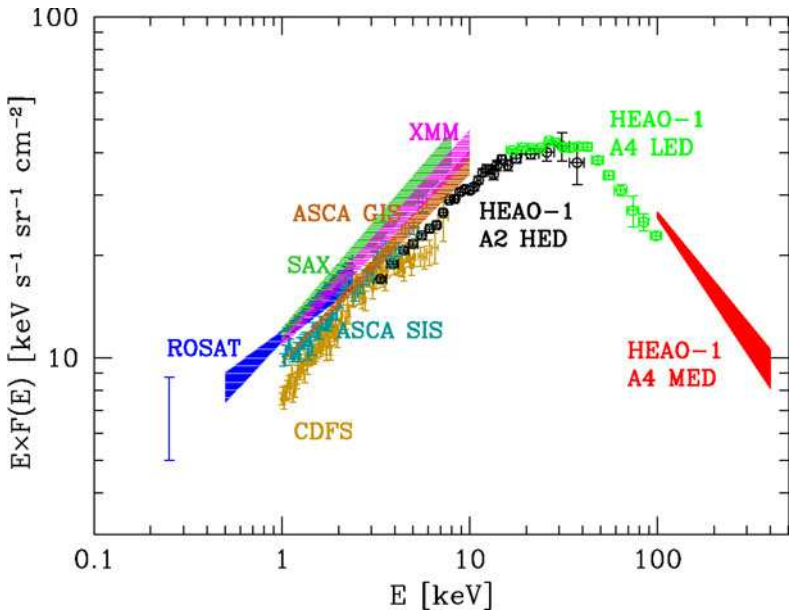

Figure 1.4: The XRB spectrum from 0.2 to 400 keV as collated from various instruments by Gilli 2004). Those instruments and the references to them are: ROSAT 0.25 keV (Warwick & Roberts 1998); ROSAT 0.5–2.4 keV (Georgantopoulous et al. 1996); HEAO-1 A2 HED + A4 LED (Gruber 1992; Gruber et al. 1999); HEAO-1 A4 MED (Kinzer et al. 1997); SAX (Vecchi et al. 1999); ASCA SIS (Gendreau et al. 1995); ASCA GIS (Kushino et al. 2002); XMM (Lumb et al. 2002); CDFS (Tozzi et al. 2001).

luminosity and redshift was found, indicating evolution of the star formation rate (SFR) in the BAL QSO sample and that intriguingly unabsorbed QSOs appeared to reside in less submm luminous hosts. This implied that unabsorbed QSOs had already passed through their main star–forming phase. Following consideration, it was determined that only an evolutionary phase might explain these findings, where the X–ray absorbed sources were observed during a transition phase between the main star–forming epoch of the galaxy and the QSO phase. Quasar feedback would remove the majority of the gas leaving behind the QSO as an optically observed QSO.

1.1.5 Radio AGN

Normal spirals will often have weak radio emission (for example from supernova remnants, see e.g. Thompson, Quataert & Murray 2009). However a fraction of galaxies are found to be highly luminous at radio wavelengths. These Radio AGN are by no means a homogeneous population and are split into Radio–Loud AGN (RL AGN) and Radio–Quiet AGN (RQ AGN). One manner of determining what constitutes a RL AGN is to use the following ratio:

$$\mathrm{R} = \frac{\mathrm{S_{5GHz}}}{\mathrm{S_B}} \geq 10 \tag{1.3}$$

where S_{5GHz} is the observed flux density at 5 GHz and S_B is the observed flux density in the optical B band (4400 Å) as described in Kellermann et al. (1989). Most RQ AGN are far weaker, with $0.1 < \mathrm{R} < 1$, though there are of course cases

near the boundary. Other definitions exist, such as that by Ivezić et al. (2002):

$$\mathrm{R} = \mathrm{Log}(\frac{\mathrm{F_{1.4GHz}}}{\mathrm{F_i}}) \geq 1 \tag{1.4}$$

where $\mathrm{F}_{1.4GHz}$ is the observed flux density at 1.4 GHz and F_i is the observed flux density in the optical i band (8060 Å) with no k–correction applied. In both equations, the flux should be taken at that specific wavelength/frequency. The choice of relating optical flux to radio power is not a coincidence. For example, Ivezić et al. (2002) find that when their sample of FIRST radio quasars are placed in a radio flux–optical plane, radio loud quasars have a redder median colour and show a 3 times larger fraction of objects with extremely red colors in the i–band.

It has also been observed that generally all RLQs have BH masses greater than $10^8\,\mathrm{M}_\odot$ (Rawlings & Jarvis 2004) which would imply at least one pre–requisite for a radio–loud source is high black hole mass. In the case of radio–quiet sources, there is a far greater range, with radio–quiet sources having BH masses similar to RLQs or as low as $10^7\,\mathrm{M}_\odot$. Therefore, merely defining a source as radio–loud or radio–quiet based on radio luminosity alone will severely bias any sample if one considers that both strong and weak radio emission are not evidence of a significantly different central engine. Of course, it is entirely possible that other parameters are responsible for radio loudness such as environment or black hole spin (see Section 1.2.3 for further discussion), and radio–loudness may even be a phase, with all AGN at some point in their lifetimes being 'radio–loud'.

The emission line features for RLQ and radio–quiet QSO (RQQ) sources are very similar (hence why it is thought that the geometry around the central black hole is almost identical). As with Seyfert galaxies, radio sources can be split into

broad–line radio galaxies (BLRGs) and narrow–line radio galaxies (NLRGs), corresponding to different orientation angles and the visibility of the accretion disk. The unified model is relatively appropriate to explain the emission lines observed in the spectra of AGN, yet an orientation model is obviously unable to explain why some AGN are extreme radio sources and have visible jets whilst others are relatively faint. Broadly speaking, these jets are highly collimated outflows of material. These are believed to originate at or near the accretion disc and carry relativistic electrons and positrons. Through synchrotron emission, these jets are visible and allows a determination of the inclination angle. Radio maps of these powerful radio galaxies often show a double–lobed structure extending as far as (in a few cases e.g PKS 0637-752, Godfrey et al. 2012) a megaparsec from the central source. These lobes are joined to the central source by the jets which are likely the energy transport mechanism for these lobes. These sources can be classified via the Fanaroff–Riley classification system (Fanaroff & Riley, 1974) which in itself offers yet another manner of classifying radio sources. FR I sources are those that have core–dominated emission, where the observed luminosity decreases as a function of distance from the central host galaxy. In FR II sources, the lobes are far brighter than the host galaxy, with increasing luminosity as a function of distance. This distinction is believed to arise due to the relativistic jets in FR IIs remaining relativistic outside the host galaxy and interacting at high speeds with the surrounding IGM and thereby dumping large quantities of energy into the medium, a highly visible feedback mechanism.

1.2 AGN Environments

Currently, it is commonly accepted that structure in the universe formed from hierarchical processes, in which smaller structures collapse to form galaxies and then, through coalescence, form larger galaxies and eventually, galaxy groups, clusters and superclusters. However, 'antihierarchical' behaviour has been observed, with dense large-galaxy-size structures collapsing at earlier epochs and evolving faster than smaller galaxies (Heavens et al. 2004; Renzini 2006). Most massive galaxies in the present day universe are found in the centres of rich clusters. A natural extension of hierarchical evolution is that most massive galaxies should be young and blue, yet observation finds that these galaxies tend to be old and red. This suggests that the bulk of stars should have formed at early times in starbursts. Furthermore, large cooling flows of material would be expected in the central regions of clusters (Fabian 1994). Contrary to this expectation, *Chandra* and *XMM–Newton* observations indicate that there is significantly less cooling than expected from cooling flow models (Böhringer et al. 2001, Peterson et al. 2003; Peterson & Fabian 2006; McNamara & Nulsen 2007). This is known as the cooling–flow problem. Feedback from the central AGN is believed to be responsible for this discrepancy (see 1.2.1).

It has been known for some time that most if not all galaxies contain a SMBH at their centres, and that black hole growth and galaxy growth appear to be correlated (Magorrian et al. 1998; Ferrarese & Merritt 2000; Gebhardt et al. 2000; Gültekin et al. 2009), though an alternative explanation is that it is simply the result of repeated mergers (see Jahnke & Macció 2011). Furthermore, both AGN acitivity and star formation peak at around $z \sim 2$ (Madau, Pozzetti & Dickinson

1998; Merloni, Rudnick & Di Matteo 2004). This indicates that either they formed from a similar reservoir of cold molecular gas and dust (e.g. Kauffmann et al. 2007) or they are affecting each other (or a mixture of both). Exactly how they are related remains poorly understood however.

1.2.1 Feedback

A wealth of simulations have been carried out over the past two decades to determine how AGN activity might affect galaxy evolution. AGN activity appears to be a requisite ingredient in galaxy models to explain the observed cutoff at the bright end of the galaxy luminosity function and the truncation of star formation in massive galaxies. It is now believed that the AGN directly pumps energy into the surrounding medium.

Efforts to include these mechanisms (e.g. Bower et al. 2006; Croton et al. 2006; Sijacki et al. 2007; Ciotti, Ostriker & Proga 2010) have generally focussed on two modes. The first of these is a "radio mode" (also "maintenance mode") whereby a relativistic jet can heat interstellar gas and the intercluster medium (ICM). This maintains a hot gaseous halo around the galaxy, suppressing further infall of mass (Best, 2007a) and acts as a mechanism for self–regulation by the BH. This method of feedback is thought to be the most efficient and is associated with BHs with low mass accretion rates (Bower et al. 2006; McCarthy et al. 2010). Secondly, a proposed "Quasar mode", which serves to stop star formation with an outflow of greater mass but of a lower velocity, which is believed to originate at the accretion disk. At the same time, this outflow removes any leftover gas that might serve to shroud the galaxy, turning it into a 'classical' optically visible QSO, and

in the process quenching star formation. This is believed to occur during periods of high accretion (Silk & Rees 1998). Simulations of these outflows suggest that around 5–15 per cent of the accretion energy must couple to the surrounding gas, accelerate it outwards and thereby prevent it being used in future BH growth (Di Matteo, Springel & Hernquist 2005; Debuhr, Quataert & Ma 2012). There is still ongoing discussion as to how these radio jets may affect or be affected by their environments, with studies both suggesting a negative (Rawlings & Jarvis 2004) and positive (Wiita 2004) effect on star formation activity. For example, Rosario et al. (2013) find that AGN are preferentially hosted by star–forming galaxies out to $z \sim 2$ rather than quiescent galaxies. The connection might then simply be that both AGN activity and star formation activity require a significant amount of gas.

1.2.2 The Host galaxy

How does this feedback affect the evolution of the host galaxy? As already discussed, AGN feedback can heat and disperse cold star–forming gas, truncating star formation. Whilst the processes behind the apparent correlation between host galaxy morphology and the presence of jets remains unclear, it appears that radio–loud AGN are preferentially hosted in elliptical galaxies (e.g. Matthews, Morgan & Schmidt 1964; O' Dowd, Urry & Scarpa 2002; Best 2007b though there are exceptions, see Keel et al. 2006). Seyfert galaxies on the other hand tend to reside in spiral galaxies (e.g. Adams 1977). This suggests the energy input from AGN is sufficient over cosmic time to drastically affect the properties of the host galaxy.

One way in which the host galaxy might be influenced by an outflow is by chemical enrichment of galactic gas and the ICM. For example, Gabel et al. (2006) have shown the QSO J2233–606 has outflows with a high metallicity which could serve to enrich the ICM. According to e.g. Hamann & Ferland (1999), most chemical enrichment is likely to occur in massive galaxies in which rapid, large scale star formation creates the majority of the galaxy, at redshifts of at least z ∼2–3. However, the expulsion of gas from a galaxy will effectively truncate star formation, and continued feedback will move metal enriched gas from the haloes of these galaxies into the ICM. This will create flatter metallicity profiles both in galaxies and in clusters than would otherwise be expected.

Simulations of galaxy mergers (Springel et al., 2005a) show AGN feedback heats the Interstellar Medium (ISM) and inhibits star formation, with outflows providing the energy and momentum feedback for the ISM of the host galaxy. On the other hand, Gaibler et al. (2012) finds that if a radio jet is oriented within the disc of the host galaxy, a ring–like structure of stars may be formed over time, where gas and dust is removed from the central regions through the creation of a shockwave which forces star formation to proceed at larger radii from the central AGN. Recent work (McCarthy et al., 2010) finds that by excluding feedback from accreting black holes in galaxy group simulations, the temperature profiles are highly peaked and in disagreement with many of the observed properties of galaxies, such as hot gas mass fractions and SFRs, as well as suffering from the overcooling problem, the resulting stellar mass fraction being several times larger than observed.

It therefore appears that even on a galactic scale, the problem of AGN feedback and how it affects its host galaxy is a non–trivial one. What then of the

surrounding environment?

1.2.3 The Environment

As far back as the late 60's, the possibility that QSOs might reside in galaxy clusters (Bahcall, Schmidt, & Gunn 1969) had already been considered. This discovery was inferred by comparing the published positions of 5 QSOs with $z < 2$ with the approximate geometrical boundaries of galaxy clusters nearby, and spectroscopy was used to determine their redshifts. The agreement in direction and redshift for these sources was taken as evidence of QSOs being associated with clusters.

Consequently, AGN have been used as signposts to high–redshift clusters and proto–clusters with great success (Ivison et al. 2000; Stevens et al. 2003; Venemans et al. 2007; Doherty et al. 2010; Galametz et al. 2010, 2012; Mayo et al. 2012; Wylezalek et al. 2013), thereby improving our understanding of galaxy formation in the early universe. It is therefore feasible that mergers may play a major role in feeding the central SMBH and enhancing star formation to levels such as those found in ULIRGs (e.g. Genzel & Cesarsky 2000). This can be imagined as the consequence of a merger bringing large amounts of gas and dust to the central regions of a galaxy, thereby providing raw material for accretion by the SMBH and a fresh reservoir of cold gas for star formation.

Some of the strongest cases of AGN feedback are visible in clusters of galaxies, where the central AGN hosted by the brightest cluster galaxy (BCG) drives large outflows of relativistic material. As noted before, material is expected to be falling onto galaxies in the centres of rich clusters in the form of cooling flows,

yet observations find there to be little doing so. As the jets propagate through the ICM, they force X-ray emitting gas aside, creating large, visible cavities that appear as areas of reduced surface brightness, indicating cooling is being suppressed (McNamara et al. 2000; Hlavacek-Larrondo et al. 2013). Energy from these cavities propagates through the ICM as shock and sound waves (Sanders & Fabian 2008).

Therefore it appears that central AGN are able to influence their host clusters on mega–parsec scales. However, the question remains whether particular types of AGN prefer specific types of environments, and is it a case of "nature versus nurture" i.e. does the AGN define its environment or is environment a defining factor in AGN properties?

An initial step towards this is investigating whether radio–loudness is influenced by environment. Yee & Green (1984) attempted to answer this question, and found that there was indeed a larger overdensity around RLQs at $0.05 < z < 0.55$. This was later refuted with a larger sample (Yee & Green 1987). Ellingson, Yee & Green (1991) added RQQs to this sample finding that RQQs appeared to prefer less dense environments. At higher redshift ($0.9 < z < 4.2$), Hutchings et al. (1999) found that RLQs occupy denser fields in the near-infrared than RQQs. However, Wold (2001) and McLure & Dunlop (2001) find the environments of RLQs and RQQs to be indistinguishable at $z \sim 0.2$ and $0.5 < z < 0.8$. These results, seemingly at odds with each other, might be explained by selection effects and small number counts. It is well known that the luminosity–redshift degeneracy will populate higher redshift samples with more extreme objects than those at lower redshifts. This might well explain the varying results. More recently, Falder et al. (2010) found that RLQs reside in denser environments than

RQQs using a similar method to that presented in Chapter 3 at $z \sim 1$. This sample differed from previous studies in that it was selected at one cosmic epoch, to minimise cosmological evolution within the sample. A strong correlation between radio luminosity and stellar mass overdensity, for which either jet confinement or black hole spin was believed to be responsible, was also found (though Mayo et al. 2012 find no correlation at 24 μm in their sample). In the case of jet confinement, the argument proffered by Barthel & Arnaud (1996) to explain the anomalously high radio emission of Cygnus A relative to its infrared emission is thus; if the AGN sits within a dense X-ray halo such as that within a cluster, efficient transfer of AGN power to the surrounding medium is directly responsible for boosting of radio luminosity. In the case of the sample presented in Chapter 3.7, it is feasible that if RL AGN prefer to reside in denser environments, the enriched ICM (from galaxy harassment and mergers in an overpopulated field) will boost radio luminosity over that of their radio–quiet counterparts, providing anomalously high radio luminosities. Indeed, Barthel & Arnaud (1996) suggest the luminosity may be boosted by up to 1.5 orders of magnitude, which might be responsible for the radio correlation observed in Chapter 3. On the other hand, various studies (Wilson & Colbert 1995; Moderski, Sikora & Lasota 1998; Tchekhovskoy, Narayan & McKinney 2010; Garofalo, Evans & Sambruna 2010; McNamara, Rohanizadegan & Nulsen 2011) suggest that black hole spin may be at least partially responsible for the observed radio properties of Type 1 and Type 2 AGN. Generally, the Blandford–Znajek mechanism has been invoked (Blandford & Znajek 1977), in which energy is extracted from a spinning black hole by the movement of magnetic fields. Garofalo, Evans & Sambruna (2010) suggest a physical difference between RL AGN and RQQs where their properties may sim-

ply be due to a retrograde or prograde black hole spin respectively (relative to the accreting material), with retrograde spin causing highly collimated jets to form. However, as noted by Garofalo, Evans & Sambruna (2010), this configuration will be dynamically unstable, and will move towards a prograde spin over time, naturally predicting a reduction in radio power to the present day. It is then feasible that in the densest environments, the AGN will likely have undergone more recent mergers with larger objects, conserving or increasing black hole spin in a particular direction. If those mergers are with galaxies of equal mass black holes or where a larger black hole spins rapidly and the merger occurs in the prograde direction relative to the black hole spin (Hughes & Blandford 2003), a retrograde system is created. Such mergers may partially explain the correlation between radio–luminosity and stellar mass overdensity observed by Falder et al. (2010). Of course, until black hole spin becomes an observable parameter, this explanation must frustratingly remain conjecture.

These prior studies have not focussed on the far–infrared (FIR) environment, instead observing stellar mass and evolved galaxies and avoiding the peak of the FIR grey–body. In reality, there have been few studies investigating how AGN activity and star formation activity in the environment are interwoven. This is directly attributable to both the difficulty with which the FIR can be observed from the ground and small datasets prior to the launch of *Herschel* and commissioning of SCUBA–2. Even so, it appears AGN reside in overdensities of star forming sources (Best 2002; Stevens et al. 2003; Greve et al. 2007; Stevens et al. 2010). In Stevens et al. (2010), it was found that there was an enhanced level of activity around QSOs relative to the field, with sources having SFRs of the order of 400–1300 $\mathrm{M_{\odot}\,Yr^{-1}}$. Intriguingly, this was still lower than that seen

around higher redshift AGN. The implication is that star formation activity is already on a downward trend as early as $z \sim 2$ in the presence of AGN.

1.3 Infrared Astronomy

Infrared radiation was originally discovered by William Herschel in 1800. Since then, improved technology allowed first radio (for obvious reasons following visible light) then higher energies like X and gamma–rays and finally near–, mid– and FIR observations. Why bother however? What does FIR astronomy show us that other wavelengths miss? FIR observations have several benefits over other wavelengths. For example, the advantage of observing in the FIR is that dust is optically thin to it. This is important as the earliest stages of star formation, planetary formation and galaxy formation are concealed by large quantities of dust. If our view is restricted to only the optical regime, the dust grains are similar in size to optical wavelengths, around one micron or less, making them effective absorbers and scatterers of that light. Far–IR and submm wavelengths are able to penetrate that dust. Secondly, and perhaps most importantly for cosmological surveys of galaxy formation and evolution, it allows us to observe sources at extreme cosmological distances. In Fig. 1.5, the effect of redshift on the SED of a source such as Markarian 231 (Mrk 231) is presented, as well as the observed flux–density in different SPIRE bands of *Herschel* (see Section 1.3.4 for further details).

As visible in Fig. 1.5, the observed flux in the 250, 350 and 500 μm bandpasses visibly varies, and at certain redshifts, it becomes more prudent to use longer wavelengths to be able to detect greater fluxes. Objects can be observed to much

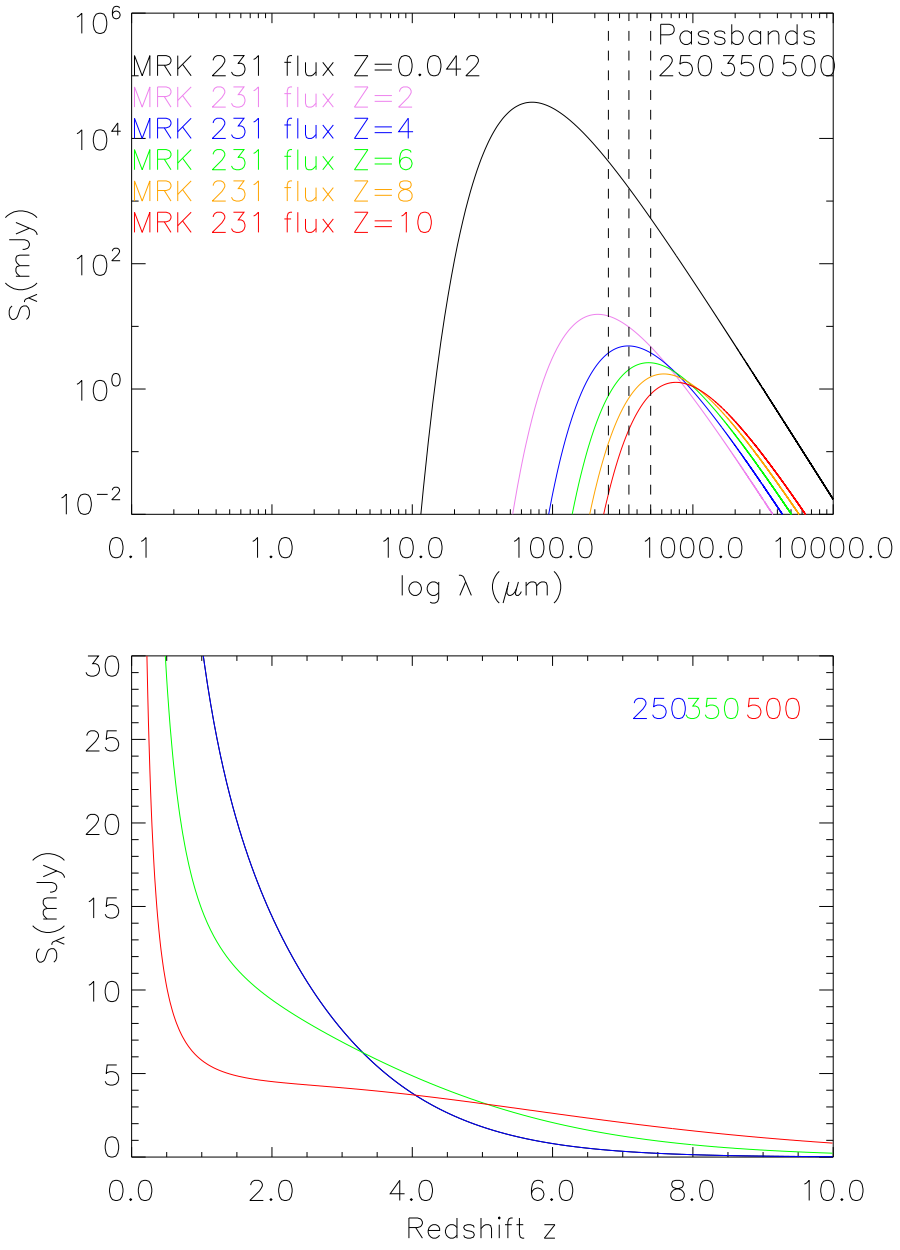

Figure 1.5: The upper panel shows a modified black body fit to the observed SED of Mrk 231 if placed at various redshifts. Clearly visible is how cosmological dimming serves to weaken the signal, as well as shifting the rest–frame wavelength to longer observed wavelengths. The lower panel shows the flux–density observed in each *Herschel* bandpass for Mrk 231 as it is observed at higher and higher redshifts. Negative k–correction allows observations to higher redshifts when using the longest (500 μm) wavelength bandpass.

greater distances due to the negative k–correction, as at greater redshifts, we are observing at shorter wavelengths on the rest–frame SED and closer to the peak. The flux density decreases much less steeply at longer wavelengths, with the negative K-correction having a sufficiently large effect at 500 μm to allow flux densities of greater than 1 mJy out to redshifts of 10, by which time the flux density at 250 μm is around zero as is 350 μm. The instrument with which they are observed must be therefore be incredibly sensitive and there will be a corresponding reduction in resolution unless this is accounted for by using a larger dish or mirror.

Of course, these benefits have come at some cost. The atmosphere on Earth hides a significant proportion of the universe's light from view. The Earth's atmosphere only allows full transmission of optical and radio wavelengths at sea level. Therefore, until the introduction of space–based telescopes in the early 80s, infrared observations were limited in scope and wavelength at which surveys could be carried out. Water vapour in the atmosphere is particularly troublesome in the infrared. Fluctuating amounts of water vapour in the atmosphere lead to varying levels of absorption, thereby increasing or decreasing the transmissivity of the atmosphere. This can cause phase fluctuations in interferometers, where the signal, propagating more slowly through moist air than dry air, arrives at antennae at different times. This causes a reduction in resolution (as the difference in arrival time contains information about the position of the source) and a weakening in signal strength. At submm wavelengths water vapour is the main contributor to atmospheric opacity, and causes attentuation of astronomical signal (signal which can then not be retrieved). Water vapour also has several strong lines due to rotational transitions across the submm and millimetre wavebands, such

as at 380 GHz ($\sim$790 μm) and 183 GHz ($\sim$1640 μm) and will radiate thermally, thereby increasing the noise on any submm observation. Finally, the atmosphere itself radiates as a black body at $\sim$270 K, which will overwhelm the astronomical signal if not compensated for. However, an estimate of the astronomical signal from a source can be derived by observing a calibrator of known flux such as a planet or galaxy. Since cold air is less able to hold water vapour than warm air, observatories are placed at high altitude or in a colder climate. Still, there is a strong diurnal effect because the heating of the ground by the sun drives much of the fluctuation in water vapour levels. In good weather atop Mauna Kea for example, observations can be carried out between 5pm and 7am, though it is often best to allow a couple of hours so that the atmosphere settles up to high altitudes.

1.3.1 The Cosmic Infrared Background and Confusion

Throughout the universe, objects are bathed in the extragalactic background light (EBL). Excluding the Cosmic Microwave background (CMB), this light is the sum of the energy radiated by all galaxies across all cosmic epochs. The energy distribution is composed of two main peaks; at $\lambda \sim 1\,\mu$m produced by starlight, and a second peak at $\lambda \sim 100$–$200\,\mu$m corresponding to starlight reprocessed and emitted by dust (Hauser & Dwek 2001). One of these components of the EBL is the Cosmic Infrared Background (CIB), which is a diffuse radiation field of extragalactic origin. It represents approximately half of the luminous power in the universe (Puget et al. 1996; Lagache, Puget & Gispert 1999; Dole et al. 2006) and can be defined as the part of the present radiation content composed of the

long wavelength output of all sources across all cosmic epochs. It is created when ultraviolet and optical photons emitted by stars are absorbed by interstellar dust and reradiated at infrared wavelengths. Foreground emission from the galaxy must be removed. For example to observe the CIB, galactic cirrus, as well as (to a lesser extent) zodiacal dust emission can all contaminate results. These contributions must be estimated and removed if the true intensity of the CIB is to be determined. Similarly, the COB and CMB have their own problems. Terrestrial airglow, the zodiacal light, galactic stars and scattered starlight from dust can all boost the observed COB. In the case of the CMB, sources of synchrotron emission, free–free emission and even the Sunyaev–Zeldovich effect (Sunyaev & Zeldovich 1970) as CMB photons pass through clusters must all be taken into account and removed. Fig. 1.6 (from Dole et al. 2006) shows the intensity of the CIB in comparison with the Cosmic Optical Background (COB) and the CMB. The boxes indicate the brightness of each component; interestingly, the CIB and COB have almost the same energy output, which in total is $47\,\mathrm{nW\,m^{-2}\,sr^{-}1}$, implying that half of the star–light ever produced has been reprocessed by dust to the infrared. Yet this is only around 5 per cent of the total energy output of the CMB!

Without some knowledge of the backgrounds present in Fig. 1.6, a full picture of the evolution of galaxies cannot possibly be created. Soifer & Neugebauer (1991), using the Bright Galaxy Survey (BGS), found that the infrared emission of local galaxies is only around a third of the optical emission. They argued that since the IRAS observes the range of wavelengths at which dust produces significant emission, that sample would be a useful proxy for infrared galaxies in the local universe. This implies extreme evolution in the infrared galaxy population

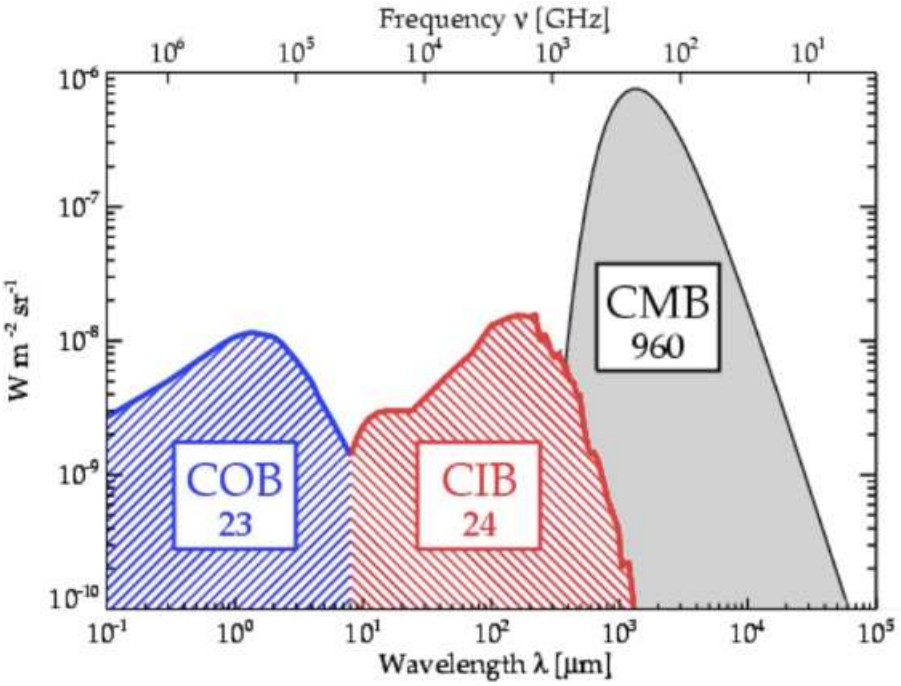

Figure 1.6: Schematic SEDs as presented in Dole et al. (2006) showing the relative brightnesses of 3 of the largest components of the extra–galactic background light. From left to right, the Cosmic Optical Background (COB), the Cosmic Infrared Background (CIB) and the Cosmic Microwave background (CMB). Their brightnessses in $\mathrm{nW\,m^{-2}\,sr^{-}1}$ are shown in the boxes.

to account for the total measured CIB. If we consider that ULIRGs have often been found to be the result of mergers (e.g. Genzel & Cesarsky 2000), the sources that make up the CIB likely carry significant information on how galaxies merge and evolve.

As with any telescope, the sensitivity limit is determined by the telescope aperture, observation wavelength and position on the sky. If one considers that the angular resolution of any imaging device is limited by the equation:

$$\theta \sim \frac{\lambda}{D} \tag{1.5}$$

where θ is the angular resolution, λ is the wavelength of light being observed and D is the aperture diameter, it is clearly visible that any increase in wavelength simultaneously leads to an decrease in the angular resolution, placing a lower limit on detail in images. This then means that infrared surveys will naturally suffer from a great deal more confusion than for example optical surveys (though in globular clusters source confusion can also be prevalent in that wavelength regime). Improvements in the sensitivity of infrared instruments have meant that fluctuations in this unresolved CIB now contribute the most noise in deep imaging, preventing an increase in the sensitivity, regardless of integration time. The most important contributions to source confusion are small scale structure in cirrus clouds at intermediate Galactic latitudes and the structure of the CIB where resolved and partially resolved extragalactic sources will dominate at high galactic latitudes. This confusion is a significant concern of far–Infrared and submm observations, as being able to discern whether a source is a target or merely a background object is difficult. Indeed, it often requires extensive work

to begin to understand its contribution (e.g. merely for *Herschel* alone: Nguyen et al. 2010; Roseboom et al. 2010; Pascale et al. 2011; Rigby et al. 2011; Smith et al. 2012).

1.3.2 Far–Infrared Emission and Star Formation: The Link

The necessity for accurate SFR estimates is relatively self–evident. If a greater understanding of galaxy formation and evolution is to be achieved, accurate estimates for the activity of galaxies over cosmic time must be derived, in various galaxy types and environments. Galaxy evolution models require an accurate SFR parameter since massive stars can chemically enrich and determine the energy of the ISM. Furthermore, the SFR density with redshift can be determined, thereby pinpointing the formation epoch of galaxies (Murphy et al. 2011).

As already noted, massive stars produce large quantities of photo–ionising radiation, and can be responsible for significant proportions of the total luminosity from a galaxy. These massive stars have short lifetimes (of the order of a few Myr), so this emission signifies recent star formation. Kennicutt (1998) was able to use stellar synthesis models to determine what observed radiation would be viable SFR tracers, such as H α which is found to trace the young massive stellar population. However, as mentioned before, these stars tend to be found within vast layers of dust and gas, enshrouding ongoing star formation and preventing the use of H α. Instead, the infrared luminosity produced by the reprocessing of radiation from these sources can be used. This assumes that the stellar radiation field is dominated by young stars such as those found within a starburst galaxy. With the stellar synthesis models of Leitherer & Heckman (1995) in hand,

Kennicutt (1998) was able to derive the following classical FIR tracer of SFR:

$$\mathrm{SFR} = 4.5 \times 10^{-44} \mathrm{L_{FIR}} (\mathrm{M_\odot\,Yr^{-1}}) \tag{1.6}$$

where $\mathrm{L_{FIR}}$ is the FIR luminosity (in $\mathrm{erg\,s^{-1}}$). The value 4.5×10^{44} is a constant derived from the population synthesis models. These stellar synthesis models were specifically created to correspond to the conditions that are prevalent within giant HII regions, HII galaxies, nuclear starbursts and infrared luminous starburst galaxies and traces diffuse gas within these regions. The Kennicutt (1998) relation assumes continuous starbursts of age $10 - 100\,\mathrm{Myr}$ and estimates the FIR luminosity over the range 8–1000 μm which is believed to contain the bolometric luminosity of the HII region/starburst. It should be noted that this wavelength range is chosen more for convenience and comparison with other studies. It is not intended to imply that dust emission from reprocessed UV dominates the QSO SED at wavelengths as short as $8\,\mu$m.

In the case of star formation, the bulk of the energy for embedded stars is found to be within this wavelength range, and by taking the total energy emitted by the source per wavelength/frequency interval, the SED of the source can be determined (see Fig 1.7 for example SEDs and how the FIR dust component compares to the rest of the SED). This allows properties such as the temperature, luminosity and nature of the source to be determined.

The 'classic' SED is the black body. A black body is a system that absorbs all electromagnetic radiation incident upon it, and re–radiates this energy at an equal rate to its absorption, thereby remaining in thermal equilibrium, described

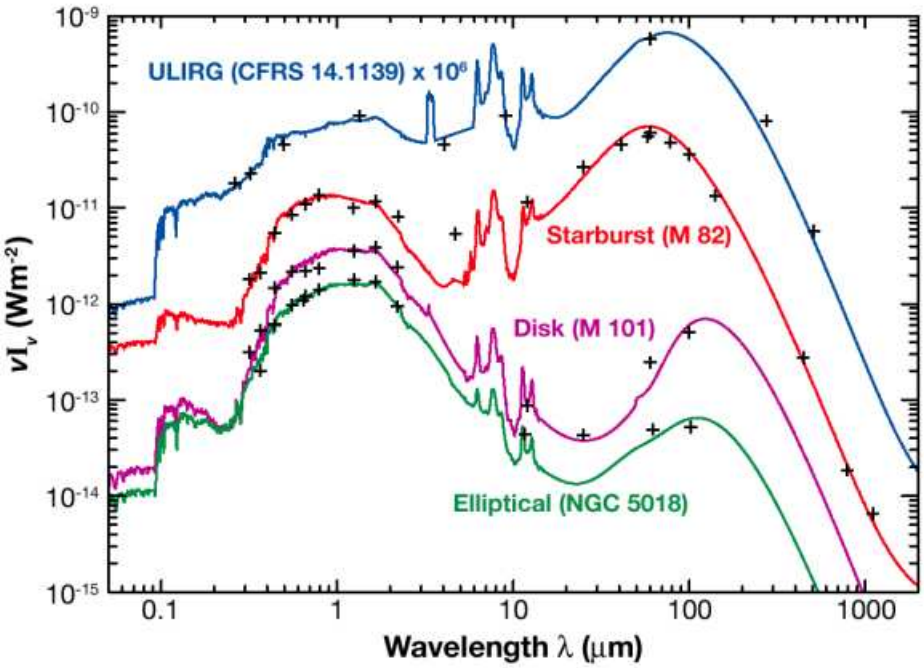

Figure 1.7: The Spectral Energy distributions of various types of galaxies from the UV to the millimetre. Clearly visible is the manner in which with increasing star formation from elliptical to ULIRG, the FIR dust model contribution increases. Figure from (Lagache, Puget & Dole, 2005).

by the equation 1.7.

$$B_\lambda(T) = \frac{2hc^2}{\lambda^5} \frac{\epsilon}{e^{\frac{hc}{\lambda kT}} - 1} \tag{1.7}$$

where we define $B_\lambda(T)$ as the spectral radiance, c as the speed of light ($2.998 \times 10^8\,\mathrm{m\,s^1}$), k the Boltzmann constant ($1.380 \times 10^{23}\,\mathrm{J\,K^1}$), and h the Planck constant ($6.626 \times 10^{34}\,\mathrm{J\ s}$) and ϵ as the emissivity. Of course in reality, this is not the case. Indeed, a true black body will have an emissivity ϵ equal to 1. Instead, a *modified* black body is required, with most real sources having $\epsilon < 1$ (see equation 1.8 for the modified form). This takes into consideration the optical depth τ_ν, dust emissivity β and the critical wavelength λ_0. Optical depth is simply the mean free path of a photon through a medium. If $\tau_\nu >> 1$ it is likely to suffer extinction. Furthermore, an Ω term must be added, which is the effective solid angle of the emitting source (in steradians). The dust emissivity parameter β is a direct representation of the physical properties of the emitting dust grains, such as size, shape and composition. The value can vary somewhat, ranging from $\beta = 1$ for amorphous carbon grains up to $\beta = 2$ for amorphous silicate grains (Dupac et al., 2003). Upon inclusion of these terms, equation 1.7 becomes (where F_λ is the radiant spectral flux density):

$$F_\lambda = \Omega \frac{2hc^2}{\lambda^5} \frac{(1 - e^{(\frac{-\lambda_0}{\lambda})^\beta})}{e^{\frac{hc}{\lambda kT}} - 1} \tag{1.8}$$

1.3.3 Previous Far–Infrared Facilities

The Infrared Astronomical Satellite (IRAS, Neugebauer et al. 1984) was the first ever space-based observatory to perform infrared all–sky surveys in the 12, 25,

60 and 100 μm bandpasses. It helped to increase the number of catalogued astronomical sources significantly, detecting about 350,000 infrared sources alone. By mission's end, it had mapped 96 per cent of the sky in each wavelength, and increased the number of catalogued sources at the time by around 70 per cent. Furthermore, it helped identify that some extreme galaxies were able to emit up to 95 per cent of their energy in the far–infrared (Soifer et al. 1987), indicating that studies in this wavelength regime were a necessary step to understanding the universe.

Following on from the success of IRAS was the Infrared Space Observatory (ISO, Kessler et al. 1996). This mission covered the wavelength range 2.5-240 μm over various spatial resolutions. At a wavelength of 12 μm, ISO was one thousand times more sensitive and had one hundred times better angular resolution than IRAS (Kessler, 1999), owing to significant improvements in detector technology. Whereas IRAS had a pixel scale of 1.5 arc minutes, each pixel on ISOCAM could image 6 arc seconds on the sky. The wavelength region in which ISO observed was of great interest as it was here that cool objects (15-300K) would radiate the bulk of their energy. However, it suffered at longer wavelengths, having limited sensitivity.

Spitzer (Werner et al., 2004) was the previous space-based observatory to *Herschel*, and many of the key programmes within the *Herschel* plan use data from the Multiband Imaging Photometer for Spitzer (MIPS, Rieke et al. 2004). At any time, $\sim$35% of sky was accessible. The MIPS instrument itself imaged in bands at 24, 70 and 160 μm and took spectral energy measurements between 52 and 100 μm, though this, as with ISO, suffered at long wavelengths, having a spectral resolution of 7%, and indeed whilst the 24 μm detector array had excellent

photometric properties, the 70 and 160 μm detectors were unable to match the relative rms error and suffered from large beam sizes (Rieke et al., 2004).

The Submm Common User Bolometric Array or SCUBA (Holland et al., 1999) on the James Clark Maxwell Telescope (JCMT) revolutionised submm astronomy, and made discoveries in two major areas; galaxy evolution in the early universe, and dust disks around nearby stars and the formation of planetary disks. SCUBA was composed of two detector arrays, observing the same patch of sky at the same time. The long-wavelength array could operate at 600, 750 and 850 μm, whilst the short-wavelength array operated at 350 or 450 μm. SCUBA was instrumental in taking our understanding of the universe to a new level, finding a submm background composed of high–redshift ultraluminous galaxies. These sources are likely the progenitors of modern day ellipticals, with SFRs in the thousands of solar masses per year but had been missed repeatedly by optical observatories due to dust absorption. However, SCUBA still suffered from problems. Merely observing the Hubble deep field North data (HDF-N) required two weeks of excellent weather and SCUBA had a rather restricted field of view, placing an upper limit on what regions could be mapped, a significant hindrance to wide-field galactic mapping programmes. Furthermore, under-sampling of the focal plane meant observations required longer integration times to reach the confusion limit. These limitations have been addressed with SCUBA-2 (see Section 1.3.5). It is believed that IRAS primarily detected the warm dust found within the inner region of spiral galaxy disks only, and that up to 90 per cent of dust in galaxies was missed as a result (Devereux & Young, 1990). Spitzer and ISO will have had less of a problem than IRAS due to using a longer wavelength at 170 μm, though this still means they will have missed any dust with temperatures less than 15K (Bendo

et al., 2003).

These telescopes have been followed by the *Herschel* Space Observatory (Pilbratt et al. 2010), the Wide–Field Infrared Survey Explorer (WISE, Wright et al. 2010). We discuss *Herschel* and SCUBA–2 in greater detail in Sections 1.3.4 and 1.3.5.

1.3.4 The *Herschel* Space Telescope

Submillimetre astronomy, (at wavelengths of 200 μm to 1mm), is very sensitive to cold gas and dust. For example, a source with a temperature of 10 K (–263 °C) emits most of its energy in a broad spectral region centred around 300 μm.

The majority of FIR emission from galaxies is due to reprocessed UV–optical stellar light from stars hidden within such cold large dust clouds. Consequently, since star formation happens within giant molecular clouds which often are opaque to optical light, this makes FIR emission a valuable tracer of ongoing star formation within a galaxy (Kennicutt 1998). The most massive stars have very short lifetimes relative to stars like our sun, and this means that their presence indicates recent star formation. By measuring the total FIR emission ($L_{\rm FIR}$) between 8–1000 μm, the total SFR for the galaxy can be determined (Kennicutt 1998). The need for a space–based infrared observatory such as *Herschel* is most evident when atmospheric transmission is taken into account. Other than a select few windows observable at high altitude such as on Mauna Kea by the JCMT at 450 and 850 μm, the atmosphere is essentially opaque to mid and far–infrared emission.

The ESA *Herschel* space observatory (Pilbratt et al., 2010) is perfect for the

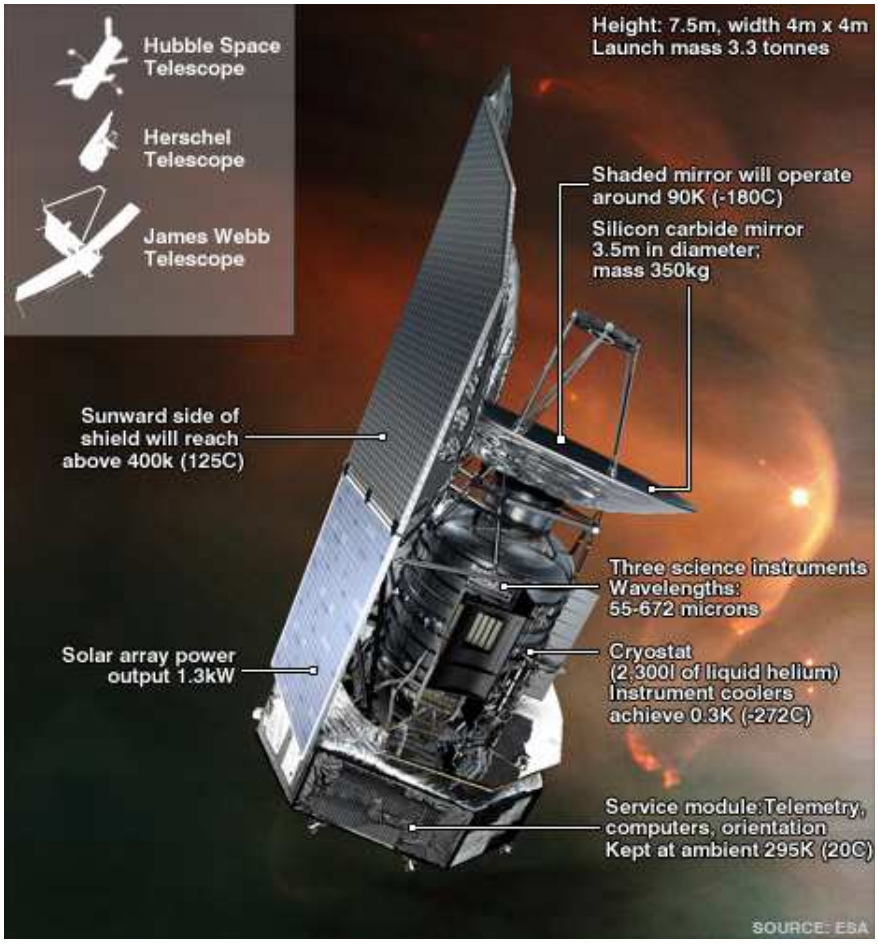

Figure 1.8: The *Herschel* Space Telescope. (Image credit: ESA)

study of objects at high redshift that are obscured by dust. It offers the user sensitive detectors, a low instrumental noise background and a large collecting area, allowing very deep surveys of the sky over large areas in submm and far infrared, covering the spectral range 55-671 μm.

1.3.5 SCUBA–2 and the JCMT

The JCMT (Fig.1.9) whose first light was back in 1987, is the largest telescope in the world designed specifically to observe at submillimetre wavelengths. It is a telescope located at an elevation of 4090 m on the extinct volcano Mauna Kea in Hawaii, USA at a longitude of 155° 30', latitude 19° 49'. The telescope uses an altazimuth mount and houses a primary mirror of 15 m in diameter. It also has a membrane placed over the antenna at all times. Whilst transparent to millimetre and submm wavelengths ($\sim$97% transmission), this membrane provides protection from the wind whilst also allowing day–time observations (visible and near–infrared radiation is reflected) and preventing damage from the sun. Mounted upon it are several different instruments, of which SCUBA–2 is of interest to this thesis.

Building on the success of the original SCUBA camera, SCUBA–2 boasts a much larger field-of-view and sky–background limited sensitivity (i.e. noise from a celestial background rather than intrinsic detector noise determines the sensitivity), with a field of view 16 times greater than SCUBA and a point–source sensitivity at least a factor of 2 better. It is cutting edge technology with many components having been created specifically for its use (Holland et al. 2013). For example, its predecessor had hit the limit in terms of scalability of pixels

per bolometer at the time. The revolution came in the form of transition–edge sensors (Irwin 1995), which make use of the resistance difference in a superconductor close to its transition region (where it becomes a true superconductor). The minimal energy input from single photon hits raises the temperature sufficiently to cause the material to transition out of its superconductor phase and significantly increase its resistance, making it a highly efficient mechanism for use in astronomy. SCUBA–2 is composed of $\sim$10,000 pixels in 2 arrays and is able to map large areas of sky up to 1000 times faster than the previous SCUBA camera. When we consider that in the 9 years that SCUBA operated, only 0.6 sq deg were observed down to the confusion limit, this will greatly increase the number counts of rare objects whose analysis until now may have suffered from a dearth of sources (e.g. in the study of FIR environments). The work performed by SCUBA–2 will be highly complementary to observations performed by *Herschel* and the Balloon-borne Large Aperture Submillimeter Telescope (BLAST, Pascale et al. 2008) as well as next–generation telescopes such as the Atacama Large Millimetre Array (ALMA). For example, at 450 m, the JCMT is able to provide a resolution 5 times finer than that of *Herschel* at 500 μm and the confusion limit is $\sim$7 times fainter, thereby allowing accurate positions to be derived.

1.4 Surveys of note in this thesis

The Sloan Digital Sky Survey (SDSS, Abazajian et al. 2003) is perhaps one of the most well known and well used surveys in the history of astronomy. For over a decade, the SDSS has provided regular annual updates of astronomical sources and has changed forever our understanding of the universe. Currently it

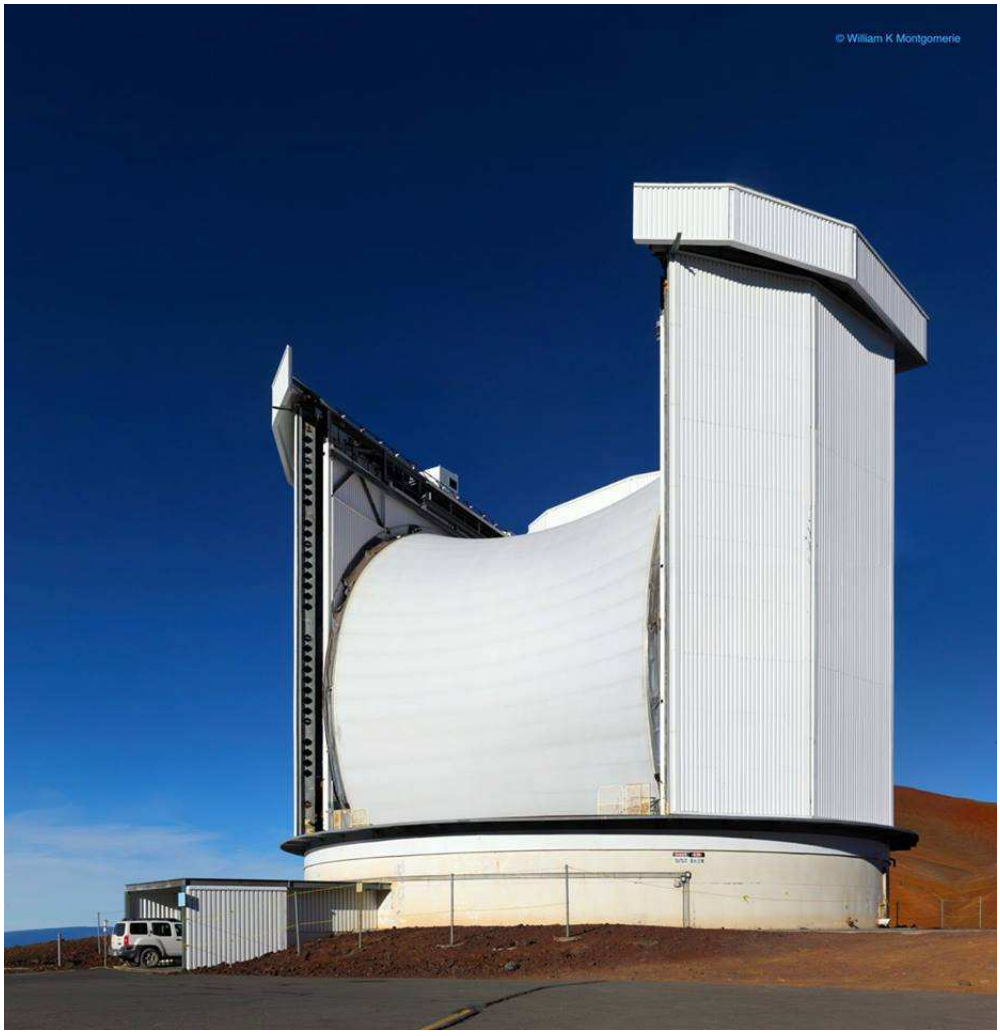

Figure 1.9: The James Clerk Maxwell telescope. (Image credit: William Montgomery, JCMT)

has imaged 12,000 sq deg. of sky with close to a million galaxies and of the order of ∼120,000 QSOs in five different wavelength bands (*ugriz*) in the wavelength ranges 3551–8921Å. Most relevant to this thesis is the SDSS QSO Catalogue (Schneider et al. 2005; Pâris et al. 2012). By using *ugriz* colours, QSOs were identified for follow–up spectroscopy reaching redshifts greater than 6, allowing a study of galaxy formation from just after cosmic reionisation (Fan, Carilli & Keating 2006) to the present day. In this thesis, the QSOs have generally been selected from the SDSS; without the available data, this thesis or the galaxy samples selected would likely not exist. By providing a uniform, large population of QSOs, it allows the creation of statistically significant samples of relatively rare objects such as BAL QSOs or RL AGN.

The *Herschel* Astrophysical Terahertz Large Area (H–ATLAS) survey is the largest survey of the sky conducted in the far-infrared (at 510 sq deg) and allows the study of of interstellar dust at scales $\simeq$ 10 times smaller than with IRAS (Eales et al., 2010). It has the benefit that all the fields covered by the H-ATLAS survey are also covered by either the Sloan Digital Sky Survey (SDSS), the 2dF Galaxy Redshift Survey (2dFGRS) or the Galaxy and Mass Assembly Survey (GAMA), giving a wealth of information on any objects at other wavelengths. It is also the first time that large samples of QSOs can have their FIR properties measured at the same time, giving the scientific community the possibility of using stacking methods and other techniques in conjunction with previous large surveys to determine the average properties of QSOs with much greater fidelity. Data from this survey has been used in Chapter 2.

The *Herschel* Multi–tiered Extragalactic Survey (Oliver et al., 2012) is a survey designed to study the evolution of galaxies in the distant universe. Using a set

of nested fields covering a total area of ~ 380 deg^2, it is designed to detect around 100,000 galaxies at $5\,\sigma$. This nested style allows the sampling of rare, bright IR luminous sources in the wide–field tiers whilst detecting lower luminosity sources in the deepest fields. These data are invaluable for answering questions such as what is the total infrared emission of galaxies, how clustered are dusty galaxies and what are the properties of galaxies too faint to be detected above the confusion limit. Coupled with observations of each field at other wavelengths, SEDs for each source will be available. Data from this survey have been used in Chapter 3.

The VISTA Deep Extragalactic Observations (VIDEO) Survey (Jarvis et al. 2013) is a survey covering 12 square degrees in multiple bands in the NIR, specifically the Z,Y,J,H and K_s bands. The driving goal behind the VIDEO survey is to investigate the evolution of galaxies and large–scale structure across cosmic time up to $z = 4$, whilst tracing AGN and the most massive clusters as far back as the epoch of reionisation. Of particular interest to this thesis is the coverage of the XMM–Lockman–SWIRE region. In combination with optical data from the Canada-France-Hawaii-Telescope Legacy Survey Deep-1 field (CFHTLS-D1, Gwyn 2011), this has been used in Chapter 3 to create a comparison sample to determine whether AGN sit in overdensities of sources and whether there is a dependence on various AGN properties.

Finally, the Cosmology Legacy Survey (CLS, e.g. Geach et al. 2013(@) is designed to take advantage of the increased mapping speed and sensitivity provided by SCUBA–2 over that of its predecessor to create large samples of submm sources at 450 and 850 μm. These wavelength bands correspond to highly redshifted luminous galaxies and AGN at the peak of activity where black holes

and galaxies are forming and allows a study of the CIB. By measuring at two separate wavelengths, it can answer various questions. The 850 μm shallow area observed will be far larger than that at 450 μm, thereby allowing a study of the clustering of the submm population as well as studying the progenitors of rich clusters. On the other hand at 450 μm which will be far deeper, accurate positions will be determined as well as allowing the bulk of the extragalactic background light to be resolved. Deep observations will also be carried out at 850 μm to determine the colours of any sources found. It will be invaluable in the years to come as the fields chosen for imaging will have multi–wavelength coverage from telescopes such as *Herschel*, ALMA, the Square Kilometre Array (SKA), and the James Webb Space Telescope (JWST). Data from this survey have been used in Chapter 4.

1.5 This Thesis

This thesis is a compilation of my research conducted during the past 3.5 years. In Chapter 2 I use data from the *Herschel* Space Observatory to investigate whether FIR emission in BAL QSOs is greater than non–BAL QSOs in an attempt to address the ongoing debate about whether the properties of BAL QSOs are merely due to an orientation effect or a separate evolutionary phase with different SMBH environment/host galaxy properties. In Chapter 3 I have analysed how the presence of an AGN can affect star formation activity in the larger cluster environment within 1 Mpc and whether any detected differences are down to the AGN itself (such as in the form of AGN feedback) or whether environmental effects can have a greater effect on a cluster using a well–selected sample of RLQs,

RQQs and RGs. In Chapter 4 I use observations carried out with SCUBA–2 on the JCMT to investigate the properties of the AGN sample, determine whether absorbed QSOs sit in overdense regions of the universe and calculate the SFRs of those companion sources. The data reduction process is also discussed and the various steps taken to produce a robust scientific result are presented. Finally, Chapter 5 provides a summary of the work as well as discussing possible future avenues of research. Throughout this research, a flat universe with a cosmology of $H_0 = 70\,\mathrm{km\,s^{-1}\,Mpc^{-1}}$, $\Omega_m = 0.3$ and $\Omega_\Lambda = 0.7$ has been assumed.

Chapter 2

The far-infrared properties and SFRs of broad absorption line quasi-stellar objects

This chapter is based on work published in the journal Monthly Notices of the Royal Astronomical Society (MNRAS, Cao Orjales et al. 2012).

In this chapter, observations carried out as part of the *Herschel*-Astrophysical Terahertz Large Area Survey (H-ATLAS; Eales et al. 2010) on the *Herschel* space observatory (Pilbratt et al. 2010) are used to examine the FIR emission of a relatively large sample of BAL QSOs and non–BAL QSOs. All but one of the BAL QSOs are HiBALs, whereas the non–BAL QSOs are taken at random (see section 2.2 for details on the selection process). In Section 2.1, details are given of the data and observations used, Section 2.2 explains the QSO samples themselves and their selection process, whilst Section 2.3 discusses the stacking analysis carried

out, as well as explaining the method used to calculate the FIR luminosities and SFRs. Finally, these findings are discussed and a summary is presented of the main conclusions in sections 2.4 and 2.5.

2.1 Data

The data used here consist of photometry and catalogues made available as part of the H–ATLAS phase 1 version 2 data release. The observations were carried out using the now decommissioned *Herschel* telescope. The survey makes use of photometry from both the PACS (Poglitsch et al. 2010) and SPIRE (Griffin et al. 2010) cameras, observing at wavelengths between 70 and 500 μm, reaching a 5 σ depth of 33.5 mJy at 250 μm. The reliability of the catalogues are improved through the use of a likelihood ratio to cross–match ID sources in different wavebands, as well as containing sources only detected at $> 5\,\sigma$ in each wavelength. A description of the map–making and catalogue creation process is available in Pascale et al. (2011) and Rigby et al. (2011) respectively, whilst the details of the cross ID process are available in Smith et al. (2011).

The sensitivity of H–ATLAS to different SFRs is dependent on redshift, and is $\sim 100\,\mathrm{M}_\odot\,\mathrm{yr}^{-1}$ at $\mathrm{z} \sim 1$ (Luminous Infrared Galaxies, LIRGs) and $\sim 500\,\mathrm{M}_\odot\,\mathrm{yr}^{-1}$ at $\mathrm{z} \sim 2$ (ULIRGs), assuming a temperature of 23.5 K and dust emissivity index $\beta = 1.82$. This is consistent with the best fitting values found by Smith et al. (2013) for a sample of 12,814 $z < 0.5$ H–ATLAS galaxies. Fig. 2.1 shows how the detectable SFR varies with redshift. Assuming this holds to higher redshifts, it can be seen that even the most powerful objects with SFR > 2000 $\mathrm{M}_\odot\,\mathrm{yr}^{-1}$ will quickly become undetectable at 5 σ just before a redshift of 3 at 250 μm and will

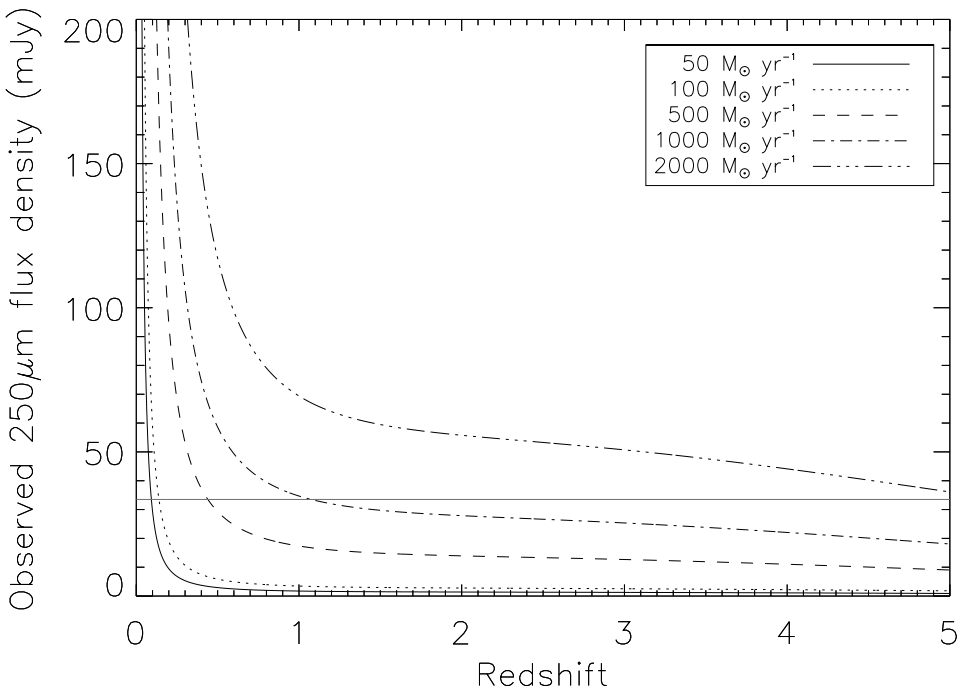

Figure 2.1: H–ATLAS survey sensitivity to different SFRs varies as a function of redshift. The different lines show different SFRs and the 250 μm flux density they will have between $0 < z < 5$. I assume a simple greybody for the FIR SED of galaxies with a temperature of 23.5 K and dust emissivity index of $\beta = 1.82$. The horizontal grey line shows the $5\,\sigma$ sensitivity of H-ATLAS at 250 μm (33.5 mJy).

be below the $1\,\sigma$ confusion noise by $z \sim 4$.

2.2 QSO Samples

BAL QSO sources were identified using the BAL QSO SDSS QSO Catalogue compiled by Gibson et al. (2009). This is based on the fifth data release of the SDSS quasar survey (SDSS DR5, Schneider et al. 2007). In total, the number of BAL QSOs within the catalogue numbers 5039 sources, identified using the 'classic' Balnicity Index as well as a more lenient version, BI_0 (the lower limit of

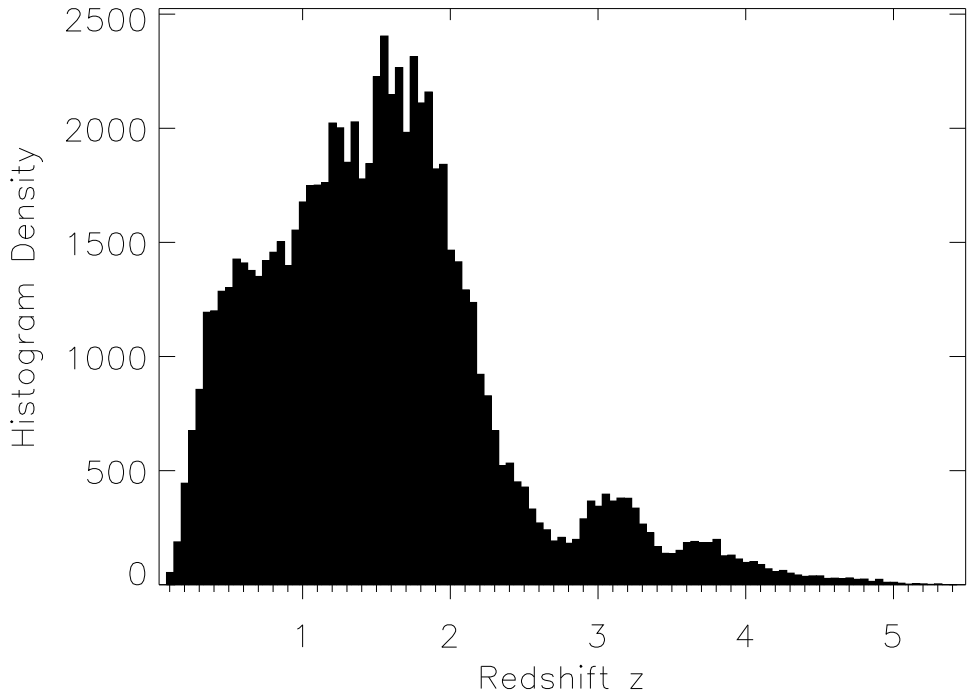

Figure 2.2: The SDSS Data Release 5 and the distribution of QSOs within the catalogue as a function of redshift.

equation 1.1 is set at $0\,\mathrm{km\,s^{-1}}$) on various absorption lines such as C IV, S IV etc (see section 1.1.3 for further details of these definitions).

The areas covered by the H–ATLAS (Eales et al. 2010) 9h, 12h and 15h fields are matched with the positions of BAL QSOs in the SDSS DR5 QSO catalogue by using TOPCAT (Taylor 2005). These three fields lie on the celestial equator and each covers an area of approximately 56 square degrees (Eales et al. 2010). At these positions, there is high coverage by other surveys. The Galaxy And Mass Assembly redshift survey (GAMA, Driver et al. 2009), the 2 degree field Galaxy Redshift Survey (2dfGRS, Colless et al. 2001, SDSS (Abazajian et al. 2003), and the Kilo–Degree Survey (KIDS), an ESO public survey, all cover these

areas of the sky, making them an ideal location for follow–up studies on galaxy evolution. The reasoning behind using an earlier release is that no corresponding catalogue had been produced for the nineth data release at the time of writing the paper. After this initial area match, 88 BAL QSOs are found within the H–ATLAS fields. Of those 88 BAL QSOs however, 5 have a given C IV Balnicity Index value of 0. These BAL QSOs have been classified using alternative lines such as Si IV or Mg II, and are considered beyond the scope of this work. The sample was then further cut using redshift and magnitude cutoffs. The SDSS i band is well suited to searching for BAL QSOs due to it being less reddened than bluer bands which will suffer from high airmasses absorbing the ultraviolet flux whilst leaving the infrared flux relatively intact. Furthermore, if it is assumed BAL QSOs host large quantities of dust and gas, it would be expected that bluer (and hence UV/optical) bands could miss significant fractions of BAL QSOs. Looking at Fig. 2.2, the greatest numbers of QSOs in general are found in the catalogue between $1 \leq z \leq 2$, with 78% of objects having redshifts less than 2, so this is a good range over which to consider redshift cuts to the selection. A redshift of $z \sim 2.3$ provides an upper redshift limit where the SDSS colour selection criteria are relatively unaffected by BAL absorption (Reichard et al. 2003b; Knigge et al. 2008), which can lead to BAL QSOs being rejected in magnitude-limited surveys at a higher rate than less–reddened QSOs of the same intrinsic luminosity. Indeed, the g—r and r—i colors of BAL QSOs tend to be affected by the presence of BAL absorption troughs, causing them to intersect or fall within the stellar locus. Since the SDSS DR5 primarily identifies QSOs as being outliers from the ugriz stellar locus as modelled by Newburg & Yanny (1997), this leads to BAL QSOs being missed (see Richards et al. 2002 for a detailed description

of the algorithm). The SDSS *ugriz* filter wavebands force a lower redshift constraint of $z = 1.5$. Below this redshift, the C IV absorption trough will extend into the UV and be unobserved by the SDSS. This is visible in Fig. 1.3, where the spectrum extends to 3800 Åonly, making it difficult to identify C IV BALs. By looking at Fig. 2.3, the greatest concentration of BAL QSO sources are between $1.5 < z < 2.3$ and absolute magnitudes $-28 < M_i < -24$. These limits are likely then the best to use in order to reduce the susceptibility of this study to the effects of luminosity or redshift evolution (e.g. Bonfield et al. 2011). This restriction provides two advantages: it allows easy construction of a non-BAL QSO comparison sample and limits the effects of cosmological evolution whilst comparing similar luminosities. Otherwise for example, as one goes to higher redshifts, the limitations in 'significant' detections would mean any created samples are composed of more extreme objects than at lower redshifts. Following the application of redshift and absolute magnitude constraints, the sample is further reduced to 50 BAL QSOs. This study has also addressed the important distinction between the 'classic' BI and the 'extended' version given in Gibson et al. (2009), BI_0, to see if this classification has any effect on the flux densities and other properties of the sample. The BI_0 differs in that the balnicity is integrated to $0\,\mathrm{km\,s^{-1}}$ rather than $3000\,\mathrm{km\,s^{-1}}$ blueward of the chosen line. As a result of this distinction, the total number of BAL QSOs following the 'classic' BI definition drops to 36. One of these, SDSS115404.13+001419.6, is a LoBAL QSO. This source is not considered in the stacking analyses in Section 4. The distribution of BAL QSOs over the 3 fields is as follows: 9 h field - 19, 12 h field - 12, 15 h field - 19.

To create a comparison sample composed of non–BAL QSOs, the full SDSS

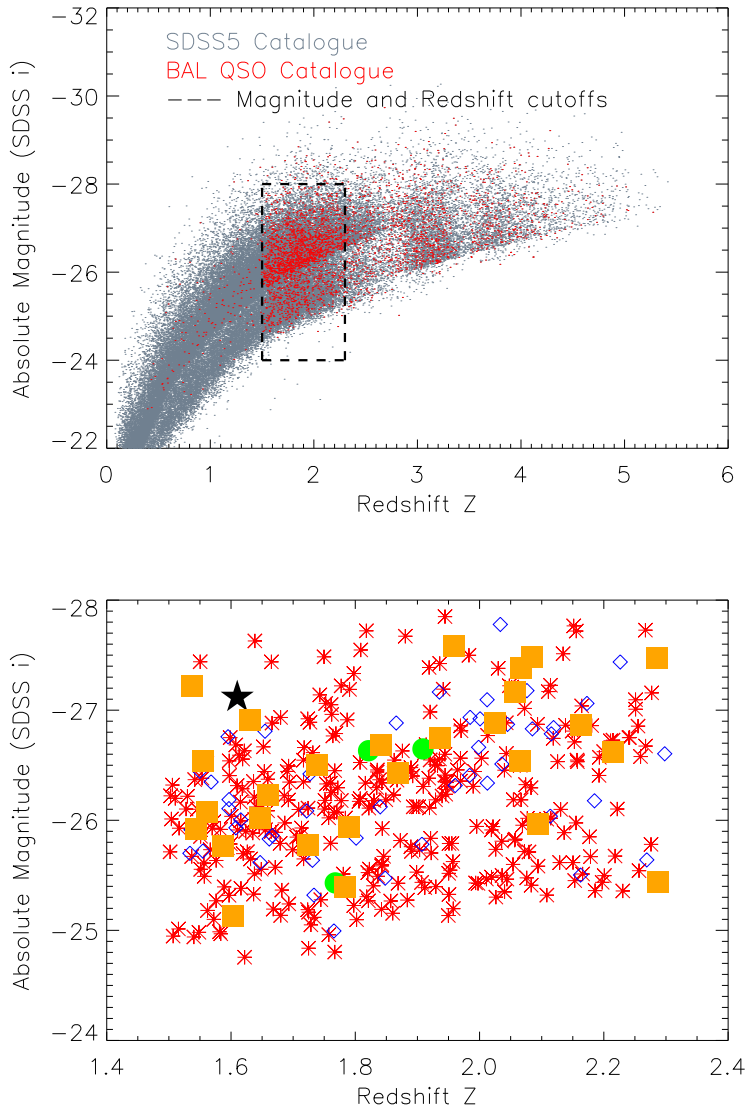

Figure 2.3: Distributions of BAL and non-BAL QSOs as a function of redshift and absolute magnitude in SDSS i band. The top panel shows the full BAL QSO and SDSS QSO DR5 catalogues. The dashed box shows the redshift and absolute magnitude cut-offs used in this study. The lower panel shows the final sample after removal of those QSOs falling outside the cited absolute magnitude and redshift cutoffs, and after statistical matching (see text for details). Red asterisks are non-BAL QSOs, blue diamonds are HiBAL QSOs, the black filled star is the solitary LoBAL QSO, green circles are the detected HiBAL QSOs and orange squares are detected non-BAL QSOs.

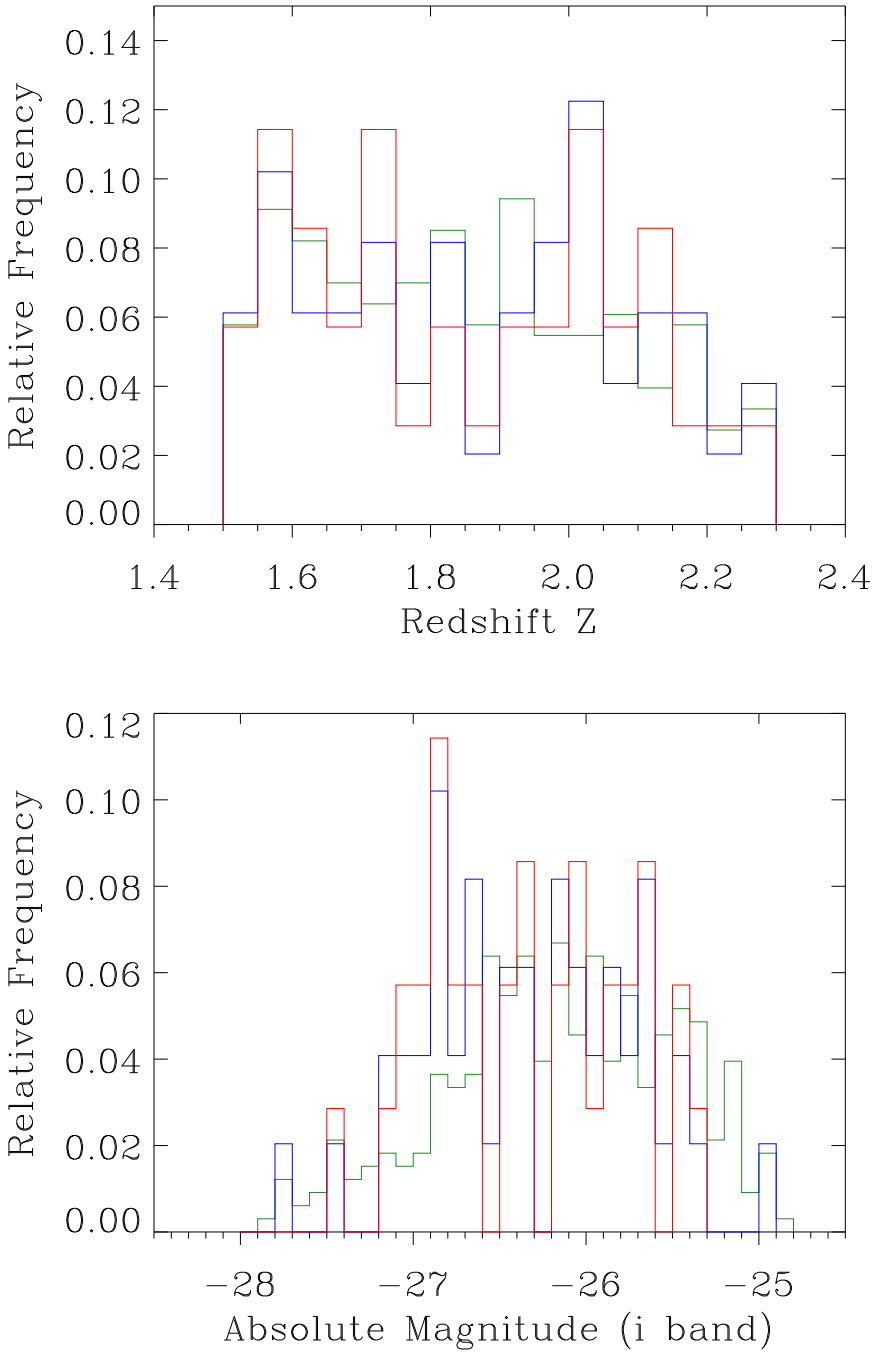

Figure 2.4: Distributions of BAL (blue is the 'extended' HiBAL sample, red is the 'classic' HiBAL sample) and non-BAL QSO (green) samples as a function of redshift and absolute magnitude in SDSS i band. The top panel shows the distribution of the QSO samples in redshift space. The lower panel shows the magnitude distribution of those QSO samples. Detected BAL QSOs have 250 μm fluxes in the range 50–80 mJy, whilst non–BAL QSOs show a slightly larger spread, between ∼35–80 mJy. This slight difference is likely due to small number statistics however.

Table 2.1: The BAL QSO Sample. The classification method used to determine the Balnicity of a source is given in the Type/Detected column, along with whether it is detected. If a source is classified using BI, then it will also be classified as a BAL QSO by the BI_0 definition. The 250 μm flux density and signal-to–noise ratio are given derived from the 250 μm flux density divided by the sum in quadrature of the instrumental noise in the corresponding pixel and confusion noise in Rigby et al. (2011). 5 σ detections at 250 μm found in the Phase 1 catalogue with matched optical/NIR counterparts are shown with their flux density values in each waveband taken from the Phase 1 catalogue. The average 5 σ limits at 250, 350 and 500 μm are 33.5, 37.7 and 44.0 mJy beam^{-1}. For undetected sources, their flux density values are the best estimates from measuring the flux density in the closest pixel of the PSF-smoothed map and noise map and are not reliably associated with R > 0.80 to a 250 μm source as for detections.

Source	z	Type/ Detected?	C IV EW (Å)	M_i	250 μm flux density (mJy)	SNR 250	350 μm flux density (mJy)	SNR 350	500 μm flux density (mJy)	SNR 500
SDSSJ084307.36−001228.4	1.7271	BI/No	7.40	−26.421	+18.43	+2.82	+13.49	+1.87	+6.00	+0.75
SDSSJ084524.10−000915.4	2.0121	BI/No	56.10	−27.095	+18.38	+3.18	+2.83	+0.42	+2.67	+7.84
SDSSJ084842.13+010044.3	1.6616	BI/No	20.00	−25.830	−4.13	−0.63	−4.24	−0.58	+0.29	+0.03
SDSSJ085316.22+012052.0	1.6663	BI/No	19.80	−25.862	+13.58	+2.11	+15.36	+2.10	+9.29	+1.08
SDSSJ085436.41+022023.5	1.9089	BI/Yes	20.70	−26.648	+55.87	+8.24	+63.14	+7.90	+39.87	+4.51
SDSSJ085609.02+001357.7	1.8401	BI/No	6.50	−26.122	+9.74	+1.51	+3.92	+0.54	−6.17	−0.72
SDSSJ085647.99+003107.4	2.2979	BI/No	8.70	−26.604	+21.94	+3.45	+19.41	+2.68	+21.41	+2.51
SDSSJ090030.36+015154.9	1.9848	BI/No	10.00	−26.935	−4.41	−0.67	−1.58	−0.21	−2.81	−0.32
SDSSJ090211.60+003859.5	1.5339	BI/No	7.60	−25.700	+16.06	+2.44	−2.35	+0.32	+2.06	+0.24
SDSSJ090331.90+011804.5	1.9072	BI/No	17.60	−25.782	+11.88	+1.85	+1.91	+0.26	+9.59	+1.11
SDSSJ090517.24+013551.4	1.7678	BI/Yes	41.70	−25.431	+57.81	+8.54	+72.79	+8.97	+52.59	+5.86
SDSSJ090523.07+001136.9	1.5600	BI/No	8.20	−26.348	+22.02	+3.44	+14.70	+2.07	+4.42	+0.52
SDSSJ090904.52−000234.5	1.7656	BI_0/No	8.50	−24.995	−3.85	−0.59	−8.18	−1.13	+0.47	−0.05
SDSSJ091110.29+004822.8	2.2691	BI_0/No	4.00	−25.640	+3.85	+0.66	+7.31	+1.09	+5.30	+0.67
SDSSJ091144.41+000423.6	1.8014	BI_0/No	5.70	−25.838	+3.08	+0.53	+0.27	+0.04	+4.79	+0.62
SDSSJ091524.29+002032.6	1.9353	BI_0/No	6.00	−27.165	+23.22	+3.56	+22.71	+3.13	+13.38	+1.57
SDSSJ091600.60+011621.6	1.8481	BI/No	15.20	−25.474	+3.08	+0.47	−8.99	−1.23	−3.42	−0.39
SDSSJ091808.80+005457.7	2.1155	BI/No	5.30	−26.785	+3.73	+0.56	−0.21	−0.03	−0.39	−0.04
SDSSJ091951.29+005854.9	2.1138	BI/No	6.90	−26.037	+4.62	+0.70	+7.60	+1.04	+9.19	+1.05
SDSSJ113510.27−003558.2	1.7335	BI/No	8.30	−25.320	+8.17	+1.25	−10.41	−1.46	−3.25	−0.37
SDSSJ113537.56+004130.1	1.5498	BI/No	15.00	−26.445	+4.52	+0.69	−4.81	−0.65	+2.29	+0.27
SDSSJ113544.33+001118.7	1.7311	BI/No	23.80	−25.637	−0.35	−0.05	+0.52	+0.07	+1.52	+0.17
SDSSJ113651.54−002836.0	1.6157	BI/No	7.50	−26.004	+12.83	+1.95	+5.46	+0.75	+5.39	+0.63
SDSSJ113934.63−005901.5	1.6079	BI/No	10.40	−25.932	+9.06	+1.39	+1.29	+0.17	−3.89	−0.44
SDSSJ114259.29−000156.4	1.9840	BI_0/No	9.30	−26.408	−3.91	−0.59	−0.06	−0.01	+8.56	+1.01
SDSSJ114333.62+013709.0	1.5547	BI/No	22.70	−25.720	+21.98	+3.36	+28.84	+3.94	−4.12	−0.48
SDSSJ114954.94+001255.3	1.5952	BI/No	4.90	−26.759	+11.45	+1.75	+19.08	+2.61	+19.67	+2.31
SDSSJ115404.13+001419.6	1.6100	BI/No	31.50	−27.119	+29.88	+4.49	+20.68	+2.86	−0.24	−0.03
SDSSJ115407.74+001113.4	1.6547	BI_0/No	7.90	−26.809	+32.72	+4.94	+57.46	+7.98	+52.36	+6.17

Source	z	Type/ Detected?	C IV EW (Å)	M_i	250 μm flux density (mJy)	SNR 250	350 μm flux density (mJy)	SNR 350	500 μm flux density (mJy)	SNR 500
SDSSJ115809.69−013754.3	1.5969	BI/No	17.70	−26.188	−0.84	−0.13	+14.16	+2.06	+3.33	+0.41
SDSSJ115940.79−003203.5	2.0334	BI_0/No	5.70	−27.779	+28.25	+4.36	+30.22	+4.51	+41.83	+5.34
SDSSJ140842.75+010828.7	1.6469	BI/No	15.80	−25.616	+2.45	+0.37	+5.46	+0.76	−1.94	−0.23
SDSSJ140918.72+004824.3	2.0008	BI/No	10.10	−26.922	+21.47	+3.32	+10.46	+1.44	+6.62	+0.77
SDSSJ141434.39−011534.4	1.5967	BI_0/No	13.70	−26.106	+12.73	+2.00	+16.34	+2.26	+18.01	+2.08
SDSSJ142050.33−002553.1	2.0850	BI/No	35.20	−26.831	+10.18	+1.76	+7.45	+1.12	−10.03	−1.29
SDSSJ142423.76+001451.0	2.1849	BI_0/No	10.30	−26.177	−2.54	−0.39	+11.23	+1.55	+6.19	+0.73
SDSSJ142820.59−005348.3	1.5357	BI_0/No	5.30	−25.914	+23.56	+3.63	+30.08	+4.13	−11.30	−1.35
SDSSJ143030.97+003440.1	1.9985	BI_0/No	14.40	−26.663	+9.03	+1.56	+0.51	+0.08	−6.34	−0.81
SDSSJ143144.65+011644.1	1.9607	BI/No	20.50	−26.316	+6.50	+1.02	+15.34	+2.10	+9.19	+1.12
SDSSJ143209.79+015256.3	2.1191	BI/No	23.20	−26.842	+16.09	+2.51	+18.54	+2,58	+5.66	+0.67
SDSSJ143627.79+004655.7	2.1625	BI_0/No	7.90	−25.503	+16.87	+2.64	+8.96	+1.25	+2.79	+0.33
SDSSJ143641.24+001558.9	1.8659	BI/No	20.80	−26.884	+3.13	+0.49	−8.01	−1.09	−3.19	−0.37
SDSSJ143758.06+011119.5	2.0450	BI/No	18.80	−26.871	+3.56	+0.59	+12.40	+1.79	+1.04	+0.12
SDSSJ143907.51−010616.7	1.8214	BI_0/Yes	7.60	−26.632	+73.35	+10.55	+42.41	+5.34	+29.32	+3.31
SDSSJ144256.86−004501.0	2.2264	BI/No	2.50	−27.438	+9.88	+1.71	+19.88	+2.99	+18.37	+2.34
SDSSJ144434.80+003305.3	2.0359	BI_0/No	7.60	−26.511	+8.44	+1.43	−4.62	−0.69	−4.20	− 0.52
SDSSJ144911.82−010014.8	2.1728	BI/No	39.60	−27.061	+4.12	+0.64	+2.79	+0.39	+5.81	+0.69
SDSSJ144959.96+003225.3	1.7217	BI/No	11.00	−26.085	+11.90	+1.87	+4.27	+0.59	−4.26	−0.51
SDSSJ145045.42−004400.3	2.0762	BI/No	18.00	−27.178	+10.38	+1.60	−1.57	−0.22	−0.74	−0.09
SDSSJ145511.44+002146.0	2.0126	BI/No	15.80	−26.338	+0.61	+0.09	+10.24	+1.41	+9.73	+1.13

DR5 QSO catalogue is used. To ensure that no BAL QSOs are included, the Gibson et al. (2009) catalogue is matched to the full SDSS DR5 QSO catalogue, with any matches within 1 arc sec of the optical i band position of each source removed from consideration. Whilst not using the full DR9 (made available just prior to publication) or DR8 may prevent us from having a larger sample, it also reduces the likelihood of including QSOs that are as yet unknown BAL QSOs. After matching to the area covered by the 9, 12 and 15 h fields and applying the same redshift and magnitude cutoffs, sources are trimmed at random from over–populated regions of the comparison non–BAL sample (determined via visual inspection of $M_{\rm i}$ and z). Multiple iterations are performed until a two-sample KS test comparison in $M_{\rm i}$ and z between the non-BAL and BAL QSO sample returned a null–hypothesis probablility of $p > 0.05$. This avoids introducing any selection bias that may arise if sources are chosen individually by eye. This leaves 329 sources. The redshift and absolute magnitude distributions of these non–BALs are then KS tested against the 'extended' and'classic' BAL QSO samples discussed previously. Comparing the 'extended' BAL QSO sample to the non–BAL QSO sample, KS tests on redshift and magnitude return p-values of 0.67 and 0.20 respectively, whilst the 'classic' sample returns 0.89 and 0.17 respectively. Running a 2-d KS test (Peacock 1983) on the redshift and $M_{\rm i}$ distributions simultaneously between the 'extended' BAL QSO and non–BAL QSO sample returns a p-value of 0.27 (0.24 for the 'classic' sample). The lower panel of Fig. 2.3 shows the final BAL and non-BAL QSO samples on the (z, $M_{\rm i}$) plane while Table 2 gives details of the final BAL QSO sample. Following these processes, the populations are adequately matched in $M_{\rm i}$ and z (see Fig. 2.4).

2.3 Analysis

2.3.1 Detection Rates

A first step is to determine how many individual HiBAL QSOs are significantly detected in the H–ATLAS data at the $>5\,\sigma$ level. The initial source catalogue is based on finding peaks in the noise–weighted PSF–filtered maps using an algorithm especially designed for *Herschel* data (see Rigby et al. 2011; Maddox et al. 2010 for further details on the extraction method). The Phase 1 H-ATLAS catalogue used a likelihood ratio technique to identify optical and near-infrared counterparts with objects detected by *Herschel* as with the SDP catalogue (Smith et al. 2011) in the phase 1 data. This involves determining the ratio between the probability that a source is correctly identified and the corresponding probability for an unrelated background source.

Three HiBAL QSOs in the sample are associated with ($5\,\sigma$) $250\,\mu$m sources in the *H*-ATLAS Phase 1 catalogue (i.e. they have reliability, $R > 0.80$; see Smith et al. 2011 for a full explanation); two of these are 'classic' BI-defined BAL QSOs whilst the third is only a BAL QSO under the BI_0 definition. For the non-BAL QSOs, 27 of the 329 have reliable $R > 0.80$ $250\,\mu$m counterparts. 0.8 is chosen as a reliability cutoff on the suggestion of Smith et al. (2011) who argues that this will ensure a low contamination rate whilst also ensuring that only one r–band source is responsible for the majority of the FIR emission. A matching radius of 5 arcsec on the SDSS positions of each $250\,\mu$m counterpart is used between the different catalogues. This radius is selected since the positional uncertainty given by Smith et al. (2011) indicates this radius will be sufficient to contain $3\,\sigma$ sources. The likelihood ratio method also uses a 10 arc second radius in associ-

ating counterparts, but upon a match of BAL QSO and non–BAL QSO optical positions to SPIRE detections, none were found to have a separation greater than 5 arc seconds. Finding only 2 'classic' BI-defined BAL QSOs and 27 non–BAL QSOs raises the question of whether there is an actual difference in the detection rate of BAL QSOs and non-BAL QSOs. 6.0 per cent of the 'extended' sample are detected (8.3 per cent of the 'classic' BI defined sample) compared to 8.2 per cent of the non-BAL sample. Since the total number of galaxies which are QSOs is much larger than these samples, as well as the detection of each individual galaxy being independent of the others, a binomial probability distribution can be assumed, where the probability is given by $Pr(K = k) = n!/k!((n-k)!)p^k(1-p)^{n-k}$. Comparing these detection rates gives a null result ($p = 0.19$ and $p = 0.23$ for the 'extended' and 'classic' sample respectively). The null hypothesis that the detected HiBALs are drawn from the same distribution as the detected non-BAL QSOs cannot therefore be rejected. This may imply that both samples will be indistinguishable in flux–density, which is investigated in the next section.

2.3.2 Stacking Analysis

To answer the question of whether HiBAL QSOs and non–BAL QSOs are intrinsically different, a stacking procedure must be used. This is a consequence of having only a few HiBAL QSO detections, which prevents a direct statistical comparison of their flux distributions. By stacking the FIR data at the optical i–band positions of H–ATLAS sources, it is possible to statistically investigate the FIR properties of 250 μm–selected galaxies. This has been used succesfully in various studies to determine the characteristic properties of sources (Dole et al.

Figure 2.5: The 250, 350 and 500 μm weighted mean flux density stacks of the 'extended' BAL and non-BAL QSO (top and bottom row respectively) samples. Each postage stamp image is 210×210 arcsec^2. In each corner in white is given the wavelength, classification, and the number of sources used to create that stack.

Table 2.2: Also included here is the determined background noise for each field at each wavelength.

	Mean background in each field		
Bandpass (μm)	9 h field (mJy)	12 h field (mJy)	15 h field (mJy)
250	1.1483±0.0003	0.9124±0.0003	1.4517±0.0004
350	2.8217±0.0003	2.7246±0.0003	3.0593±0.0003
500	0.3046±0.0003	0.2721±0.0003	0.8491±0.0003

2006; Bethermin et al. 2010).

The FIR flux densities used in this section are taken directly from the final PSF-convolved images for all three H-ATLAS fields. Cutouts of set size (210×210 arcsec^2) of the region surrounding each HiBAL/non-BAL QSO are generated, and these are co-added, each pixel being weighted by the noise to give a final weighted mean. The weighted mean stacked flux density value of each source is taken to be that at the centre of the stacked image which is the closest pixel to the catalogue position in either the Gibson et al. (2009) BAL or Schneider et al. (2007) SDSS QSO samples.

Background subtraction is performed by randomly selecting a sample of 40,000 pixels from each field to create a mean background for that field at that wavelength. This mean background can then be subtracted from every pixel in the cutout images for each QSO. These mean values for each wavelength are shown in Table 2.2, while Fig. 2.5 shows the BAL and non-BAL QSO stacked images at each wavelength.

At longer wavelengths, the stacked HiBAL QSO image is visibly less distinguishable from the background, which is expected due to increased confusion noise and a higher instrumental noise; galaxies at 500 μm are also expected to

be fainter than their 250 μm counterparts, since the Rayleigh–Jeans tail is being sampled in this redshift range. Table 2.3 shows the central pixel values of the stacks. It is found that there is no statistical difference between HiBAL QSOs and non-BAL QSOs; their flux densities in all bandpasses are the same within the errors. This result holds for both the 'classic' and 'extended' BAL QSO samples.

A second method is used in an attempt to reproduce the results as a sanity check using the Institut d'Astrophysique Spatiale (IAS) stacking library. It stacks data to allow a statistical detection of a faint signal using positions of galaxies detected at shorter wavelengths as with the previous method but has also been tested and validated with galaxy clustering in mind, something which may affect the previous results (see Bethermin et al. 2010 for further details). The background is again subtracted prior to stacking, yet there is still found no difference between the HiBAL QSO and non-BAL QSO samples in each bandpass and the IAS values are in agreement with the previous values within the errors (see Table 2.3). The discrepancy in values can be attributed directly to the added step of weighting each field stack individually. A drawback of the IAS method is that only sources within an image are stacked. Therefore, to stack across the three fields a second stacking procedure involving the stacks for each field must be created. These field stacks have no noise component, so the error is derived by sampling the weighted mean. The error on that weighted field stack may not be fully representative and is somewhat subject to the area sampled to derive the error, so the way each field stack is added will differ slightly to the individually added AGN stack.

It should be noted that submillimetre flux densities may still be overestimated due to clustering of sources if they emit in the SPIRE bands, but since sources

Table 2.3: The HiBAL ('extended' and 'classic' samples) and non-BAL QSO FIR weighted mean flux densities in the 250, 350 and 500 μm bandpasses. The number in brackets gives the number of objects within each stack.

	HiBAL QSO and non-BAL QSO flux densities		
Bandpass (μm)	'Extended' stack (49, mJy)	'Classic' stack (35, mJy)	non-BAL stack (329, mJy)
250	12.34±1.29	11.13±1.70	11.48±0.51
350	11.11±1.42	9.57±1.67	9.62±0.58
500	7.18±1.18	5.46±1.59	7.42±0.57
	IAS HiBAL QSO and non-BAL QSO flux densities		
Bandpass (μm)	'Extended' stack (49, mJy)	'Classic' stack (35, mJy)	non-BAL stack (329, mJy)
250	12.35±1.25	11.19±1.61	11.43±0.52
350	11.01±1.44	9.88±1.71	9.49±0.59
500	7.25±1.19	5.42±1.67	7.60±0.58

around the QSO at high redshifts cannot be identified accurately, there is little that can be done to solve this problem. It should also be emphasized however that the effects of confusion should be the same for both HiBAL QSOs and non-BAL QSOs since they are treated in an equal manner within both methods.

To ensure these results (specifically, no difference between HiBAL and non–BAL QSOs) are not merely due to the presence of strong detections within the sample, weighted mean stacks with $5\,\sigma$ detections excluded have been produced. The median of these detectionless samples have also been taken. The numerical values of this analysis can be seen in Table 2.4. Whilst there is a definite decrease in derived flux density, there is still no difference between the weighted means for each sample across the 3 separate wavebands. This trend seems to continue when only medians are considered; the only exception being at 500 μm where it appears non–detected non–BALs are significantly brighter than their BAL counterparts.

Table 2.4: The HiBAL ('extended' and 'classic' samples) and non-BAL QSO FIR weighted mean flux densities and medians in the 250, 350 and 500 μm with detections excluded. The median with detections included are typeset in bold. The errors quoted on the median are simply the standard error on the median (assuming a Gaussian distribution).

HiBAL QSO and non-BAL QSO weighted mean flux densities			
Bandpass (μm)	'Extended' stack (mJy)	'Classic' stack (mJy)	non-BAL stack (mJy)
250	9.05±1.20	8.57±1.78	7.50±0.63
350	7.56±1.65	6.58±1.88	6.10±0.58
500	5.34±1.39	4.15±1.39	6.60±0.55
Median HiBAL QSO and non-BAL QSO flux densities			
Bandpass (μm)	'Extended' stack (mJy)	'Classic' stack (mJy)	non-BAL stack (mJy)
250	8.65±1.63	8.76±1.78	6.19±1.18
	8.93±2.84	**8.93±2.94**	**7.39±1.18**
350	5.46±1.93	5.46±2.08	6.43±0.79
	7.45±3.16	**5.47±3.65**	**6.43±1.26**
500	3.32±2.04	2.67±2.06	8.47±0.86
	4.42±2.57	**2.67±2.65**	**5.46±1.07**

One is loath to take this single data point as evidence of a difference in the two populations however, particularly when at 250 and 350 μm the medians suggest the opposite. At 500 μm it is likely that the large size of the beam coupled with small number statistics is sufficient to ensure the BAL median is far lower than that of the non–BAL sample.

The Gaussian errors quoted in Tables 2.3 and 2.4 must be treated with caution, since background noise will be non-Gaussian owing to confusion noise, so simply dividing the signal by the measured noise on the stack may not be sufficient to truly calculate the σ at which any results are detected. Two further tests must therefore be performed. To determine quantitatively whether the stacked

Table 2.5: The KS statistics and probabilities of each sample in comparison with a randomly selected sample of flux densities taken from the H-ATLAS fields. The fraction shows how many random stacks had flux densities greater than the QSO sample stacks.

Bandpass (μm)	250	350	500
	'Extended' BI_0		
KS statistic	0.49	0.36	0.29
KS probability	$< 10^{-10}$	$< 10^{-5}$	0.0004
Fraction	0	0	0
	'Classic' BI		
KS statistic	0.47	0.33	0.32
KS probability	$< 10^{-5}$	0.0006	0.0012
Fraction	0	0	0
	non–BAL QSOs		
KS statistic	0.39	0.31	0.25
KS probability	$< 10^{-10}$	$< 10^{-10}$	$< 10^{-10}$
Fraction	0	0	0

HiBAL QSOs are detected significantly, flux densities from 120,000 randomly chosen positions in the field have been measured following the method described in Hardcastle et al. (2010). The random background compared with the HiBAL and non–BAL QSO stacked central fluxes are shown in Fig. 2.6. Using a KS test, one can examine whether the flux densities of the stacks are statistically distinguishable from those taken from randomly chosen positions, as a KS test is not influenced by the noise properties.

In comparison to the background, HiBAL QSOs at all wavelengths are detected using both classification schemes. The significance of the 250 μm detection for 'extended' BI_0 HiBAL QSOs is well over $5\,\sigma$ ($p < 10^{-10}$), and as expected, the significance decreases towards longer wavelengths, being lowest at 500 μm ($p = 0.0004$). The larger sample of non-BAL QSOs is also detected with high

significance above the background at all wavelengths ($p < 10^{-10}$). Returned KS probabilities are shown in Table 2.5. A KS test is also used to compare the distribution of flux densities between the HiBAL QSO samples and the non-BAL QSO samples (see Table 2.5), as this will be sensitive to outliers which may skew the distributions and bias the derived values in tables 2.3 and 2.4. At 250, 350 and 500 μm their p-values are $p = 0.35$, 0.67, and 0.36 respectively for the 'extended' sample when comparing the BAL QSO sample with the full non-BAL QSO sample. The classic sample is similarly indistinguishable. The null hypothesis that the HiBAL and non–BAL QSOs are drawn from the same underlying flux density distibution can therefore not be rejected.

A second test is performed where 120,000 stacks are created using flux densities extracted from random positions, with the number of elements in the stack equal to the elements in the comparison sample stack, i.e. 49, 35 and 329, and then these random stacks are compared with the stacked flux densities of the HiBAL and non-BAL QSO samples. The fraction of random stacks where the weighted mean flux density exceeds the weighted mean flux density in the QSO sample stacks provides an estimate of the probability of the detection of the HiBAL QSO stack being just a background fluctuation. It is found that none of the 120,000 flux density stacks extracted at random positions have larger weighted mean flux densities than the HiBAL or non-BAL stacked flux densities as shown in Table 2.5.

Therefore, taking the results of these tests in hand would suggest that these sources are not merely background fluctuations and that the stack values are the product of real sources rather than serendipitous stacks. Yet there is no differ-

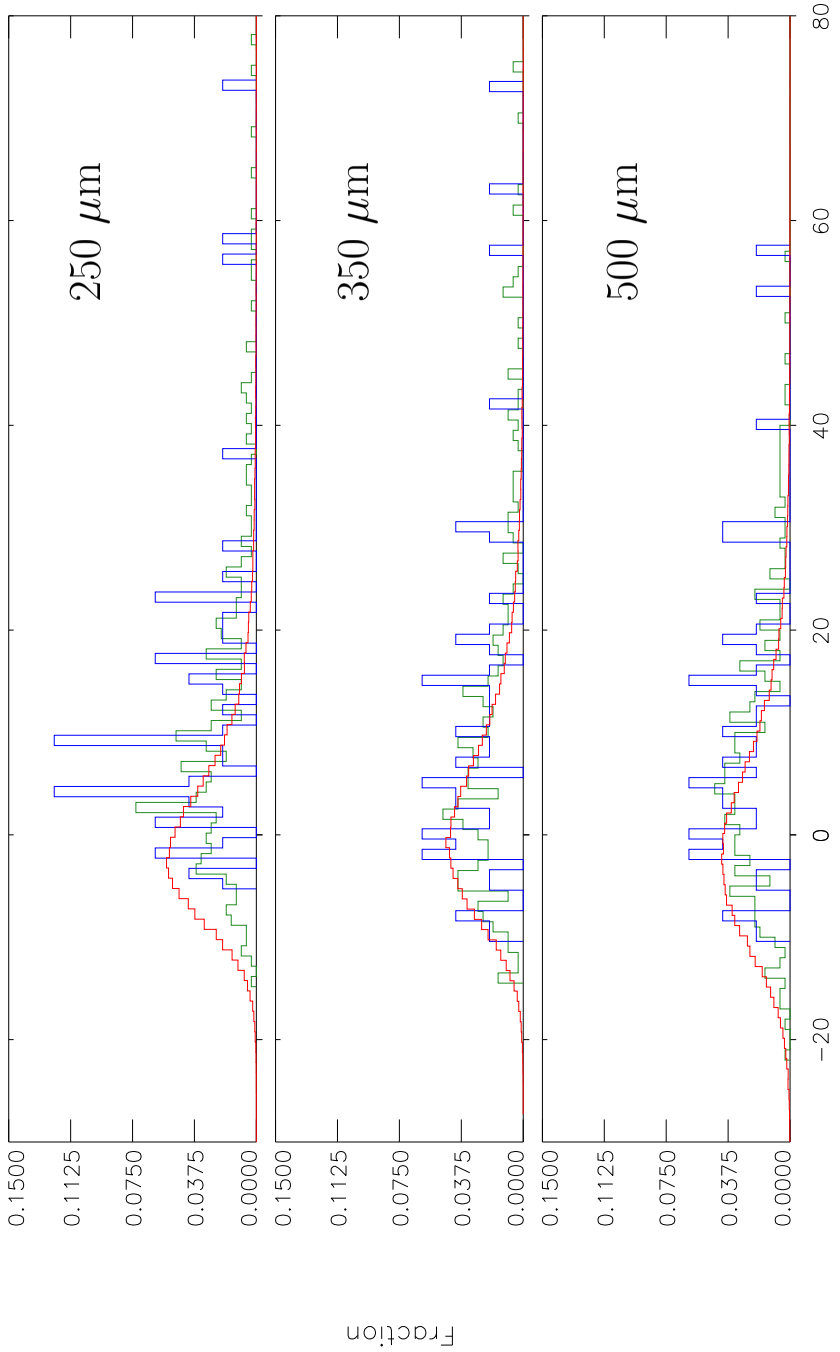

Figure 2.6: The distribution of flux density at each wavelength for the full BAL (blue outline) and non-BAL QSO (green outline) samples in bins of width 1 mJy. The random background flux densities are shown as a red outline.

ence between the distribution of flux densities between the HiBAL QSOs and the non–BAL QSOs, which implies that HiBAL QSOs are merely an orientation effect rather than an evolutionary phase. These results are discussed in greater detail and how they fit into the 'bigger picture' in Section 2.4.

2.3.3 FIR luminosities and SFRs

Galaxies detected by *Herschel* are mostly star–forming galaxies, with those detected by H–ATLAS specifically being Luminous Infrared Galaxies (LIRGs, defined as galaxies with infrared luminosities $> 10^{11}\,\mathrm{L}_{\odot}$). The FIR emission in these detected sources corresponds to reprocessed light from star formation, mostly UV radiation from massive O and B type stars which passes through the dusty clouds in which such star formation is enshrouded. If HiBALs and non-BALs are physically different, it might be expected that they would have differing SFRs, particularly if they are different evolutionary phases with differing dust masses produced by ongoing SF.

There is limited information on the shape of the SED of the QSOs and therefore a suitable template must be chosen in order to compute FIR luminosities (L_{FIR}). The primary galaxy chosen for this purpose is Mrk 231. Mrk 231 is an Ultraluminous Infrared Galaxy (ULIRG) believed to be a QSO that has begun to remove the dust and gas that until now has obscured it (Smith et al. 1998), though the central QSO remains covered by a semi-transparent cloud (Reynolds et al., 2009). Of the local ULIRGs, it is the most luminous, with a luminosity at 8–1000μm of $3.2 \times 10^{12}\,\mathrm{L}_{\odot}$, and shows similar broad absorption line features as this sample, having been classified as a BAL QSO. A second template is chosen to

act as a lower extreme, IZw1, a local Seyfert type 1 galaxy in the nearby universe at $z = 0.0589$ (Ho & Kim 2009).

To determine the luminosity of each source, a greybody model as discussed in Hildebrand (1983) is fitted to FIR data points retrieved from the NASA Extragalactic Database (32 and 7 respectively for Mrk 231 and IZw1), constraining the data points so as to exclude a contribution from AGN heated dust emission (see Fig. 2.8). A caveat of this method is that this means the SED fit only takes into account the kpc scale dust emission, it misses out the circum-nuclear emission, from which much of the bolometric luminosity of Markarian 231 is believed to originate, up to 70 per cent, compared with an average of 35–40 per cent for other ULIRGs (Veilleux et al. 2009). Furthermore, the lower number of data points for IZw1 will mean a larger error on any derived parameters for that template. As visible in Fig. 2.8, Mrk 231 has significantly higher FIR emission than IZw1 which is likely due to different stellar populations or differing dust distributions.

To derive the parameters for the greybody in each case, χ^2 minimisation techniques are used to determine the total $L_{\rm FIR}$ for each template source as well as the errors on beta and temperature which are required for error estimates on SFRs (see Fig. 2.9). Estimates are further weakened by the degeneracy between source size and opacity, leading to values of λ_0 and ω which are not well constrained (see Fig. 2.10).

The observed flux density at $250\,\mu$m is an excellent measure of the SFR, yet will need to be K-corrected (see subsection 1.3.4 for further details) before it can be used. Since the redshifts of all sources are known, a ratio method can be applied between the $250\,\mu$m flux density of either the Mrk 231 or IZw1 greybody

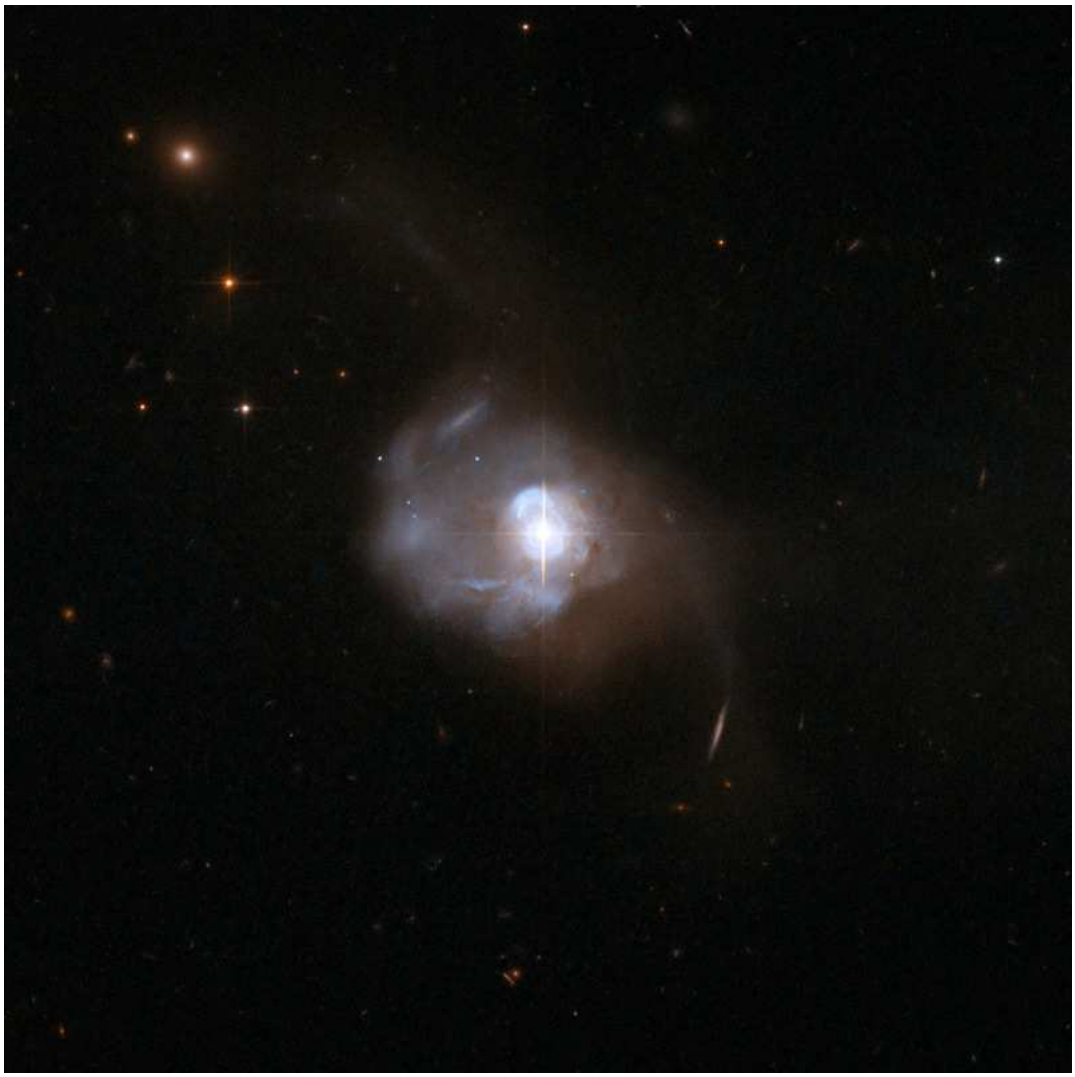

Figure 2.7: A Hubble image of Mrk 231. From this image it appears that the galaxy remains somewhat shrouded in dust, though emission from the central region is also clearly visible. Image credit: NASA/Hubble

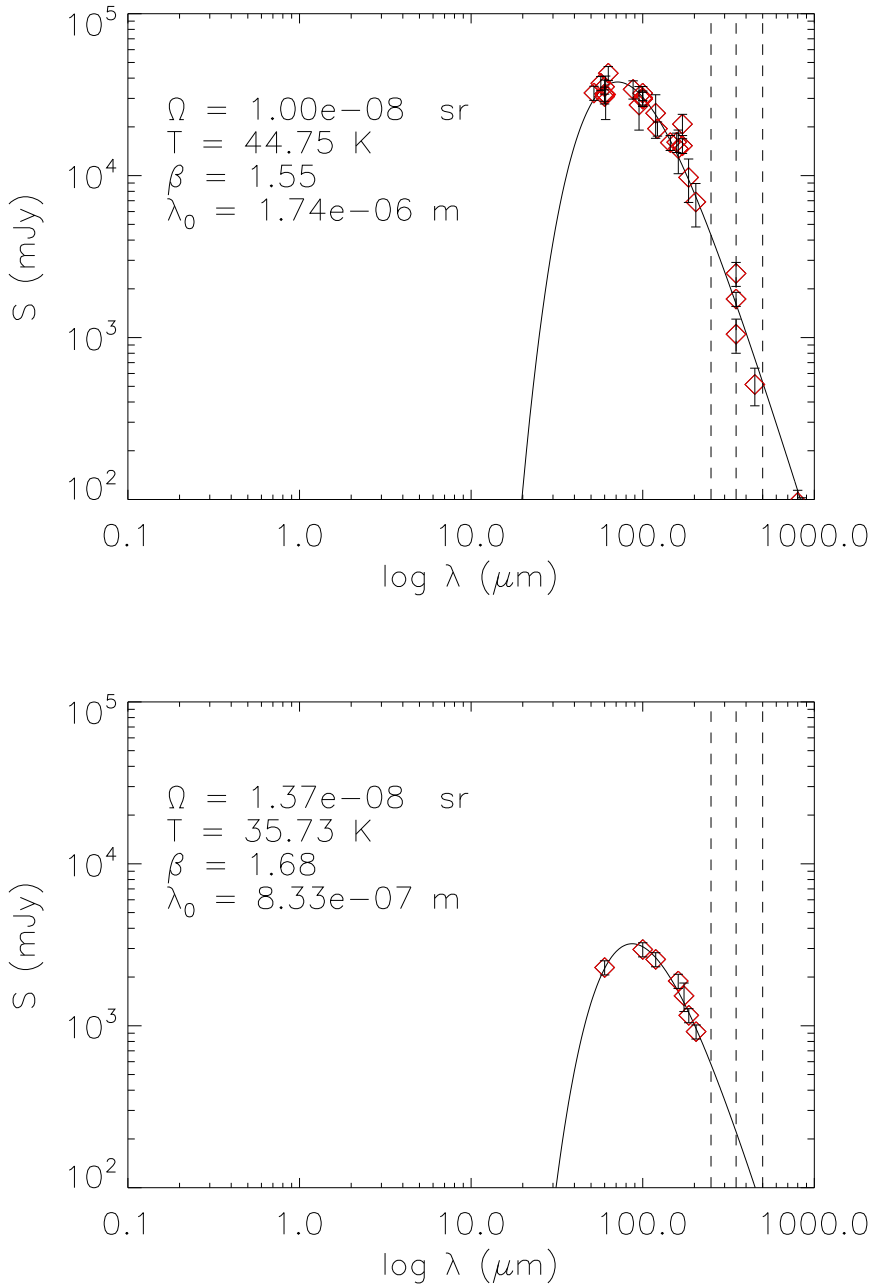

Figure 2.8: The derived SEDs of Mrk 231 (top panel) and IZw1 (bottom panel) following χ^2 minimisation techniques. Mrk 231 is clearly visible as having significantly higher FIR emission as well as having a slightly shorter rest–frame peak wavelength than IZw1 (which may be attributable to different stellar populations or differing dust distributions). Alongside each SED are the derived parameters for each curve. The dashed lines show where the 250, 350 and 500 μm wavebands fall on the SED.

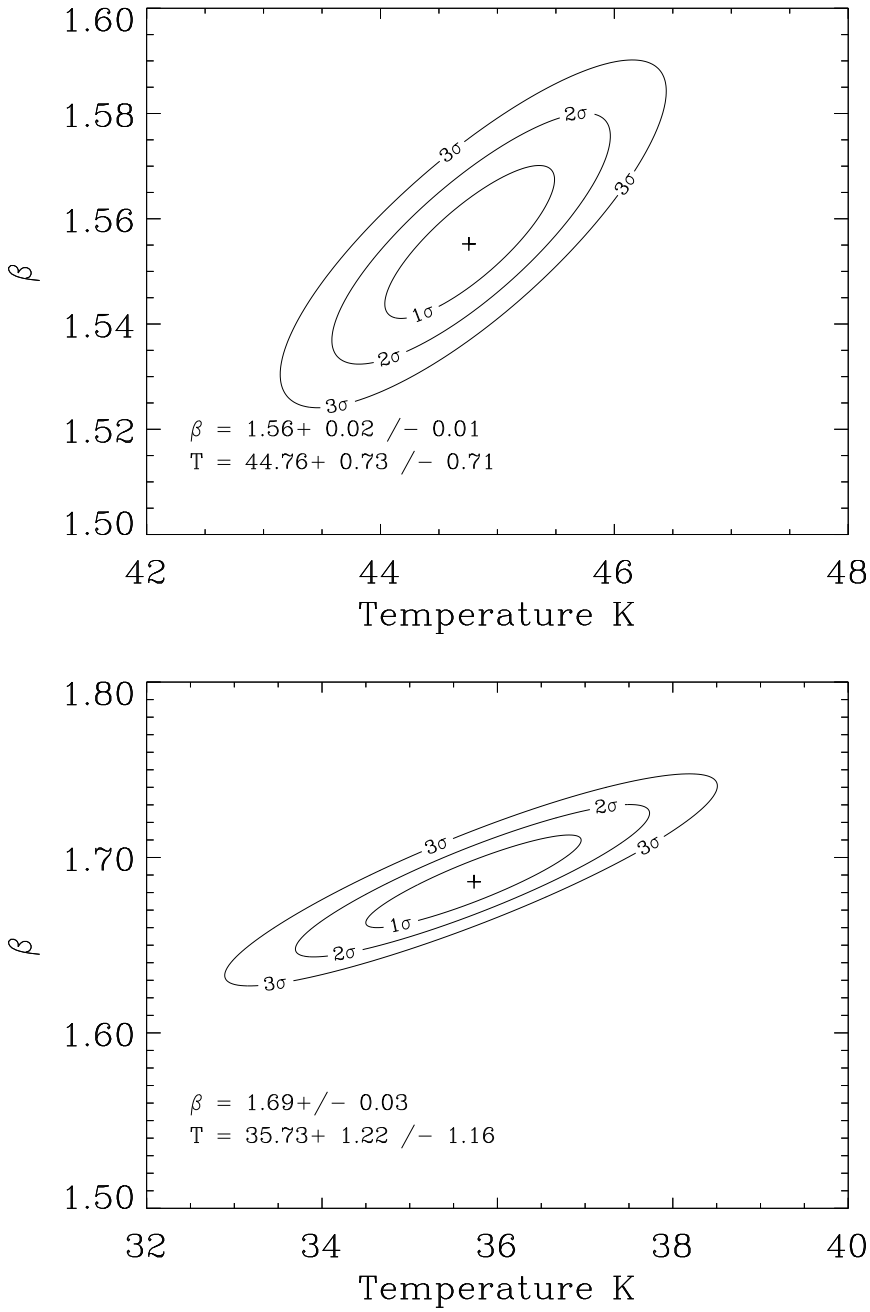

Figure 2.9: Contour plots showing the range of error on the temperature and dust emissivity index β when using Mrk 231 (top panel) and IZw1 (bottom panel) as a greybody template. The plots show the range of allowed values out to $3\,\sigma$ in temperature and β.

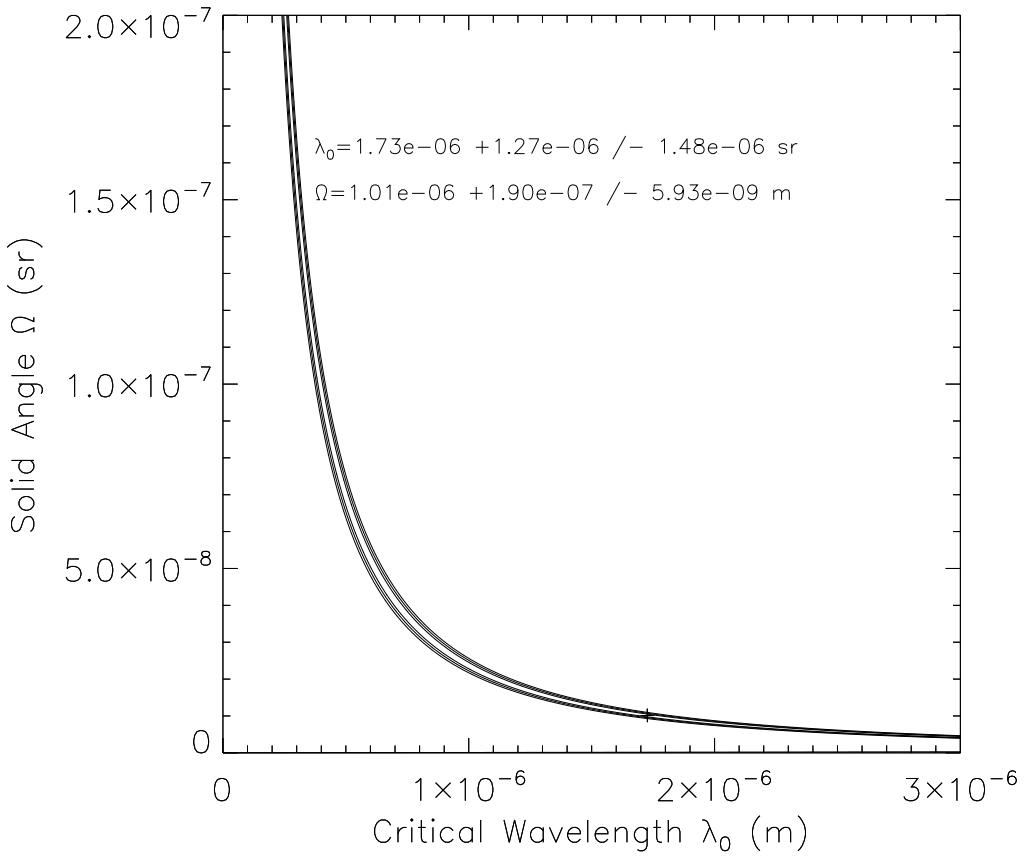

Figure 2.10: This plot shows an attempt at determining the range of error on source size Ω and critical wavelength λ_0, through the use of χ^2 contours (using a procedure similar to Fig. 2.9). The degeneracy between source size Ω and critical wavelength λ_0 means that error estimates for those parameters cannot be derived.

templates if placed at the redshift of the QSO in each sample and the 250 μm flux density of the QSO. This implicitly assumes that the QSO has the same FIR SED as the greybody template, but is required since there are insufficient data points to fully fit a greybody model otherwise. The calculation of SFR was then performed in the standard manner using the relationship with L_{FIR} published by (Kennicutt, 1998) in equation 1.6. The results of these calculations are presented in Table 2.6.

The average Kennicutt SFR is 245 ± 21 $M_{\odot}\,yr^{-1}$ for the 'extended' and 229 ± 25 $M_{\odot}\,yr^{-1}$ for the 'classic' sample (Table 2.6); these values are consistent. Note that these estimates are determined from weighted stacking of the individual luminosities and SFRs derived from the 250 μm flux density of each galaxy rather than calculated from the weighted stacked flux density values in Table 2.3 so there will be some slight variation, particularly if there are some outliers in the 'classic' sample which may boost the derived SFR. However, the HiBAL and non-BAL average SFRs remain consistent within the errors. It is found that the 3 detected HiBAL QSOs have SFR > 1000 $M_{\odot}\,yr^{-1}$. The fitted SED of Mrk 231 to each waveband for each detected BAL QSO can be found in the Appendix. Since the possibility that some fraction of the FIR emission comes from dust heated by the AGN cannot be excluded, these SFRs should be regarded as upper limits, as currently, the FIR emission is assumed to be solely due to obscured star formation. The average FIR luminosities presented in Table 2.6 for both the BAL and non-BAL QSO samples are, on their own, sufficiently large to classifiy them as ULIRGs. It should also be noted that the derived SFRs for each SPIRE band for IZw1 are more consistent than those determined for Mrk 231. This suggests

Table 2.6: The SFRs and FIR luminosities of the detected BAL QSOs within the sample (indicated by an asterisk), along with the weighted mean SFR in the 250, 350 and 500 μm bandpasses and weighted mean for the 'extended' , 'classic' and non-BAL samples as a whole using Mrk 231 and IZw1 as templates. The SFR of the rare LoBAL QSO 115404.13+001419.6 has also been calculated. It must be emphasized however that it is not reliably associated with R > 0.80 to a 250 μm source as with the detected HiBAL QSOs and instead is the best estimate from measuring the flux density in the closest pixel of the PSF-smoothed map. At 500 μm it has a negative flux so SFRs are not included. The quoted L_{FIR} (using the ratio method for 250 μm) and SFR estimates are determined from weighted stacking of the individual luminosities and SFRs of each galaxy rather than calculated from the weighted stack values in Table 2.3 (shown in the flux density column), though the error will be underestimated as a result of confusion noise.

SDSS Source	z	Flux density	$\log_{10}(L_{FIR}/L_{\odot})$	SFR ($M_{\odot}\,yr^{-1}$)			
		(250 μm)	(Mrk 231)		(Mrk 231)		
		(mJy)	(250 μm)	250	350	500	Mean
*085436.41+022023.5	1.9089	55.87±6.81	12.87±0.07	1322±199	2353±364	3158±754	1559±175
*090517.24+013551.4	1.7678	57.81±6.77	12.85±0.06	1248±183	2386±369	4092±787	1473±164
*143907.51−010616.7	1.8214	73.35±6.95	12.97±0.06	1640±212	1535±318	2297±724	1608±176
115404.13+001419.6	1.6100	29.88±6.65	12.51±0.10	580±139	694±250	...	607±121
'Extended' BAL QSO	...	12.34±1.29	12.14±0.04	245±21	343±39	453±96	267±19
'Classic' BAL QSO	...	11.13±1.70	12.11±0.05	229±25	300±46	401±115	245±22
Non-BAL QSO	...	11.48±0.51	12.10±0.02	222±8	315±15	528±36	243±7
		(250 μm)	(IZw1)		(IZw1)		
		(mJy)	(250 μm)	250	350	500	Mean
*085436.41+022023.5	1.9089	55.87±6.81	12.75±0.10	1007±227	1506±343	1824±532	1159±189
*090517.24+013551.4	1.7678	57.81±6.77	12.71±0.10	921±204	1625±357	2341±597	1094±177
*143907.51−010616.7	1.8214	73.35±6.95	12.84±0.09	1224±259	972±269	1320±471	1103±187
115404.13+001419.6	1.6100	29.88±6.65	12.37±0.13	413±121	427±170	...	418±99
'Extended' BAL QSO	...	12.34±1.29	11.95±0.05	157±17	183±26	231±57	165±14
'Classic' BAL QSO	...	11.13±1.70	11.94±0.08	142±19	153±30	184±66	144±18
Non-BAL QSO	...	11.48±0.51	11.86±0.02	127±6	153±10	257±22	134±5

that dust in BAL QSOs at higher z is likely cooler than that found in the low–z analogue Mrk 231. It is worth considering that even though a change in β from 1.0 to 2.0 may only affect final SFRs as much as 1.5 times, a change in temperature from 23.5 K to 45 K can change the determined SFR by a factor of ~ 3 (see Figs. 2.11 and 2.12) when using a normalised greybody model assuming a flux density of 33.5 mJy. When applied to the flux densities of the detected sources (e.g. ~ 55 mJy), a similar spread in values is found, which does not change the final conclusions.

2.3.4 FIR luminosity and C IV absorption–line equivalent width

From an analysis of submillimetre wavelength data, Priddey et al. (2007) found a weak correlation between FIR flux density and C IV absorption–line equivalent width. The sample studied was composed of 15 BAL QSOs taken from the Large Bright Quasar Survey (LBQS, Hewett, Foltz & Chaffee 1995). These sources were spread between redshifts of 1.5 to 3, and their absolute B–band magnitudes were extrapolated from measurements at 2000 Å(which may have biased the sample; see Section 2.4). A stronger statistical link between submillimetre detection rate and C IV absorption–line equivalent width was also discovered; i.e., of the 15 BAL QSOs they observed, all 6 ($>2\,\sigma$) detections in the 850 μm band had a C IV absorption–line equivalent width of ≥ 25 Å. A KS test returned a probability of 0.01 that the detections and non-detections had the same C IV absorption–line equivalent width.

With the larger sample presented in this thesis, it would be trivial to examine

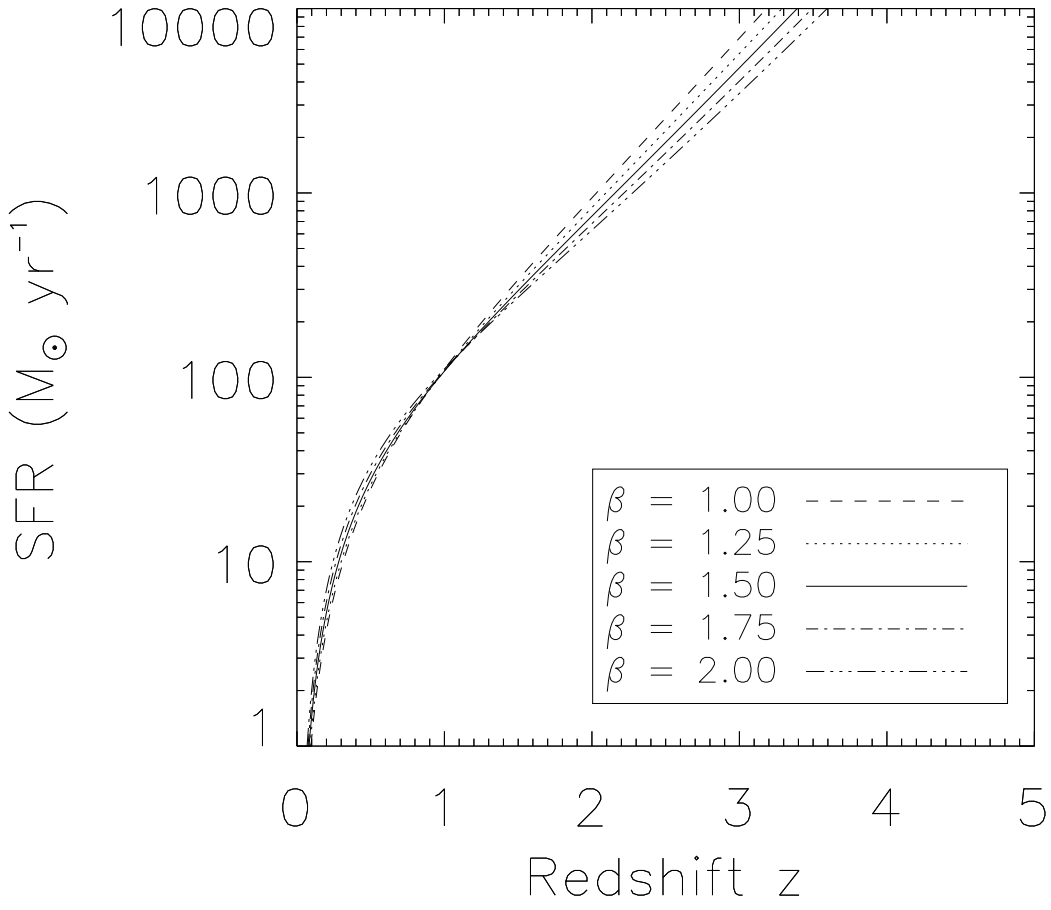

Figure 2.11: The SFR calculated using Kennicutt's relation (equation 1.6) for a greybody with a temperature of 23.5 K and five different values of β. The adopted 250 μm flux–density is equal to the H–ATLAS 5 σ level cutoff (33.5 mJy).

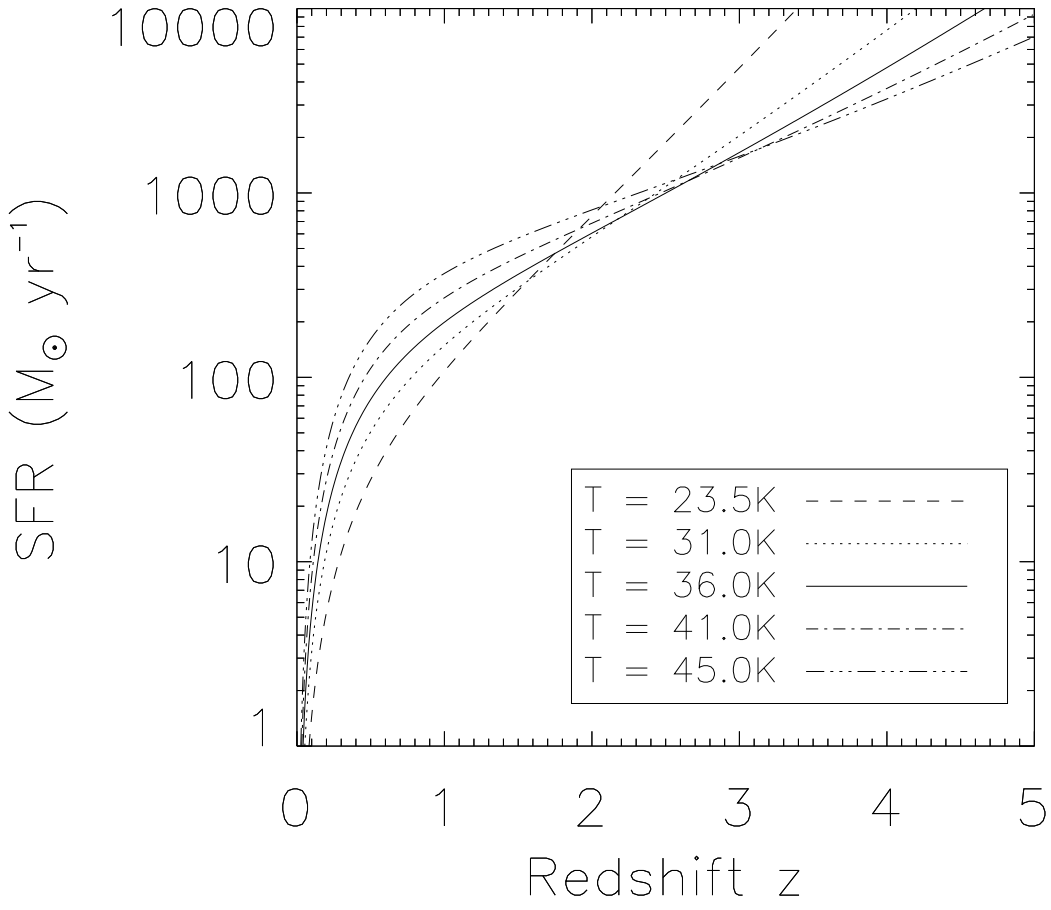

Figure 2.12: The SFR calculated using Kennicutt's relation (equation 1.6) for a greybody with a β of 1.5 and five different values of temperature. The adopted 250 μm flux–density is equal to the H–ATLAS 5 σ level cutoff (33.5 mJy).

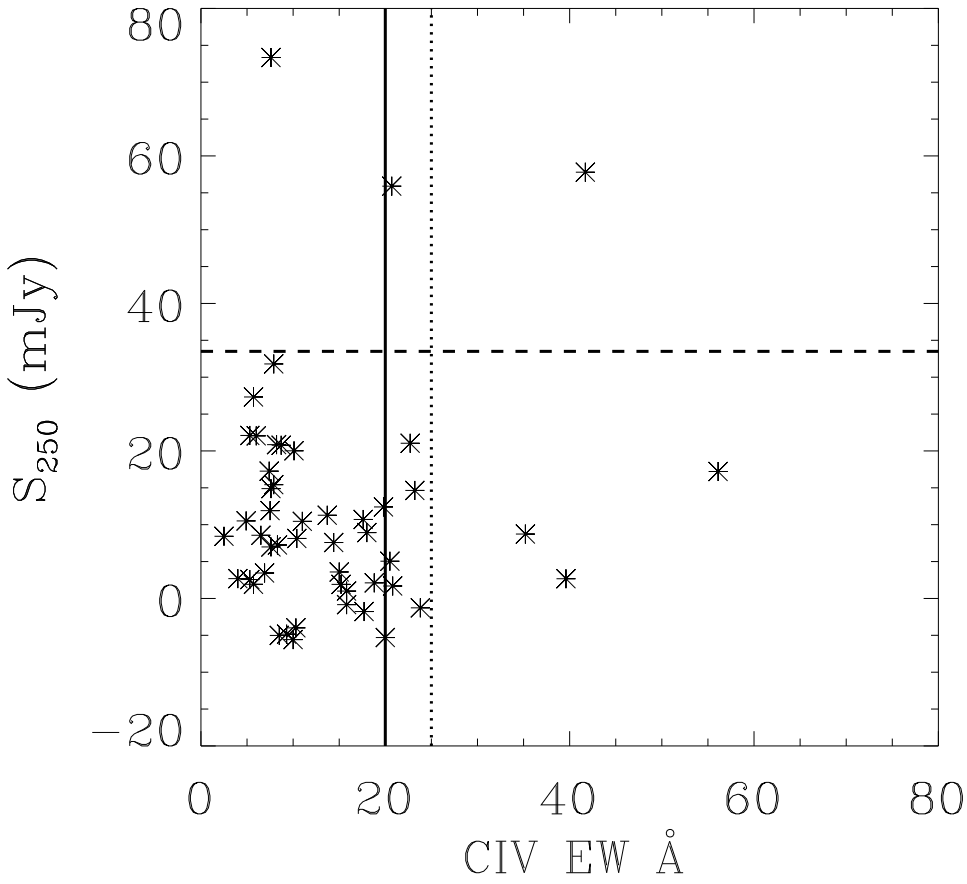

Figure 2.13: The distribution of all 49 HiBAL sources in the data as a function of 250 μm flux–density and C IV equivalent width. The horizontal dashed line shows the H–ATLAS 5 σ level. The solid black line is a 20 Å cutoff, whilst the dotted line shows that used by Priddey et al. (2007). As is visible, in terms of detections there is only one detected source if a 25 Å cutoff is used and only 2 if it is lowered to 20 Å. This is in stark contrast to the 6 sources found by Priddey et al. (2007) albeit at a lower significance.

whether the Priddey et al. (2007) result was merely a consequence of small number statistics. The close proximity to the peak of the obscured star formation SED at 250 μm will also mean the results presented here should be more sensitive to any effects by the BAL wind. If C IV absorption–line equivalent width does affect FIR flux density as Priddey et al. (2007) suggest, it would also be prudent to use only the strictest definition of balnicity so as to select those sources with the strongest winds. By selecting only those HiBAL QSOs within the 'classic' sample, the likelihood of contamination by non–BAL QSOs is reduced due to the stricter velocity space constraint imposed by the BI compared to the BI_0 used by Gibson et al. (2009) (see Section 1.1.3) to create the BAL QSO catalogue from which the 49 HiBAL QSOs studied here are taken from.

Unfortunately, the combination of a high C IV absorption–line equivalent width cutoff ($\geq$ 25 Å) and few detections in the full sample means that no $5\,\sigma$ detections are associated with 'classic' BAL QSOs. Whilst this is not ideal, the relatively large size of the sample means a variety of cutoffs can be used to test whether C IV absorption–line equivalent width affects the FIR emission of the host galaxy. Furthermore, any true underlying physical relationship involving the C IV absorption–line equivalent width will be expected to correlate with luminosity rather than flux density, as this will account for any biases arising from variations in redshift. Therefore, the $L_{\rm FIR}$ luminosities of each HiBAL QSO using the assumed T and β for Mrk 231 and IZw1 were determined.

With these changes in mind, the first cut–off is chosen as $\geq$ 20 Å which selects 11 bright HiBAL QSOs to compare with the remaining 24 in the classic sample. These two populations are then compared using a Mann–Whitney test (Mann & Whitney 1947) to determine whether a greater FIR lumnosity correlates with a

larger C IV absorption–line equivalent width. Contrary to the findings of Priddey et al. (2007), the test returned probabilities of 0.23 and 0.22 (for the Mrk 231 and IZw1 templates respectively) using the 250 μm data point, which indicates that there is no significant evidence for a difference in the two subsamples. Even with a variety of cutoff values and no luminosity template applied for all 3 bandpasses, at no point does the Mann–Whitney test suggest one population has larger FIR luminosities/flux densities than the other.

In an attempt to extend this finding to the rest of the BAL QSO population, a KS test was performed to determine whether the distribution of C IV absorption–line equivalent widths within the restricted HiBAL QSO sample were representative of those within the parent population of BAL QSOs as defined by Gibson et al. (2009) from the overall SDSS DR5 QSO catalogue (Schneider et al. 2007). A KS test on the C IV absorption–line equivalent widths of each population returns $p = 0.12$, suggesting the sample can be taken as representative. Fig. 2.14 shows histograms of the two C IV absorption–line equivalent width distributions which appear to be relatively similar. These results would imply that HiBAL QSOs do not have a dependence on C IV absorption–line equivalent widths, that the components responsible for each (i.e. UV line–radiation driven wind and extended star formation in the host galaxy) do not influence each other and are separate. This would, in combination with the other results in this work, support the view that HiBAL QSOs are merely an orientation effect. Any UV–absorbing component will be optically thin to FIR emission so no dependence on viewing angle or absorption strength is to be expected at SPIRE wavelengths.

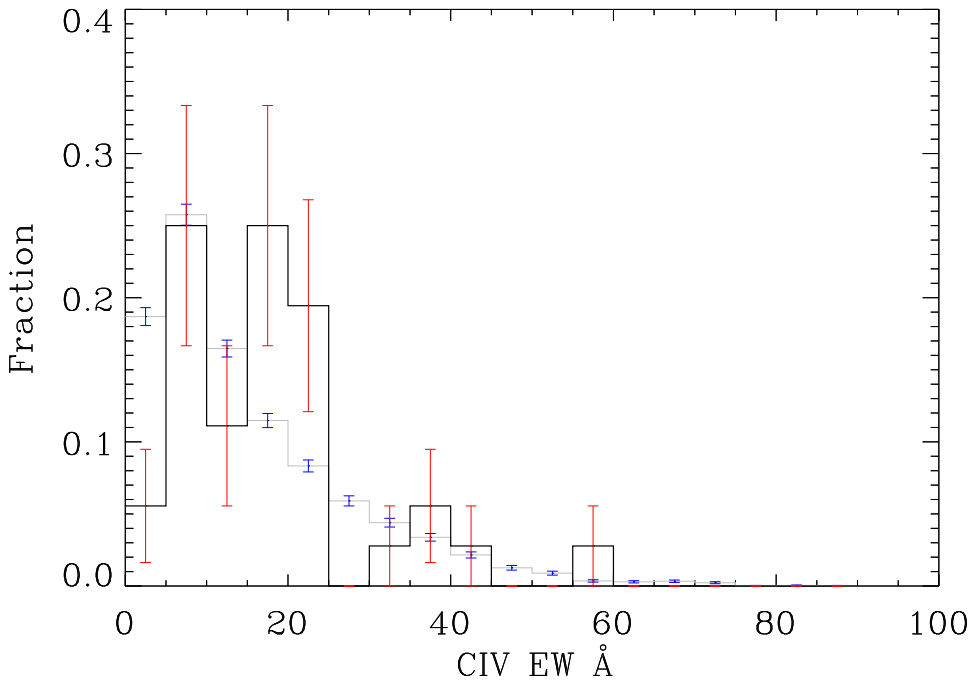

Figure 2.14: The distribution of C IV absorption–line equivalent width for the full Gibson et al. (2009) sample (grey) and the 'classic' BAL QSO sample (black outline) in bins of width 5 Å. One source in the Gibson et al. (2009) sample is omitted in the figure, SDSS090901.80+535935.7, having a C IV absorption–line equivalent width of 193.9 Å. All others have C IV absorption–line equivalent widths below 90 Å.

2.4 Discussion

This study shows that the FIR properties of HiBAL QSOs are statistically indistinguishable from those of non-BAL QSOs. It is also found that FIR emission has no dependence on C IV absorption–line equivalent width. Therefore the FIR luminosity has no dependence on the absorption strength of the outflow, and the results do not require an evolutionary link between HiBAL and non-BAL QSOs. Rather a simple orientation effect argument is sufficient.

Priddey et al. (2007) found tentative evidence for a link between C IV absorption–line equivalent width and submillimetre wavelength detection (albeit with a $2\,\sigma$ detection threshold). As discussed by Priddey et al. such a link could be used to argue that BAL QSOs are in a distinct evolutionary phase along the lines proposed by Page et al. (2004, 2011) where the QSO wind is in the process of terminating an epoch of enhanced star formation. The results in this study do not support this weak evidence for such a link between FIR output and C IV absorption–line equivalent width. The discepancy may be linked to a possible selection effect discussed by Priddey et al.; that the most reddened QSOs must be intrinsically more luminous to meet their blue selection criterion, and therefore the most extreme objects, which might host the most powerful outflows would have higher dust reddening and higher FIR/submm output. This could explain why no such correlation is seen in this work, since the SDSS i band does not suffer reddening to as large a degree as the bluer bands in which past samples of QSOs were selected.

However, a caveat to the results found here is that the sample is composed almost entirely of HiBAL QSOs. LoBAL QSOs or their rarer FeLoBAL cousins,

which may well show FIR properties inconsistent with a simple orientation scheme hypothesis (see below) have not been considered here. Yet the samples of Willott, Rawlings & Grimes (2003) and Priddey et al. (2007) were also mostly composed of HiBAL QSOs. The Priddey et al. (2007) sample contains only 1 known LoBAL QSO, and many of the Willott, Rawlings & Grimes (2003) QSOs classified as LoBAL QSOs are uncertain due to Mg II moving out of the spectral range at $z > 2.26$.

Regarding studies at other wavelengths, the findings of Green et al. (2001) carried out using the *Chandra* X-ray observatory provide weak evidence that HiBAL QSOs appear X-ray weak due to intrinsic absorption, and that their underlying emission is actually the same as that of non-BAL QSOs (Gallagher et al. 2002, 2006; Gibson et al. 2009), which supports an orientation scheme. In contrast, even taking into account intrinsic absorption, LoBAL QSOs remain X-ray weak. An analysis of X-ray absorption performed by Streblyanska et al. (2010) suggests that LoBALs and HiBALs may be physically different objects. This is reinforced by composite SEDs ranging from X-ray to radio generated by Gallagher et al. (2007) who find similarities between the SEDs of HiBALs and non-BAL QSO but differences between these populations and LoBALs. However, it should be noted that the absorbed nature of BAL QSOs means that their X-ray data are limited in quality, so these findings cannot be taken as conclusive.

Certainly LoBAL QSOs are found to have redder spectra than other types (Reichard et al. 2003a), implying a larger dust mass in the vicinity of the SMBH. The idea that LoBALs and FeLoBALs form a separate evolutionary class finds support from the work of Farrah et al. (2007) and Urrutia et al. (2009). Farrah et al. (2007) argue that FeLoBAL QSOs are galaxies where a massive merger

driven starburst is ending, and the last remnants of a dust cocoon are being removed by a rapidly accreting supermassive black hole at the galaxy's centre. The SED fits of those detected at longer wavelengths (4/9) require a starburst component of the order of several hundred solar masses per year, which is taken to imply that FeLoBAL QSOs are associated with ULIRGs. Similar conclusions are drawn in Farrah et al. (2010) who find that FeLoBAL QSOs span a range of spectral shapes, consistent with the idea that they may be a transition phase in the lifetime of an AGN. However, as noted in their papers, the small and inhomogeneous sample sizes render such conclusions tentative. A larger sample was presented by Farrah et al. (2012) of 31 objects with optical to far–infrared photometry. These were found to all be highly luminous ($> 10^{12}\,L_{\odot}$), yet the bulk of IR emission in the majority of sources came from the AGN rather than a starburst component. The mid–IR and far–infrared properties of the FeLoBAL QSOs spanning the redshift range $0.8 < z < 1.8$ presented by Farrah et al. further reinforce the idea that they are a class apart from the general QSO population.

Urrutia et al. (2009) also found an unusually high percentage (32 per cent using the conservative BI selection) of LoBAL QSOs in a sample of dust reddened type-1 QSOs; in fact all of these objects can also be classified as FeLoBALs. The orientation hypothesis is irreconcilable with such findings allowing an evolutionary hypothesis to be invoked, even with the caveats offered by Urrutia et al. (2009).

The subset of the full Gibson et al. (2009) sample studied here contains only one QSO, SDSS115404.13 + 001419.6, classified as a LoBAL. These objects are rare, making up only 15 per cent of all observed BAL QSOs. A very deep C IV absorption trough (greater than anything seen in the HiBAL sample), combined with a high flux density (29.88 ± 6.65 mJy at $250\,\mu$m) makes it a conspicous

member of the sample investigated here. However, little can be said of an entire population from one object. Future work in the FIR/submillimetre wavebands targeting LoBALs and/or FeLoBALs would be invaluable.

2.5 Conclusions

1. Using a stacking analysis it has been determined that HiBAL QSOs at $1.5 \leq z < 2.3$ are statistically indistinguishable in terms of FIR luminosity (and therefore SFR) from a matched sample of non-BAL QSOs. This result is broadly consistent with previous work conducted at submillimetre wavelengths (Willott, Rawlings & Grimes 2003; Priddey et al. 2007). The average FIR luminosities of both the HiBAL and non-BAL samples are $> 10^{12}$ $L_{\odot}$, sufficient to classify them as ULIRGs. Weighted mean SFRs (strictly upper limits using this relation due to the possibility of dust heating by the AGN and the BAL QSOs having overdensities of neighbours) have been calculated for the HiBALs of 245 ± 21 $M_{\odot}\,yr^{-1}$ for the 'extended' and 229 ± 25 $M_{\odot}\,yr^{-1}$ for the 'classic' sample from the flux density at $250\,\mu$m.

2. While Priddey et al. (2007) found tentative evidence for a dependence of submillimetre flux density on C IV absorption–line equivalent width, here no such dependence at FIR wavelengths is found. It is possible that the Priddey et al. result may have been due to small number statistics and selection effects as noted in the discussion.

3. Within each sample, 3/49 HiBALs and 27/329 non-BALs are detected at $> 5\,\sigma$ significance. The detection rates for the two species are statistically

indistinguishable.

Taken together these results suggest that BALs (strictly HiBALs) can be unified with non-BAL QSOs within a simple orientation scheme where a BAL QSO is observed only if a nuclear outflow intercepts the line-of-sight of the observer. This is in line with the findings of other authors such as Willott, Rawlings & Grimes (2003), Gallagher et al. (2007), and Priddey et al. (2007), that suggest HiBALs and non–BAL QSOs to be drawn from the same parent population. The recent work by Hall et al (2011) and Vivek et al. (2014) indicating absorption line variability in LoBAL QSOs would imply even the LoBAL phenomenon is an orientation effect possibly complicated by material moving across the line of sight, though the sample is smaller than the one studied here. With the current data it is not possible to definitively say whether (Fe)LoBALs can similarly be accommodated within this scheme or whether they form a distinct population perhaps caught at a key phase in their evolution. Future observations at FIR/submillimetre wavelengths would be valuable in this respect.

Chapter 3

On the excess of Luminous Infrared Galaxies around AGN at $z \sim 1$

3.1 Introduction

This chapter details the work undertaken as part of the Spitzer Herschel Active Galactic Survey (SHAGS). A large sample of AGN are used to investigate the FIR environments of AGN at $z \sim 1$. Previous work by a variety of authors has shown that AGN appear to preferentially reside within fields containing overdensities of galaxies (e.g. Hall & Green 1998; Best et al. 2003; Hutchings et al. 2009; Galametz et al. 2012; Mayo et al. 2012). As a result, AGN have been used in the past to signpost the densest regions of the dark matter density (e.g. Stevens et al. 2003, 2010) to explore the environments of AGN at the highest redshifts. However, the SHAGS sample was compiled so as to avoid the degeneracy found in many AGN

samples between luminosity and redshift which besets any flux or volume limited surveys. This effect can be seen in Figure 3.1, where the SDSS is visibly unable to detect low luminosity AGN at high redshift. At lower redshifts, a smaller volume also means that the SDSS does not sample a large enough volume to detect the high–luminosity AGN it finds at higher redshift. The SHAGS sample is limited to a single cosmic epoch at $z \sim 1$, sampling AGN over 5 magnitudes in the SDSS i–band. A total of 171 environments are investigated, composed of RLQs, RQQs and radio galaxies (RGs). How the samples were selected is discussed in greater detail in Section 3.2.

Observations by *Herschel* at 250 μm are used, which samples light emitted near the peak of the rest–frame FIR emission from dust. As noted before, this FIR emission corresponds to reprocessed UV light from star formation; UV radiation from massive young O and B type stars is absorbed by the dusty clouds in which such star–formation is hidden, hence providing an insight into ongoing star formation within the host galaxy. This work is an analysis of the most uniformly selected sample of luminous AGN to date at high redshift.

It is natural to ask whether the environments of RL AGN and RQ AGN are different. This question has been posed by various authors who find results that are at odds with each other. Yee & Green (1984) found that RLQs appeared to exist in marginally more overdense fields in the redshift range $0.05 < z < 0.55$, though a later study with a larger dataset and improved techniques contradicted this result (Yee & Green 1987). At higher redshift ($0.9 < z < 4.2$), Hutchings et al. (1999) found that RLQs occupy denser fields in the near–infrared than RQQs. However, Wold (2001) and McLure & Dunlop (2001) find the environments of RLQs and RQQs to be indistinguishable at $z \sim 0.2$ and $0.5 < z < 0.8$. It is likely

that these results have suffered from small number statistics and/or selection effects.

There remains a dearth, however, of studies investigating environments at a single epoch at FIR wavelengths. Kotilainen et al. (2007) discusses samples at redshift 1.2 and higher, while Kukula et al. (2001) investigated a sample of 9 AGN with $0.8 < z < 1.0$. These studies were carried out using NIR imaging, but concentrate mostly on the host galaxy, where they agree that radio–loud objects have higher luminosity hosts, but this misses the environments. Perhaps the most comparable study is that conducted by Best (2002) looking at $z \sim 1$ clusters with SCUBA. He finds a significant overdensity with detected sources having SFRs of $> 1000\,\mathrm{M_\odot\,yr^{-1}}$. However, the sample is composed of only four clusters, and are likely some of the most massive and therefore easily detectable clusters at their epoch, introducing an inherent selection bias to extreme sources within their fields.

In this chapter, FIR observations of the environments of AGN are used to determine the overdensity of star–forming galaxies in the vicinity of AGN and whether there is evidence for a preference with AGN type or radio–loudness or some other property. Section 3.2 describes the properties of the sample and how they were chosen, along with the reasoning behind those choices. Section 3.3 details the data reduction involved in producing science quality catalogues and maps, whilst Section 3.4 details the work performed to produce a suitable comparison sample, matched in redshift and with a selection of sources in their environments chosen similarly to those in the SHAGS AGN environments. It should be stressed here that whilst the data reduction discusses the data in all 3 SPIRE wavebands, the analysis is restricted to only the 250 μm maps. This is

due to the greater resolution offered at 250 μm as well as being closer to the peak of emission from star–forming regions at $z \sim 1$. Since there is a strong possibility that all the SHAGs maps will be used by other SHAGs consortium members in the future (e.g. for SEDs), parameters pertaining to the data reduction performed on the 350 and 500 μm maps (e.g pixel–scales, PSF FWHMs etc) are also provided. Section 3.5 then presents the methods and results used in the overdensity analysis, as well as a correlation analysis. Finally, a discussion of the results can be found in Section 3.6 and a summary of the main conclusions follows in Section 3.7.

3.2 The SHAGS sample

The sample selection for this work was performed and completed prior to the beginning of my PhD by Matt Jarvis (Jarvis et al. in prep). However, this paper has not yet reached publication and is currently unavailable, yet the properties of the sample are required to understand the analysis performed in this chapter.

The AGN sample is composed of 75 RLQs, 70 RQQs and 26 RG, a total of 171 AGN. These have been selected over the redshift range $0.9 \leq z \leq 1.1$. The reasons for this redshift range were three–fold; QSOs can be investigated over a large range of luminosities (5 magnitudes), the sources are bright enough that a large sample can be observed in a relatively small amount of time, and finally, these redshifts allow easy follow-up observations in CO with upcoming telescopes such as the ALMA. Furthermore, it is the minimum redshift at which there is a sufficiently large population of high–luminosity quasars which can be compared

to high–redshift quasars. This means that the effects of cosmological evolution and k–correction uncertainties are minimised, and the presence of both Type–1 and Type–2 AGN allows for tests of AGN unification schemes (e.g. Antonucci 1993).

The initial sample of QSOs were selected using their optical colours in the fifth data release of the SDSS Quasar Survey (Schneider et al. 2007). The immense size of the SDSS Quasar catalogue provides a sufficiently large sample that RLQs and RQQs can be selected in identical ways. These were then referenced to several radio surveys; the NRAO VLA Sky Survey (NVSS; Condon et al. 1998), the VLA Faint Images of the Radio Sky at Twenty–cm (FIRST, Becker, White, & Helfand 1995) and the Westerbork Northern Sky Survey (WENSS; Rengelink et al. 1997) to determine which QSOs were RLQs and which were RQQs.

RLQs were defined as those which had a low–frequency WENSS (325 MHz) flux density of greater than 18mJy, which is the $5\,\sigma$ limit of the WENSS. Where there was no coverage by WENSS, the rest frame 325 MHz flux density was extrapolated from the NVSS survey at 1.4 GHz using a spectral index of $\alpha = 0.7$. RQQs are those sources that were undetected by the Faint Images of the Radio Sky at Twenty–cm (FIRST, Becker, White, & Helfand 1995) survey at the $5\,\sigma$ level. FIRST was chosen for this level since it provides a more sensitive flux density limit than WENSS.

Finally, the RGs were selected from the low–frequency radio samples 3CRR (Laing et al. 1983), 6CE (Eales 1985), 7CRS (Willott et al. 1998) and TOOT surveys (Hill & Rawlings 2003). Therefore the smaller sample of RGs is simply due to a lack of known RGs at $z \sim 1$. All of the AGN included in the sample have already been observed with *Spitzer* and observations by *XMM–Newton* or

SWIFT exist or have time allocated for all the RLQ and RQQ sample. Fig. 3.1 shows the distribution of SHAGS AGN against the fifth data release of the SDSS (Schneider et al. 2007).

The radio luminosity distribution shows how the RLQs and RQQs are broken up, as well as showing that the derived radio luminosities of the RGs are generally higher than the RLQs (see Figure 3.2). The apparent dichotomy between RL AGN and RQQs is due to the different survey depths of WENSS and FIRST, thereby leaving a relatively large gap uncovered by the sample. Rather than a drawback, this may have the benefit of strengthening any difference between the environments of the Type–1 AGN in the sample.

3.3 Data Reduction

All AGN fields have been observed using both the PACS (Poglitsch et al. 2010) and SPIRE (Griffin et al. 2010) cameras. This work uses only 250 μm data to derive overdensities as whilst the blue channel of PACS may have a better resolution (3.2 arcsec for 75 μm) it does not reach the same depth as SPIRE, requiring far longer integration times to reach the confusion limit, and in the case of 100 μm, will not sample close to the peak of the FIR modified black body at z $\sim$ 1 as 250 μm emission does. As noted before, the data reduction for 350 and 500 μm is addressed here, but the maps are excluded from the analysis owing to the lower resolution and, as with PACS, being further from the black body peak.

Observations of 150 fields were carried out with *Herschel* as part of program OT1_jstevens_1 (PI Stevens) using SPIRE. The observations were taken in small map mode using the SPIRE (Griffin et al. 2010) instrument aboard *Herschel* (Pil-

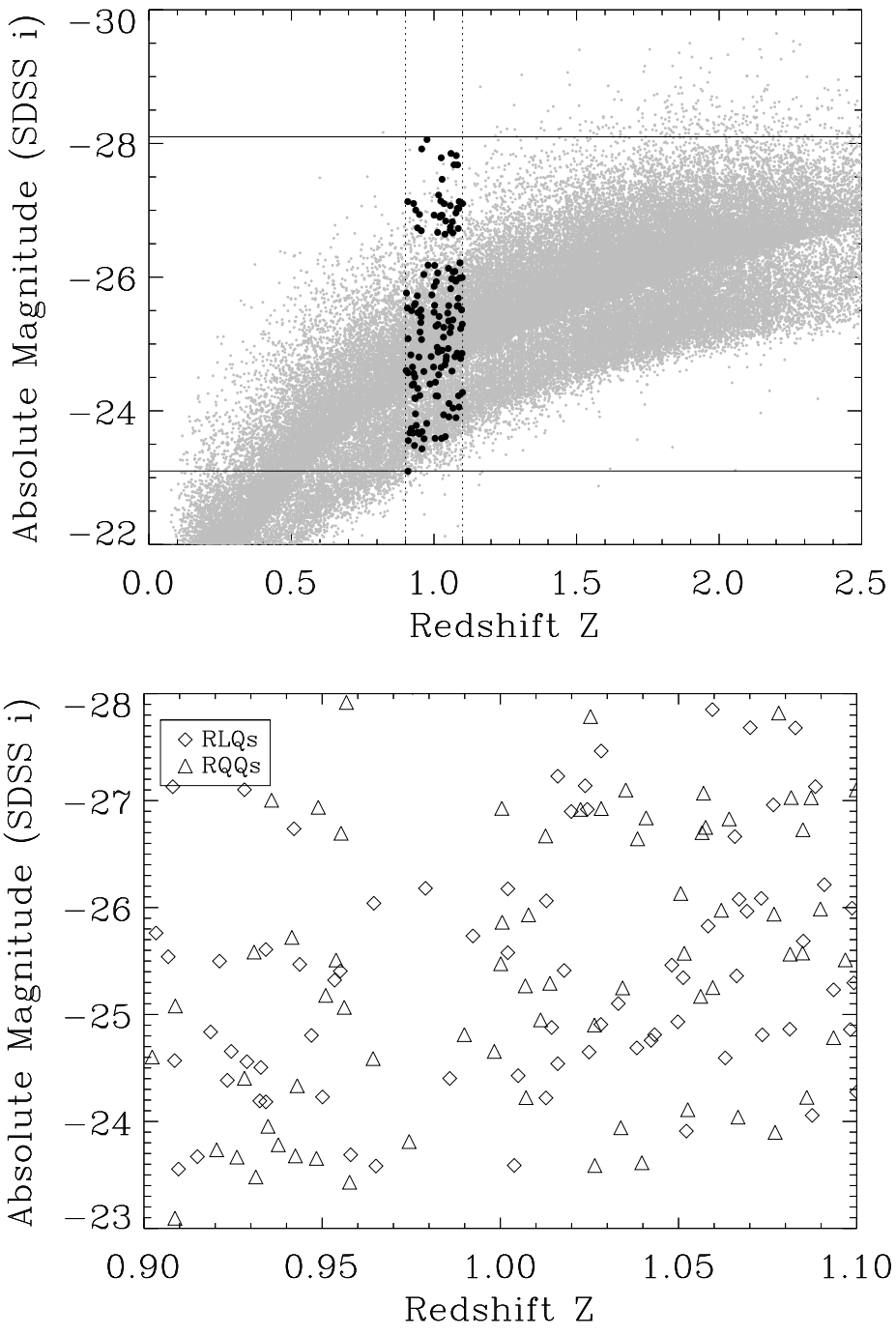

Figure 3.1: Redshift plotted against optical magnitude. In the upper panel, the black dots are the selected AGN, whilst the grey dots are the AGN in the SDSS fifth data release. The SHAGS sample spans five magnitudes over a redshift range of $0.9 < z < 1.1$. This small redshift range was chosen to minimise evolutionary effects within the sample, as well as allowing a study of any luminosity–generated effects. In the lower panel, the sample is broken down into RLQs and RQQs. RGs are not shown here since they were selected from the low–frequency radio samples and have no comparable optical data.

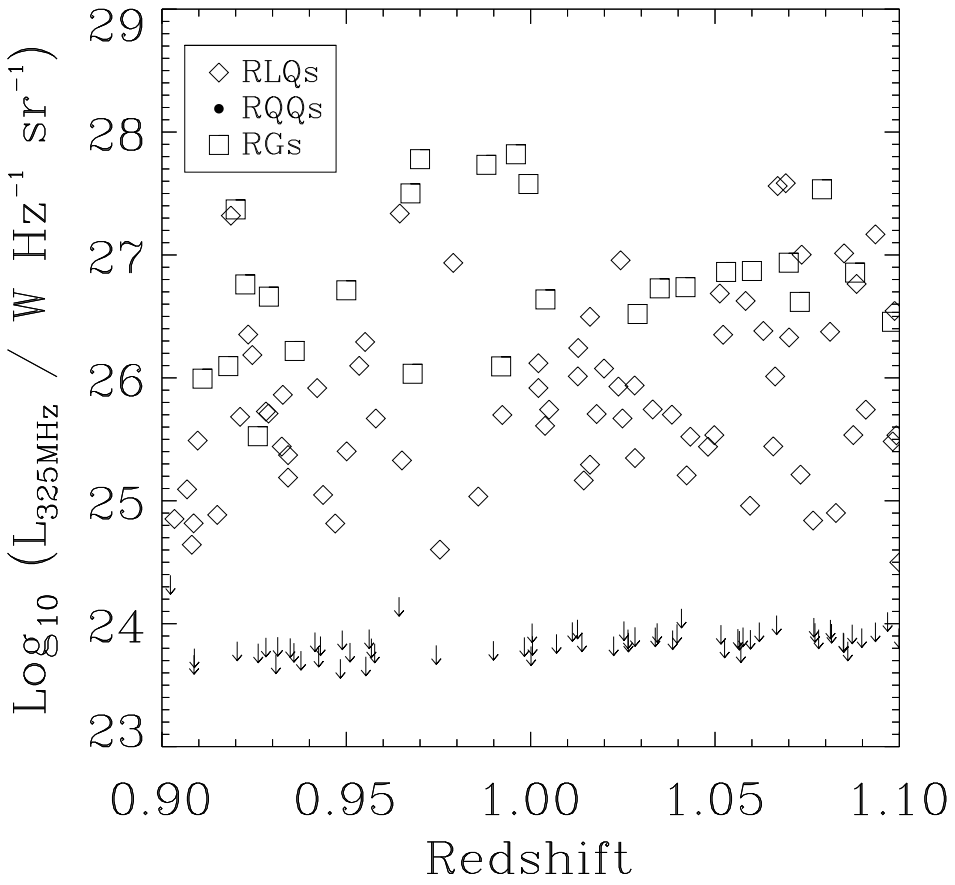

Figure 3.2: 325 MHz radio luminosity versus redshift for the sample. RLQs are shown with diamonds, RQQs with arrows (they are derived upper limits) and RGs with squares. As discussed in the text, the apparent gap is merely a selection effect of the difference in survey depths at which WENSS and FIRST operated rather than a true dichotomy between the radio luminosities of RLQs and RQQs.

bratt et al. 2010). This consists of using nearly orthogonal scans (84.8 degrees). The alignment of these scans will mean the area covered by both these scans will cover a central square with length 5 arcmin. Due to the circular arrangement of the arrays on the sky however, the 'reliable' region (suitable for scientific analysis) is approximately circular and has a diameter of 5 arcminutes and merely corresponds to where the coverage by individual bolometers (and hence integration time) will be largest relative to the rest of the map. Each of the scans involved the telescope scanning the survey region at a constant rate (e.g. 30 arcsec per second in small map mode), with the voltage across each of the bolometers in the three SPIRE band arrays being sampled at a frequency of 18.6 Hz (Griffin et al. 2010). This method produces data for each bolometer known as a timeline.

The timeline data downloaded from the *Herschel* Science Archive (HSA) were then reduced using the small map pipeline within HIPE. SPIRE 250, 350 and 500 μm maps were then generated using the default naïve map–maker. The naïve mapping algorithm simply regrids generated data onto the sky, with each sample having its flux densities assigned to the nearest pixel. However, there are various routines in the pipeline designed to ensure the resultant maps are of the highest quality and free from artifacts. For example, SPIRE uses arrays of distributed bolometric detectors cooled to $\simeq 300$ mK in each band to measure the sky radiation, from which the data are combined to estimate sky emission. These arrays also contain thermistors that help to monitor temperature variations which can lead to artifacts in the final maps unless accounted for. The cold temperature has the added benefit that instrumental noise is kept to a minimum. There still remains the problem of glitches which are somewhat more difficult to account for. SPIRE suffers from two types of glitches; large events that are due to single direct

hits on an individual bolometer, and smaller co–occurring glitches, attributed to ionising hits on the silicon substrate upon which the bolometers in an array are supported. These are automatically removed in the standard processing pipelines included in the Herschel Image Processing Environment (HIPE, Ott 2010) v10 which has been used in this analysis. Visual examination of the final images indicates the pipeline is working correctly in the mapmaking.

The SPIRE photometer point spread function (PSF) is estimated for each band by the *Herschel* data processing team using Gaussian fits to observations of Neptune, which appears as a point source and provides high S/N. The mean full width at half–maximum (FWHM) in each band used in the initial 150 observations is 18.1, 24.8 and 35.2 arcsec for the 250, 350 and 500 μm bands respectively (Griffin et al. 2010). SPIRE flux calibration is estimated to be better than 10 per cent, from an initial 15 per cent (Swinyard et al. 2010) at each band, with a high correlation between bands.

The default pixel sizes in each band are 6 arcsec/pix, 10 arcsec/pix and 14 arcsec/pix. For subsequent analysis and to be able to use some of the findings from the *Herschel*–Astrophysical Terahertz Large Area Survey (H–ATLAS, Eales et al. 2010), the resolution is set to 5 arcsec/pix, 10 arcsec/pix and 10 arcsec/pix for the 250, 350 and 500 μm bands respectively for these first 150 observations. Each generated map also comes with a corresponding error and coverage map as separate extensions. The error map is the 1 σ standard deviation of all the data points falling within a given pixel whereas the coverage is the number bolometer samples within that pixel N_i with the central pixels by definition having the largest sampling. Flux density calibration is performed by the standard SPIRE data reduction pipeline with the resulting maps being calibrated in Jy beam^{-1}.

Flux density pixelisation correction factors as documented by Rigby et al. (2011), of 1.05, 1.11 and 1.04 are applied for the three bands respectively which were the best estimate of the correction factors at the time the data were reduced for the resolution used.

In the case of the remaining 21 fields, the selected targets overlapped with larger surveys or other observations and therefore had to be retrieved from those respective surveys: 17 AGN from HerMES, (Oliver et al., 2012), a RQQ from the Herschel Virgo Cluster Survey (HeVICs, Davies et al. 2010), and the observation of 3C 343, a RG, were available as either raw observations from the Herschel Science Archive, or as publicly available raw processed maps produced by each respective team. In the case of 3C 343 and 2 H–ATLAS sources, the map–merging tool available in HIPE was used to join the available images together and produce final maps of equal resolution to the first 150 fields with pixelisation correction factors applied, whilst those taken from HerMES or HeVICs were left at the default pixel size (6/10/14 arcsec). An example of a final image can be seen in Figure 3.3.

3.3.1 Background Estimation

Prior to source extraction, a background had to be calculated and removed for each field. In each field, the contribution from background sources, as well as increasing confusion noise will serve to boost derived flux–densities. The presence of cirrus or other dust may also signficantly change the flux density of any sources within the field.

A common method of determining the background is to use a grid to split

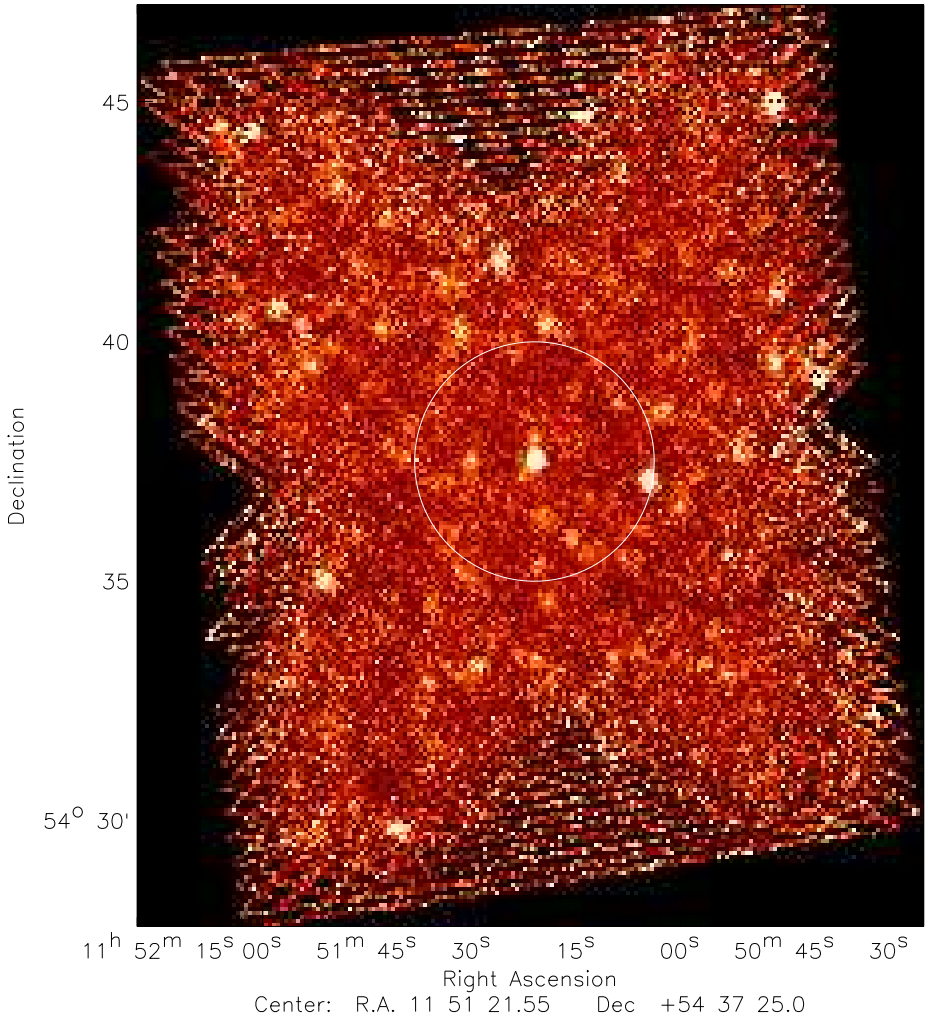

Figure 3.3: An example map immediately following map creation. This shows the environment of SDSS115120.46+543733.1 with the 'reliable' region of the map highlighted in white, a circle of diameter 5 arcmin, corresponding to around 1.2 Mpc at the redshift of the source. The separate cross–scans are clearly visible, with turnaround data included so as to maximise any future analysis if required.

an image into separate boxes of a certain size. These boxes are then sampled to create some clipped average background value before interpolating between the values at the original pixel sampling. Generally, this is acceptable, tracking small scale variations whilst being efficient.

With this in mind, a similar method as that described in Rigby et al. (2011) was attempted using bi–cubic spline (BCS) interpolation. Multiple boxes of 30×30 pixels were sampled, taking the peak value of a histogram of those pixels as the background, across the images before attempting an interpolation between the varying boxes to smooth the background subtraction. However, it was found that due to the small size of the majority of the maps the number of pixels sampled were too small to determine an accurate background, with maps using just this method being particularly vulnerable to the introduction of severe bright or dark spots near the edges as well as the presence of significant positive and negative regions (see Section 3.3.2 for a discussion). An alternative was found in the form of *Nebuliser*, part of the CASUTOOLS suite (Irwin, 2010). *Nebuliser* is designed with the removal of medium to large scale emission. Following testing it appears to be able to deal with the discontinuity near the edges of the maps far better than the BCS method previously used. *Nebuliser* works by using two separate sliding filters, the values of which are then clipped at a set sigma to determine the background. This is repeated for a certain number of iterations which can be set by the user. The combination of these separate filters, the non–linear nature of *Nebuliser*, its ability to iterate over both axes simultaneously and the resulting maps suggest it is less susceptible to large steps such as those found at the edges of the maps. Similarly to the BCS method, the size on a side of the median and linear box filters were set at 30 pixels, using the 2D filtering option.

The removal of bowling around bright sources and bright artifacts was handled by k–sigma clipping, which was left at the default range of -10–$3\,\sigma$ following testing which appeared to remove artifacts satisfactorily. The default number of iterations, 3, were also used as the background appeared to be suitably removed in all fields and little difference in the final maps was noticed when iterations were increased. The derived background using both methods for one of the fields showing the greatest contamination from cirrus is shown in Fig. 3.4, as well as the image before and after using *Nebuliser* to remove large–scale emission.

Following the removal of large–scale galactic emission, the problem of confusion noise from background sources remains. As noted in Section 1.3.1, improvements in sensitivity mean that this noise is dominated by resolved structure in the CIB as well as partially resolved extragalactic sources. The negative k–correction in the FIR is a double–edged sword; whilst allowing studies of high–redshift sources that are difficult if not impossible at shorter wavelengths, it contaminates the emission from those sources with light from sources at even earlier cosmic epochs. Indeed, extensive work has been performed on the confusion noise present at each wavelength for *Herschel*, and therefore a similar analysis is not performed here. Instead, to account for the noise attributable to background sources, the values from Rigby et al. (2011) are taken. These values are within $1\,\sigma$ of those found within other works and are 5.3, 6.4 and 6.7 mJy for the 250, 350 and 500 μm bands.

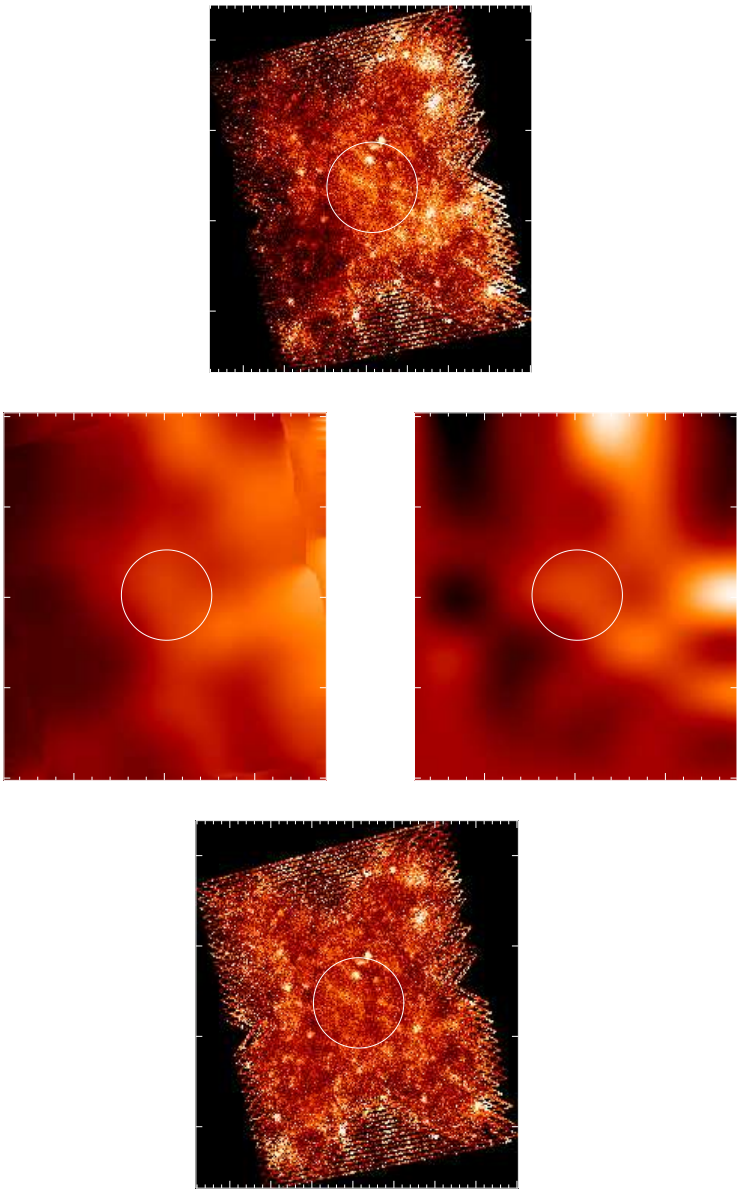

Figure 3.4: Before and after background subtraction for the field of SDSS075339.84+250137.9. This field shows a strong degree of contamination from dust within the Milky Way and a dichotomy from one side of the image to the other (top panel). This is therefore a prime example of the efficacy of *Nebuliser*. The middle panels show the derived backgrounds for *Nebuliser* (left panel) and using a BCS method (right panel). It is clearly visible that *Nebuliser* is less susceptible to iindividual sources as well as edge effects. The bottom panel shows the resultant image after *Nebuliser* has been applied. The white circle of radius 2.5 arcmin shows the 'reliable' region, and is the region of interest for this chapter.

3.3.2 Source Extraction

To produce PSF–filtered maps and photometric catalogues, the SussExtractor (Savage & Oliver 2007; Smith et al. 2012) source extraction algorithm within HIPE was used. SussExtractor has been designed specifically to deal with SPIRE images and is able to produce PSF–convolved images whilst simultaneously extracting source information. The flux estimate in any given pixel is given by equation 3.1

$$\mathrm{F_{source}} = \frac{\alpha}{\beta} \text{ where } \alpha = \sum_{\mathrm{i=1}}^{\mathrm{N_{pixels}}} \frac{\mathrm{d_i P_i^2}}{\sigma^2} \text{ and } \beta = \sum_{\mathrm{i=1}}^{\mathrm{N_{pixels}}} \frac{\mathrm{P_i^2}}{\sigma^2} \tag{3.1}$$

whilst the error on the flux density estimate is derived from $1/\sqrt{\alpha}$. In equation 3.1, d_i is the value of the i^{th} data pixel of the subset of pixels being convolved, P_i is the (Gaussian) PSF, and σ_i is the standard deviation of the noise associated with that pixel. In this manner, SussExtractor convolves the image map with the Gaussian PSF. Once the maps have been created, SussExtractor then searches for local maxima in a map created from the flux density estimate divided by the flux density error within some user–defined region. A local maximum is a pixel that has a greater value than all its neighbours and is considered a detection if it has a signal–to–noise ratio (SNR) greater than a set value. To provide an initial catalogue which can then later be pruned for $5\,\sigma$ sources, the SNR limit for SussExtractor is set at $3\,\sigma$. This will remove sources whose flux density is less than 3 times their instrumental noise; confusion noise must be added separately by the user to the ouput noise estimates. By default, the region of interest is set equal to the default value of 1.5 pixels which corresponds to ~ 7.5 arcseconds at 250 mum. A Gaussian function is then fitted to the pixels above and

Table 3.1: The set FWHM and beam areas used as part of the source extraction process in each band with SussExtractor.

Band	FWHM	Beam Area
250	18.1	423
350	24.8	751
500	35.2	1587

below, left and right of the source pixel to improve the position over simply using the centre of the pixel. The PSF–filtered map produced by SussExtractor with detected sources within the 'reliable' region is shown in Fig. 3.5. As mentioned before, 'reliable region' is the area of the map considered by the *Herschel* team (following an examination of possible scanning strategies) to be of suitable quality for guaranteed scientific use (Waskett et al. 2007) and is the region of sky with the greatest bolometer coverage. The positional uncertainty is estimated by the algorithm as $0.6 \times \mathrm{FWHM} \,/\, \mathrm{SNR}$. There is a reliance on the signal–to–noise ratio due to the confusion present in FIR and submm observations. This confusion will mean greater positional uncertainties for fainter sources, as the shape of a point source is distorted by other nearby sources of similar or greater flux. Values for the FWHM and beam areas (simply, the area of the PSF in the map) of the applied PSFs are visible in Table 3.1.

It should be noted, however, that the quoted values for FWHM are for images with 5, 10 and 10 arcsec per pixel for the three SPIRE bands as derived by Rigby et al. (2011) and the beam areas are for 1 arcsec/pixel resolution images from the SPIRE data reduction manual. The values will not be entirely appropriate for even the small increase in size to 6 arcsec/pixel. This is expected, however, as the basic beam parameters vary as a function of pixel scale. This is due to the derived surface brightness reconstruction being less certain at lower resolutions,

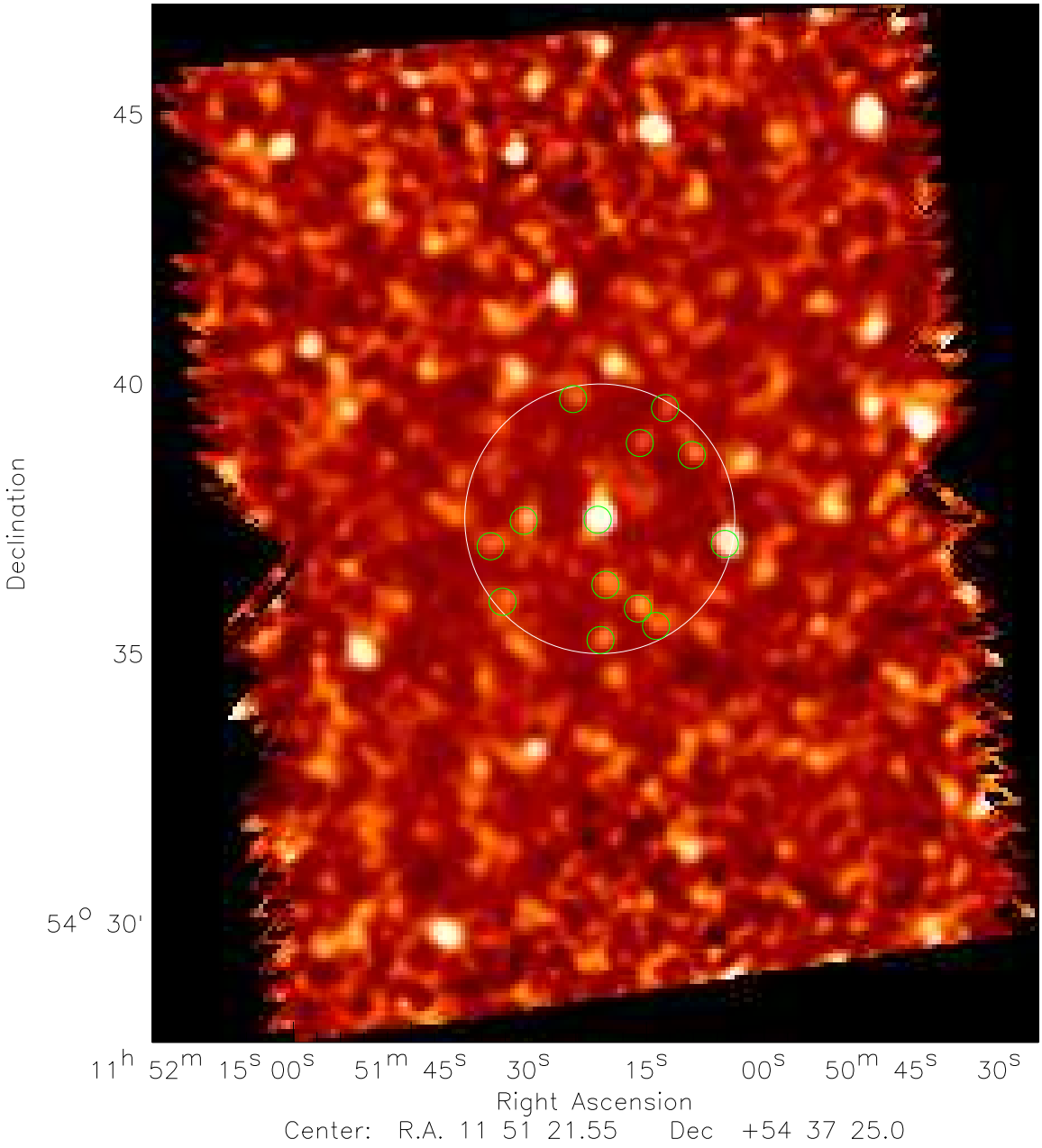

Figure 3.5: The PSF–filtered map for SDSS115120.46+543733.1, with only those sources within the 'reliable' region highlighted. These are sources with flux–density values greater than 10 mJy, approximately 3 times the instrumental noise in those pixels. This is the image searched for peaks by SussExtractor when determining flux–density values. SussExtractor has also visibly tried to fill in missing pixels, though this will introduce a large number of spurious sources in regions where there is little data (such as near the edges or between individual scans of turnaround data.

with the Airy ring pattern losing form at higher radii from the source peak. As recommended in the SPIRE data reduction manual, the quoted beam areas are used, and the FWHM is varied as a function of pixel scale. For the default pixel sizes of 6,10,14 arcsec/pixel at each SPIRE wavelength, FWHM of 18.2, 25.2 and 36.3 arcsec are used. An incorrect FWHM would mean a source possibly being detected as two or more sources (dependent on the FWHM selected of course), thereby increasing the returned number of sources in the maps.

Due to the spread in depth, source cuts have been made so that all analysed sources are detectable using a conservative $5\,\sigma$ level. This is simply the $5\,\sigma$ level of the shallowest (and therefore noisiest) image in the sample thus ensuring that any sources used could be detected in any image, even after instrumental noise and confusion noise are taken into account. This is necessary since the majority of the maps are deeper than the H–ATLAS/HerMES sources that make up a fraction of the SHAGS sample (see Fig. 3.6) and if not implemented could lead to a severe bias and errors in any subsequent overdensity calculations.

A suitable flux density cut is determined by plotting flux density against SNR (Fig. 3.6). A visual estimate then provides a conservative limit for the shallowest Lockman–SWIRE source, which is taken as the $5\,\sigma$ flux density limit. This has the value 35 mJy. Putting this limit into context, if one assumes a dust temperature of 23.5 K and a dust emissivity index β of 1.82, this work only samples luminous infrared galaxies (LIRGs) with SFRs greater than $\sim 114\,\mathrm{M}_{\odot}\,\mathrm{yr}^{-1}$. These values have been shown by Smith et al. (2013) to be the best fitting parameters for a sample of 12,814 $z < 0.5$ H–ATLAS galaxies. Whilst this is a relatively high flux–density cut, it is in line with the SNR cutoffs used by other works such as H–ATLAS and HerMES and should ensure the majority of the catalogue can be

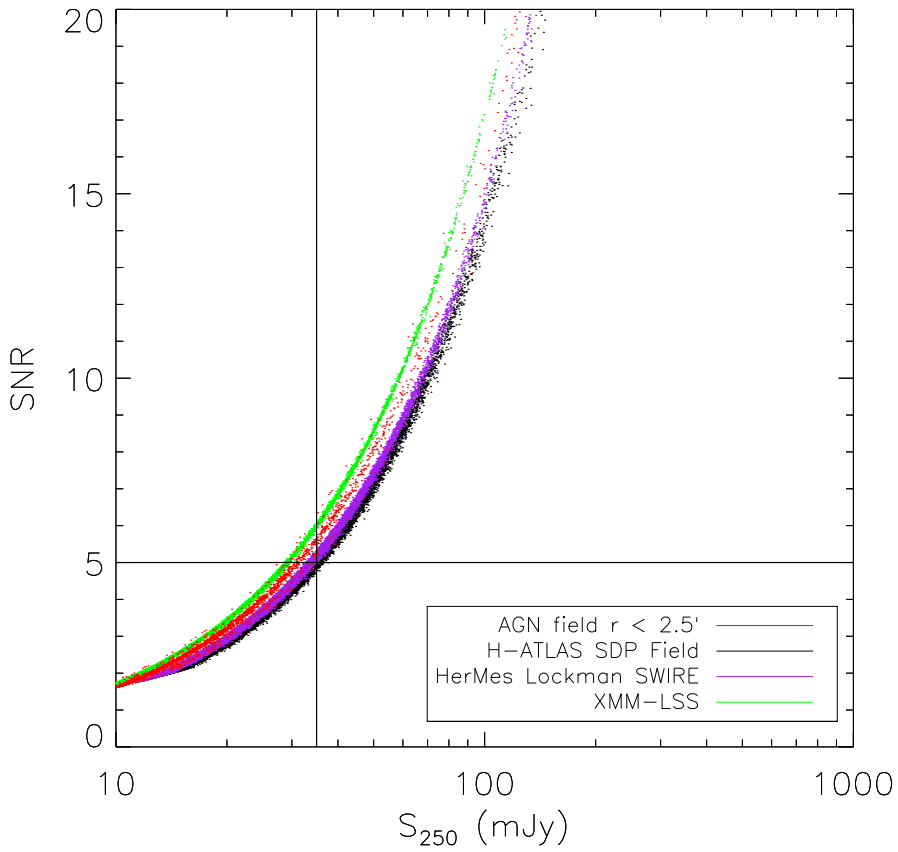

Figure 3.6: The 250 μm flux–densities of all sources found by SussExtractor plotted against the signal–to–noise ratio for that source. The red points correspond to sources found in the 'good' region of the small maps, which corresponds to around 1.2 Mpc from the central AGN at $z \sim 1$. Also plotted here are those sources extracted from two fields observed as part of other surveys which contain AGN in the SHAGS sample as well as the XMM–LSS–SWIRE field from which a comparison sample is generated.

associated with 'real' sources.

The fraction of detections at a given flux density that are spurious is a way of testing how reliable a source catalogue is. Spurious detections can be produced by cosmic ray hits (glitches), inaccurate background removal methods, or simply be caused by noise in the map that is produced from the accumulated uncertainties in multiple bolometer samples for that pixel. If there is no confusion noise, i.e. only instrumental noise plays a part, a measure of the SNR will provide a probability of whether a source is spurious. To check for spurious sources, the flux density maps are inverted, and re–entered into SussExtractor. The procedure allows a comparison of what effect the background subtraction is having as well as indicating regions where use of turnaround data may be affecting source catalogues. Sampling across the inverted fields, it is found that the BCS method has a far greater number of spurious sources. Indeed, whilst at $3\,\sigma$ the BCS method appears to offer a better alternative (10 spurious sources per field cf. 14), at $5\,\sigma$ there are 3 times fewer spurious sources on average in maps treated by *Nebuliser* (1.2 cf. 3.7 per map). Furthermore, one would expect at most around 1 source to be spurious at the $5\,\sigma$ level, thereby implying the BCS method is actively introducing spurious sources into the maps. This has the added benefit of strengthening the argument for a strict 5σ limit. The reason for the discrepancy between the two background methods is relatively simple; the BCS method is more susceptible to the presence of significant deviations from the mean background. At lower flux densities, the correction to the background will be smaller in the BCS maps, and the sheer number of $3\,\sigma$ sources serves to obscure the effect. Furthermore, individual positive sources will boost the BCS correction for regions with relatively low–level noise. However, around the largest

deviations from the mean of the map, the bi–cubic spline significantly removes flux–density in the map, causing regions of negative flux to become stronger. In contrast, *Nebuliser* has a far lighter touch, such that at lower flux–densities, the correction will not actively introduce sources nor remove them, and around the largest sources will not overcompensate for their presence. Edge effects also cause the BCS method to be far more susceptible to regions that are particularly noisy.

3.3.3 Completeness

The next step is to correct for incompleteness arising from non–optimal source extraction. This is investigated by inserting artificial sources into the maps, and then performing source extraction to recover them. The completeness is then simply the number of extracted sources divided by the number of inserted sources. Initially, a total of 100 artificial sources with Gaussian PSFs were individually and randomly added so as to avoid increasing the confusion with multiple sources. The Gaussian parameters in Table 3.1 were derived from fitting a 2–D Gaussian to observations of Neptune with a custom 'fine–scan' mode by the *Herschel* team. Empirically derived PSFs from the SHAGS fields are not used, as they will be more susceptible to error, owing to few strong sources within the fields and posisble distortions from nearby sources. Using such a small sample also means that the processing time for each field remains manageable. The small size of the 'reliable' area also placed a strict limit on the number of sources that could be input at a time into each field. Twenty flux density bins with flux–densities in the range of 10–3000 mJy meaning a total per field of 2,100 injected sources were selected. These are chosen to have FWHM equal to the beam size in each SPIRE

band for each pixel resolution and were scaled to the necessary flux. Example images of input sources at 35 mJy and 3 Jy are visible in Fig. 3.7. The reasoning behind the lower flux density limit was to sample below the flux density cutoff to approximately the $3\,\sigma$ instrumental noise level whilst the upper limit was required due to the presence of a 2.1 Jy source at 250 μm in one of the fields corresponding to a nearby galaxy. Futhermore, the number of sources per field seemed sufficient since the output completeness values were sufficiently smooth not to warrant further time or processing power spent on this problem (see Fig. 3.8).

Sources are classified as recovered if they are within half the FWHM of their input position and their extracted flux density is between 0.8 and 1.2 times the flux density of the artificial source inserted. This should ensure that no matches are made to a source too distant or too faint. Since the typical positioning error for a > 5 σ source is known to be 2.5 arcsec or less at 250 μm (Pilbratt et al. 2010; Smith et al. 2012; Rigby et al. 2011) this radius should mean that no real matches are missed. To eliminate scatter in the derived completeness, the data points were fitted with the empirical model shown in equation 3.2 (Coppin et al. 2006):

$$Completeness = \frac{S^a}{b + cS^a} \tag{3.2}$$

where S is the flux density in each bandpass and a, b, and c are constants. The reasoning is twofold. Firstly, this will eliminate any scatter in the derived completeness curves. Secondly, by calculating an analytical solution, flux density values without a sampled completeness can still be corrected. Fig. 3.8 shows the

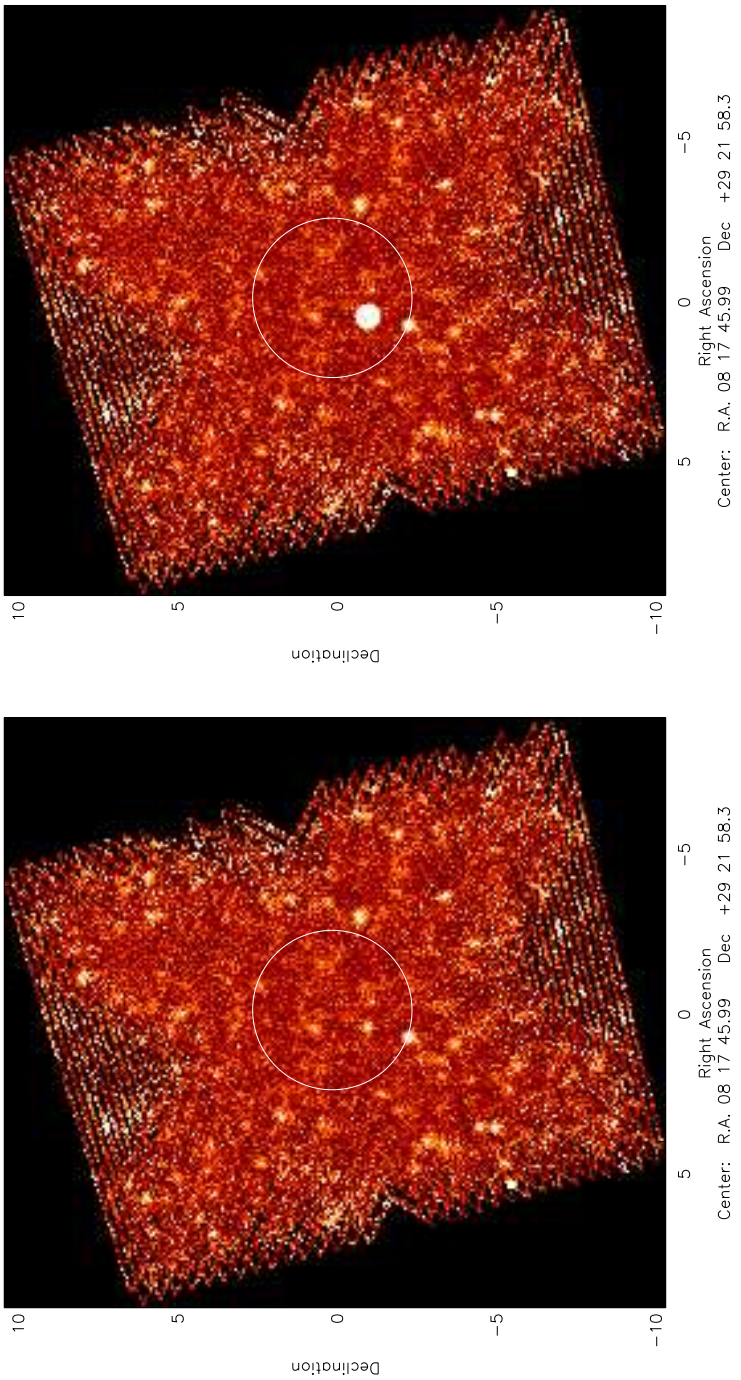

Figure 3.7: Two example images following insertion of a single artificial source in the field of RG 5C7.82. In the left panel, a source with a flux–density of 35 Jy has been inserted, and is just visible to the left of centre. The right panel shows the same field but with an artificial source of 3 Jy at the same position, which is clearly distinguishable as a large circular point source.

completeness for the radio galaxy 5C7.82. A completeness curve is derived for each separate field as the variation in depths will lead to differing completeness curves.

In Fig. 3.8, it is clearly visible that there is a strong dependence on flux density as expected. At lower flux densities, this is likely due to bright sources hindering the detection of faint sources as well as serendipitous sources which may serve to boost the number of recovered sources. At higher flux densities, this confusion becomes less prominent and the likelihood of a recovery becomes dependent on positional uncertainty rather than positive or negative regions in the maps causing the artificial source to drop out of consideration.

The catalogues are shown to be between $\sim$40–80 per cent complete (as visible in Fig. 3.9 for RLQs and RQQs). This high degree of incompleteness in some fields comes from both the conservative restriction placed on a 'true' source as well as the confusion noise, which will have a larger effect on fainter sources. Several of the most incomplete fields have multiple sources within the 2.5 arcmin radius specified and this will obviously have an effect on the final derived completeness for that field. Within the distribution, there also appear to be several fields that overlap in both completeness and absolute magnitude. However, on closer inspection it is found that the fields serendipitously have very similar completeness corrections following fitting and their absolute magnitudes are within 0.001 of one another. Furthermore, whilst it appears there may be a weak correlation with absolute magnitude, performing correlation analyses using Spearman Rank and Kendall Tau tests suggests it falls far short of statistical significance ($p \sim 0.22$).

The returned astrometry from SussExtractor has also been investigated, and

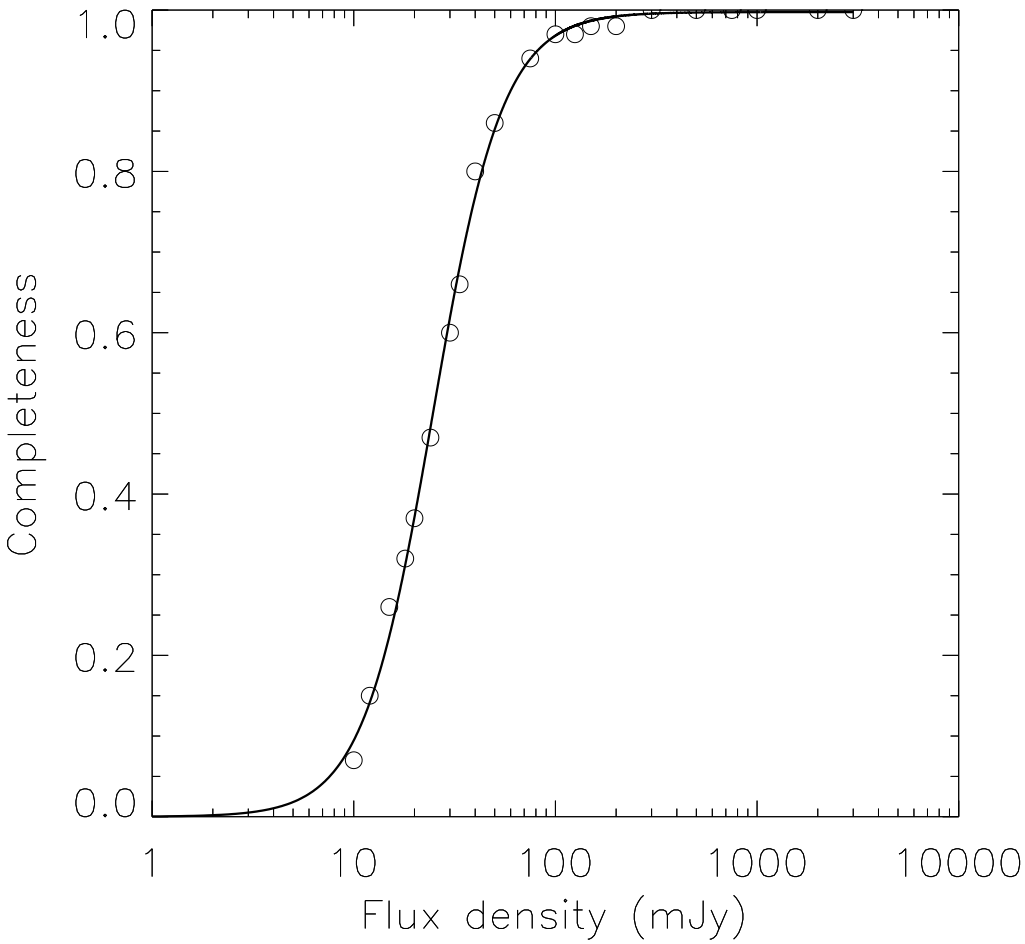

Figure 3.8: The completeness curve for the inner region of the field of 5C7.82, showing how completeness varies as a function of flux density for that field at 250 μm. The circles show the fitted data points for the flux densities used.

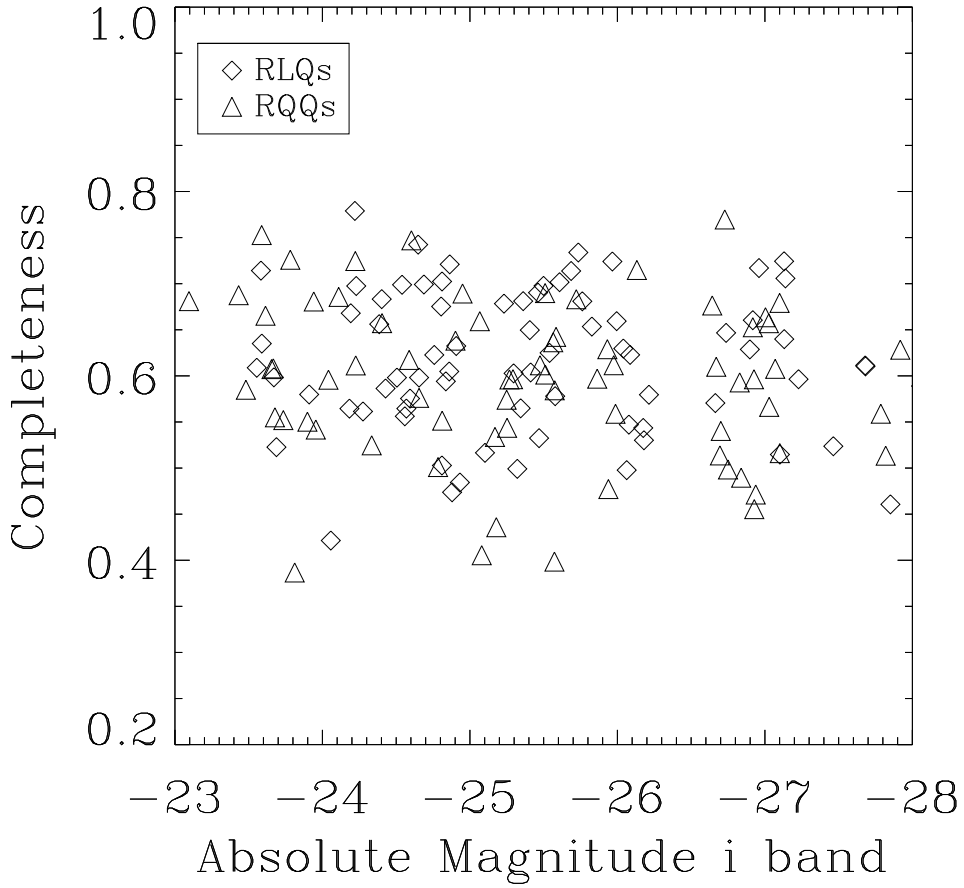

Figure 3.9: Plot showing the optical luminosity (rest-frame SDSS i–band) versus the completeness at the chosen flux density limit (35 mJy) for Type 1 AGN within the sample. With the exception of 5 outliers around some of the brightest QSOs with large numbers of companion sources, all fields are found to be > 45 per cent) complete at the chosen flux density limit.

an insignificant offset is found between the extracted and input artificial source catalogues. As visible in the lower panel of Fig 3.10, the positional error varies with flux density (being smallest for the highest flux density bin). The cause of this discrepancy as a function of flux density is likely due to source blending, which may serve to elongate a faint artificial source and increase the uncertainty in the derivation of its true centre. In the upper panel of Fig 3.10, one can see that the majority of sources are well within ∼3 arcsec, with the spread of offsets outside this range due to fainter sources. The positional errors in RA and Dec of ~ 2.6 arcsec for $\sim$ 5-σ sources at 250 μm are consistent with the value of 2.4 found by (Rigby et al., 2011) and Smith et al. (2012), and cited as the absolute pointing error by Pilbratt et al. (2010).

Finally, the mean values of the $\log_{10}$(extracted flux density/input flux density) for all investigated AGN fields has been determined. Fig 3.11 shows how it varies over the sampled flux densities within the 'reliable' region. Flux correction factors have then been determined for catalogue sources in Table 3.2. This quantity is calculated by determining what factor is required to give approximately zero mean offset in flux density between the extracted and input artificial source flux densities. The mean $\log_{10}$(extracted flux density/input flux density) has been calculated for each field which is then normalised to the number of fields to give the flux–correction factor.

It appears that SussExtractor is generally able to adequately reproduce the expected flux density of any recovered artificial source, being within ~ 3 per cent of the true value for all sources above the chosen flux density cutoff. This is encouraging when one considers that the combined calibration and photometric uncertainties can be up to 7 per cent, particularly for sources close to the

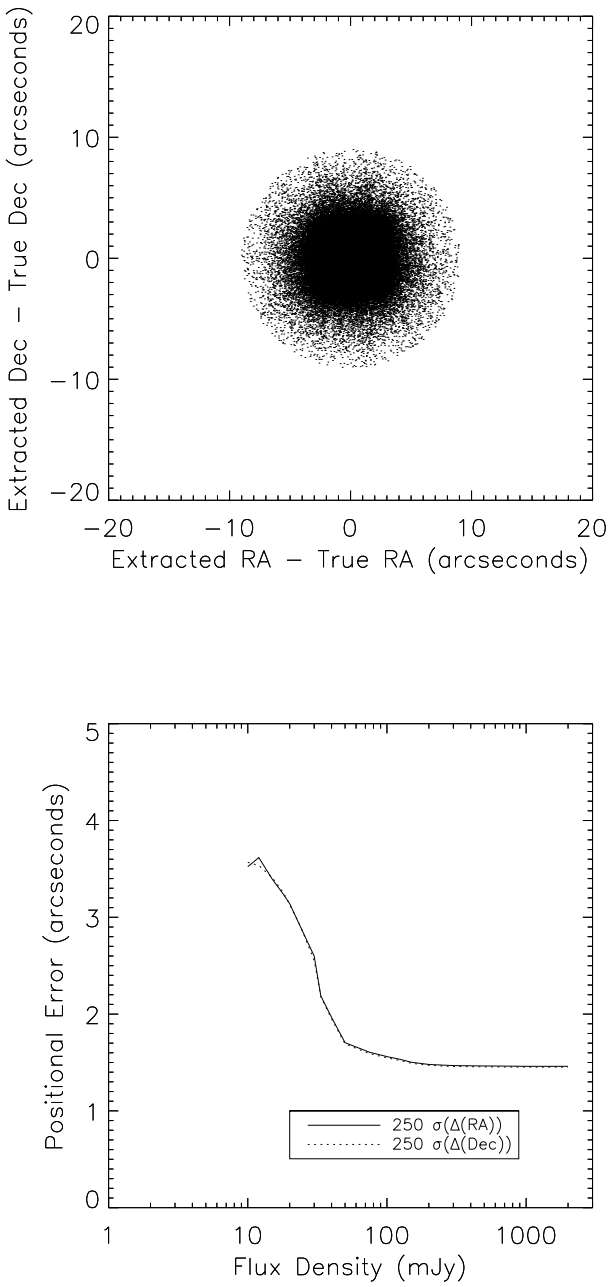

Figure 3.10: The upper panel shows the positional offsets (arcsec) in RA and Dec for extracted artificial sources at 250 μm. The lower panel shows the 1 σ standard deviation in position offset in each bandpass as a function of flux density. As can be seen, fainter sources suffer from a large offset likely due to source blending causing the exact derived centre to be off.

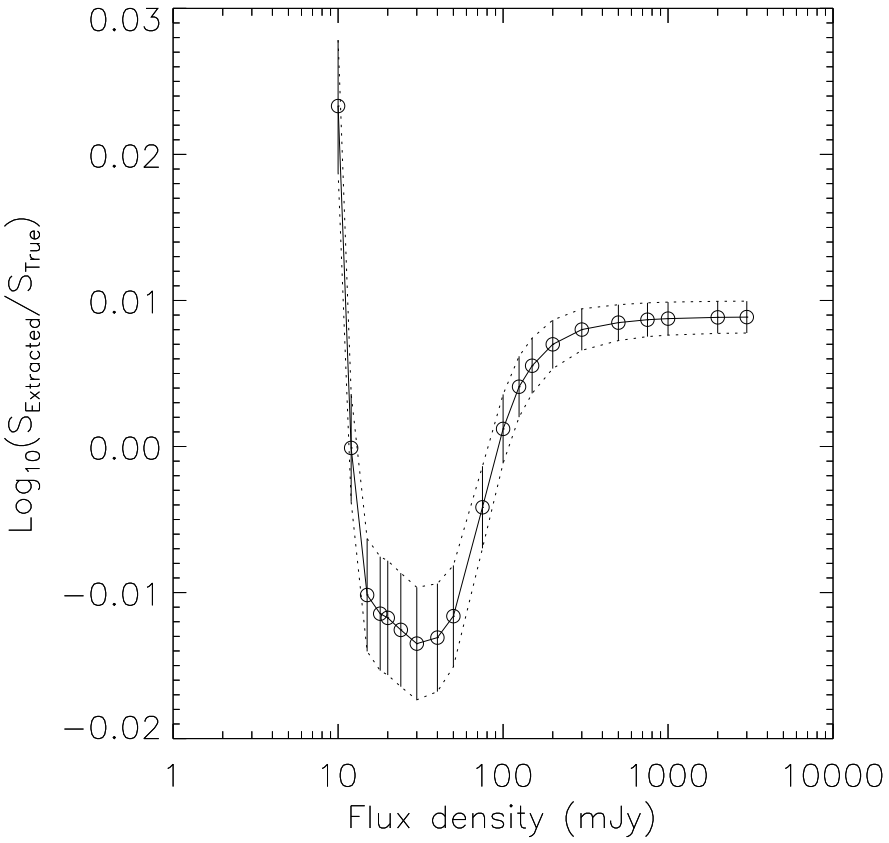

Figure 3.11: $\mathrm{Log_{10}(S_{Extracted}/S_{True})}$ as a function of flux density for all the fields in the 'reliable' region. Error bars are the rms of the $\log_{10}$(Extracted Flux density/Input Flux Density) at that flux density.

Table 3.2: The mean flux correction (FC) factors as a function of flux density at 250 μm. They are determined by the ratio of the mean of the extracted flux density S divided by matched input flux density values. The mean across all fields is then taken as the below value. To apply a correction, the flux density of a source should be divided by the closest corresponding corrective factor.

Catalogue Flux Density (mJy)	Mean $FCF_{250_{\mu m}}$	Mean value $Log_{10}(S_{Extracted}/S_{True})$
10	1.055	0.023
12	0.999	−0.0001
15	0.977	−0.010
18	0.974	−0.011
20	0.973	−0.012
24	0.972	−0.013
30	0.970	−0.013
40	0.970	−0.013
50	0.974	−0.012
75	0.990	−0.004
100	1.003	−0.001
125	1.009	0.004
150	1.013	0.006
200	1.016	0.007
300	1.019	0.008
500	1.020	0.008
750	1.020	0.009
1000	1.020	0.009
2000	1.021	0.009
3000	1.021	0.009

confusion limit. Therefore, it is expected that generally any real sources within the catalogues will be adequately dealt with, returning a flux density within 3.5 per cent (or $\sim$1 mJy) of the value of the reduced map. The visible trend in Fig. 3.11 is a consequence of the manner in which SussExtractor smoothes and determines what constitutes a 'real' source and is by no means trivial. At the faintest flux densities, confusion noise will be of prime concern. Flux–boosting is a well–known curse of FIR and submm surveys due to the rich backgrounds in any observation. Furthermore, in dense fields such as those expected around AGN in the SHAGs sample, source blending can also augment the determined flux densities over the true value for a galaxy. However, when dealing with real sources already in the maps, the faintest sources will likely be underestimated by SussExtractor. This is because it smoothes the maps and finds the peak of this smoothing assuming a zero mean background. The drawback of this method is that the faintest sources will likely be surrounded by negative pixels, thereby lowering the derived flux density. In the case of artificial sources, they are as likely to fall in regions of positive flux–density as they are in negative. Therefore, if SussExtractor assumes a zero mean background when it is in reality either positive or negative, the boosting can go either way. It is these minor details that cause the dip and indicate SussExtractor is a somewhat conservative extraction algorithm around the flux–density cutoff. Since the pixel distribution in each field is positively skewed owing to larger numbers of positive detections, any zero mean map such as that assumed by SussExtractor will likely be below zero rather than above zero for the faintest sources as it tries to compensate for the skewed distribution. These positive pixels will also be more likely than negative pixels to already lie near a detected source and this will mean a lower likelihood of a

'new' detection if an artificial source lands there, thereby forcing the mean flux density for recovered sources further down (conversely, at the lowest flux density, serendipitous matches would appear to boost the flux density as with those at 10 mJy). When all fields and all artificial sources are considered, this leads to a dearth of artificial sources at lower flux densities with correspondingly lower recovered flux densities than the brightest sources where positional uncertainties are the dominant factor rather than confusion noise. The question is then what should or can be done to mitigate this effect? Since the FCFs are at such a small level and knowing that SussExtractor removes flux whilst confusion and blending add flux, it was decided that the extracted catalogues should be left alone. One could use only the brightest source FCFs, giving a reduction of ~ 2 per cent. As noted by Smith et al. (2012), this would only partially deal with the enhancement by flux boosting rather than appropriately dealing with the slight artificial lowering by SussExtractor. As noted before, these values are well within the total uncertainty given for the SPIRE instrument, which may in fact lead to inclusion of 'real' sources that should not be present. It is therefore entirely possible that some fraction of sources are missed above the chosen flux density cutoff within at most ~ 1 mJy. However, erring on the side of caution is preferable to artificially boosting counts.

3.4 Creating suitable comparison catalogues

To determine whether AGN sit in overdensities of the universe, there are several possible methods available. A general 'background' density can be derived through the use of large area surveys such as those available to this work or a

suitable comparison sample of galaxies at the same redshift can be used. Each has its own benefits, but this work presents the results using a comparison sample, for the following reasons; firstly, the sample can be selected so as to make it indistinguishable in redshift, colour etc. Secondly, the derived background density will be derived in a manner similar to that used on the SHAGS AGN themselves using annuli (see Section 3.5), and will provide some information on density as a function of radius from the central source. An annulus approach has been performed several times before (e.g. Smith, Boyle & Maddox 2000; Best et al. 2003; Falder et al. 2010) and is found to be effective in detecting overdensities around AGN at various wavelengths.

A comparison sample has been drawn from the HerMES XMM–LSS–SWIRE field. This field contains data from various multi–wavelength instruments such as *Spitzer*, VISTA, and the Canada France Hawaii Telescope (CFHT), which will reduce the uncertainty on any derived redshifts and allow colour and magnitude selections to be performed. One drawback of this method however, is the relatively small area covered by the VISTA–VIDEO survey. This will mean repeated sampling of the same 250 μm sources, yet considering that the central comparison source will vary with each density sampling and not all comparison sources will have a 250 μm source within 1 Mpc, this only provides further information for the analysis and should not be taken as a hindrance.

The SPIRE data for the XMM field is treated in the same manner as the AGN fields. A background is calculated and subtracted using *Nebuliser*, completeness is derived and the same flux–density cutoff is applied to extracted sources in each field.

3.4.1 SHAGS

The availability of SDSS data in the AGN fields provides an excellent manner of determining which sources are likely at high redshift. The 3.6 μm positions (derived by Falder et al. 2010 from IRAC images of the SHAGS fields using SExtractor) are firstly matched to 4.5 μm positions within 1 arcsec, in order to follow the matching technique employed by the SERVS team (Mauduit et al. 2012) and ensure consistency between IRAC selections in the SHAGS sample and comparison sample. This resultant catalogue is further constrained to remove possible stars and also make the galaxies sampled comparable to those selected by Falder et al. (2010) in their overdensity analysis. Following the work of Falder et al. (2010) who remove any sources with CLASS_STAR > 0.8 and a flux–density less than 13.1 μJy, the same limit is applied. In that work it was found that raising the level as high as 0.95 had a negligible effect, suggesting most sources with CLASS_STAR > 0.8 were also above 0.95. Each 250 μm source is then matched within 7.2 arcsec to the nearest IRAC neighbour. This radius is chosen as it is approximately three times the positional error on 250 μm positions as shown in Section 3.3.3, and should ensure that if a 250 μm source has an IRAC counterpart, it is included. This leaves 341 sources within the AGN fields.

The catalogues are then matched to suitable optical counterparts in the r–band using SDSS photometry. The r–band is selected as it is 95 percent complete at a far deeper magnitude (AB mag 22.2) than all other SDSS bands except the g–band. g–band photometry is not used as it will not be as sensitive to galaxies with higher dust content, which is to be expected if one considers that emission at 250 μm indicates ongoing, shrouded star formation. A r–band limit of 22.4 is

selected, to ensure the catalogue is at least 95 percent complete whilst allowing for the inclusion of possible fainter sources. The catalogue is then matched within 1 arcsec to the DR7 QSO catalogue (Schneider et al., 2010), to ensure no QSOs are rincorrectly removed. Whilst a ninth data release exists (Pâris et al. 2012), it currently does not have the same coverage as the DR7 catalogue, so it is not used here. Any 'star' in the SDSS DR10 with a matching QSO in the DR7 QSO catalogue remains in the SDSS catalogue, otherwise it is removed. These optical counterparts are then filtered to remove stars or sky lines using the TYPE flag. As a final step, the SDSS catalogue is matched to the leftover SHAGS sources with IRAC counterparts. This leaves 193 sources, but 63 of these sources are found outside a 1 Mpc radius. This is due to an upper limit imposed by Falder et al. (2010) during data reduction on the region that can be sampled. The small size of the IRAC images (4.4×4.4 arcmin) relative to the 'good' region of the *Herschel* data (a circle with radius 2.5 arcmin) means the SHAGS fields can be analysed out to a radius of approximately 1 Mpc at $z \sim 1$. Otherwise a distance around 1000–1200 kpc at the redshift of each AGN is undersampled in the number of IRAC counterparts due to the search radius extending outside the IRAC sampled area of the sky.

3.4.2 The XMM field

The data available from the VISTA–VIDEO survey is used in the XMM field to create two different types of catalogues. One is a comparison sample of galaxies at $0.9 \leq z \leq 1.1$, whilst the other corresponds to galaxies in the environs of the comparison sample, filtered to remove foreground sources and matched to

IRAC and 250 μm counterparts. The methods used to create both catalogues are described here.

3.4.2.1 Comparison Sample

The VISTA–VIDEO survey contains photometric redshifts which allow a suitable comparison sample of $0.9 \leq z \leq 1.1$ galaxies to be created, providing an alternative method to simply taking a general density across a large region of the sky (or as with Falder et al. 2010, the use of adjoining observations with no redshift data). The sheer number of viable sources in the VISTA–VIDEO data allows the use of strict cuts to ensure only the best sources are used.

The first step is obviously to filter the VISTA–VIDEO data for any sources with derived redshifts between 0.9 and 1.1. The standard deviation in z of these sources is determined to be ~ 0.06. Therefore, these sources are further constrained by removing any sources with half the difference between their lower derived $1\,\sigma$ redshifts and higher derived $1\,\sigma$ redshifts greater than 0.05. The CFHTLS–D1 and VISTA–VIDEO data have been used by the VIDEO team to determine likely photometric redshifts using a fitting procedure, as well as to deduce whether those sources are likely QSOs or stars. The catalogue is then filtered for these; each source has been assigned a χ^2 value by the fit to a variety of different source templates. Anything with CHI_BEST less than CHI_STAR or CHI_QSO is taken to be a galaxy. Finally, only those sources with at least a $5\,\sigma$ detection in the K_s band are used. This has two benefits; firstly, it should ensure that only the brightest, largest sources in stellar mass remain. Secondly, the K_s band is the shallowest VISTA band. Therefore, the likelihood of a reliable detection or non–detection in the other VISTA bands is increased, thereby

strengthening any derived photometric redshifts. The application of these cuts leaves 5884 sources. The g–i and j–K_s colours of the remaining sources are examined visually, with the result that all sources are away from the stellar locus and the majority are unlikely to host QSOs. These sources are then matched with SERVS data within 1 arcsec. This radius is chosen as the majority of the sources are found within 1 arcsec of each other. The SERVS data are cut at $5\,\sigma$ in both the 3.6 and 4.5 μm bands to again ensure only a highly reliable match. This leaves 3618 sources. However, to make a truly comparable sample to the SHAGS AGN, the catalogue must be cut further so that the sample is statistically indistinguishable in both redshift and IRAC colours. By matching in redshift, a similar spread in cosmic time is sampled, whilst matching in IRAC colours and magnitude ensures the galaxies are of similar stellar mass to the AGN within the SHAGS sample.

Unfortunately, a match in [3.6]–[4.5] AB colour is not possible. Upon determination of the colours of the SHAGS and XMM comparison samples, it is found that there is very little overlap. Indeed, the majority of the SHAGS AGN appear to have significantly more emission at 3.6 μm and 4.5 μm (see Fig. 3.12) than the comparison sample. This is likely attributable to excess emission arising from the presence of an active AGN; specifically the torus. As noted by Hatziminaoglou et al. (2008) and Hatziminaoglou, Fritz & Jarrett (2009), one of the most important dust features is found at $\geq 1\,\mu$m, attributed to sublimation of graphite dust grains in a dusty torus. This causes the quasar locus to occupy a well–defined region of IRAC colour space (Lacy et al. (2004), separate from objects dominated by stellar emission. Therefore, in galaxies hosting AGN, one would expect higher levels of emission at 3.6 and 4.5 μm owing to contamination from the AGN. This

boosting by a dusty torus is likely responsible for the strong dichotomy in colours between the SHAGS and the chosen galaxy comparison sample.

A last cut is made owing to the presence of a higher number of sources at lower redshifts within the range of $0.9 \leq z \leq 1.1$, which is sufficient to cause the samples to be significantly different upon application of a KS test (p=0.024). Therefore a random sample of galaxies is taken, sufficient to maximise the number of sources remaining whilst ensuring the samples are statistically indistinguishable. A sample of 3300 sources remains, with a redshift distribution statistically indistinguishable from the SHAGS sample ($p = 0.056$).

3.4.2.2 Environment

To create a suitable catalogue with which foreground sources in the XMM field are removed, the VISTA–VIDEO data are filtered again. Stars are once again removed as in the creation of the comparison sample, but instead of redshift, cuts are made in r–band magnitude so all remaining sources have $r < 22.4$ as with the SDSS catalogue. As with the 250 μm sources in the SHAGS fields previously, 250 μm sources in the XMM field are matched within 7.2 arcsec to IRAC counterparts (with the same constraints on CLASS_STAR and flux–density). This leaves a total of 1105 sources in the region covered by both SERVS and the HerMES 250 μm data. These are then matched again within 1 arcsecond to the the CFHTLS–D1 data which has been cut in r–band magnitude at 22.4, leaving only 126 sources over the area covered by both VISTA–VIDEO and CFHTLS–D1 data (a far smaller fraction of the area covered by HerMES and SERVS). An analysis of the effectiveness of this removal is presented in Section 3.4.3.

Due to some concern over whether a simple r–band cut could be made at the

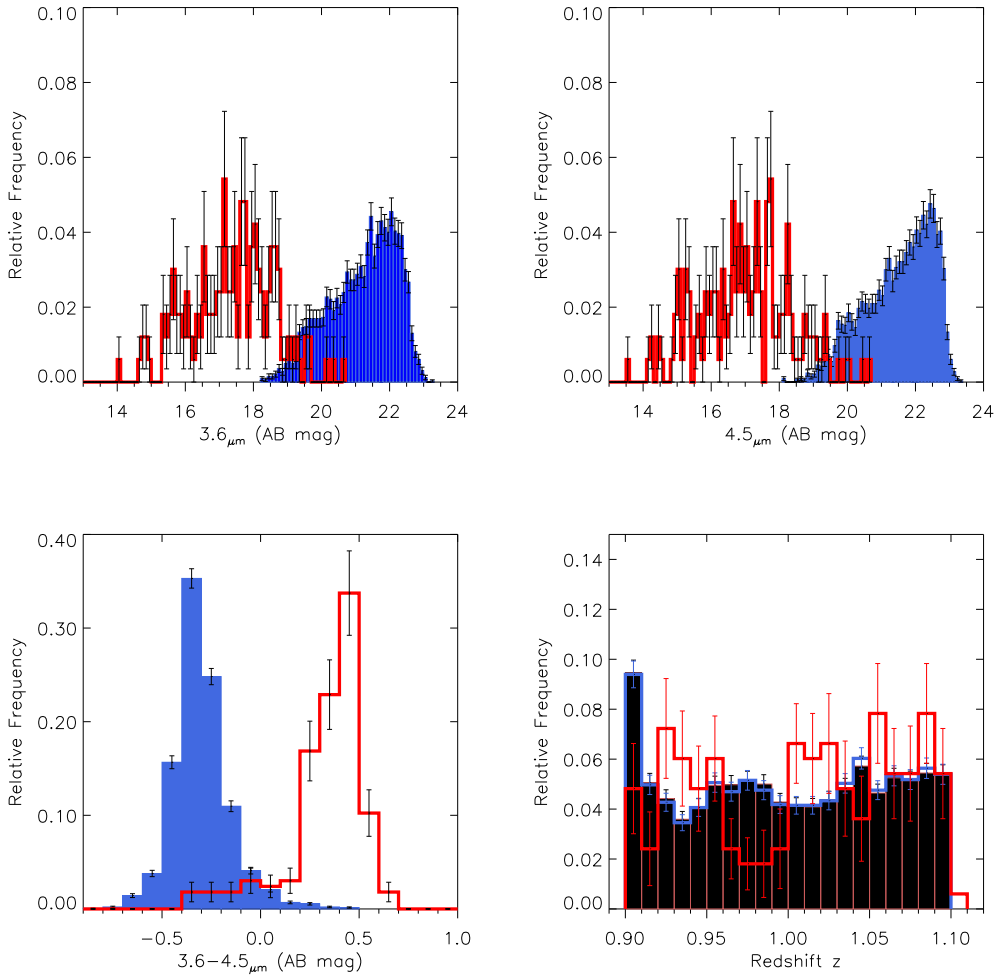

Figure 3.12: The distribution in (from upper left panel) 3.6 and 4.5 μm AB magnitudes, 3.6–4.5 μm colour and z for the XMM comparison sample (blue) and the SHAGS sample (red) after matching the distributions in redshift. The overlapping region above [3.6]–[4.5] = 0.1 contains only 55 sources, too few to modify the distribution sufficiently to match in colour and magnitude.

same level in both catalogues, the variance in r–band magnitude between the SDSS and CFHT r–band magnitudes was investigated. A prime region for study where both instruments have overlapping observations is Stripe 82, specifically the Wide Area W4 field observed as part of the CFHTLS. The SDSS catalogue for the field was filtered so only galaxies were present. These were then matched to the CFHT positions. The derived ModelMag parameter in SDSS and the Mag_Auto parameter from CFHT were compared for sources below an r–band magnitude < 22.4.

As visible in Fig. 3.13, at 17th magnitude and fainter, the two measures are relatively similar and still follow a 1:1 ratio. It is only for the brightest sources that the r–band magnitudes significantly deviate from one another. This is likely due to the difference in how the magnitude of a source is determined for each survey and the inherent difficulty in determining the 'edge' of a galaxy. In the CFHTLS, a version of the Kron magnitude (Kron 1980) found in SExtractor is used, integrating to 2.5 times a radius that contains ~ 1 per cent of the sky flux and will contain more than 90 per cent of an object's total light. In the case of the SDSS, a model magnitude is fit based on either a de Vaucouleurs profile (de Vaucouleurs 1953) or purely exponential profile. Depending on the fitted profile, multiples of the effective radius (the isophote within which is contained half the light from a source) are used and the profile is truncated by the SDSS, so some flux may be artificially removed. Therefore, for the largest and/or brightest sources, this difference will be significant enough that the magnitude derived by the SDSS is lower than that derived by SExtractor. However, the percentage of sources in the W4 field sample with magnitudes above 17th magnitude is ~ 11 per cent. This would mean approximately only 37 (of 341) and 35 (of 318) sources

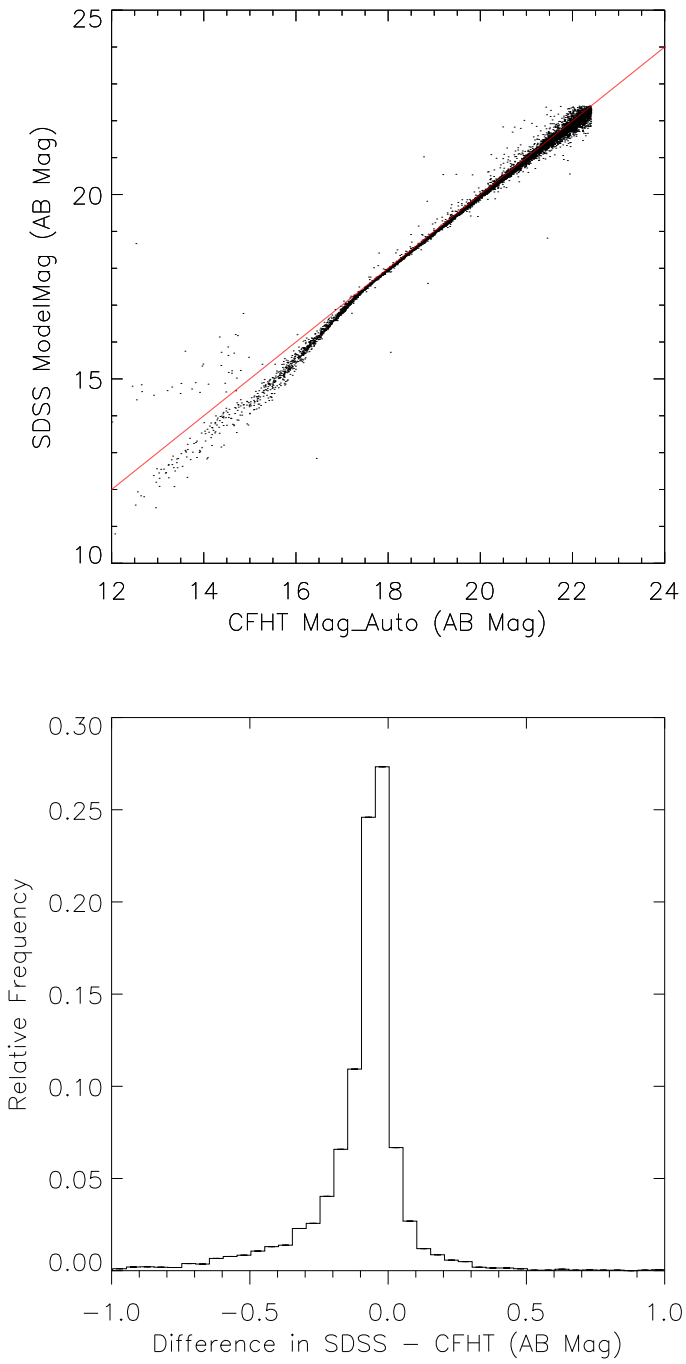

Figure 3.13: The distribution in r–band magnitude for a sample of galaxies in SDSS and CFHT. The upper panel is the ModelMag of SDSS against the CFHT Mag_Auto r–band magnitude. The red line shows a 1:1 relation. As visible, for the brightest sources the magnitudes significantly differ. This is likely due to their being the largest on the sky and therefore will cause a greater deviation. In the bottom panel the difference in magnitudes for the sample below r–band < 22.4 is shown. The majority are within 0.2 magnitudes.

for the SHAGS and XMM comparison sample environments will suffer from this problem, so the majority of the sample will remain unaffected by this difference in magnitude calculation.

3.4.3 How effective is the foreground removal?

The likelihood of there being contamination within the fields from low redshift sources is a genuine concern. Any foreground (i.e. $z < 0.9$) sources will increase the perceived density and weaken the signal from sources within the selected redshift range. The smaller volume being sampled at low–redshift relative to high–redshift sources will cause a strong degree of cosmic variance, hence the importance of foreground removal. Of course, high–redshift sources should also be accounted for. The availability of SDSS, IRAC and VISTA–VIDEO data allows a consistent treatment of both the AGN fields as well as the comparison sample previously mentioned.

The cross–matched IRAC/250 μm data can also be used to determine what quantity of sources might feasibly be at the correct redshift within the observed AGN fields and the XMM field for comparison with the statistical analysis later. In order to do so, the IRAC colour dependence on redshift derived by Falder et al. (2010) using the HYPERZ package (Bolzonella et al. 2000) combined with the stellar synthesis models of Bruzual & Charlot (2003) has been utilised.

The plot in Fig. 3.14 shows the the colour of six commonly used models versus redshift. These are a single burst model, four exponentially decreasing SFR models with timescales $= 1$, 2, 3, and 15 Gyr designed to represent elliptical, S0, Sa, Sb, and Sc type galaxies, as well as a model with a constant SFR (Im).

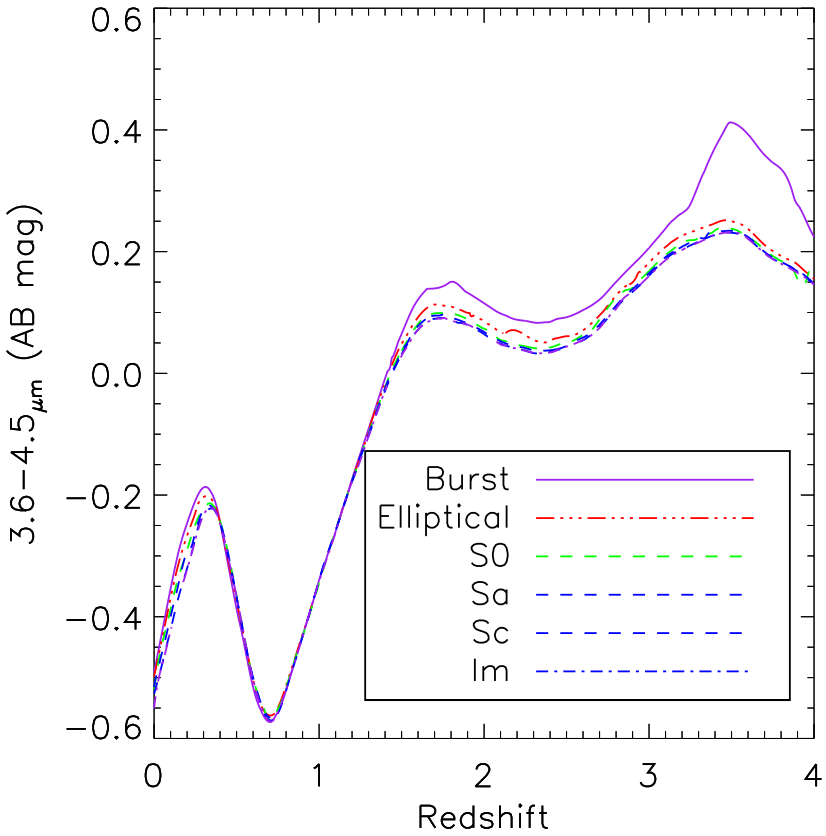

Figure 3.14: IRAC [3.6]–[4.5] AB color vs. redshift, as derived by Falder et al. (2010) using the Bruzual & Charlot (2003) stellar population models and the hyperz software package Bolzonella et al. (2000). The figure shows the range of colors produced with six different commonly used models. These are a single burst model, four exponentially declining SFR models representing elliptical, S0, Sa, and Sc type galaxies with τ = 1,2,3, and 15 Gyr, respectively, and a model with a constant SFR (Im) with no reddening.

It is clearly visible that regardless of galaxy type, the 3.6–4.5 μm colour remains similar out to a redshift of $z \sim 1.5$. The key thing to note is that for $z > 1.5$ this colour space provides a good method for identifying galaxies most likely to be at high redshift. Therefore, in combination with estimates of foreground contamination, the percentage of sources likely at high redshift in each sample can be identified.

Upon plotting the colour distribution prior to and after foreground source removal in the SHAGS fields (see Fig. 3.15), the shifted peak in the colour distribution no longer indicates a distribution dominated by low–redshift sources. Indeed, as much as 67 percent of sources around SHAGS AGN are at $z > 1.5$. However, the fraction below indicates as much as 0.25 sources per AGN are at approximately the correct redshift. The removal of SDSS counterparts should ensure that low–z sources are kept to a minimum.

Derived VISTA–VIDEO photometric redshifts on sources allow a direct visualisation of the distribution in redshift of removed 'foreground' sources in the XMM comparison sample. The number of sources that may be incorrectly removed can also be estimated. Similarly to the colour distribution around the SHAGS AGN, Fig. 3.16 shows before and after foreground removal, whilst also showing the redshift distribution of the removed sources. As before, the peak shifts to indicate the majority of the sources in the sample are at high–redshift. As hoped, it appears an r–band cut is most effective at removing sources with redshift $0 < z < 0.5$, but also removes some higher redshift sources. Upon investigation of these sources, many of the highest redshift sources are QSOs which will also likely be removed in the SHAGS sample. Meanwhile, at $0.9 \leq z \leq 1.1$, there are 6 sources, of which 2 are QSOs. Therefore, it is expected that perhaps

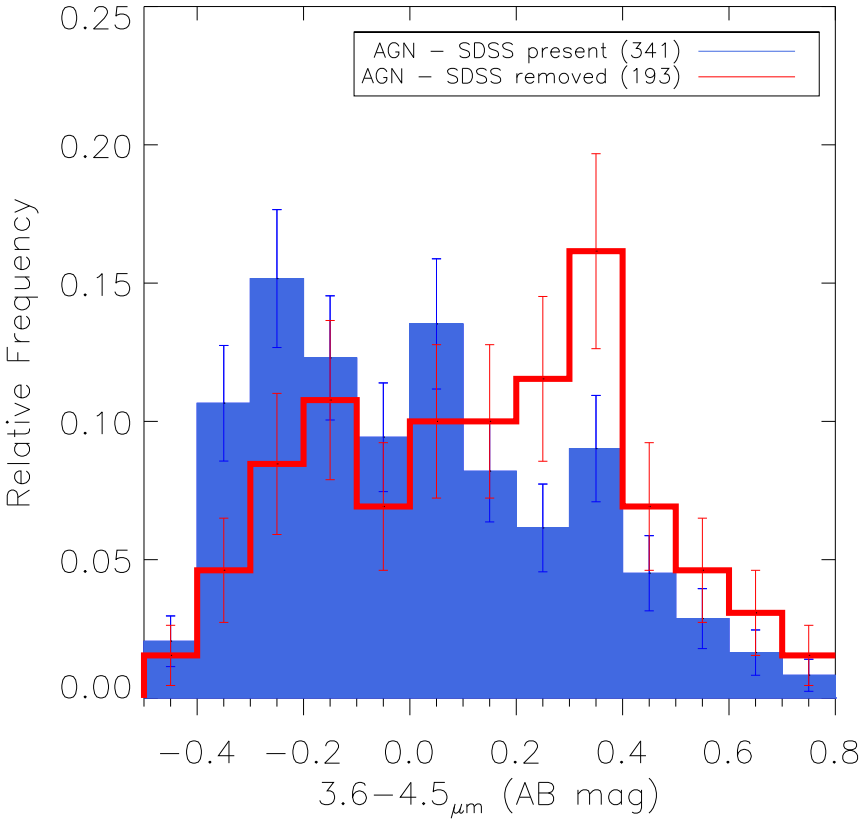

Figure 3.15: Once foreground sources are removed in the AGN fields, the peak source colour shifts to high redshifts ($z \sim 2$), and indicates as much as 67 percent of sources around the SHAGS AGN are at redshifts > 1.5. The error bars are the Poisson errors within each bin, whilst the binsize is approximately equal to the average 3.6 and 4.5 AB error on the magnitude added in quadrature for each source. Prior to foreground removal, there are 240 sources within 1 Mpc of the AGN. After removal of foreground sources, only 130 sources remain.

2 per cent ($\sim$3 galaxies of 191) of the sources removed using the SDSS catalogue might be within the right redshift range.

Of course, there are some effects that should be taken into account which might boost or lessen the number of sources found. This work has attempted to either estimate or compensate for their effect. Firstly, the possibility that some fraction of those sources in the SHAGS and XMM fields at high–redshift might be boosted in number via lensing has been considered, a consequence of observing towards concentrations of high mass. However, the geometry of a background at z$\sim$2 and a lensing cluster at z$\sim$1 is not optimal, so any contamination should be minor. Best (2002) already consider sources at z$\sim$1 and find that a higher number density of ellipticals at this redshift will still individually have Einstein radii of only 1–2 arcsec, suggesting that this is unlikely to affect source counts significantly in the work presented here. Secondly, Papovich et al. (2008) found a population of galaxies at z$\sim$0.5 with a significantly redder colour than that predicted by models or with reddening. These galaxies will almost certainly contaminate the colour space predicted to be occupied by high-z galaxies, though by matching with SDSS and CFHT counterparts the likelihood of this happening should be reduced. Finally, the presence of dust in this colour space will lead to some scatter in the 3.6–4.5 μm colour. The heating of said dust by the interstellar radiation field, as well as reflection and scattering of light by dust will serve to complicate any modelled SEDs in this colour space. However, as shown by Falder et al. (2011) for an elliptical galaxy, whilst extinction will increase the scatter on the 3.6–4.5 μm colour across the redshift range studied in this sample relative to a reddening–free SED, it does not prevent this method being used to identify galaxies above z$>$1.3.

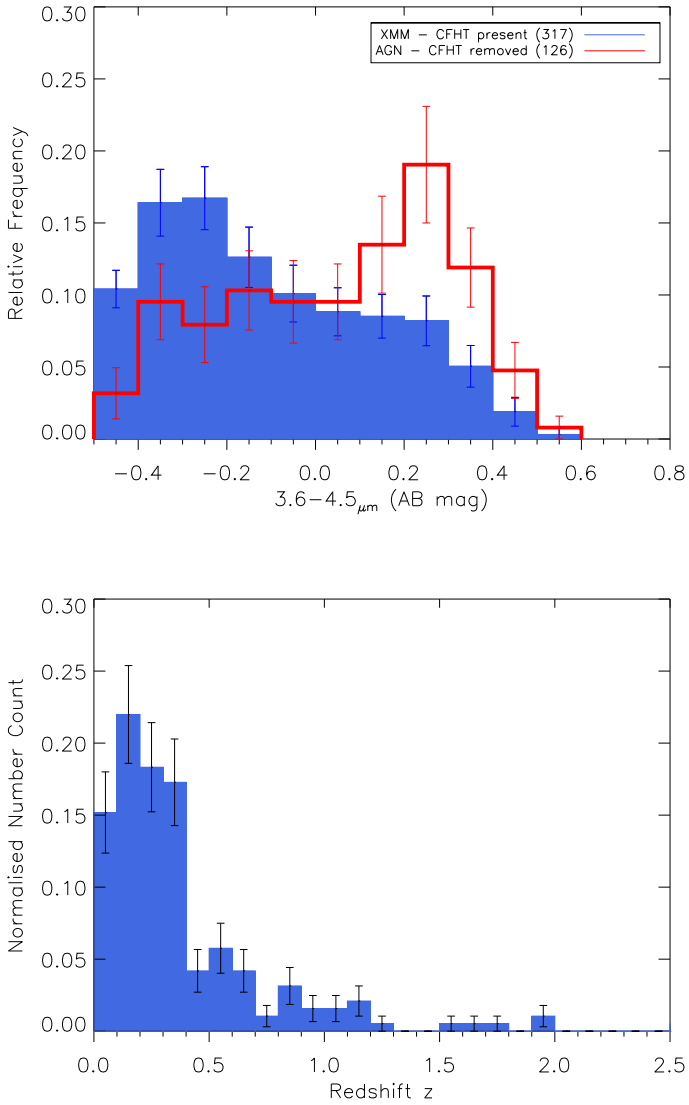

Figure 3.16: The upper panel shows the IRAC colour distribution before and after likely 'foreground' sources are removed. The peak of the distribution shifts to indicate the majority of the sample are now found at high redshift. The lower panel shows the redshift distribution of removed sources in the CFHTLS–D1 data with IRAC and 250 μm counterparts. Whilst a significant number of low redshift sources are removed, some high redshift objects are also removed. A small percentage ($\sim$2 per cent) are at the desired redshift, though a similar effect will likely occur in the SHAGS fields so this is not a great concern.

In summary then, the IRAC colours of the SHAGS sample suggest that any overdensity at z $\sim$ 1 will be attributable to only a few sources, around 0.25 sources per SHAGS AGN. It should be noted, however, that the errors on the colours, the possibility that the IRAC models may not be representative for all galaxies and the implicit assumption only one source is responsible for 250μm emission likely makes this an uncertain estimate to within a factor of a few.

3.5 Statistical Analyses

The main analysis in this chapter is based on a method similar to Best et al. (2003) and Falder et al. (2010). Annuli are placed concentrically around each QSO, the source density in each is then determined and a background density derived from the XMM comparison sample is subtracted.

A problem to note is the presence of a detected AGN. This will bias the results, giving an overdensity in the first annulus. Therefore, any 250 μm source found within 7.2 arc seconds of the optical position of an AGN or XMM comparison sample galaxy is removed and the area sampled in each annulus is changed accordingly. At most only 28 250 μm sources can be associated with AGN when using the IRAC/250 μm match. These sources will be investigated in a subsequent paper (Kalfountzou et al. in prep). This in itself suggests star formation within AGN host galaxies is already a rare occurrence at z $\sim$ 1, or at least AGN host weaker star formation than at earlier epochs. This is in line with work by other authors (e.g. Hatziminaoglou et al. 2010; Bonfield et al. 2011) who find few AGN in their samples hosting ongoing star formation when observed using *Herschel*.

When choosing and applying concentric annuli, there are various problems that arise from the limitations of both *Herschel* and the IRAC images used to match IRAC counterparts. Firstly, owing to the larger FWHM of the SPIRE instrument in each waveband, an inherent restriction is placed on how small the innermost annulus can be made. Falder et al. (2010, 2011) used 300 and 700 kpc as their radius. However, at z $\sim$ 1, 300 kpc is approximately equal to twice the FWHM at 250 μm, imposing a strict limit on the maximum possible number of detectable sources within the central annulus. As noted before, an upper radial limit of 1 Mpc is imposed. This is an appropriate maximum region size at 250 μm, since the literature suggests that overdensities can extend out to 1.6 Mpc (Best et al. 2003). A central annulus radius of 500 kpc is chosen, as it allows the greatest number of annuli within 1 Mpc whilst avoiding the lower limit of 300 kpc. Since Falder et al. (2010) detected an excess even using a 700 kpc radius, if there is a similar overdensity in star–forming galaxies, it should be detected. The results from multiple fields are combined to minimise Poisson errors further and to improve the significance of any densities within the fields overall.

3.5.1 All AGN vs Overdensity

To begin with, the comparison sample background density (see Table 3.3 for the derived density in each annulus) is subtracted from each AGN annulus bin to derive the overdensity relative to the XMM comparison sample. The error bars for each of the AGN fields are the combined Poisson errors of the count in the AGN field added in quadrature to the Poisson error derived for the comparison sample 'background'.

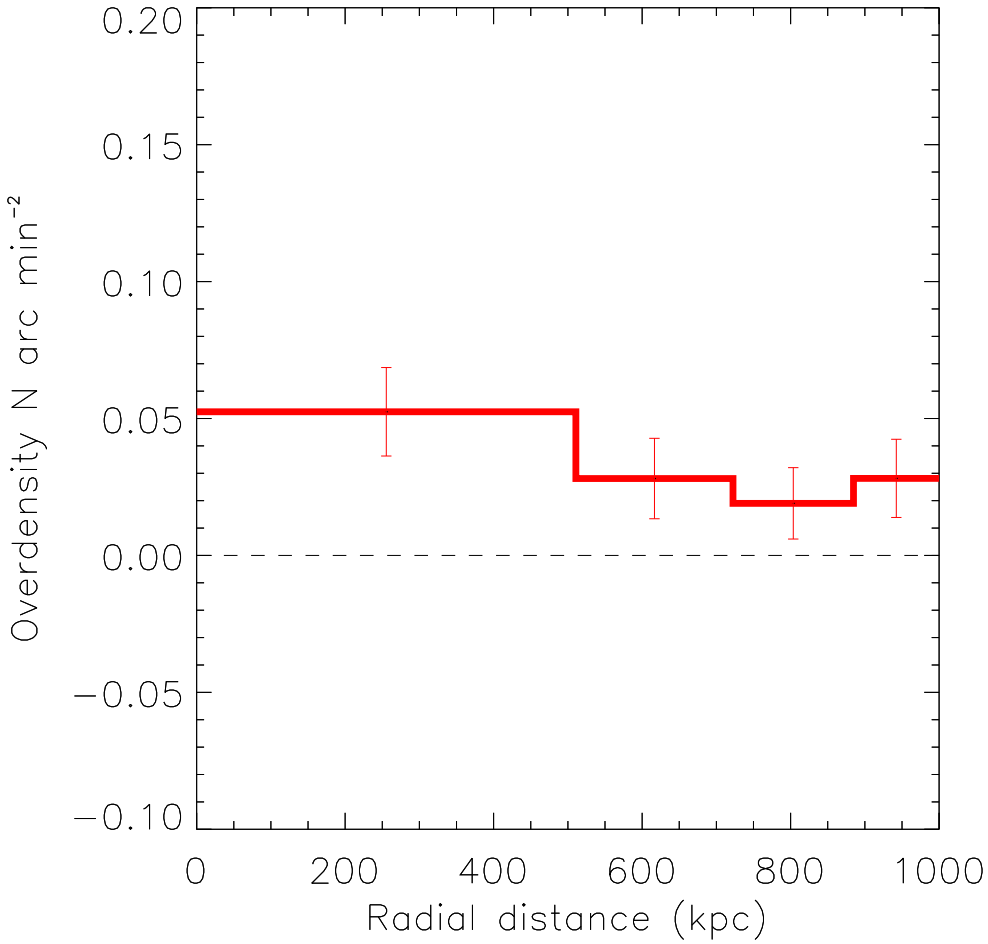

Figure 3.17: Source overdensity within $\sim$1000 kpc at z $\sim$ 1 as a function of radial distance for the entire sample of AGN relative to the XMM comparison sample. The error bars are the result of stacking in quadrature the errors on each fields over–density, which in turn are the result of adding the Poisson error on the source density measured in the AGN field to the Poisson error of the source density measured in the comparison sample, both scaled by the mean completeness correction in each case. The dashed line marks the zero level.

Table 3.3: The derived XMM comparison sample density alongside the SHAGS overdensity within 1 Mpc of the central AGN/galaxy. The overdensity shown in Fig. 3.17 is tabulated for each bin and overall within 1 Mpc of the central AGN using XMM comparison sample background density, also shown here. The table shows the density/overdensity (N/Δ N), the error on the density/overdensity (err N/Δ N) and the significance of the result (σ).

	XMM Density			SHAGs Overdensity		
Bin	N (arcmin^{-2})	err N (arcmin^{-2})	σ	Δ N (arcmin^{-2})	err Δ N (arcmin^{-2})	σ
1	0.048	0.002	24	0.052	0.016	3.25
2	0.050	0.003	16.7	0.028	0.015	1.87
3	0.046	0.002	23	0.019	0.013	1.46
4	0.053	0.003	16.7	0.028	0.014	2.00
All	0.049	0.001	49	0.032	0.007	4.57

Within 1 Mpc, it appears many have some overdensity (e.g. see Fig. 3.20). However, taking overdensities on a field by field basis is prone to larger Poisson errors. Fig. 3.17 shows the stacked values for each annulus out to 1 Mpc for the entire AGN sample using the XMM comparison sample. Due to the increased statistical significance of each bin, there appears to be tentative evidence for an overdensity of star–forming galaxies around the AGN in the sample, particularly within the first annulus. Regardless, the source overdensity appears relatively uniform within 1 Mpc when one considers the error on each bin. The significance of the density/overdensity within each annulus is determined by dividing the overdensity by the error. Results are shown in Table 3.3, which shows the value of each annular bin of the histogram shown in Fig. 3.17. Within 1 Mpc, it appears the detected overdensity is attributable to only ~ 0.45 sources per AGN assuming a circle of 1 Mpc covers approximately 14 arcmin^2 squared on the sky.

Since the XMM comparison sample has not been matched in [3.6]–[4.5] AB colours or magnitudes, it is likely that objects of similar stellar mass are not being

compared. If this has some bearing on the environment, i.e. a denser environment leads to a larger stellar mass in the central AGN, this may introduce a bias towards higher overdensities. However, the 3.6 μm magnitude can be used as a proxy for stellar mass, as at z $\sim$ 1, this is close to the peak of the SED produced by old evolved stellar populations (assuming minimal/no AGN contamination from a dusty torus). The top and bottom 10 per cent of comparison sample sources with the greatest and smallest emission at 3.6 μm are selected and the density around each sample compared to determine how great the variation might be. Whilst the density appears greater on average around the brightest 10 per cent (0.056 ± 0.004 cf. 0.052 ± 0.004 N arcmin^{-2}), there is no difference within the errors. This suggests that density is insensitive to the stellar mass of the comparison sample. However, this also means that the detected overdensities are real rather than a consequence of differences in the comparison sample.

3.5.2 AGN type vs Overdensity

A similar analysis is performed after splitting the sources into their various AGN types. The results of this analysis are shown in Fig. 3.18. Radially, whilst the numerical overdensity appears to decrease at larger distance from the central AGN, the errors prevent any conclusion other than that the overdensity is uniform within 1 Mpc. Furthermore, when each AGN type is considered, this lack of radial dependence is visible in all cases, and would suggest they inhabit similarly dense environments.

However, upon taking the entire 1 Mpc region, there appear to be significantly larger overdensities around RL AGN than RQQs in star formation, particularly

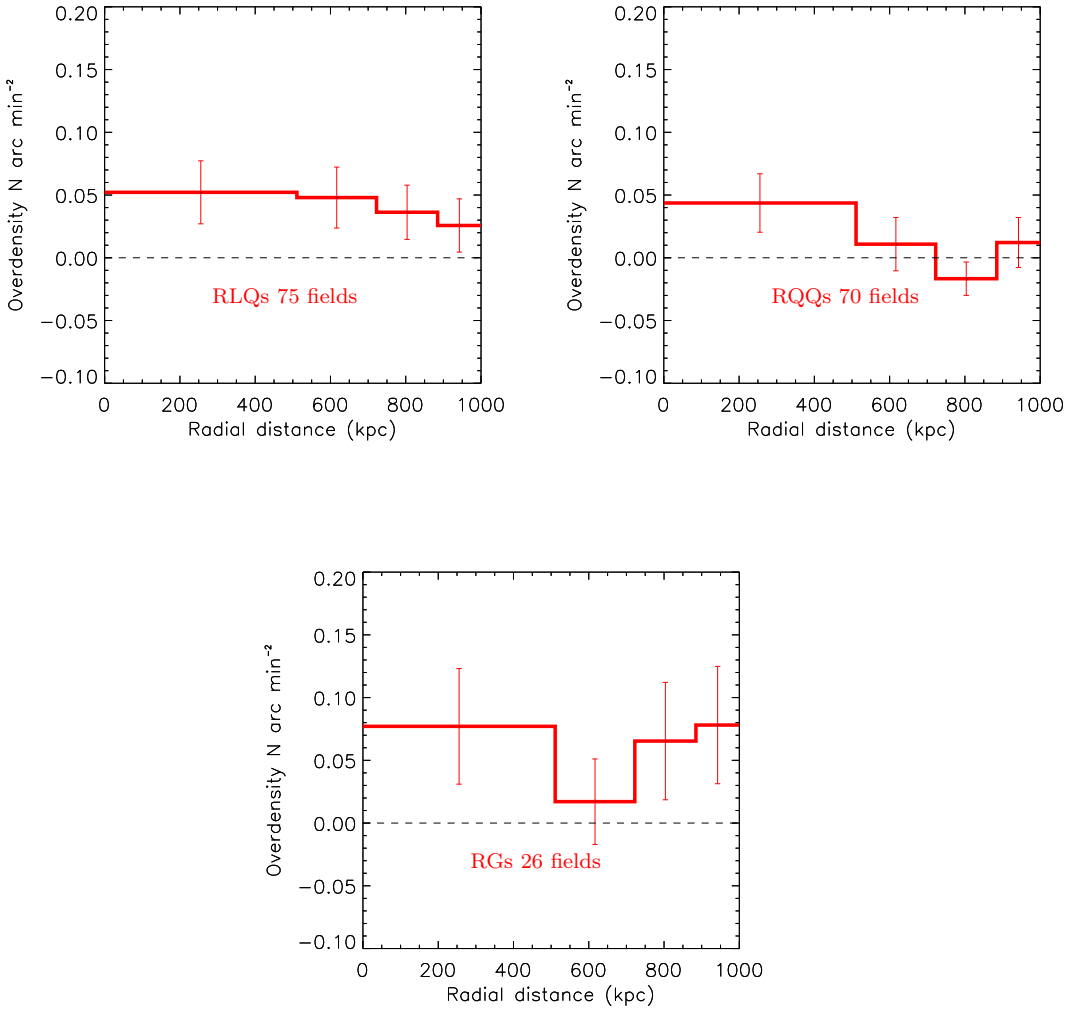

Figure 3.18: Histograms showing the stacked source overdensity for the AGN subsamples. From left to right, the plots show RLQs, RQQs, and RGs. The error bars are the result of stacking in quadrature the errors on each fields over–density, which in turn are the result of adding the Poisson error on the source density measured in the AGN field to the Poisson error of the stacked source density measured in the comparison field, both scaled by the mean completeness correction in each case. The dashed line marks the zero level.

Table 3.4: The overdensity shown in Fig. 3.18 tabulated for each annulus and overall within 1 Mpc of the central AGN. The table shows the overdensity (Δ N), the error on the overdensity (err Δ N) and the significance of the result (σ).

AGN type	Bin	Δ N (arcmin^{-2})	err Δ N (arcmin^{-2})	σ
Radio Loud	1	0.052	0.025	2.00
Quasars	2	0.048	0.024	2.00
	3	0.036	0.022	1.64
	4	0.026	0.021	1.21
	All RLQs	0.041	0.012	3.42
Radio Quiet	1	0.044	0.023	1.91
quasars	2	0.011	0.021	0.052
	3	-0.017	0.013	-1.31
	4	0.012	0.20	0.70
	All RQQs	0.012	0.010	1.20
Radio	1	0.077	0.046	1.67
Galaxies	2	0.017	0.034	0.50
	3	0.065	0.047	1.38
	4	0.078	0.047	1.66
	All RGs	0.059	0.022	2.68

around RGs. This is in line with the results of Falder et al. (2010) who also found that RGs exhibited the greatest overdensities at 3.6 μm. The significance of the overdensity in each annulus for each of these subsamples is visible in Table 3.4 which shows the results across the 4 annuli as well as the combination of all four annuli.

There are two possible reasons for this. Either the central AGN is influencing star formation on Mpc scales, or the most powerful radio galaxies are generally found in richer environments. It is therefore logical to investigate whether there is a correlation between the mass of the central AGN, its radio luminosity, and the detected overdensities around these objects.

3.5.3 AGN properties vs Overdensity

If AGN occupy the densest regions of the universe at that epoch, the hierarchical model would imply that there may be a greater concentration of mass in their vicinity. However, would this greater concentration of mass increase the gas and dust available for SF, or would it be counter productive, with mergers and galaxy harassment truncating star formation? Secondly, could AGN feedback from higher luminosity radio sources have a significant impact on their environments?

Initially, the sample is investigated for evidence of a trend between black hole (BH) mass and SF overdensity. BH mass estimates are taken from Falder et al. (2010), with their method described therein. As noted by them, RG estimates are not available since the requisite broad line region is obscured in these objects. Due to the large errors on individual fields, stacking is once again used to increase the significance of any results. From Fig. 3.19, no strong trend is visible and the errors overlap in all bins. If one compares the overdensity distributions as a function of BH mass for each AGN type, a KS test returns a p–value of 0.08, which suggests the RLQ and RQQ samples are drawn from the same parent population. In contrast, a Mann-Whitney test returns a p–value of 0.03. This would suggest that RLQs are likely to have greater overdensities in their environs than RQQs. The mean black hole masses of the RLQ and RQQ samples lie within 1σ of each other ($\log_{10}(\mathrm{M_{BH}}/\mathrm{M_{\odot}}) = 8.87 \pm 0.06$ and 8.81 ± 0.06 respectively), so both samples should be similarly dense regions of the universe. This may explain the contradictory results encountered when one considers the degree of scatter on individual fields.

Fig. 3.18, combined with the derived numerical overdensity within 1 Mpc tentatively suggests that powerful radio sources may sit in overdensities slightly higher than RQQs. This indicates there may be an intrinsic relationship between radio luminosity and overdensity, with radio loud sources preferring denser environments. As noted before, Falder et al. (2010) found a significant correlation ($>$ 99 per cent level) between the highest luminosity sources and evolved stellar mass, so it is not beyond the bounds of possibility that a similar trend might exist with star–forming galaxies. On an individual basis, the large errors on each field prevent a strong conclusion being formed, and obscure any possible correlation between radio luminosity and star formation overdensity. However, as visible in the bottom panel of Fig. 3.20, upon stacking the SHAGS fields it appears the environments of the most extreme radio sources are significantly more overdense when compared to the least powerful sources. This difference disappears however on attempting to determine whether a particular AGN type is responsible.

To place these results on a more statistical footing, correlation analyses are performed to search for possible trends within the sample, both regardless of AGN classification and split into separate types. Since upper limits are available for the RQQs, a survival analysis technique like the Cox Proportional Hazard test (CPH) can be utilised, as well as other measures of correlation such as the Spearman Rank (SR) and Kendall Tau (KT) tests. The entire 1 Mpc region is sampled since it provides the greatest number of sources with which to compare each field. As well as applying the tests to the entire sample in black hole mass and radio luminosity, the analysis is also constrained to those sources with radio luminosities above the cutoff between Fanaroff–Riley I (FRI) and Fanaroff–Riley II (FRII) radio sources at $\log_{10}(\mathrm{L}_{325}/\mathrm{W\,Hz^{-1}\,sr^{-1}}) = 25$. This is chosen

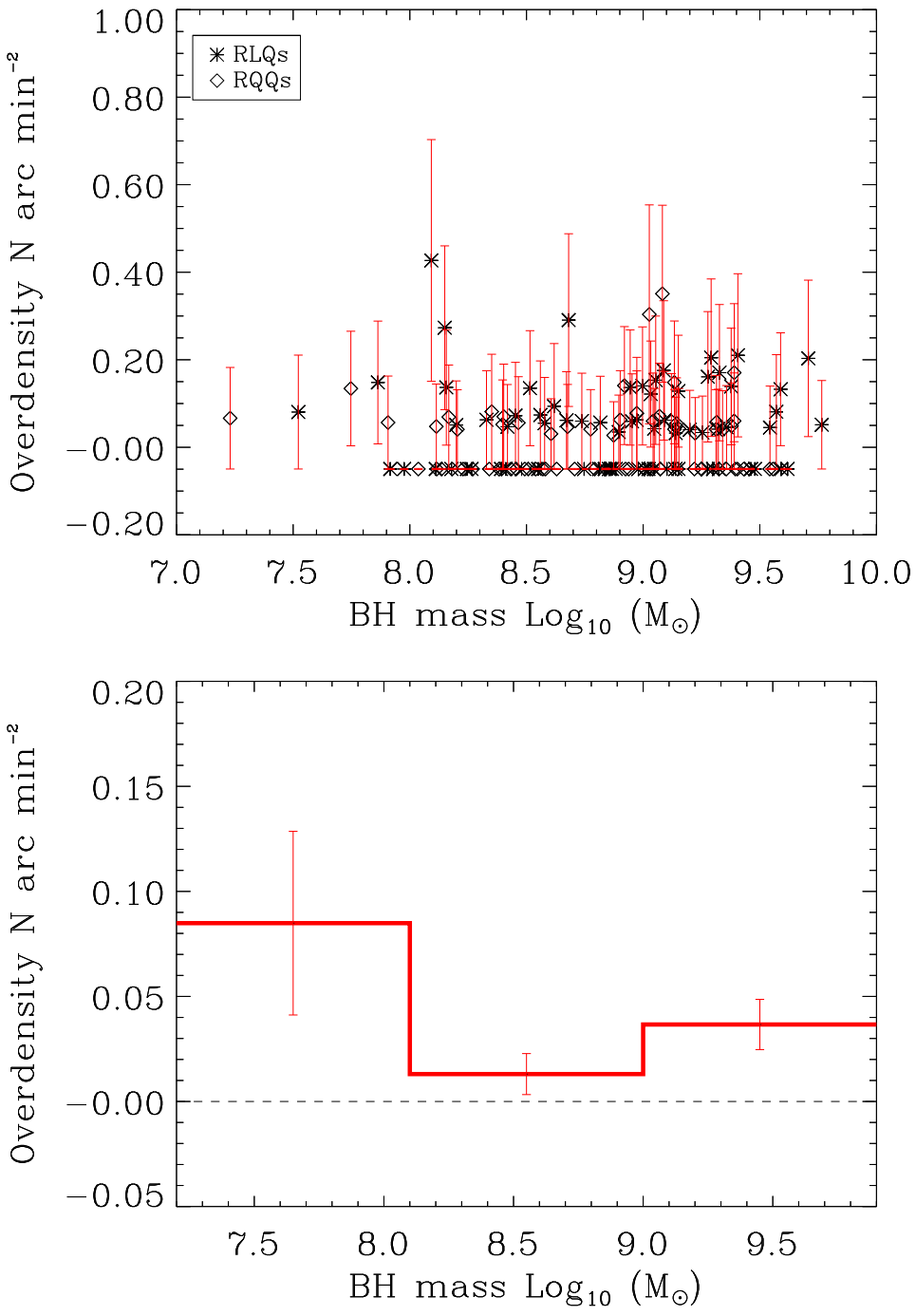

Figure 3.19: The top panel shows individual field overdensities as a function of BH mass and stacked SF overdensity bins as a function of BH mass. No correlation is readily apparent when fields are studied on an individual basis. In the bottom panel, RLQs and RQQs (for which BH mass estimates exist) have been stacked, but there appears to be no clear trend present.

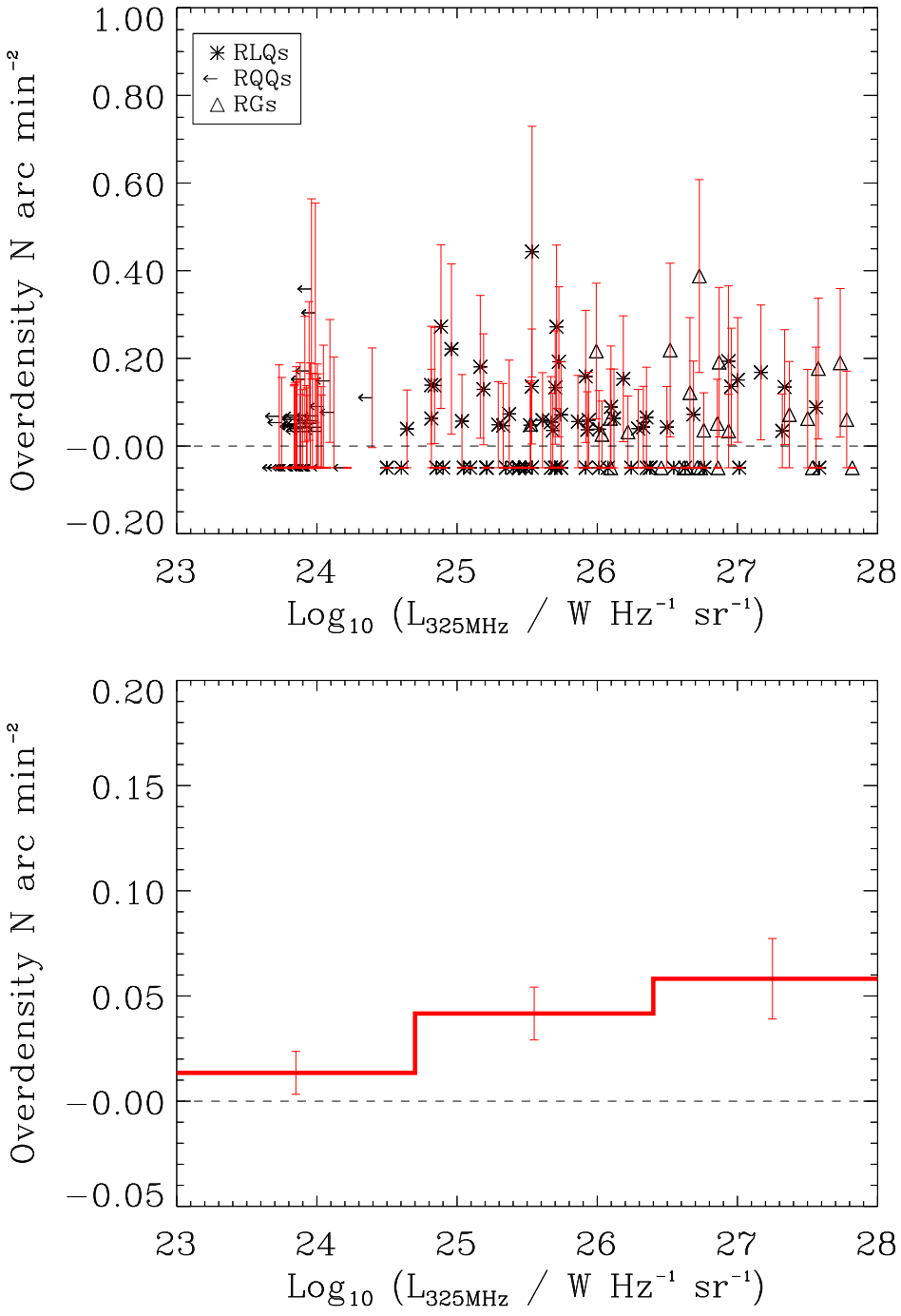

Figure 3.20: The top panel shows the individual overdensities per field. The small number of sources per field introduces large errors on the overdensity in each field, which may obscure any possible correlation. However, it appears star formation activity is not dependent upon radio luminosity at a first glance. The bottom panel shows the stacked overdensity (RLQs+RQQs+RGs) as a function of radio luminosity. It appears there is a general increase towards higher radio luminosities, with the most powerful radio sources having significantly higher overdensities to less powerful sources.

since there is a divergence in the space–density evolution with redshift, with higher luminosity radio sources appearing to evolve more strongly than lower luminosity sources (Clewley & Jarvis 2004; Sadler et al. 2007). Whilst there appears to be no correlation with BH mass (see Table 3.5), there is some evidence ($\sim$95–97 per cent) for a correlation with radio luminosity when all sources are considered. This correlation disappears when only the most extreme sources ($\log_{10}(\mathrm{L}_{325}/\mathrm{W\,Hz^{-1}\,sr^{-1}}) > 25$) are considered, contrary to the findings of Falder et al. (2010) who find strong correlations for these groups using all statistical tests. However, this is at 3.6 μm, which as noted before, will trace evolved stellar populations rather than ongoing star formation. These results suggest that radio power and star formation overdensity are linked at z $\sim$ 1. It also once again raises the question of whether RL AGN and RQQs must be treated as entirely separate physical entities or are instead part of a continuum of sources (see Falder et al. 2010 for further discussion on this point).

3.5.4 Star–Formation Rates

Due to the imposed source cuts only LIRGs are present in the catalogue, with SFRs greater than $\sim 114\,\mathrm{M_\odot\,yr^{-1}}$ at $z = 1$. However, is there a particular SFR at which companion galaxies peak, and do those companions have different properties for each AGN type?

The SFRs in this analysis are calculated using the Kennicutt relation (Kennicutt 1998), where the FIR luminosity is determined by assuming T= 23.5 K and an emissivity index $\beta = 1.82$. A modified black body model (Hildebrand 1983) is used which is found to be appropriate when dealing with FIR emission to deter-

Table 3.5: The results of correlation analyses with Spearman rank (where applicable) and Kendall tau tests for a search radius of 1 Mpc. The coefficients shown are the correlation coefficient, whilst the significance is the confidence level at which the null hypothesis (i.e. no correlation) is rejected. In the case of the Cox hazard proportional test, the coefficient is the output χ^2 value. Analyses are performed as a function of BH mass and radio luminosity including all sources, as well as using more conservative cuts on only the most extreme radio sources. Survival analysis on the radio luminosity data is also performed as the RQQ radio luminosities are upper limits.

	Test	Coefficient	Significance
Quasars	Spearman Rank	0.033	0.309
BH Mass vs Overdensity	Kendall tau	0.046	0.339.
RLQs	Spearman rank	0.054	0.359
BH Mass vs Overdensity	Kendall tau	0.085	0.429
RQQs	Spearman rank	-0.030	0.196
BH Mass vs Overdensity	Kendall Tau	-0.042	0.221
All AGN	Spearman rank	0.161	0.961
(Radio Luminosity vs overdensity)	Kendall tau	0.197	0.958
	Cox Hazard	4.461	0.965
AGN ($L_{radio} > 25$)	Spearman rank	0.151	0.848
(Radio Luminosity vs overdensity)	Kendall tau	0.189	0.833
AGN ($L_{radio} > 26$)	Spearman rank	0.0225	0.888
(Radio Luminosity vs overdensity)	Kendall tau	0.278	0.862

mine SFRs. To determine how the SFR distribution varies as a function of AGN type, the SFR distribution for the SHAGS AGN is determined and normalised to the total area of sky sampled for each type. A similar process is performed to derive the SFR distribution around galaxies in the XMM comparison sample. This distribution is then subtracted from that of the SHAGS sample to leave only overdensity. It is implicitly assumed that all 250 μm sources sampled within 1 Mpc of an AGN/comparison sample galaxy are at the redshift of that AGN/galaxy. Whilst for the majority of sources this will lead to incorrectly derived SFRs, the contribution and difference from those at $z \sim 1$ will remain upon subtraction. Fig. 3.21 shows the distribution of SFR, for the entire sample and split based on AGN classification.

The results indicate that SFR overdensity is only slightly above the background level, with low level SFR (relative to earlier epochs) going on around all AGN types. Higher ($\geq 500\,M_\odot\,yr^{-1}$) SFRs appear to be non–existent. Split based on AGN type, it appears RLQs and RGs may have a higher number of LIRGs (100–200 $M_\odot\,yr^{-1}$) relative to RQQs. Indeed, RQQs appear to sit in regions close to the background level, but the large errors prevent further conclusions being drawn based on AGN type. The implications of these results are discussed further in Section 3.6.

3.5.5 Stellar Mass Overdensity vs SF Overdensity

It has already been noted how significantly higher overdensities were found by Falder et al. (2010) in evolved stellar mass compared to those found here in star formation. A natural question to ask is whether there is some correlation

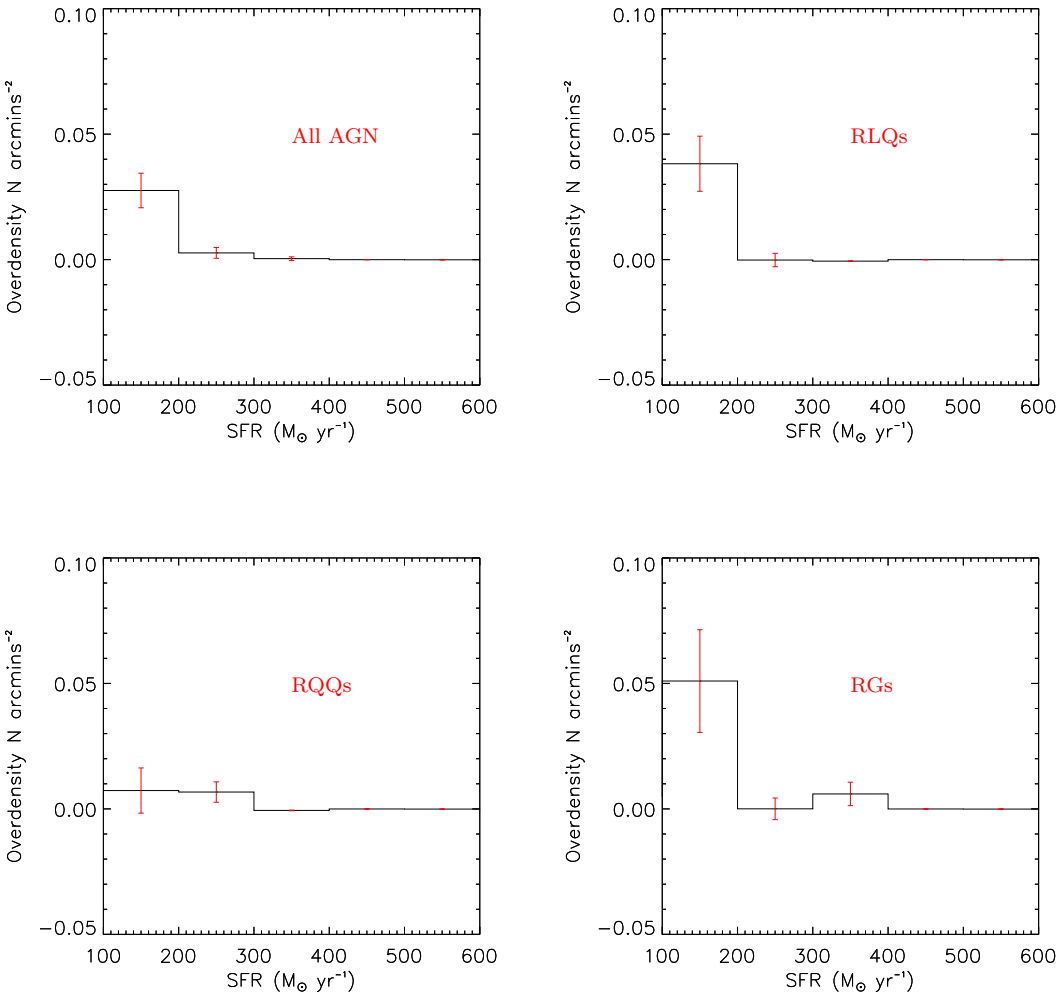

Figure 3.21: The SFR overdensity distribution around AGN, overall and split in AGN classification. A bin size of 100 $M_\odot\,yr^{-1}$ is used here which is found to give the greatest significance in each annulus. As visible, it appears RL AGN inhabit significantly more active environments, with the majority of star formation present in greater numbers of LIRGs at 100–200 $M_\odot\,yr^{-1}$. The error bars are the Poisson errors for the AGN fields and background added in quadrature both scaled by their appropriate completeness corrections.

between the two. For example, do fields with higher stellar mass overdensities present higher star formation overdensities, suggesting star formation overdensity is related to galaxy mass or is the picture more complex?

With this in mind, the determined overdensities for every field in both star formation and stellar mass are taken and the distribution is plotted as shown in Fig. 3.22, with the data binned in stellar mass to see whether a trend is visible when sources are stacked. Each data point is the stacked stellar mass/star formation overdensity of all fields in a stellar mass bin of width 6 sources/arcmin^2. These points are not fixed to the centre of the stellar mass bin so as to best show how the distributions vary between bins and between AGN types in both stellar mass and star formation overdensity. There appears to be a discernible trend for RLQs (see Fig. 3.22), with increasing star formation overdensity in the fields with high stellar mass overdensities, though this is not apparent for RQQs or RGs. Performing correlation analyses using Spearman Rank and Kendall Tau tests on the distribution of the sample, it is found that when all AGN are considered, there is no evidence for a correlation, yet restricting the analysis to RLQs indicates a strong (>99 per cent) correlation with stellar mass. If this trend is related to radio luminosity, it is entirely possible that a larger sample of RGs might also show such a trend, particularly when one considers that for the most powerful RL AGN ($L_{\rm radio} > 26$), Falder et al. (2010) found a strong dependence on radio luminosity.

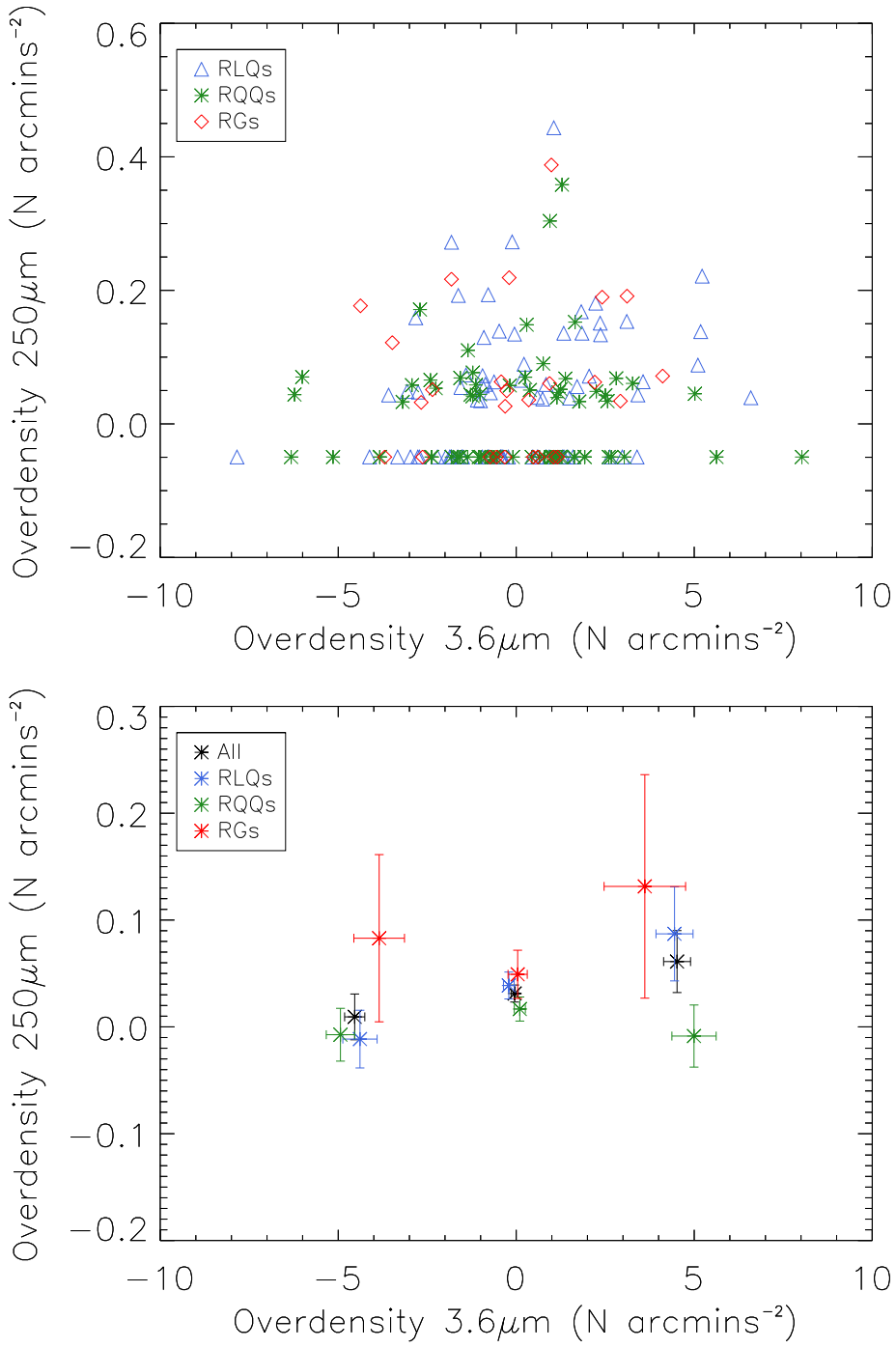

Figure 3.22: The upper panel shows the individual overdensities per field in both SM and SF. The bottom panel shows the stacked star formation overdensities as a function of SM overdensity, split into each AGN type as well as overall. It appears there is a general increase in star–forming galaxy overdensity towards higher SM overdensities, with RLQs appearing to have a strong trend relative to other AGN types. The relative lack of RG fields may obscure any correlation (if present) and prevent a similar conclusion for RGs.

3.6 Discussion

There are several caveats to these findings that must be considered before attempting to interpret how these results fit into the current cosmological framework.

Firstly, a lack of sources around individual fields will reduce the ability of correlation tests to detect a correlation. After considering contamination from both high and low–z sources, an average of ~ 0.4 sources per AGN within the required redshift range are responsible for an overdensity in star–forming sources. This introduces a significant degree of scatter. Whilst it may not completely obscure some correlations (e.g. with radio luminosity), it may prevent a detection if the correlation is more subtle, such as possibly with BH mass.

Secondly, the flux density limit imposed on the catalogue further constrains any possible conclusions. As noted before, the chosen flux density cutoff corresponds to $\sim 114\,\mathrm{M_\odot\,yr^{-1}}$ at $z = 1$ i.e. this work is sampling only LIRGs in the fields of the SHAGS AGN. This could mean a large contribution from smaller SFR galaxies is omitted. Even if there were no instrumental error on a galaxy at $\mathrm{z} \sim 1$, the confusion noise at 250 μm of a relatively shallow survey like the HerMES Lockman–SWIRE prevents the $5\,\sigma$ level being less than ~ 27 mJy, and corresponds to $94\,\mathrm{M_\odot\,yr^{-1}}$, essentially preventing the detection of all but the most active star–forming galaxies. However, if LIRGs dominate the star formation budget in these environments, as they have been found to dominate the cosmic star formation budget by $\mathrm{z} \sim 1$ (Le Floc'h et al. 2007; Magnelli et al. 2009), one would expect that half of the comoving total infrared luminosity density would be generated by LIRGs. Therefore, this work is still sampling a major contributor in

the evolution of these environments.

Finally, this work is limited by the resolution of *Herschel*. Many sources at 250 μm are found to have large numbers of 3.6 μm sources within the beam. It may then be the case that several sources have ongoing star formation but the beamsize is too large to prevent individual identifications, which will lower the number of detected 250 μm sources within the field relative to 3.6 μm. Attempts have been made to offset and quantify the effect of this issue on the source number estimates, both by applying a completeness correction as well as using IRAC data to determine the number of sources that may be at the correct redshift. It should be noted that the comparison sample will suffer the same limitations, yet it is encouraging that similar number estimates are arrived at for the number of sources responsible for any overdensity using IRAC and *Herschel* data with significantly different methods.

The results in this work suggest that as little as 5.5 Gyr after the big bang, the majority of the stellar mass has already been assembled, yet the fields of AGN remain relatively fertile regions of star formation. Overdensities at the $\sim$2–4 σ level are found around RL AGN within a 1 Mpc radius, whilst around RQQs star–forming galaxy counts are at the background level. The overdensities are far lower than those found in stellar mass, which is consistent with the growing consensus on 'downsizing' in star formation from higher redshifts. At earlier epochs, the intra–cluster–medium (ICM) may have been denser and thus allowed enhanced star formation to take place. If one considers that the progenitors of these AGN are likely submillimetre galaxies (Smail et al. 1997; Blain et al. 2002; Stevens et al. 2003, 2010) where frenzied star formation is observed on the order

of several thousand solar masses per year, the larger overdensity present in stellar mass relative to star formation is easily explained. Tidal interactions and halo stripping (Bekki 2009) will increase the density of the IGM (thereby possibly leading to the observed radio luminosity–star formation overdensity correlation; see next paragraph), whilst mergers and other such extreme events can serve to produce starbursts and star formation within galaxies (Sanders et al 1988; Bournaud et al., 2011).

Whilst no strong evidence for a correlation with BH mass is readily apparent, there may yet be present a correlation with radio–luminosity when considering all AGN. Falder et al. (2010) found a dependence of 3.6 μm overdensity on radio luminosity, particularly for Fanaroff–Riley (FR) Type II galaxies at the 95 per cent confidence level. This result was attributed to either jet confinement (Barthel & Arnaud 1996) or black hole spin (Wilson & Colbert 1995; Moderski, Sikora & Lasota 1998; Tchekhovskoy, Narayan & McKinney 2010; Garofalo, Evans & Sambruna 2010; McNamara, Rohanizadegan & Nulsen 2011). In this work, the relative weakness of the radio luminosity–star formation overdensity correlation might be explained by a rapid decline in the material available for star formation as the system approaches a virialised state and galaxy interactions become rarer. Cooling flows and filaments will draw material toward the inner regions of the cluster (e.g. Gaspari, Ruszkowski & Sharma 2012) thereby starving field galaxies of material, yet will still allow jet–confinement to continue around radio sources and the denser ICM may still support star formation overdensities above the background level though far lower than earlier epochs. This would explain why Falder et al. (2010) find significant overdensities within 200–300 kpc of the AGN, whilst here it is a struggle to find any radial dependence on overdensity within 1 Mpc.

Furthermore, when comparing the derived overdensities in stellar mass and star formation, a strong (> 99 per cent) correlation around RLQs is found, suggesting that larger stellar mass overdensity causes a higher star formaton overdensity. It is possible that the mechanisms behind this involve galaxy–galaxy interactions other than mergers such as tidal/gravitational shocks (Gnedin 2003) or flybys (Sinha & Holley–Bockelmann 2007) between evolved neighbouring galaxies and bluer gas–rich galaxies still forming stars. From Falder et al. (2010) it is known that RL AGN inhabit more overdense regions at 3.6 μm, so this may also explain the discrepancy between RLQs and RQQs, and may imply that a larger sample of RGs would show a similar trend.

This simple material starvation scenario combined with weaker galaxy interactions yet a higher number of evolved stellar mass companions at this epoch would also explain the observed SFR distribution. Around RL AGN, the environment appears to be significantly more active in star formation, with both higher numbers of star–forming galaxies and higher SFRs. However, for all AGN, this activity is composed entirely of LIRGs and suggests companion galaxies are significantly less gas–rich than at earlier times. The majority of LIRGs in these fields are feasibly individual galaxies because "normal" isolated disc galaxies are gas-rich enough to reach LIRG-like activity (Daddi et al. 2010; Tacconi et al 2010), but it remains true that the strongest starbursts (ULIRGs and Hyper-LIRGs) will be predominantly merging systems (e.g. Elbaz & Cesarsky 2003). Therefore, if gravitational shocks, flybys and mergers are more prevalent in the crowded systems of RL AGN, a higher number of LIRGs would be expected than around RQQs. Around RQQs, the companion sources may rely on asymmetries or morphological disturbances which arise internally (Bournaud et al. 2008) to

reach LIRG luminosities. They may also be more gas–rich as there is a low level of ($\sim 1.64\,\sigma$) sources with SFRs of 200–300 $\mathrm{M_\odot\,yr^{-1}}$, which would be consistent with less harassment allowing galaxies to better retain their grip on material for star formation in the environments of RQQs.

Finally, as to the character of these sources, whereas the SHAGS AGN are the progenitors of modern–day massive ellipticals found at the centres of the brightest clusters, it is possible that the sources in their environments form some fraction of modern day S0 galaxies. Tidal interactions in the above scenario are insufficiently strong to produce ellipticals but can produce S0s (Gnedin 2003). Studies find that the elliptical and S0 fraction increases steadily from $\mathrm{z} \sim 1$ to the current epoch in the densest regions, whilst increasing significantly from $\mathrm{z} \sim 0.5$ until now in intermediate density regions (e.g. Postman et al. 2005; Smith et al. 2005). This would tie in with the observed SFR distribution of mainly LIRG activity and the dearth in star formation observed in clusters in the local universe.

3.7 Conclusions

This chapter presents an analysis of star–forming source overdensities around some of the most massive objects in the universe at $\mathrm{z} \sim 1$ in an attempt to determine whether there is a relationship between AGN and environmental density with regards to young star–forming galaxies. The following results are found:

1. For the 171 sampled fields, AGN show on average a small overdensity of star–forming galaxies, which once low and high–redshift sources are accounted for consists of ~ 0.4 star–forming galaxies in every AGN field. This overdensity appears to be relatively uniform and extends out to the Mpc–

scale. However, upon comparing the overdensity based on AGN type, it appears RL AGN inhabit significantly more active environments than their RQQ cousins.

2. There is found no evidence of a trend with BH mass though a correlation with radio luminosity is present, which suggests an environmental dependence for radio loudness. This correlation is only found when all AGN are considered which is in stark contrast to Falder et al. (2010) who also find a correlation when only the most luminous AGN are sampled. The removal of this correlation for the most luminous sources can be explained if the material available for star formation has been removed due to mergers or material transport in towards the central AGN, thereby preventing a correlation being detected. The small number of sources in each field also likely plays a role in obscuring a correlation.

3. RL AGN appear to inhabit significantly more active environments upon a comparison of the SFR distribution of their companion sources. These companions are generally made up of LIRGs with SFRs of 100–200 $M_\odot\,yr^{-1}$, far lower than that observed at earlier epochs. This may be explained by higher levels of galaxy interactions around RL AGN. In contrast, around RQQs less harassment may have allowed a fraction of sources to retain their gas to reach SFRs of 200–300 $M_\odot\,yr^{-1}$.

4. A strong correlation between star formation and stellar mass overdensity around RLQs exists within the sample. It is entirely possible that following the strong correlation with radio luminosity found by Falder et al. (2010), one might expect a similar trend for RGs, though the small sample size and

small number counts may serve to obscure any correlation.

As mentioned in Section 3.6, these results can be explained if the majority of the available stellar mass has already been assembled by $z \sim 1$ and overdensities are primarily dependent on environmental effects rather than any influence by the AGN itself. With regard to the radio–loudness/overdensity correlation, whilst weak for SF overdensity, it is strongly visible in Falder et al. (2010) and in work by Donoso et al. (2010). This further supports the idea that the environment plays a large role in the evolution of an AGN, though what parameters are responsible is still not entirely clear. Mergers, tidal interactions and other mechanisms such as those suggested by (Gnedin 2003) and(Sinha & Holley–Bockelmann 2007) serve to remove the available gas and dust in the cluster at earlier times, thereby reducing star formation relative to earlier epochs. Ongoing harassment is responsible for the large number of sources with LIRG luminosities in the environments of RL AGN which are already known to have higher overdensities of evolved stellar mass. In contrast, around RQQs it is feasible that internal disturbances within the companion galaxies are responsible for ongoing star formation rather than outside effects.

The reduction in material owing to the harassment discussed is likely responsible for the observed increase in S0's as found by Postman et al. (2005) and Smith et al. (2005) from z$\sim$1 to the present day in the densest clusters, and ties in well with what is observed in the SHAGS fields.

Chapter 4

A new XMM–Newton–selected sample of absorbed QSOs

4.1 Introduction

In this chapter, observations taken by SCUBA–2 at the JCMT in Hawaii have been used to study the submm environments of a sample of XMM–Newton selected X–ray absorbed QSOs. This follows on from work conducted on a similar sample by Page et al. (2001, 2004) and Stevens et al. (2005, 2010). The earlier sample was composed of X–ray absorbed AGN, with absorption column densities of the order $10^{22}\,\mathrm{cm}^{-2}$. The sample had been selected so as to avoid a correlation between X–ray luminosity and redshift, and was observed with the original SCUBA instrument (Holland et al. 1999). In these studies, several important discoveries were made.

Using Mrk 231 as a template source for a modified black body model, it was found that of five AGN, the four highest redshift sources were all detected and

had ULIRG–level FIR luminosities. A determination of the contribution to the total FIR from the central AGN implied that the majority of the emission could only be coming from massive ongoing starbursts within the host galaxy, with SFRs of $> 1000\,\mathrm{M}_{\odot}\,\mathrm{yr}^{-1}$. Furthermore, when split based on redshift, the entire sample had a bi–modal distribution and the skewed detection rate implied cosmological evolution in the host galaxies, with higher SFRs at higher redshifts. A tentative trend was found to exist between FIR luminosity and redshift, which further implied cosmological evolution.

Secondly, when the original sample was compared with a group of 20 non–X–ray absorbed QSOs selected in a similar way, it was found only one source was detected above the $3\,\sigma$ level. This is quite a severe disparity when one considers that 50 per cent of the original X–ray absorbed sample were detected above the $5\,\sigma$ (5 mJy) level. This finding was irreconcilable with the standard 'unified' AGN theory, and the difference was attributed to these absorbed sources being a transition phase between an obscured, high SFR source and an ordinary QSO phase (Page et al. 2011).

Finally, upon studying the environments of five of these sources it was found that they all sat within overdensities attributed to sources with 2–4 mJy. At the redshifts studied, this implied ULIRG levels of activity, with derived SFRs using analogues such as Mrk 231 and Arp 220 of between 400–1300 $\mathrm{M}_{\odot}\,\mathrm{yr}^{-1}$. This suggested that these fields would evolve over cosmic time to become some of the most massive clusters observed in the present day (Stevens et al. 2010).

However, these works only studied a relatively small redshift range ($1.7 < z < 2.8$) and mapped only a small area ($28\,\mathrm{arcmin}^2$). This prevented conclusions being drawn about evolution of the environment with redshift, and lacked large num-

bers of bright sources.

The work presented here aims to use the increased mapping area of SCUBA–2 combined with a larger sample over a greater redshift range to remedy some of these unresolved questions. For the purposes of number counts, 850 μm is a better wavelength for study than 450 μm, which is far more sensitive to changes in the weather at the time of observation. Therefore, whilst data at 450 μm have been reduced, the analysis presented here mainly concerns results found at 850 μm rather than 450 μm (though the flux–densities of AGN at 450μm are included).

The layout of this chapter is as follows: in Sections 4.2 and 4.3 the sample, observations and data reduction processes performed are detailed. This is followed by an analysis of the reduced data and what these results may imply in Section 4.4. Finally, an interpretation of the results within a cosmological framework and how they may fit into currently understood theories on galaxy formation and evolution is discussed in Section 4.5 and a summary is provided in Section 4.6.

4.2 Sample Selection

The sample selection for this work was performed by Alina Streblyanska and will be presented in Streblyanska et al. (in prep). However, the properties of the sample are required to understand the analysis performed in this chapter, therefore a brief summary is provided here.

The sources here were selected by matching the optical SDSS DR6 quasar catalogue (Schneider et al. 2007) with the X–ray 2XMMi catalogue (Watson et al. 2009), restricting the selection to only those sources with at least two broad

permitted emission lines, and showing absorbed X–ray emission. This gave a total of 50 sources, which after redshift ($1 < z < 3$) and X–ray luminosity $\log(L_x, \mathrm{erg\,s^{-1}}) > 44.3$ constraints have been applied gives 20 sources. These limits are similar to those imposed on the original ROSAT selected sample (Page, Mittaz & Carrera 2000, 2001). However, the new sample now has absorbing column densities that are on average an order of magnitude higher than the previous sample. Table 4.1 shows some of the properties of the final observed sample.

In Fig. 4.1, the sensitivity of SCUBA–2 assuming a flux density cutoff of 1.5 mJy (similar to the depth used in these observations), is used to determine what range of SFRs are detectable at 850 μm with varying temperatures. As before with *Herschel*, a temperature T of 23.5 K and dust emissivity index β of 1.82 (Smith et al. 2013) are assumed, but a hotter temperature of 41 K and emissivity index of 1.95 are also input. This is in keeping with parameters fitted to a sample of SCUBA–2 QSOs by Priddey & McMahon (2001), albeit at $z > 4$. In comparison with *Herschel* (see Fig. 2.1), Fig. 4.1 indicates SCUBA–2 is far more sensitive to star formation out to high redshift assuming similar cold temperatures and emissivity indexes as those found by Smith et al. (2013). Indeed, the emission remains above the confusion limit out to $z \sim 5$. The difference in sensitivity can be attributed to the differing dust temperatures assumed. For cold sources, the peak of the modified black body SED is passed relatively quickly, leading to the drop–off visible in the upper panel of Fig. 4.1. However, for the hottest sources, negative k–correction will mean the sampled wavelengths are still ascending the Rayleigh–Jeans tail, hence the noticeable increase in flux density above $z \sim 1$ in the lower panel of Fig. 4.1. A hotter dust temperature will mean a lower emitted flux at 850 μm, since the bulk of the emission shifts to shorter wavelengths, hence

Table 4.1: The full SCUBA–2 sample selected prior to observations, composed of 20 sources. Every object is an X-ray absorbed QSO.

Source	RA	Dec	z	2–12 keV X–ray luminosity (erg s^{-1})	Upper Error (erg s^{-1})	Lower Error (erg s^{-1})	Absorption Column Density (cm^{-2})	BAL?
J030238.16+000203.4	45.659	0.034	1.3483	3.47×10^{44}	4.0×10^{44}	2.97×10^{44}	2.73×10^{22}	Yes
J083709.64+484020.6	129.290	48.672	1.671	8.39×10^{44}	1.55×10^{45}	3.41×10^{44}	2.555×10^{23}	No
J085723.99+090349.0	134.349	9.063	1.049	5.96×10^{44}	7.22×10^{44}	4.83×10^{44}	6.39×10^{22}	No
J092138.45+301546.9	140.410	30.263	1.589	2.34×10^{44}	3.75×10^{44}	1.16×10^{44}	9.35×10^{22}	Yes
J094021.12+033144.7	145.088	3.529	1.284	2.22×10^{44}	3.19×10^{44}	1.51×10^{44}	1.257×10^{23}	No
J095749.98+013354.1	149.458	1.565	2.011	3.67×10^{44}	7.89×10^{44}	6.75×10^{42}	1.523×10^{23}	No
J095834.74+014502.3	149.644	1.750	1.8886	3.01×10^{44}	3.89×10^{44}	2.18×10^{44}	6.5×10^{21}	Yes
J095835.98+015157.0	149.649	1.865	2.934	4.67×10^{44}	6.19×10^{44}	1.38×10^{44}	2.52×10^{23}	Yes
J095944.47+051158.3	149.935	5.199	1.595	6.42×10^{44}	8.89×10^{44}	4.2×10^{44}	7.32×10^{22}	No
J100205.36+554257.9	150.522	55.716	1.151	5.94×10^{44}	6.57×10^{44}	5.43×10^{44}	4.4×10^{21}	Yes
J100341.29+050533.2	150.922	5.092	2.045	3.07×10^{44}	7.05×10^{44}	0.0	5.91×10^{22}	No
J103301.50+583749.8	158.256	58.630	1.344	8.04×10^{44}	1.23×10^{45}	4.46×10^{44}	7.89×10^{22}	No
J105201.35+441419.8	163.005	44.238	1.791	5.95×10^{44}	7.58×10^{44}	4.35×10^{44}	6.7×10^{22}	Yes
J120522.18+443140.5	181.342	44.527	1.921	5.12×10^{44}	6.51×10^{44}	3.86×10^{44}	1.4×10^{22}	Yes
J122637.02+013016.0	186.654	1.504	1.552	1.03×10^{45}	1.36×10^{45}	7.39×10^{44}	5.48×10^{22}	Yes
J125930.97+282705.5	194.879	28.451	1.094	3.51×10^{44}	3.84×10^{44}	3.21×10^{44}	1.77×10^{22}	Yes
J130948.57+534634.7	197.452	53.776	2.436	6.21×10^{44}	9.07×10^{44}	3.47×10^{44}	7.6×10^{22}	No
J142623.49+603021.8	216.597	60.506	1.935	1.38×10^{45}	1.96×10^{45}	9.1×10^{44}	1.737×10^{23}	No
J144625.48+025548.6	221.606	2.930	1.883	7.31×10^{44}	1.25×10^{45}	2.92×10^{44}	9.61×10^{22}	Yes
J144935.95+631835.9	222.399	63.309	1.735	1.19×10^{45}	1.63×10^{45}	7.53×10^{44}	4.92×10^{23}	No

the relatively feeble 850 μm flux density for a source at 41 K.

Several 'background' fields are also selected, with the aim of using these to derive expected number counts over a large enough area such that bias due to cosmic variance should be negligible. A suitable survey is the CLS (discussed in Section 1.4). Several fields are selected; the UKIDSS–Ultra Deep Survey field (UDS), the Lockman Hole Owen field (LH), and the SSA–22 (SSA). All selected fields have rms depths of between 1 and 2 mJy, making them suitable for a comparison study with the rms $\sim$1.5 mJy AGN fields.

4.3 Observations and Data Reduction

Observations were carried out in February 2012 and 2013 with the SCUBA–2 instrument mounted on the JCMT for 17 of the 20 sources. Typical zenith opacities during the observations in both semesters were $\tau_{wvm} = 0.04$–0.08 (i.e. Band 1–2 conditions), measured every 1.2 seconds along the line of sight. The 'Daisy' scan mode (Holland et al. 2013) was chosen as it would provide the fastest means of observing the selected targets, whilst not sacrificing exposure time and providing a nominal circular field of view with a radius of 3 arcmin (though there will be data outside this with a lower integration time). This mode keeps the pointing centre on one of the four SCUBA–2 sub–arrays at all times during exposure. The measured effective FWHM at these wavelengths are approximately 9.8 and 14.6 arcsec respectively for 450 and 850 μm (Dempsey et al. 2013).

Each object was observed up to a maximum of 3 times, with each observation lasting $\sim$30–40 minutes and simultaneously observing at both 450 and 850 μm. Nightly flux calibration was achieved by observation of astronomical sources with

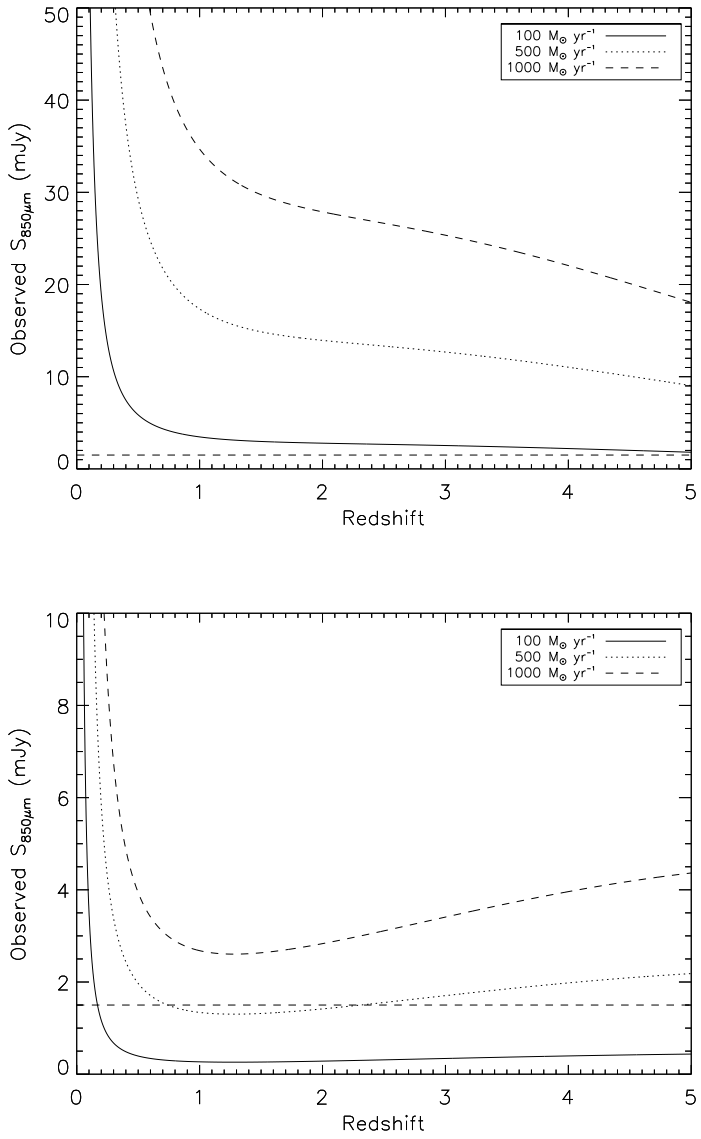

Figure 4.1: SCUBA–2 sensitivity to different SFRs varies as a function of redshift. The different lines show different SFRs and the 850 μm flux density they will have between $0 < z < 5$. The top panel assumes a simple modified black body for the FIR SED of galaxies with a temperature of 23.5 K and dust emissivity index of $\beta = 1.82$. The lower panel assumes a temperature of 41 K and dust emissivity index of $\beta = 1.95$. Clearly evident is the reduced sensitivity to even the most extreme star–bursts in hotter hosts assuming the same emissivity index. The horizontal dashed line shows the approximate confusion limit at 850 μm (1.5 mJy) for the reduced observations.

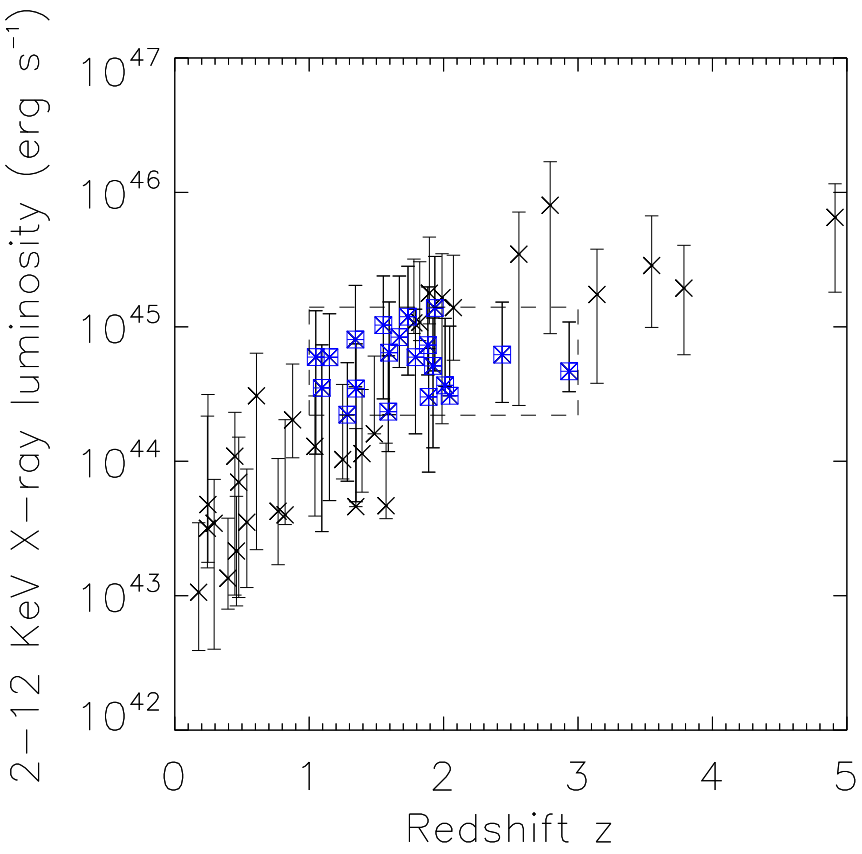

Figure 4.2: Plot showing the X-ray luminosity in the 2–12 keV band versus redshift for a new sample of 50 X–ray absorbed QSOs. From these 50, 20 were initially selected within the dotted box for observation by SCUBA–2. These sources have been selected so as to show no correlation between X–ray luminosity and redshift (Pearson correlation coefficient = 0.045).

known flux properties, as well as to test the focus and pointing of the instrument during the run and were observed prior to and after each observation. This was part of ongoing calibration efforts by the JCMT team to determine Flux Correction Factors (FCFs), which are required to convert between the measured signal in Picowatts (pW) to Janskys (Jy). The FCF is simply the ratio between the known flux S in Jy and the measured signal in pW, I_0. All calibrators were observed using a Daisy scan-pattern (Holland et al. 2013), designed specifically for observation of point and compact sources, with observations lasting approximately four minutes each.

As well as using Uranus and Mars as calibration sources, other well known compact and extended sources were observed during the run such as CRL 618, also known as the Westbrook Nebula. It is a proto–planetary nebula which has only recently ($\sim 100\,\mathrm{yr}$ ago) started on its journey towards a post–AGB state (Kwok & Bignell 1984). As such, it is still composed primarily of molecular gas and has been extensively studied in the sub–millimetre (e.g. Jenness, Robson & Stevens 2010). It is relatively compact, having a FWHM of 8.0 and 14.6 at 450 and $850\,\mu$m (Dempsey et al. 2013). Arp 220 was also observed as a calibrator source. It is a nearby ULIRG, and is well studied in the submillimetre. Its host galaxy properties are discussed in greater detail in Section 4.4.3.

4.3.1 Map making

The data were reduced using the dynamic iterative map–maker found in the SMURF package (Jenness et al. 2011; Chapin et al. 2013). The algorithm processes data in two stages; a pre–cleaning stage, and the iterative process itself is

Table 4.2: Observing log of the SCUBA–2 Observations presented in this chapter. The number of scans also includes the noise and flat–field scans. Each scan lasts up to $\sim$30 seconds. Generally the opacity range across each observing run was between 0.04 and 0.08 (Grade 1–Grade 2 weather) as given by the JCMT water vapour radiometer at 183 GHz and CSO tau at 225 GHz. Each observation was performed in the Daisy–scan mode.

Name	Date (yy/mm/dd)	N_{scans}	τ_{wvm}	$\tau_{225\,GHz}$
J030238	2012/02/17	81	0.055	0.042
	2012/02/18	81	0.044	0.046
	2012/02/19	81	0.057	0.068
J083709	2012/02/17	168	0.060	0.073
J085723	2012/02/17	156	0.045	0.046
J094021	2012/02/18	160	0.055	0.071
J092138	2012/02/18	156	0.065	0.075
J095749	2012/02/18	158	0.045	0.056
J095834	2013/02/17	138	0.064	0.050
J095835	2012/02/18	160	0.045	0.045
J095944	2013/02/17	182	0.069	0.079
J100205	2013/02/17	183	0.064	0.054
J100341	2013/02/20	60	0.069	0.076
J103301	2012/02/17	184	0.060	0.097
J105201	2013/02/20	183	0.066	0.059
J120522	2012/02/17	162	0.068	0.071
	2012/07/10	162	0.065	0.065
J122637	2013/02/17	183	0.073	0.087
J130948	2012/02/17	174	0.044	0.062
	2013/07/10	174	0.058	0.063
J144625	2012/02/18	80	0.047	0.046
	2012/06/24	80	0.049	0.062
	2012/06/25	160	0.052	0.051

composed of several models (COM, EXT, AST, NOI). Initially, flat–fields bracketing each observation are used to convert to pW units by calibrating the bolometers, whilst steps and spikes within the data are removed. The threshold is set at the default $10\,\sigma$ level with a moving boxcar. The data are also down–sampled to match the requested pixel size.

In the iterative process, the algorithm attempts to firstly model and remove the common mode signal (COM), which will be dominated by signal from atmospheric water and ambient thermal emission. The extinction due to the atmosphere is then modelled and compensated for (EXT) using readings from the water vapour monitor. The reduction of blank fields differs somewhat from the standard pipeline in that normally a high pass filter (600 arcsec) is used to remove $1\,/\,f$ noise, but in blank fields this is found to cause problems when there is very little signal in the map and will remove objects of interest. Instead, both a low– and high–pass band filter are applied with angular scales of $2 < \theta < 120$ arcsec, in keeping with the reduction method applied to the CLS data. The data are then regridded as part of the AST step, where the astronomical signal itself is modelled (AST). This helps to reduce the noise, which is then also measured (NOI) and used to subsequently weight the bolometers by using data in the first iteration. This is also used to estimate the χ^2 tolerance in a fit determined by the map maker, which can also be specified by the user. The variance of the data in each pixel is used to create a weighted mean of all scans for that observation. FCFs, dependent on the semester in which the source was imaged, are applied (see Table 4.3). Similarly to the CLS survey, a correction of ~ 10 per cent is applied to each FCF so as to compensate for flux lost due to filtering in each map. The CLS found this correction factor by inserting a bright Gaussian point source

Table 4.3: The canonical FCFs for each date. Since several observations were taken prior to July 2012, these have had greater FCFs applied to those images.

Date	FCF - 450μm Jy/pW/beam	FCF - 850μm Jy/pW/beam
January 2012 - July 2012	606	556
July 2012 onwards	491	537

into the time series data of each observation and determining how the source was affected (Geach et al. 2013(@).

The output from the iterative map–maker provides an sdf file composed of 2 parts: a signal extension and a variance extension. This variance was converted to noise for each pixel as the standard deviation of the sources within that pixel, and a signal–to–noise map was created for an initial look at detected sources within each field.

The final maps have a resolution of 2 arcsec per pixel in both bandpasses, an example of which can be seen in Fig. 4.3 with the accompanying variance map. Clearly visible is the radial dependence on sensitivity, a defining feature of the 'Daisy–scan' method. The exposure time for each pixel decreases radially as fewer bolometers provide data for each pixel. Consequently, this leads to an increase in noise at only 3 arcmin from the centre of the map of $\sim$35 per cent. This is in stark contrast to the pong maps provided for the CLS, where the noise never rises above 20 per cent, even in a 2 degree pong map. Hence why pong maps are considered better for statistical conclusions such as source counts (see Section 4.3.3 for a discussion on how the radial dependence of the noise in Daisy maps is treated in this work with regard to source counts).

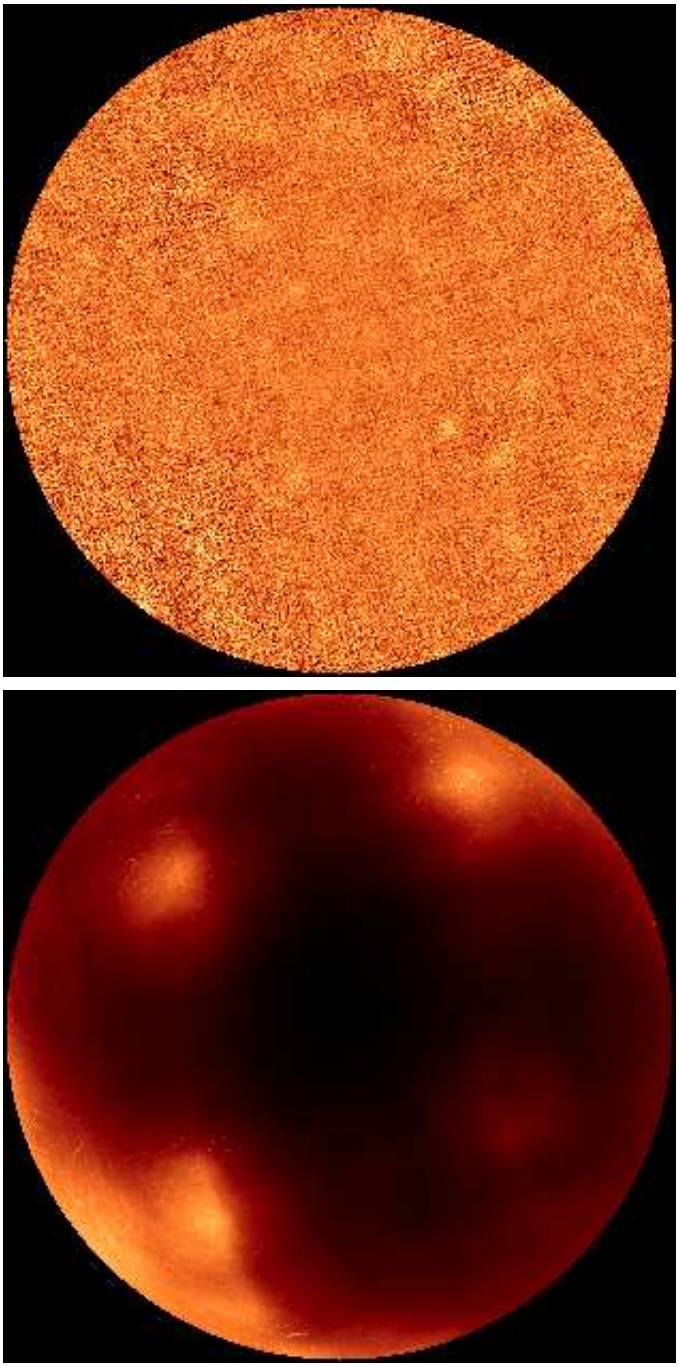

Figure 4.3: The mosaicked signal and variance maps of J030238.2+000204 at 850 μm. Some sources are already discernible at this stage in the fields, though in a few cases these also correspond with high variance and may therefore be boosted by the noise. These features can be enhanced by using a matched filter, the effect of which is visible in Fig. 4.4.

4.3.2 Source Extraction

Point sources are identified by using an estimate of the beam in each waveband to create a beam–convolved map. This map is constructed by first estimating the background on large scales by smoothing the map with a Gaussian with FWHM set to 9.8 and 14.6 arcsec at 450 and 850 μm respectively. This background is then subtracted from the original map, and the background–subtracted image is further smoothed with the effective PSF at each wavelength. This PSF has also been similarly background subtracted in the same way so as to estimate the effective shape of a point source in this background–subtracted map. An example of the final beam–convolved map for source J030238.2+000204 is presented in Fig 4.4. The maps for every field can be found in the Appendix.

To determine both the flux density and position of sources within the maps, an SNR map is firstly created by dividing the beam–convolved map by the error map. The error map is merely the standard deviation of the noise values within a pixel. An iterative search is then performed whereby the pixel in the SNR map with the largest value is found and its position recorded. The flux density estimate at that position is taken from the beam convolved flux–density map, along with the corresponding error from the error map. To then ensure that any pixels likely associated with this local maximum are removed, a Gaussian scaled to the peak flux density value is subtracted from the beam convolved map and then the SNR map is created once more. This is found to adequately remove point sources. This continues until no pixels in the SNR map are found above some user–defined value.

However, what SNR value should be chosen so as to ensure minimal contam-

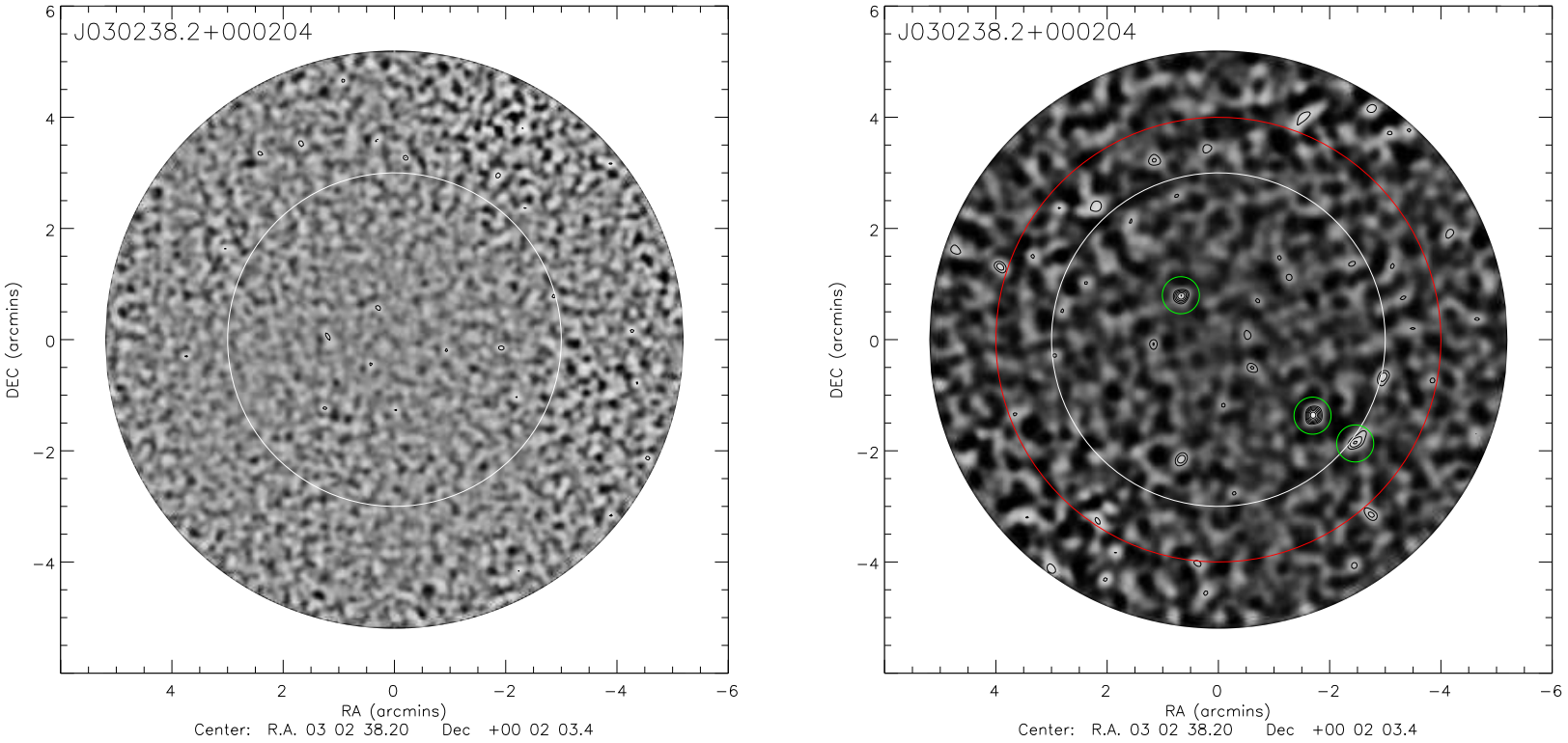

Figure 4.4: The 450 and 850 μm maps of J030238.2+000204 (left and right panels respectively). In the 850 μm map, extracted sources with SNR greater than 5 σ (green circles) have been highlighted. It appears the AGN is not significantly detected at this level (see Section 4.4.1 for further details), though there are visibly bright sources present in the environs and further out, suggesting this may not be due to a faulty reduction but a real physical phenomenon. The contours correspond to 3, 4, 5, 6, 7, 8, 10 and 12 σ levels. In white is marked the 3 arcmin 'nominal' noise region and the red circle in the 850 μm observation shows the area used to sample source counts in that field in Section 4.4.2.

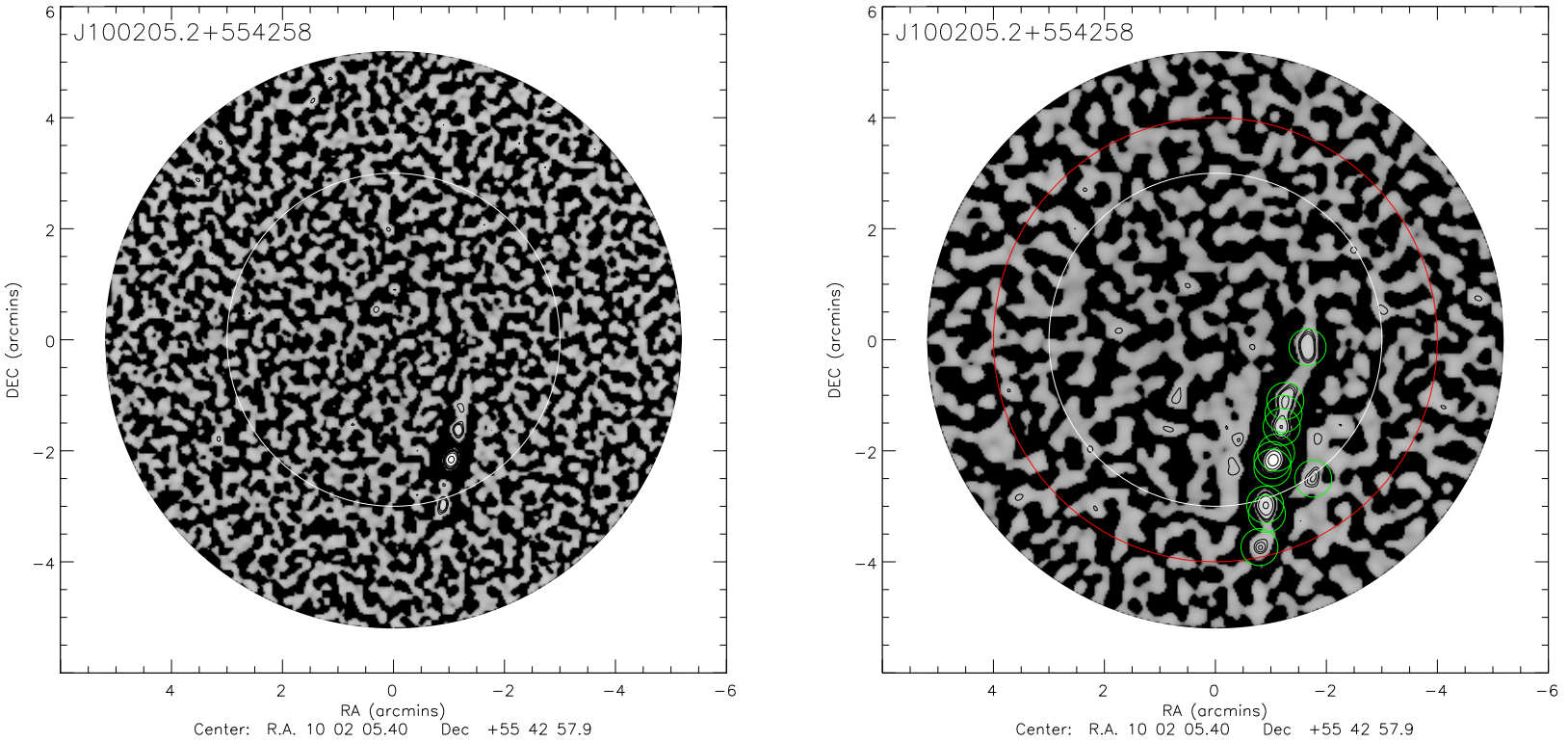

Figure 4.5: The 450 and 850 μm maps of J100205.36+554257.9 (left and right panels respectively). In the 850 μm map, extracted sources with SNR greater than 5 σ (green circles) have been highlighted. The foreground galaxy, clearly visible to the lower right of centre, extends across a significant portion of the central 3 arcmin region in both wavebands. The large flux–density of the source also leads to a high concentration of sources being found, and significant bowling features are present. Following repeated attempts to mask out the contribution from this galaxy, the field has been discarded from the source count analysis. In white is marked the 3 arcmin 'nominal' noise region and the red circle in the 850 μm observation shows the area used to sample source counts in that field in Section 4.4.2. The contours correspond to 3, 4, 5, 10, 20, 50, and 100 σ levels.

ination by spurious sources? There are two methods that can help select such a cutoff. The first of these involves creating a histogram of pixel values found within all AGN fields. Whilst there is expected to be a Gaussian distribution of pixel values arising due to noise, there will also be a characteristic positive tail which is indicative of real sources being present in the maps. A Gaussian can be fit to the negative part of the pixel distribution such that, assuming the noise is Gaussian, the contribution from spurious sources can be estimated. This is a suitable method since real sources will not emit negative flux densities so these pixel values are strictly due to noise. This method is slightly complicated by the field of J100205.36+554257.9. The presence of a foreground galaxy is visible in Fig. 4.5. This complicates the selection of an SNR cutoff, because whilst the source extraction method presented previously performs well in identifying point sources, it fares far worse for extended sources, finding multiple 'sources' in close proximity. Furthermore, owing to the strength of the emission by the foreground galaxy, several regions of the galaxy are well above even $10\,\sigma$ and introduces bowling artifacts which will only serve to broaden the Gaussian distribution and lead to an overestimation of the SNR level for all fields. Multiple attempts have been made to remedy this through the use of masking designed to deal with extended sources. However, the source is visible in individual observations making it difficult to compensate for. This field is therefore excluded from this SNR analysis and the source count analysis presented in Section 4.4.2. The sample histogram of pixel values in the remaining 16 fields is shown in Fig. 4.6, from which it appears only a SNR cutoff of 4.5–$5\,\sigma$ will be sufficient to ensure minimal contamination by spurious sources. It should be noted that due to negative bowling around bright sources, the fitted Gaussian will be slightly wider than the 'real'

noise contribution.

As a second followup method, the maps are also inverted and searched for positive peaks associated with (previously negative) sources. Unlike the previous method, there is no assumption made about the distribution of the noise. Following source extraction, it appears the stricter cutoff of $5\,\sigma$ must be used. At $4.5\,\sigma$, 6 spurious sources are found across 16 fields in comparison with 39 'real' sources. At $5\,\sigma$, this drops to only 1 source, which is directly attributable to a deep bowling feature in the map of source J122637.02+013016.0. This high SNR means that any analysis of the source counts in these fields will be sensitive to only the most extreme sources present, yet it unfortunately appears to be a necessary sacrifice to ensure the detected sources are 'real' and not due to noise.

Following this analysis and subsequent source extraction, a total of 23 sources are found across 16 fields with an SNR of $5\,\sigma$ at $850\,\mu$m. Source extraction is also performed on the several 'background' fields from the CLS mentioned before. These are necessary to determine the expected number counts whilst reducing any bias that may be introduced from cosmic variance. Setting a similar $5\,\sigma$ limit, 36, 21, and 27 sources are found for the UDS, LH, and SSA22 fields respectively. Fig. 4.7 shows the extracted fluxes and signal–to–noise ratio of sources found within the AGN fields compared with those found in the CLS fields. Also overlaid are lines corresponding to noise levels of 1, 2, and 3 mJy per beam and how this affects the derived SNR. The inclusion of the noisier edges, particularly in the case of the UDS leads to some bright but noisy sources present within the catalogues. This is addressed in Section 4.4.2.

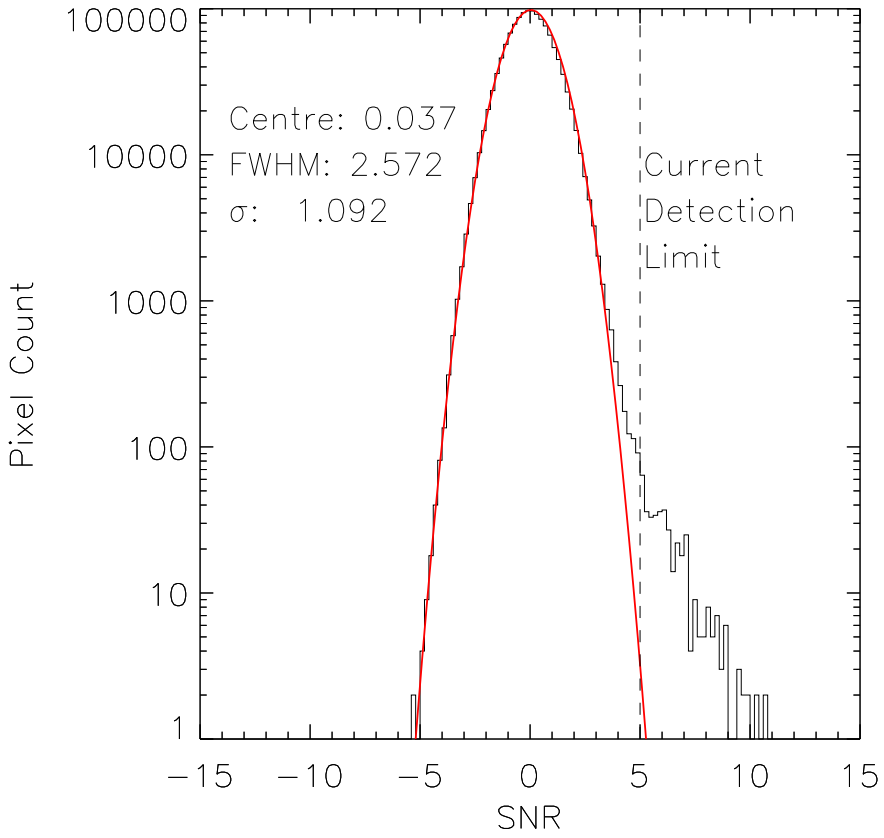

Figure 4.6: A histogram of pixel SNR values in the 850 μm maps. Clearly visible is the positive tail indicating the presence of real astronomical sources. A Gaussian (solid red line) has been fitted to the negative part of the data so as to determine what SNR is sufficient to remove likely spurious sources. However, for the sake of clarity, one should be aware that the excess of positive pixels between the Gaussian and the SNR cutoff are real sources, but a 5 σ limit will ensure the majority or all pixels are likely from real sources. Furthermore, due to negative bowling around bright sources, the Gaussian will be slightly wider than the 'real' noise contribution, so a 4.5–5 σ cutoff is likely conservative.

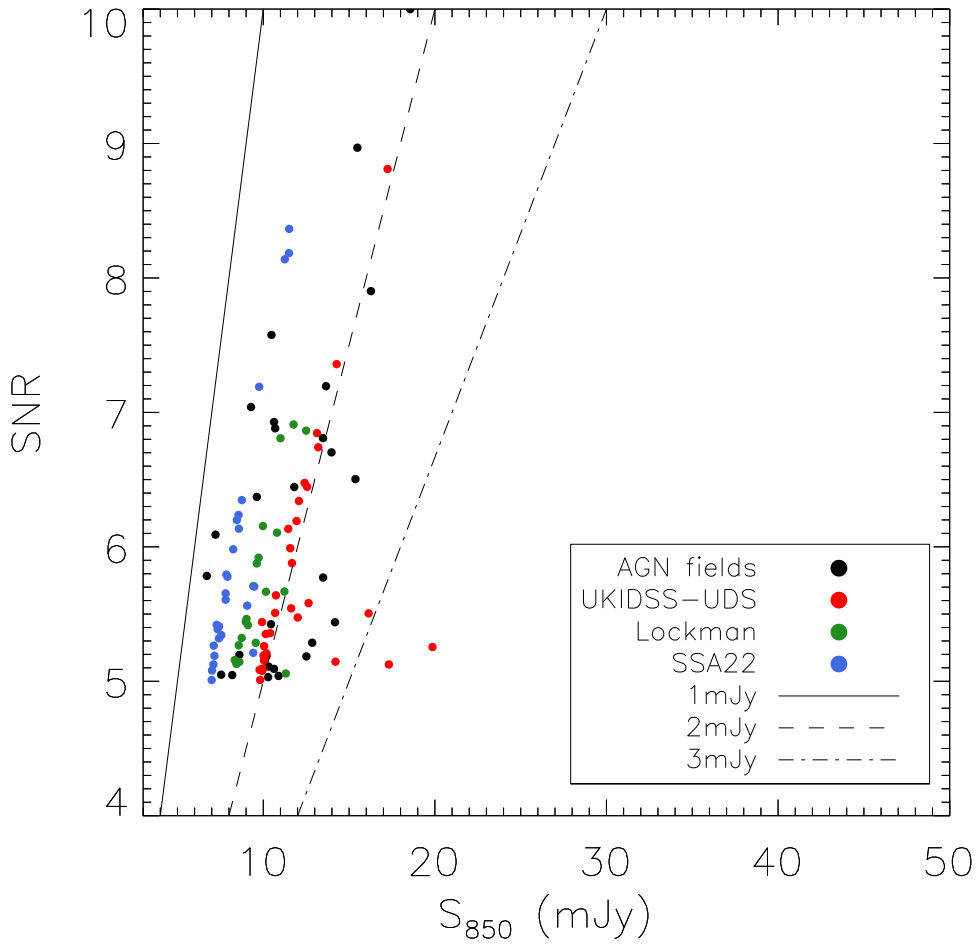

Figure 4.7: Plot showing the the flux–density/SNR distributions of the CLS and AGN fields. As visible, there is a significant overlap between the background and the observations, and a large spread in the values and noises of sources within the fields. The lines correspond to noise levels of 1, 2, and 3 mJy per beam. The inclusion of the outer, noisier edges populates the sample with some bright but noisy sources. For example, the two UDS sources with noises above 3 mJy are found at the very extremities of the map, where the noise will be highest. Not shown on this plot are 3 sources in the UDS field at 53, 55, and 129 mJy, detected at σ levels of > 15.

4.3.3 Completeness

Completeness is estimated in a similar manner to that performed in Section 3.3.3. So as to be able to investigate the noise fully in each map, a noise term had to be introduced into the treatment and determination of the completeness of each field. Due to the approximately radial dependence in sensitivity (although the noise is not entirely uniform at set radii from the centre), the completeness was created as a 2–D surface, which would allow an in-depth analysis of the effect of variations in noise across the field on source detection rate.

Sources were binned in noise, finding pixels with values in bins of width 0.1 mJy between 1 and 6.2 mJy. For those fields where there were no pixels within a certain range, the completeness was set as a NaN value to indicate no analysis was performed there. Within each noise bin, sources of varying flux density were then introduced at those pixel positions giving a total of 500 artificial sources per flux value per noise value per field. The flux density range was this time set between 4 mJy, below the SNR limit at which any source would be recovered and 25 mJy (though treatments at 50–60 mJy and 125–135 mJy were created for the UDS field due to the presence of $\sim$55 mJy and 129 mJy sources) in bins of 1 mJy. Each source had a Gaussian PSF and each was individually and randomly added within each of the AGN fields so as to avoid increasing the confusion with multiple sources. The FWHM were again set to be equal to the beam size in each band and were overlaid on the existing observations. Sources were again classified as recovered if they were within half the FWHM in each bandpass of their input position and their extracted flux density was between 0.8 and 1.2 times the flux density of the artificial source inserted. Using a SNR cutoff of $5\,\sigma$

as in the source catalogues was also a further constraint. This analysis produces a grid of completeness values for each corresponding flux/noise value, which has then been interpolated over to provide a smooth surface as visible in Fig. 4.8 for the field of J130948.57+534634.7. The effect of noise is clearly discernible, with higher noise values preventing all sources being detected, even at the highest input flux–densities.

Flux correction factors are also derived. Similarly to Chapter 3.7, the correction factor is the mean of the extracted source divided by the input flux density. This allows an estimation of the noise–dependent flux boosting when dealing with sources close to or at the SNR limit. Where there are few sources recovered, the FCF appears to be preferentially affected by the presence of sources that have had their flux densities boosted, leading to a sharp upturn in the interpolated surface, visible in Fig. 4.8. This surface can be used to de–boost the fluxes measured for each point source in each field.

4.4 Analysis

4.4.1 Detection Statistics

As visible in Table 4.4, it appears no AGN are detected at the $5\,\sigma$ level at either $450\,\mu$m or $850\,\mu$m, a surprising result when one considers that in the original sample, 50 per cent had $850\,\mu$m flux–densities above the $5\,\sigma$ level. In this sample only 2 are present at 2–$3\,\sigma$. The possibility that the maps may be incorrectly reduced has been considered, though the presence of other significantly detected sources within the maps suggest that incorrect reduction is not the cause. On

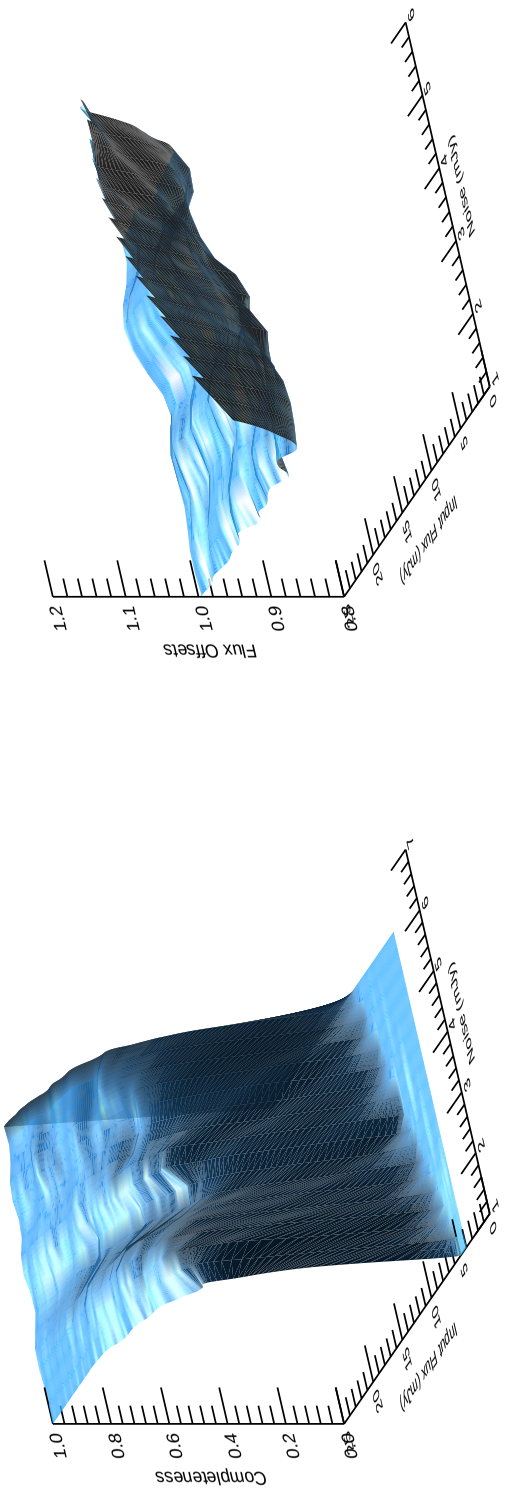

Figure 4.8: Example completeness (left) and flux correction (right) surfaces for the field of one of the observed AGN, J130948.57+534634.7. As the noise increases, the flux density at which sources begin to be recovered increases as expected. Consequently, as visible in the flux correction surface, it also causes recovered sources at lower flux densities to be skewed towards the bright end of the allowed range.

average, there appear to be ~ 1.5 $5\,\sigma$ sources within 312 arc seconds of the AGN position.

In order to be certain the AGN remain undetected, the maps are stacked on the position of the AGN themselves. Optical SDSS position coordinates are used to create a weighted mean of the pixels immediately around each AGN. The stacks presented in Fig. 4.9 include all AGN. Whilst a source is clearly visible in the optical i–band, at 450 and 850 μm no source is readily apparent. Indeed, the peak of the bright source at 850 μm is only $2\,\sigma$, hardly a strong detection. When one considers that the average flux–density for the non–absorbed QSO sample in Page et al. (2004) was ~ 0.62 mJy, it appears that the highly absorbed sources presented in this work are no different to 'ordinary' QSOs. It should be noted that the sample in Page et al. (2004) and the sample presented here will be appropriately matched in parameters such as redshift, X–ray luminosity etc, as both selections have been matched to the original absorbed QSO sample.

In the original sample it was found that almost all observed QSOs above $z > 1.5$ were detected. Whilst the AGN are not detected individually, might a restriction in redshift or a correlation test suggest a dependence on redshift? As noted before, this sample was selected in X–ray luminosity to avoid the usual redshift–luminosity correlation, so a difference or correlation would suggest an evolution in the host galaxy properties between high and low redshift sources. As with the original sample, the AGN are split into low–redshift ($z \leq 1.5$) and high–redshift ($z > 1.5$). Upon stacking, it is found that there does not appear to be any difference in the sources at low and high–redshift (see the lower panels of Fig. 4.9). What is encouraging is that stacking based on balnicity supports the conclusion arrived at in Chapter 2; there is no difference in BAL and non–

Table 4.4: The extracted flux–densities of each AGN at 450 and 850 μm. As visible, it appears only two sources are detected above $2\,\sigma$ at 850 μm. This may suggest that star formation in the host galaxies has been entirely shut off, possibly by AGN feedback.

Name	RA	DEC	450 μm			850 μm		
			Flux density (mJy)	Error (mJy)	SNR	Flux density (mJy)	Error (mJy)	SNR
J030238.1+000203	45.659	0.034	−32.20	17.30	−1.86	0.51	1.28	0.40
J083709.6+484020	129.290	48.672	−19.30	17.67	−1.09	−0.30	1.38	−0.22
J085724.0+090349	134.349	9.064	10.05	15.38	0.65	1.54	1.59	0.97
J092138.4+301546	140.410	30.263	11.80	24.96	0.47	1.14	1.76	0.65
J094021.1+033144	145.088	3.529	33.07	30.66	1.08	−1.41	1.95	−0.72
J095750.0+013352	149.458	1.565	19.74	14.99	1.32	−2.44	1.42	−1.72
J095834.7+014502	149.645	1.751	11.02	24.29	0.46	0.45	1.75	0.26
J095835.9+015200	149.649	1.866	−16.66	14.00	−1.19	1.99	1.49	1.33
J095944.4+051157	149.935	5.199	16.03	15.10	1.06	2.44	1.38	1.77
J100205.2+554258	150.522	55.716	−18.08	22.19	−0.80	−1.66	1.55	−1.07
J100341.2+050531	150.922	5.092	−9.51	32.76	−0.29	−0.76	2.62	−0.29
J103301.5+583749	158.256	58.630	0.93	21.79	0.04	3.28	1.46	2.25
J105201.3+441417	163.006	44.239	−2.01	18.93	−0.11	2.12	1.56	1.35
J120522.1+443141	181.342	44.528	12.63	24.69	0.51	1.52	1.33	1.14
J122636.9+013016	186.654	1.504	7.34	23.57	0.31	1.30	1.57	0.83
J130948.4+534634	197.452	53.776	−8.46	11.03	−0.77	2.99	1.03	2.91
J144625.6+025549	221.606	2.930	13.00	12.96	1.00	−1.21	1.28	−0.95

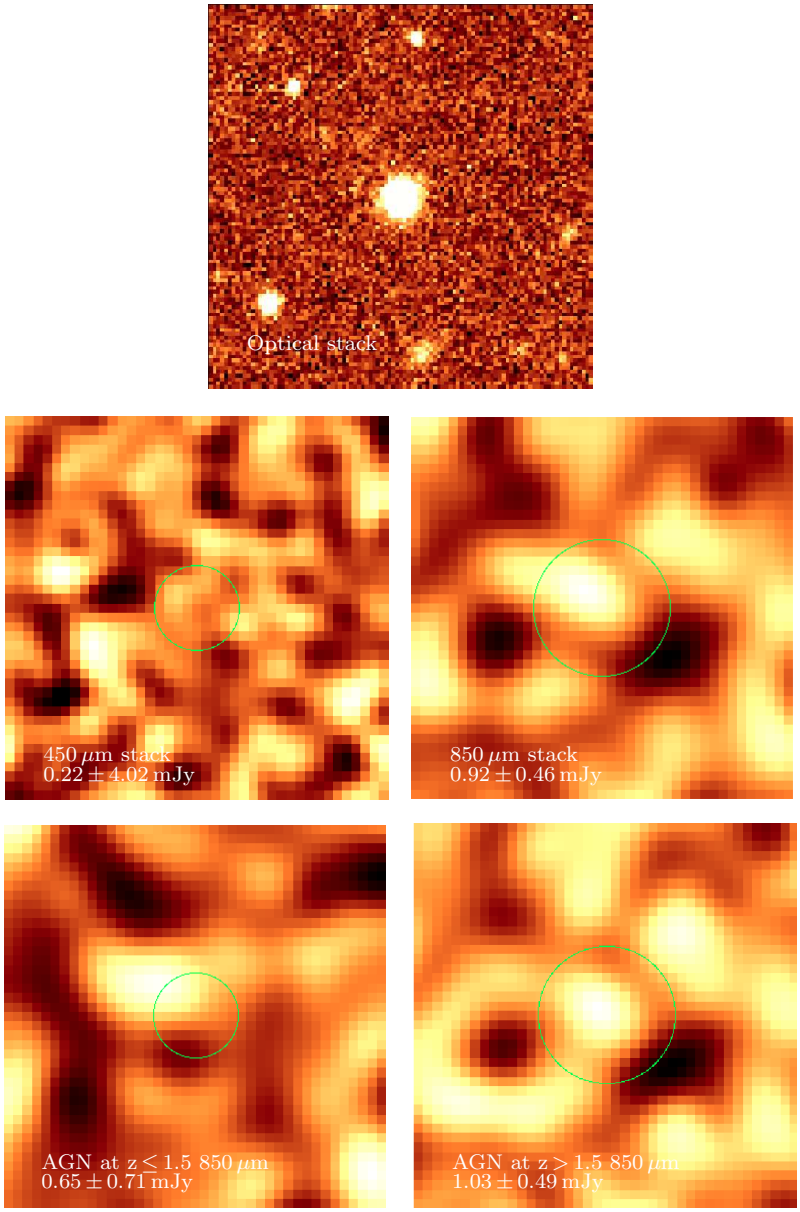

Figure 4.9: The weighted mean images in optical (top), 450 (middle left), and 850 μm (middle right) for all AGN. The bottom row are the 850 μm stacks for sources at $z \leq 1.5$ (bottom left) and $z > 1.5$ (bottom right). Clearly visible in optical, at 450 and 850 μm it appears there is very little emission from the absorbed sources in the sample, an intriguing result. This suggests star formation is either already at a very low level in these systems, below the sensitivity of SCUBA–2, or is entirely turned off. The green circle shows the beamsize at each wavelength.

Table 4.5: The weighted mean flux–densities of the SCUBA–2 stacks presented in Fig. 4.9. From this method it appears there is no real difference between various sub–samples, with all sources having similar flux–densities.

Subsample	Sources Used N	Flux–density (mJy)
$450\,\mu$m	17	0.22 ± 4.02
$850\,\mu$m	17	0.92 ± 0.46
$z \leq 1.5$	5	0.65 ± 0.71
$z > 1.5$	12	1.03 ± 0.49
BALQSOs	9	0.62 ± 0.67
non–BAL QSOs	8	1.25 ± 0.63

BAL QSOs. Table 4.5 presents the numerical values of the central pixels in the SCUBA–2 stacks of Fig. 4.9, as well as the weighted mean flux of BALs and non–BALs in the sample.

As a final series of tests, the flux–densities at $850\,\mu$m are tested for a correlation with absorption column density, X–ray luminosity, and redshift. Fig. 4.10 shows these quantities plotted against each other. There does not appear to be any strong correlation. However, to be sure, a Generalised Kendall Tau test is applied to the sample. A Spearman Rank test will be unreliable for samples smaller than 20–30 data points. In each case, they return no evidence of a correlation, with the lowest p–value being that between absorption column density and $850\,\mu$m flux–density at 0.12.

4.4.2 Source Counts

Following the derived completeness correction and flux correction factors, a preliminary estimate of the number of sources as a function of flux–density can be deduced. There are two methods that can be used here; differential source counts and integral source counts. Differential counts have the advantage that they do

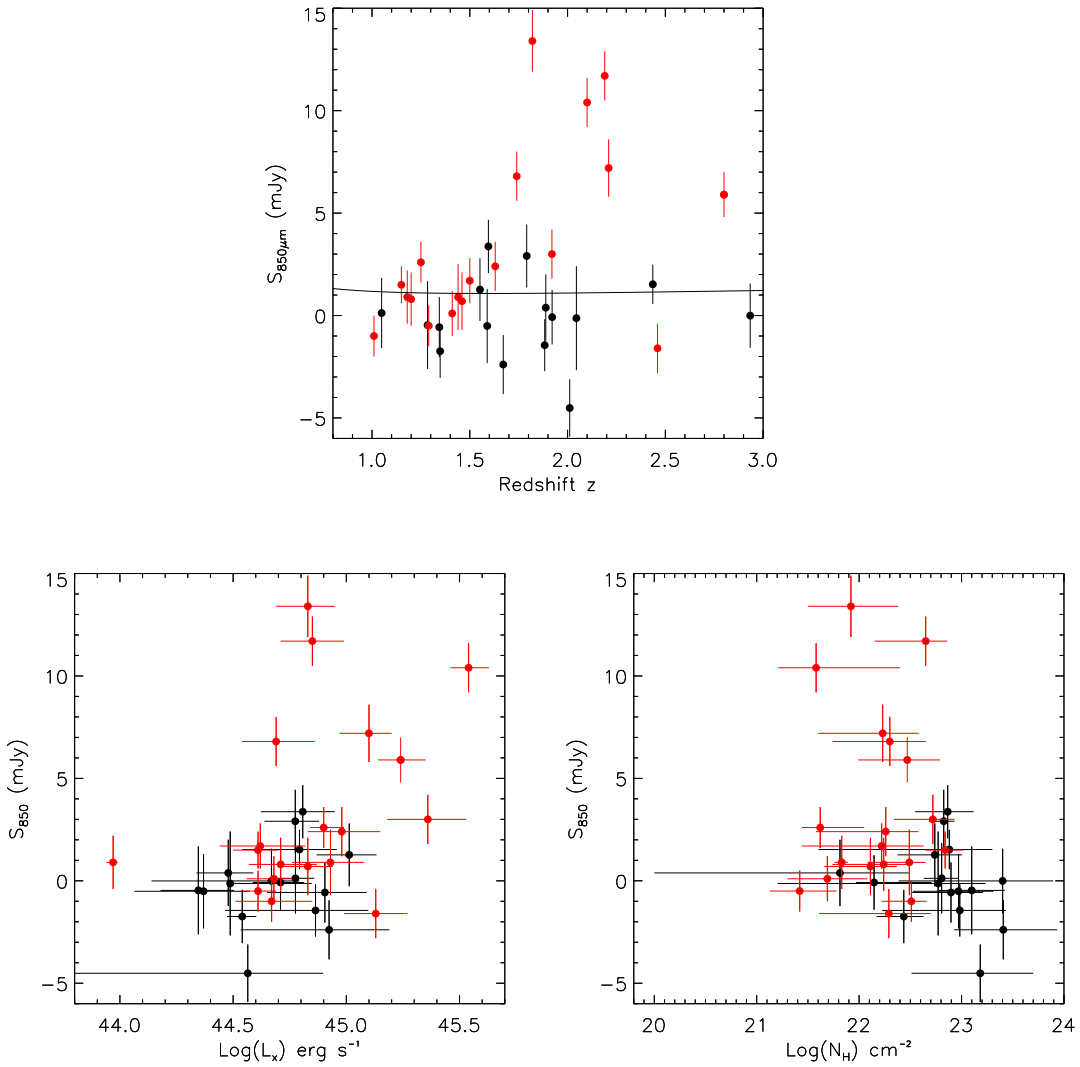

Figure 4.10: AGN 850 μm flux–density at the position of the AGN against redshift, X–ray luminosity, and absorption column density. One of the error bars has been cut in the plot for X–ray luminosity; this is because it extends to 42.8 and its inclusion prevents the rest of the sample being appropriately spaced. It appears there are no correlations with these parameters in the AGN sample presented in this work (black circles). For comparison, the original X–ray absorbed QSO sample as presented in Stevens et al. (2005) is also shown here in red which showed evidence for evolution across cosmic time. The solid black line in the upper panel is the expected 850 μm flux–density of the X–ray absorbed LoBAL QSO Mrk 231 over the redshift range of the sample.

not depend on the counts at higher flux densities, thereby reducing the degree to which they are correlated. However, they also have the drawback that a large number of sources must be sampled, otherwise bins will be underpopulated and a large degree of scatter will be introduced. So as to be able to compare to previous works and avoid the problem of small number counts, the differential counts have been integrated to estimate the cumulative source distribution.

Another concern is at what distance from the central AGN, or indeed what area, should be used in this analysis. As previously mentioned, Best et al. (2003) find that overdensities around AGN extend as far as 1.6 Mpc. The 'nominal' noise region in the AGN maps correspond to $\sim$1.4 Mpc at the redshift of the AGN observed. However, restricting the analysis to only a 3 arcmin radius removes almost half the $5\,\sigma$ sources in the AGN fields, leaving only 14 out of 23. Using a 4 arcmin region corresponding to a co–moving radius of $\sim$1.9 Mpc avoids using the noisiest parts of the field and ensures almost all (22 of 23) sources remain within the catalogue. Therefore, arguably it is best to restrict the sampling to this region if an overdensity is expected around AGN. Restricting the sampling in the CLS fields to the uniform part of each field and avoiding the noisy ring around the edge will also mean the noisiest sources are excluded, whilst still ensuring a sufficiently large sampled area to avoid cosmic variance. With this reasoning in mind, the total area surveyed by the AGN fields in this work is 804 arcmin^2 or 0.223 degrees^2. This is in comparison to the total area for the 3 CLS fields surveyed of 4572 arcmin^2 or 1.270 degrees^2.

The integrated counts for the AGN and CLS fields in Table 4.6 have been compared to previous works taken over the past decade with SCUBA and LABOCA (Borys et al. 2003; Coppin et al. 2006; Scott, Dunlop & Serjeant 2006; Knudsen,

Table 4.6: The derived differential and integrated source counts in bins of 2mJy beginning at 6mJy for the AGN fields and the CLS, rounded to the nearest integer value. The integrated count remains at 1 at 20 mJy for the CLS as there is still a source at 53 mJy. The errors are the Poisson error on the count scaled by the completeness correction added in quadrature for each field.

Flux Density	Differential Count dN/dS (mJy^{-1}) deg^{-2}		Integrated Count N(>S) (deg^{-2})	
(mJy)	AGN	CLS	AGN	CLS
6.0	62 ± 28	59 ± 14	204 ± 48	171 ± 17
8.0	41 ± 23	72 ± 15	143 ± 39	99 ± 13
10.0	67 ± 28	21 ± 5	102 ± 31	26 ± 6
12.0	24 ± 12	5 ± 2	35 ± 14	9 ± 4
14.0	5 ± 5	2 ± 1	11 ± 8	4 ± 3
16.0	6 ± 6	1 ± 1	6 ± 6	1 ± 2
18.0	-	-	-	1 ± 1
20.0	-	-	-	1 ± 1

van der Werf & Kneib 2008; Beelen et al. 2008; Weiß et al. 2009; Stevens et al. 2010).

As visible in Fig. 4.11, there is a large degree of scatter between various source counts when compared to those derived in this work. A Schechter function (Schechter, 1976) has been fitted to the CLS data. This has the benefit of being physically motivated, in that at high luminosities very few galaxies are found (an exponential truncation), whilst at low luminosities the distribution behaves more as a power law. This work uses the same Schechter function as that in Coppin et al. (2006):

$$\frac{dN}{dS} = \frac{N'}{S'} S \left(\frac{S}{S'}\right)^{\alpha} exp\left(\frac{-S}{S'}\right) \tag{4.1}$$

It has fitted parameters of $S' = 10$ mJy, $N' = 30^{+7.30}_{-7.29}\,deg^{-2}$, $\alpha = -3.89^{+0.52}_{-0.58}$. At the bright end, the data sits well within the errors of all of the work, whilst at

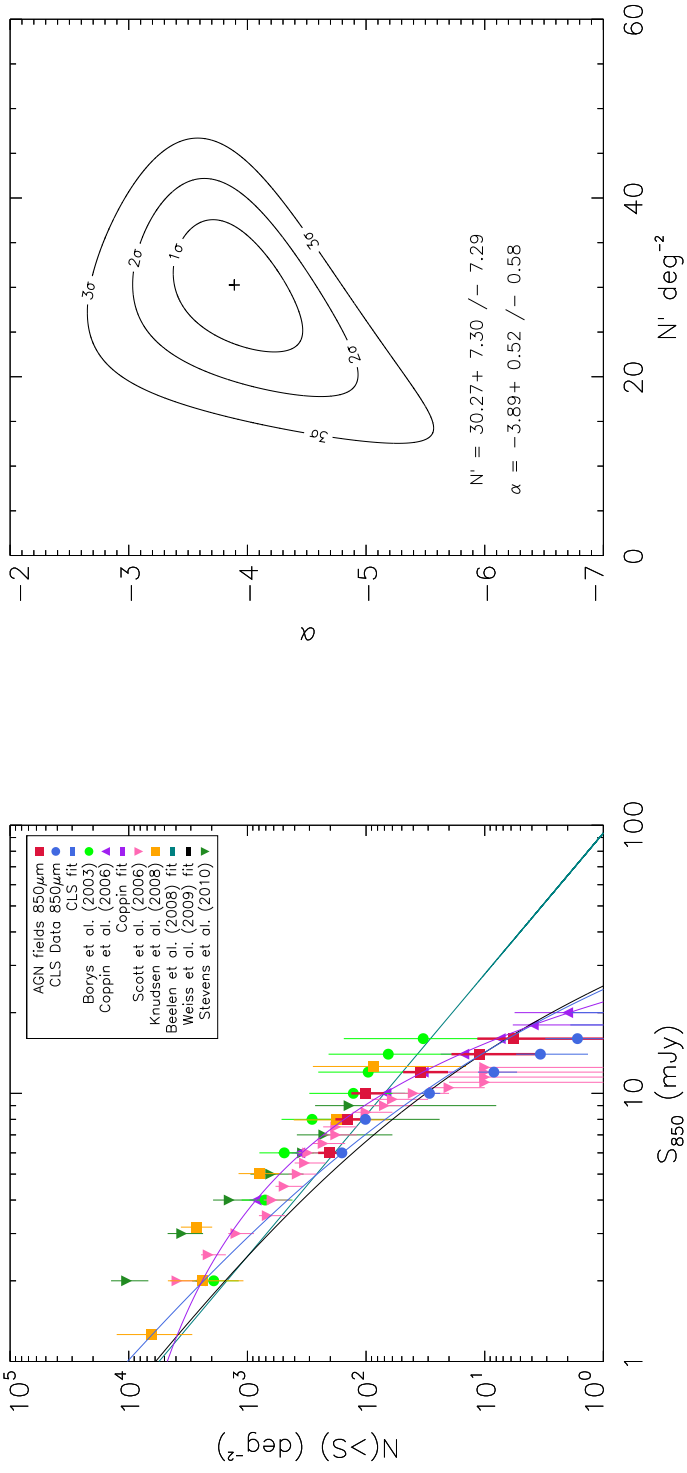

Figure 4.11: The derived integrated number counts are visible in the left panel. The results from previous authors are included for comparison with the source counts derived in this work. In this study, it is found a Schechter function (CLS fit, blue) is a suitable fit to the number counts, but in previous investigations (e.g. Beelen et al. 2008), power laws have also been used. As is clearly visible, an overdensity is discernible around AGN fields when compared with the blank fields of the CLS, though it is of a lower magnitude than that found by Stevens et al. (2010) when compared with Coppin et al. (2006). The error bars are the Poisson errors of the AGN counts/CLS counts, with each field added in quadrature, corrected for completeness. In the right hand panel, the contour plot shows the range of error on N' and α for the fit to the CLS data used in this work.

the faint end it appears to agree well with Borys et al. (2003) and Weiß et al. (2009). Of course, in relation to previous works, it appears there is no overdensity visible around AGN if, for example, data by Scott, Dunlop & Serjeant (2006) are used. However, caution is urged as these previous results will be highly prone to varying completeness corrections, sensitivities and flux–density cutoffs (which can be somewhat arbitrary). Therefore the CLS data remains the best comparison data set, having been reduced in an identical manner. Whilst an attempt to fit a Schechter function to the AGN data was also performed, the large degree of scatter on individual bins in the differential data led to a sharp turnover and a prediction of far lower source counts than what has been observed by various works. With the low number counts and relatively large errors, it is likely that this would provide an erroneous prediction and indeed is in contrast to previous studies around AGN (e.g. De Breuck et al. 2004; Stevens et al. 2004; Venemans et al. 2007; Stevens et al. 2010; Rigby et al. 2014).

From Fig. 4.11, it is clearly visible that whilst the overdensity around this sample of X–ray absorbed QSOs is not as large as that observed by Stevens et al. (2010), there appears to be a small overdensity relative to a blank–field in certain bins. This difference appears greatest close to the break in the luminosity function, but weakens as fainter fluxes are included in the integrated count. The large variation on the completeness correction will dominate the number count in the faintest bin, which, in conjunction with small number counts and cosmic variance to which the AGN fields will be more susceptible, is likely responsible for the weakened difference between AGN and CLS fields.

The effect of varying area is a strong factor on the final counts in the AGN fields. Lowering the area surveyed to a 3 arcmin radius around each AGN leads to

a boost of almost 50 sources with flux–densities greater than 6 mJy, an addition of almost 25 per cent to the counts found using a 4 arcmin area. Conversely, an increase in sampled area to the full 5 arc minute region leads to a drop in source counts within the same bin of around 37 per cent. Therefore, the effect of area cannot be underestimated when it is considered that the boosting using 3 arcmin occurs after almost half the 'real' sources are removed. This is a prime example of the effect the completeness correction, combined with area, is having on the final count. However, regardless of area, the counts remain within the error bars of previous studies.

4.4.3 FIR Luminosities and SFRs

The final question that can be asked for now of these companion sources then regards their properties; how active are they? To do so, the SEDs of various galaxy analogues have been fitted in a manner akin to that in Chapter 2, to get an idea of the possible upper and possible limits. There is again limited information on the shape of the SED of the companion sources within the AGN fields, and therefore suitable templates must be chosen in order to compute FIR luminosities ($L_{\rm FIR}$). Mrk 231 and IZw1 have already had templates produced, but a third, Arp 220 can also be added. As with Mrk 231, it is a ULIRG. However, it differs from Mrk 231 in that the 'galaxy' is actually an ongoing collision producing an extreme starburst environment. This may perhaps be a more reasonable assumption for the host properties of the SMGs present within the AGN fields (Dekel et al. 2009) than Mrk 231, which has a significant AGN component in its SED (as noted previously, up to 70 per cent of its bolometric

luminosity may rely on the AGN). It is also a highly obscured galaxy, and may therefore be analogous to the sources studied in this chapter.

As before, to determine the luminosity of each source, a modified black body model as discussed in Hildebrand (1983) is fitted to FIR data points retrieved from the NASA Extragalactic Database. The data points are constrained so as to exclude a contribution from AGN heated dust emission (see Figure 4.12), for which, in the case of Arp 220, there are two active black holes (Graham et al., 1990). An FIR luminosity of $\log(L_{\rm FIR}/L_{\odot}) = 12.07 \pm 0.11$ is derived, which is equivalent to a SFR of $209 \pm 1\,{\rm M}_{\odot}\,{\rm yr}^{-1}$. This suggests that if the detected sources are analogues of Arp 220, they have SFRs in the range 588–$2010\,{\rm M}_{\odot}\,{\rm yr}^{-1}$ (for a flux–density range between 6–18 mJy). Similarly, using Mrk 231 and IZw1 as analogues suggests these sources will have SFRs in the range 765–$4624\,{\rm M}_{\odot}\,{\rm yr}^{-1}$ (this upper limit assumes an 18 mJy source at $z = 3$). This is more than sufficient to assemble the bulge of a large galaxy within a few hundred million years, suggesting these sources are the progenitors of modern day ellipticals, as previously argued by various authors (e.g. Blain et al. 2002). In contrast, applying the same templates to the central AGN, the values are far smaller, between ~ 10 and $1100\,{\rm M}_{\odot}\,{\rm yr}^{-1}$ over the redshift range of the AGN studied. This would suggest the sources in the environment and the AGN themselves have very different host galaxy properties, possibly as a direct consequence of an outflowing wind. The implications of this are discussed further in the next section.

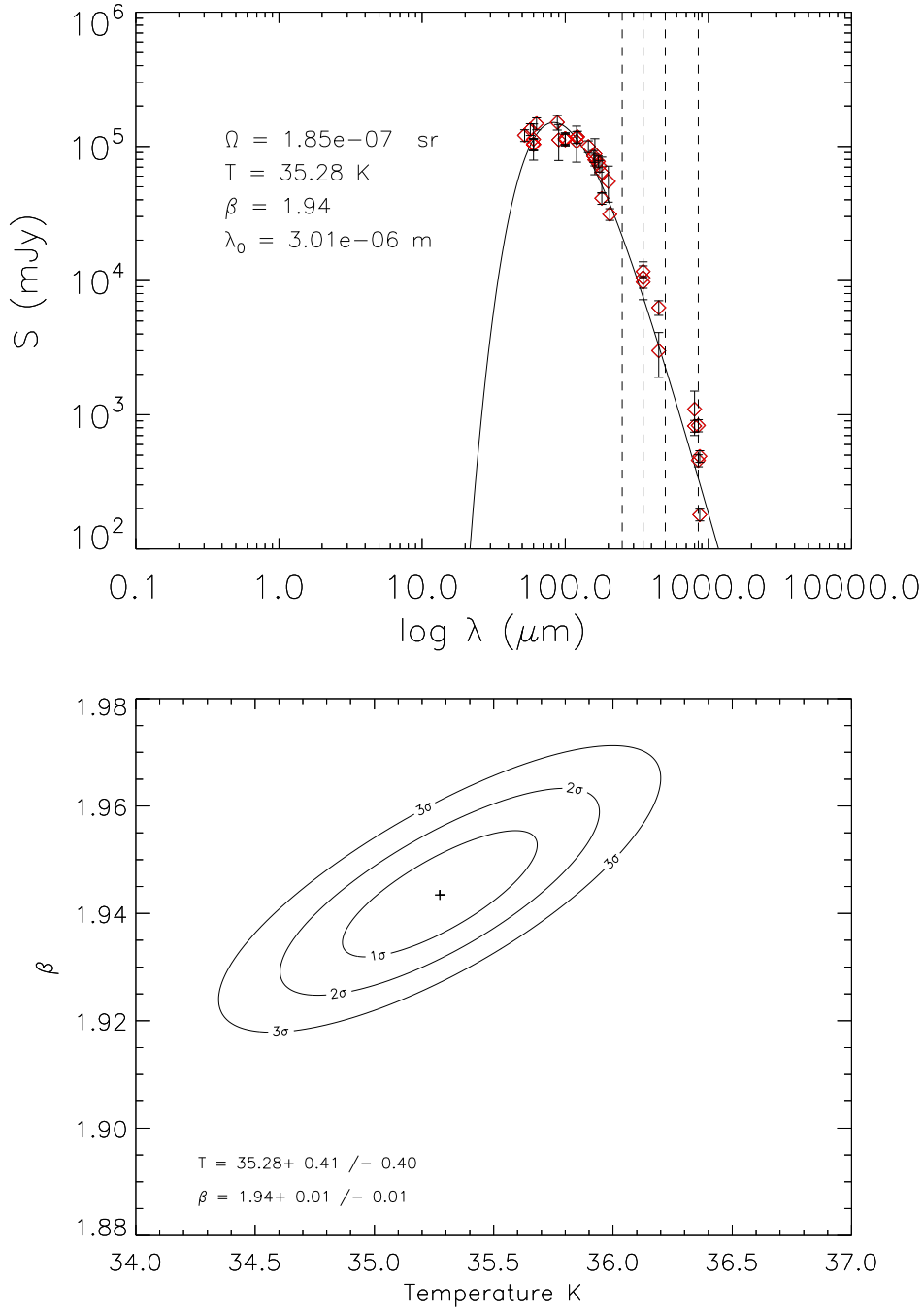

Figure 4.12: The fitted modified black body template for Arp 220 as well as the derived errors on β and temperature. The dashed lines in the SED plot show where the 250, 350, 500, and 850 μm wavebands fall on the SED.

4.5 Discussion

The results in this Chapter suggest that X–ray–absorbed QSOs with $6.5 \times 10^{21} \leq N_H \leq 2.6 \times 10^{23}$ have very little (relative to SMGs at these epochs) or no star formation ongoing in their host galaxies and that they are similar to unabsorbed QSOs at the same cosmic epoch. The lack of detections is by no means an indicator of a low SFR; the predicted flux–density of Mrk 231 in Fig. 4.10 indicates that even a submillimeter luminous ULIRG will be barely above the confusion noise. However, these findings are still in stark contrast to the those found by Page et al. (2004) and Stevens et al. (2005, 2010).

It is possible these results may be an unforeseen consequence of the sample selection. Over half (9) of the observed sources presented in this new absorbed sample are BAL QSOs. A further 3 may yet be BALs, but their low redshifts (below $z < 1.5$) prevent an identification of the C IV line ($\lambda\,1550$ Å) if it is present. The results in Chapter 2 would then suggest they would have similar flux–densities as a non–BAL QSO population. If the unabsorbed sample are all non–BALs it is perhaps unsurprising that they are a similarly undetected population. In contrast, the original sample contains only 1 known BAL QSO (RX J124913.86–055906.2), yet the subsample studied in Page et al. (2011) all show evidence of outflows of varying velocities. A sample of FeLoBALs currently being investigated (Vestialbuio et al., in prep) also appear to have very low flux–densities, similar to the sample presented here and consistent with the hypothesis that the observed properties of BAL QSOs are an orientation effect. That sample is composed of 15 sources and suggests that FeLoBAL QSOs are not caught in a separate evolutionary phase, in contrast to the claims of Farrah et al. (2012) from which 5 of the

sources are taken. One can then attempt to join these separate types together within a galaxy evolution scenario.

Firstly, if X–ray absorbed sources are indeed evidence of a separate evolutionary phase (part of the 'quasar mode'), it is feasible that star formation has been suppressed by massive outflows of material from the central AGN in the plane of the host galaxy. Recent work by Page et al. (2012) suggests AGN with X–ray luminosities above $10^{44}\,\mathrm{erg\,s^{-1}}$ will have had their star formation suppressed. In that work, 176 AGN were selected from the Chandra Deep Field–North (CDF–N) over the redshift range $1 < z < 3$. These sources were then observed with data from *Herschel* at $250\,\mu$m. Intriguingly, 25 per cent of sources were detected when their X–ray luminosities were in the range $10^{43} \leq \mathrm{L}_X \leq 10^{44}\,\mathrm{erg\,s^{-1}}$. Upon selecting only those with X–ray luminosities above $10^{44}\,\mathrm{erg\,s^{-1}}$, no AGN were associated with $250\,\mu$m sources. With regards to the sample studied here, every AGN is above this latter cutoff. It may be that this absorbed sample has undergone very rapid evolution due to a massive outflow (hence the significant increase in absorption column density relative to the original sample), placing these sources already at a point just after the fuel for star formation has been blown away to produce an optically visible QSO, hence the lack of detections. Indeed, Page et al. (2011) find that the X–ray absorption in the original X–ray–absorbed sample is likely due to ionised, QSO–driven winds and furthermore, they suggest that these absorbed QSOs will have large mass outflow rates. This would then lead to the observed properties of BAL QSOs being dependent on an orientation effect where the BAL wind might still be visible in a reduced fraction of sources, yet the effect has already been felt in the host galaxy. It also does not preclude the possibility that unabsorbed or non–BAL QSOs at these redshifts have already undergone

this rapid evolution and no longer show the same X–ray–absorption, but only if all QSOs have an absorbed QSO phase. This would explain the similarity between BAL and non–BAL QSOs. Whilst this may be a valid interpretation, it should be pointed out that a similar study conducted by Harrison et al (2012) using a larger sample of 730 AGN across three separate fields found there was no clear evidence for a suppression effect based on X–ray luminosity, with contradictory results depending on the field studied. However, as noted in that work, whether a change is observed in the mean SFR will depend on the relative timescales of the luminous AGN phase and the star formation truncation process. If they are similar in length, detecting a change will be difficult, unless the sample is selected in order to represent a specific evolutionary phase.

A second possibility is that the AGN studied here are already post–starburst galaxies at this redshift. This scenario differs slightly from above in that the central AGN has prevented material from falling onto the host galaxy through the effect of the 'radio mode', and therefore the available gas in the galaxy has been exhausted with strong evolution. It is already known that the most massive galaxies evolve far more rapidly than intermediate and low mass hosts, with their prime star formation epoch being at higher redshifts (Heavens et al. 2004). This would explain the high absorption column densities, as the AGN has as yet been unable to blow away all of the enshrouding gas and dust left over from rampant star formation. Indeed, these sources may be caught before the switch from the 'radio mode' to the 'quasar mode'. However, this explanation is physically unacceptable. Firstly, it would require in each case that the observations have been made coincidentally at a point in the evolution of the galaxy when all the fuel for star formation has been disrupted in presumably multiple nurseries within

the galaxy, rather than having some other effect effectively remove the gas. This is difficult to reconcile when one considers that these sources will likely have a variety of masses and therefore differing host galaxy compositions. Secondly, and most importantly, it would require that the duty cycles of AGN are significantly longer than the starburst lifetime. This is known to not be the case. For example, Bird, Martin & Kaiser (2008) find a lifetime on the order of $\sim 1.5 \times 10^7$ yr for FRII AGN yet Tacconi et al. (2008) argue that the SMG phase may last as little as 100 Myr.

Finally, the lack of detections may be as simple as the host galaxies of these AGN having warmer dust temperatures against which submm surveys are biased. Recent work using PACS and SPIRE studies that sample the peak of the SED in sources at $z \leq 4$ indicate that ground–based observations of SMG samples suffer strongly from dust temperature selection effects (Magnelli et al. 2012; Swinbank et al. 2014). Indeed, an object must be cold to be detected by ground–based submm telescopes (this effect is visible in Fig. 4.1). *Herschel* also confirmed that 'optically faint radio galaxies', which are undetected in submm surveys, have strong radio emission, a sign suggestive of strong star formation with warmer dust temperatures (Magnelli et al. 2010). It is therefore feasible that the sample might have still have relatively strong star formation, yet are not detected. Observations at shorter wavelengths would be invaluable in determining whether this sample suffers from the same problem, and radio observations might settle whether star formation is ongoing. If nothing else, these observations provide upper limits on the cold dust emission of these absorbed sources.

Regarding the source counts around the studied AGN, it appears that based on detected sources, the environments of AGN are more dense than the blank–field

background. Of course, the study is limited to bright sources yet the difference is noticeable. Somewhat frustratingly, the large degree of scatter on the differential counts around the AGN, likely a consequence of small number counts and cosmic variance prevents a suitable fit being applied to extrapolate to fainter sources. This scatter likely explains why the integrated fit is better for the CLS, which has a higher number count and will be less susceptible to cosmic variance due to sampling a larger area. Indeed, for source counts, it is suggested that a pong map such as the ones used by the CLS are used instead. Pong maps never go above a 20 per cent difference in the noise relative to the centre of the map, whereas with the AGN maps, the noise can increase by as much as 35 per cent. The likelihood here is that, since the completeness correction and choice of area become dominant factors in the determination of source counts towards low flux–densities, this leads to the uncertainty preventing the fit from producing an accurate trend. In comparison to previous works, it must be noted that there will have been varying flux cuts and different areas used. This explains the large degree of scatter on the data points. In the case of the AGN fields, it appears they are within the error bars of previous studies, yet the CLS fields appear to be somewhat less dense than, for example, the fields studied by Coppin et al. (2006). On the other hand, it is relatively in keeping with the fit derived by Weiß et al. (2009), and a fitted Schechter function passes through previous data points until around the 1 mJy mark.

Finally, in regards to the nature of these sources, submm galaxies have already previously been associated with the elliptical galaxies seen today (e.g. Blain et al. 2002). As determined in that work, any SCUBA galaxy with a flux ≥ 5 mJy will have a derived luminosity greater than $10^{12}\,L_{\odot}$. This is the most reasonable

assumption, as elliptical galaxies will require a significant period of time in which the galaxy undergoes star formation on the order of $1000\,\mathrm{M}_{\odot}\,\mathrm{yr}^{-1}$ for around 1 Gyr. When one considers the derived SFRs using the templates in this chapter, it is easy to conclude that this is the case. Indeed the selected SNR cutoff makes this analysis sensitive to only the most extreme sources at their respective epochs.

4.6 Conclusions

An analysis of 17 highly absorbed QSOs has been conducted using SCUBA–2 data to determine their properties and for 16 of these, the properties of sources within their fields and whether these AGN sit in overdense regions of the universe. The results of this analysis are as follows:

1. None of the AGN are detected at $850\,\mu$m at an rms of ~ 1.5 mJy. This is in contrast to a previous sample studied by Page et al. (2004) at similar rms in which half were detected at $5\,\sigma$. Following a stacking procedure, no strong source is readily apparent (0.92 ± 0.46 mJy). Upon calculating SFRs using a variety of templates, even the most powerful source has a SFR of $1088 \pm 494\,\mathrm{M}_{\odot}\,\mathrm{yr}^{-1}$. This suggests that star formation in the host galaxies of these AGN has been either significantly weakened or entirely shut down.

2. The AGN appear to reside in overdensities of bright sources when the integrated counts at $5\,\sigma$ are considered, particularly around the break in the luminosity function. A Schechter function is fit to the CLS data which generally agrees well with observed blank field counts by previous authors. The overdensity around AGN is far more marginal however than that discovered

by Stevens et al. (2010), particularly at the faint end. This is likely a result of small number counts as well as cosmic variance.

3. The SFRs of the detected sources in the fields of the observed AGN using 3 differing template galaxies predict maximum SFRs of $\sim 4624\,M_{\odot}\,yr^{-1}$, far in excess of what might be seen in the current epoch. These sources are likely the progenitors of modern day elliptical galaxies as suggested by others (e.g. Blain et al. 2002), and will evolve to become some of the most massive galaxies at their epoch.

As discussed in Section 4.5, it may be that the sources studied here have had their star formation suppressed, possibly at an earlier stage in the galaxy's evolution. From recent work by Page et al. (2012), sources with X–ray luminosities above $10^{44}\,erg\,s^{-1}$ all appear to have their star formation suppressed, which is linked to the intense activity of the central black hole. The derived SFRs for the AGN using various templates are far smaller than the range of SFRs determined for the surrounding SMGs (1088 cf. $4624\,M_{\odot}\,yr^{-1}$ assuming a Mrk 231 analogue placed at the redshift of the source). Considering that all of the sources studied here are above this luminosity cutoff, it could be argued a similar process has impacted upon the host galaxy of these AGN. The high incidence of BAL QSOs within the sample supports the claim by Page et al. (2011) that 'shielding gas', a key component of the BAL wind model, is responsible for the absorption column density. BAL QSOs and absorbed QSOs can then be joined together in a slightly more complex view of the BAL phenomenon than is generally considered. One may join the evolution and orientation scenarios of BAL QSOs and absorbed QSOs together, as considering the work of Choi et al (2012), one is loath to en-

tirely disregard the effect a BAL wind may have on the host galaxy. For example, a BAL wind may influence the host galaxy over time (which would explain the findings by Page et al. 2004 and the sources studied here). If black hole growth and bulge growth are fed by the same reservoir, it is possible that the 'shielding gas' and BAL wind will still be visible as the AGN processes the material already in its environs, long after the galaxy has ceased to be enshrouded by gas and dust, but their detection will be more reliable on orientation (if for example the covering factor diminishes over time owing to less material). This would then adequately explain the similarities between the absorbed and unabsorbed QSOs, as well as BAL and non–BAL QSOs. If a BAL classification is reliant on orientation, non–BAL QSOs may still have a wind present, or be in a phase so long after the BAL phase that they are unabsorbed, i.e. the 'shielding gas' has been exhausted and material in the environs of the black hole is no more. The end observable result would be the same however; galaxies in which star formation has been suppressed and show minimal output in the submm, the only difference being whether a BAL wind is still present and acting far less effectively on a galaxy already deprived of material.

Chapter 5

Conclusions and Further Work

5.1 Summary of Main Results

This thesis is composed of work performed over the past 3.5 years investigating the effect of AGN on both their host galaxies and their environments with a view to further understanding how the presence of an AGN affects the evolution of its surroundings or indeed vice versa. To do so, multi–wavelength studies have been conducted in the FIR using data from both *Herschel* and SCUBA–2 to observe statistically significant numbers of galaxies at a variety of redshifts ($1 < z < 3$).

In Chapter 2, the host galaxies of a sample of BAL quasars have been studied to determine whether BALs could be the 'smoking gun' evidence of AGN feedback. Using observations performed by *Herschel* with the SPIRE instrument at 250, 350 and 500 μm, the largest sample to date of HiBAL QSOs has been assembled to provide a statistical basis for searching whether HiBALs are in a separate evolutionary phase to ordinary QSos. Rather than restrict the analysis to only one classification method, both the 'classic' BI and 'extended' BI_0 version used by Gibson et al. (2009) have been used to create large samples of comparison BAL QSOs in case of the BI_0 being too lenient and allowing the possible entry of

non–BAL QSOs into the sample. A comparison matched sample of 329 non–BAL QSOs has then been selected against which to compare the FIR flux–densities. These samples have been matched in both redshift and magnitude using derived redshifts and magnitudes from SDSS photometry and spectroscopy providing 50 BAL QSOs (36 of which are 'classic' defined BALs, of which one is a LoBAL QSO). Using two stacking methods, it is found that HiBAL and non–BAL QSOs appear to have similar emission across all 3 observed SPIRE bands, regardless of classification method (see Table 2.3 for the numerical values). However, due to a concern that the noise in the H–ATLAS fields might not be Gaussian and therefore the derived errors on the stacks are not truly representative, boostrap methods have been used in conjunction with KS tests to determine whether the distribution of our BAL and non–BAL QSOs are significantly different from a randomly chosen background. These results are found to be statistically significant suggesting the observed properties are a real phenomenon and not merely due to background fluctuations. When the detection statistics of each sample are compared using a binomial probability distribution, it is found that the null hypothesis that they were drawn from the same parent populations could not be rejected. Finally, by applying a set of grey–body models to the determined SPIRE wavelengths, FIR luminosities and SFRs were found that further supported the idea that physically, the two samples were composed of similar objects with ULIRG luminosities. Whilst there is evidence in the literature that using only one wavelength may significantly overestimate the SFR, the relatively consistent results between populations at each wavelength when redshift is taken into account imply a lack of difference between BALs and non–BALs. As an additional investigation, the tentative correlation found by Priddey et al. (2007)

between C IV equivalent width and detection rate has been addressed and found to likely be due to small number statistics, with a Mann–Whitney test finding no evidence of different properties when the sample is split based on C IV equivalent width. The main conclusion of this study is that it appears HiBALs are not a separate evolutionary phase, the properties of which can easily be explained by a simple orientation effect scenario where we only see HiBALs when our line–of–sight intersects the outflowing material. The same cannot be said of LoBALs (of which there is only one found in the imaged area) or FeLoBALs, which studies such as Farrah et al. (2012) suggest may well be the sought for evolutionary phase.

In Chapter 3, *Herschel* SPIRE data at 250 μm have been used as part of the SHAGS sample of high–redshift AGN. One of the main aims of the sample was to break the degeneracy between luminosity and redshift, a major concern in many prior flux or volume limited AGN samples. The AGN have been selected at a single cosmic epoch at $z \sim 1$ but spanning 5 magnitudes in optical luminosity, allowing the creation of a sample composed of some of the most massive sources at that epoch as well as less luminous (and therefore less massive) AGN, with RLQ, RQQs and RGs all selected so as to test unification schemes. As part of ongoing efforts to understand whether radio–loud AGN inhabit on average denser environments than radio–quiet sources, the *Herschel* data allows a study of the activity of these environments. These data were taken both from observations pertaining to the SHAGS survey as well as other large surveys such as HerMES or H–ATLAS to maximise the available AGN under investigation. Completeness and flux correction factors are derived through the insertion of artificial sources in each field within approximately 1 Mpc of the AGN, consistent with the best sampled

part of the field and a flux–density cutoff applied at the $5\,\sigma$ level to ensure sources were real. Due to the sensitivity of *Herschel*, the study is restricted to sampling LIRGs, with SFRs as low as $\sim 114\,\mathrm{M}_{\odot}\,\mathrm{yr}^{-1}$ at $\mathrm{z}=1$ at $250\,\mu$m assuming a modified black body model. A wavelength of $250\,\mu$m is chosen as it has the greatest resolution and corresponds well to where the peak of the dust model should be (around $100\,\mu$m in the rest frame of the system). Using multi-wavelength data from IRAC, VISTA–VIDEO, CFHT, SDSS and *Herschel*, suitable catalogues have been created for the SHAGS environments. These same data have been used to create a comparison sample of VIDEO galaxies with a similar redshift distribution. Sources in the environs of these AGN/galaxies have been matched to IRAC counterparts and those with optical counterparts in the r–band have been removed in an attempt to remove foreground sources. The contamination likely due to sources at high redshift has been investigated using IRAC colours, models by Bruzual & Charlot (2003), and the hyperz package (Bolzonella et al. 2000), whilst the effectiveness of foreground removal using optical counterparts has also been explored. An overdensity is then calculated by determining the 'background' density from the comparison sample. Whilst not at the same level as at earlier epochs, it appears the environments of AGN still have overdensities of star forming galaxies, approximately 0.4 sources in every field. No significant radial dependence can be inferred owing to the large errors on individual annuli. However, on taking all sources within a 1 Mpc annulus, it appears RL AGN reside in significantly more overdense fields than RQQs. Intriguingly, a marginal correlation is found between radio luminosity and star formation overdensity, akin to that found by Falder et al. (2010) at $3.6\,\mu$m, which suggests that radio power is dependent on environment. A correlation also appears to be present between

stellar mass and star–formation overdensity for RLQs. Upon calculating the SFRs of companion galaxies, it appears RL AGN sit in overdensities of 100-200 $M_{\odot}\,yr^{-1}$ LIRGs, whilst RQQs appear to be close to the background level. This dichotomy may be a direct result of greater numbers of evolved galaxies in the environments of RL AGN harassing galaxies through tidal interactions etc. The sources in the environs of the AGN are likely the progenitors of modern day S0 galaxies whose population increases steadily from $z \sim 1$ to the present day (Postman et al. 2005; Smith et al. 2005) and could feasibly be forming at this time if weak tidal interactions between cluster members are able to form S0 galaxies.

Finally, in chapter 4 we continue the work performed by Page et al. (2004) and Stevens et al. (2005, 2010) on a new sample of X–ray absorbed QSOs. In the first sample, X–ray absorbed AGN with absorption column densities of order $10^{22}\,N\,cm^{-2}$ were observed with the original SCUBA instrument (Holland et al. 1999) from which several important discoveries were made (see Section 4.1). Those findings led to the conclusion that absorbed sources were caught in a transition phase between a highly dusty, high SFR source and an optically visible QSO phase (Page et al. 2004, 2011). Furthermore, the environments of five of these absorbed sources showed overdensities of ULIRGs, suggesting these clusters would become some of the most dense clusters visible in the local universe. In this thesis, observations using the SCUBA–2 instrument on the JCMT were taken in February of 2012 and 2013. These new X–ray absorbed QSOs have absorption column densities an order of magnitude higher than their predecessors. Data reduction has been performed using the dynamic iterative map–maker found in the SMURF package (Jenness et al. 2011; Chapin et al. 2013). The reduction of blank fields in this thesis differs somewhat from the standard blank field pipeline

in that normally a high pass filter (600 arcsec) is used to remove $1 / f$ noise, but in blank fields this is found to cause problems when there is very little signal in the map and will remove objects of interest. Instead, both a low and high pass band filter are applied with angular scales of $2 < \theta < 120$ arcsec. Source extraction has then been performed on the fields, with a relatively high cutoff chosen to avoid the inclusion of spurious sources due to varying depths in the observations. Similarly to Chapter 3, catalogue reliability tests have been performed, though the uneven nature of the noise in SCUBA–2 maps combined with a need to use a larger area means the completeness and flux–correction factors are modelled as surfaces rather than 2–D lines (see Figs. 3.8 and 4.8 for a comparison). So as to compare number counts to a blank field, 3 CLS fields at similar depths have been taken and completeness and flux correction simulations etc applied to sources found within the fields. Of particular note is the lack of detected AGN sources. Whilst companion SMGs are visible in the environs of the AGN position, the AGN themselves are generally found to be around the 1–3 σ level (taking the exact pixel position). Stacking on the position of the AGN to increase the SNR does little to remedy the problem; at 850 μm only a 2 σ detection is visible. In an attempt to determine whether there might be some degree of evolution with redshift as found in the previous absorbed QSO sample, or indeed whether the presence of a BAL might preclude a lower flux–density, AGN are stacked in various ways. From this, it appears there is no difference in the properties of high and low redshift sources, and somewhat reassuringly (based on the findings in Chapter 2), no difference between BAL and non–BAL QSOs. The high X–ray luminosities of the sample combined with the findings of Page et al. (2012) and the high fraction of BAL QSOs may suggest that these non–detections are to be expected;

they are the effect of a powerful AGN actively removing gas and dust from the host galaxy and in the process shutting down star–formation. Differential and integrated source counts have also been derived for both the AGN and CLS blank fields, and a Schechter function has been fitted to the CLS fields for which there are available more sources. These results indicate that these absorbed sources sit within overdensities of sources with SFRs of the order of several thousand solar masses per year. The SFRs have been derived using several analogues; Mrk 231, a local ULIRG and LoBAL QSO, Arp 220, another local galaxy undergoing a major merger, and finally IZw1, a relatively quiescent source which provides a possible lower limit. Unfortunately, the large degree of scatter on individual bins prevents an accurate fit being made to the AGN counts for fainter flux–densities. This may be a result of the completeness being unable to fully account for sources at the SNR cutoff level combined with high variance between AGN fields due to small areas, cosmic variance and differing noise properties.

5.2 Conclusions

Prior to this study, AGN were already believed to significantly affect their host galaxies. However, it was still unclear whether BAL QSOs were a sign of AGN feedback or merely an orientation effect, and various authors were at odds over whether AGN properties were reliant on environment or were intrinsic to those sources. The energy, mass and momentum of the outflows in the ‘quasar mode‘, believed to be responsible for the BAL phenomenon, were certainly sufficient to drive dust and gas away from the centres of galaxies (e.g. Choi et al 2012). This could feasibly reproduce the observed M_{BH}–σ relation (Ferrarese & Merritt

2000; Gebhardt et al. 2000; Gültekin et al. 2009). However, no study to date has focussed on submm wavelengths in close proximity to the peak of the SED of obscured star formation within the host galaxies or companions in the large–scale environment. This is a severe handicap in any model that aims to truly understand galaxy evolution from early cosmic epochs to the present day. Without some idea of the 'ongoing' star formation at a particular redshift in the host galaxies and environments of AGN, any conclusion on the effect of an active black hole on its surroundings will omit, for example in the most extreme galaxies, up to 95 per cent of the bolometric luminosity (Soifer et al., 1987) and ignore an important stage in any galaxy's life.

This aim of this thesis has been to provide a new series of data in a previously unexplored wavelength range to answer several questions at the forefront of AGN evolutionary scenarios. The results of this work yield further evidence for HiBAL QSOs being a geometric effect in an entirely new wavelength range, suggest that RL AGN prefer dense star–forming environments at $z \sim 1$ and argue *prima facie* against the findings of Page et al. (2004, 2011) that suggest obscured AGN are in a separate evolutionary phase.

First, some thoughts on the effect of AGN on the host galaxy. As noted in Section 1.1.3 and discussed in Section 2.4, a considerable amount of study has been afforded to the BAL phenomenon in an attempt to determine whether these objects truly are the transition phase between a highly obscured star–forming phase and a classical optically visible QSO. Of course, the model proposed by Murray et al. (1994) is just as enticing, in which the observed properties of a BAL QSO are solely due to whether an observers line of sight intersects the outflowing wind. For the first time, this work has used *Herschel* SPIRE observations to determine

whether BAL QSO hosts are in submm–luminous galaxies, consistent with an evolutionary scenario, in which BAL QSOs are found earlier in the evolution of their host galaxy than a non–BAL QSO with a correspondingly higher SFR.

From those data, this work has been able to sidestep the problem inherent in using X–ray, UV and optical wavelengths to resolve the mystery. Whilst the UV–absorbing region may impose the observed absorption troughs in the optical band, being reliant on the geometry of the central engine, that region will be optically thin to FIR and submm radiation. This study finds that not only is there no difference in submm flux between HiBAL and non–BAL QSOs, consistent with work at submm wavelengths (e.g. Willott, Rawlings & Grimes 2003; Priddey et al. 2007), there appears to be no correlation between submm flux and C IV equivalent width. This suggests then, that in addition to HiBAL and non–BAL QSOs having similar SFRs, that the BAL outflow has had no measurable effect on the host galaxy within the past $\sim$10–100 Myr (if a population of young stars are assumed to be responsible for heating the dust). Recent work by Vestialbuio et al. (in prep.) on FeLoBALs at 850 μm suggests that even the rare FeLoBAL QSOs which make up a tiny fraction of the BAL QSO population and have been suggested as the transition phase are not the answer to visible AGN feedback. HiBALs, LoBALs and FeLoBALs cannot be taken to be anything more than ordinary QSOs observed at a particular angle.

The correspondence of BAL QSO properties with X–ray absorption is most evident in Chapter 4, which offers observers another mechanism of selecting likely BAL QSOs. The high incidence ($\sim$50 per cent) of BAL QSOs in the sample would suggest X–ray absorbed QSOs with high ($> 10^{23}$ cm^{-2}) absorption column densities are over 3 times as likely to host a BAL outflow than the general population

and would indicate a very high covering factor if reliant on orientation alone. This finding provides strong support for the argument presented by Page et al. (2011) where the X–ray absorption is due to the 'shielding gas' in the radiative disk–wind model, a required component in a BAL wind. When compared with the incidence of BAL QSOs in other studies ($\sim$15 per cent), it would appear these sources have far higher covering factors, which could be taken as evidence of evolution over time towards lower covering factors.

Perhaps then the complexities of BAL QSOs in a galaxy's evolution must be rethought; BAL winds are not simply observed because of a particular orientation or an evolutionary phase, they may be both. One is loath to discard BAL QSOs entirely as a mechanism in the evolution of a host galaxy, considering the energy injected into the ISM from such an outflow. It is possible that BAL QSOs might be coincident with a ULIRG phase, such as in Mrk 231, but perhaps the samples investigated here are caught too late. There is no reason why the BAL outflow might cease to exist after the obscured phase, it may merely be in a weakened state. The high incidence of BALs in this new sample of absorbed QSOs could be interpreted as them being caught at an earlier phase than those studied in Chapter 2.5, but still well after the period during which the effect of the BAL wind might be evident. Under the assumption that QSOs are classified as BAL QSOs when our line of sight intersects an outflowing wind, it would be expected that non–BAL QSOs might also host said wind. The similarity in absorbed and non–absorbed QSO submm fluxes can only be explained if they have already undergone quenching. If the BAL wind covers a larger angle at earlier times, coincident with a greater absorption column density, and black hole growth and star formation are fed from the same reservoir (e.g. Kauffmann et al. 2007), this

would suggest that the AGN might still be processing whatever material is left over from a shrouded phase. In the case of unabsorbed QSOs, they may have already exhausted that material and no longer show X–ray absorption, or the 'shielding gas' is merely no longer in our line of sight. This would also allow the findings of the previous sample discussed by Page et al. (2004) to fit neatly into this scenario; they were serendipitously caught at an earlier phase in their evolution.

Whilst the work presented in Chapter 3.7 does not relate to BAL QSOs, it does provide some insight into the larger–scale evolution of galaxies and clusters. Previous works (such as those discussed in Section 1.2.3) had been at loggerheads to determine whether the central AGN or its environment determine the properties of a cluster and whether radio loudness is a consequence of 'nature' or 'nurture'. However, by not concentrating on a single cosmic epoch, significant differences in the host galaxies and environments of the selected AGN would be introduced, muddying the waters and introducing a variety of uncertainties.

The work presented here implies that the properties of the central AGN, at the very least radio–loudness, are a consequence of the central engine already residing in far denser environments. Essentially, large scale cluster evolution influenced by the central AGN is highly unlikely, it is the environment that dictates both the AGN properties and the characteristics of the cluster in which it resides.

This interpretation is supported unambiguously by the SHAGs sample, in that Falder et al. (2010) found a significant overdensity of evolved stellar mass at $z \sim 1$. This would argue the environment was already dense at early epochs and rich in material with which to form stars. This richness has allowed the same regions to maintain their overdensity in star–forming galaxies to $z \sim 1$, as presented in

this work. Of course, whilst an overdensity in star–forming galaxies exists, it is far less significant than that found for stellar mass. This can be explained by ongoing mergers and funnelling of material towards the central regions over time, removing the fuel available for star–formation whilst still ensuring jet confinement and boosting of radio–luminosity in the densest regions. As noted before, black hole spin may explain the AGN radio properties or at the very least be another parameter. AGN residing in the densest environments will undergo more mergers, thereby increasing the spin state of the black hole (and consequently, the radio power). At $z \sim 1$, field galaxies that have evaded mergers are becoming virialised and suffering more flybys and tidal disruptions, which, as argued by Gnedin (2003) are not strong enough to produce ellipticals but can produce S0's, thereby reproducing effectively the increase in lenticulars to the present day (e.g. Postman et al. 2005).

5.3 Further Work

With the advent of new facilities, the study of galaxy evolution across cosmic time will benefit from larger, more sensitive surveys. However, how might they relate to the work presented in this thesis?

With regard to the work carried out as part of Chapter 2, the obvious next step would be to increase sample sizes to produce a more representative result. From there however, the main restriction is observation time. Whilst *Herschel* has now been decommissioned, there remains a wealth of data to analyse, much of which is now public. A larger matched sample of BAL QSOs including HiBAL, LoBAL and FeLoBAL QSOs could feasibly be created, and rather than being limited to

the chosen redshift range in this work, this study could be extended to higher redshifts to determine whether there is a visible difference over cosmic time, and indeed whether different types of BALs become more prevalent at high redshift. For example, the C IV feature can be detected easily in the SDSS in the redshift range $1.7 \leq z \leq 3.6$. If a specific class are more prevalent, such as FeLoBALs, this might indicate they are a separate evolutionary phase (though care would need to be taken to ensure no selection bias e.g. from erroneous classification due to missing C IV, Al II, or Mg II lines at low redshift or high redshift). An estimation of comparative dust masses, luminosities and SFRs could also be performed. Analysis of BAL spectra where possible/available could create composite spectra and determine whether characteristic lines might lead to stronger FIR emission (which Cao Orjales et al. 2012 argues against) and indeed whether higher derived dust masses correlate with stronger specific lines such as C IV or whether there is a variation in the spectrum. In doing so, a full appreciation of the various types and their properties over various cosmic epochs could be determined. BALs with rare properties such as radio loudness could also be investigated in the same way, to try to deduce whether they would be found in significantly different host galaxies. Next–generation surveys such as SDSS IV and telescopes such as the Large Synoptic Sky Telescope (LSST) will significantly boost the sources available for study and would play a prime role in this future analysis.

With regard to the study of AGN environments, simply increasing the sample sizes would make the sample more robust. A series of samplings at various cosmic epochs such as another at $z \sim 2$ and $z \sim 3$ could also be carried out to see how the environments change over cosmic time, though obviously sample sizes will suffer. Furthermore, a comparison sample with matched colours, redshifts etc would also

strengthen the argument of whether there remains an overdensity in star forming galaxies at redshift $z \sim 1$. With next–gen radio telescopes such as LOFAR and the SKA, a wealth of new AGN can be discovered over large areas at high angular resolution. Companions in the current SHAGS fields could be investigated as to whether they hide AGN in this way. Multi–wavelength observations of the fields will also allow SEDs for the companion sources to be derived and if spectra are available, the host galaxy properties of those companions could be studied to attempt to determine whether they are S0s, spirals or elliptical galaxies, or indeed are mergers. The improved resolving power of ALMA and the Cerro Chajnantor Atacama Telescope (CCAT) will be invaluable in resolving far more counterparts than has been possible using *Herschel* and single 250 μm sources will be resolved into multiple counterparts all of which are still forming stars. This might help to offset one of the main problems in this thesis, in that more sources will be discernible in each field, thereby accurately determining which galaxies are responsible for FIR emission. Using ALMA, it will be possible to trace CO molecular gas, the second most abundant gas in the universe, so the SFR properties of sources within the AGN fields will be able to be determined and provide a second measurement of the SFR in each galaxy.

Finally, as a followup to the work performed in Chapter 4, observations at shorter wavelengths could be performed using 3.6 μm and 4.5 μm onboard the *Spitzer* space telescope as part of its warm mission, or using the Mid–Infrared Instrument (MIRI) which will be on the James Webb Space Telescope (JWST) between 5 and 28 μm. These would allow an estimation of the stellar mass, thereby providing a further constraint on the current evolutionary status of each source. Furthermore, this would also allow the construction of SEDs for each

source, providing an estimate of the contribution to the bolometric luminosity from each component (i.e. the AGN, dusty torus, obscured star formation) to be determined. Indeed, work is ongoing on the original X–ray selected sample (Ali et al. in prep) to determine the SEDs of the companion sources within the fields and constrain the contribution from each component. Therefore it is feasible that a similar study could be performed on this far more highly absorbed sample, and a more accurate SFR for each companion source arrived at rather than using the analogues within this work. By using multi–wavelength studies, number counts could be further constrained with the higher resolution of ALMA or CCAT. The FIR luminosity/redshift correlations found in previous papers could also be investigated. Larger samples of absorbed sources could also be observed using the Cerro Chajnantor Atacama Telescope (CCAT) when it is eventually completed in 2017. The enhanced resolution will complement studies performed by ALMA and SCUBA–2 between now and then.

Appendix A

.1 Scaled SEDs

This section shows how the scaled Mrk 231 and IZw1 SEDs used to derive luminosities and redshifts for the detected and non–detected sources compare to the existing data points at 250, 350 and 500 μm for each source. In black is the fit to the 250 μm band, green is 350 μm and red is the 500 μm band. The error bars on the data points are the error on each flux density value, composed of the instrumental and confusion noise. For J085436.41+022023.5 and J090517.24+013551.4, there is little agreement between the expected flux density assuming a Mrk 231 SED and observed values. However, J143907.51-010616.7 appears to have an SED very similar to that of Mrk 231, so likely has similar temperature and dust properties. IZw1 appears to have better agreement for J085436.41+022023.5, with 2 of the 3 observed data points covered by the SED fit to the 350 μm data point. Unfortunately, J090517.24+013551.4 remains with no overlap between the SEDs fit at various wavelengths, though there is less difference between predicted flux densities across the SED than assuming a Mrk 231 template. As noted in the text, this would suggest colder dust temperatures than that in Mrk 231, though the dust properties (amorphous carbon grains or amorphous silicate grains) are

evidently not similar to either template.

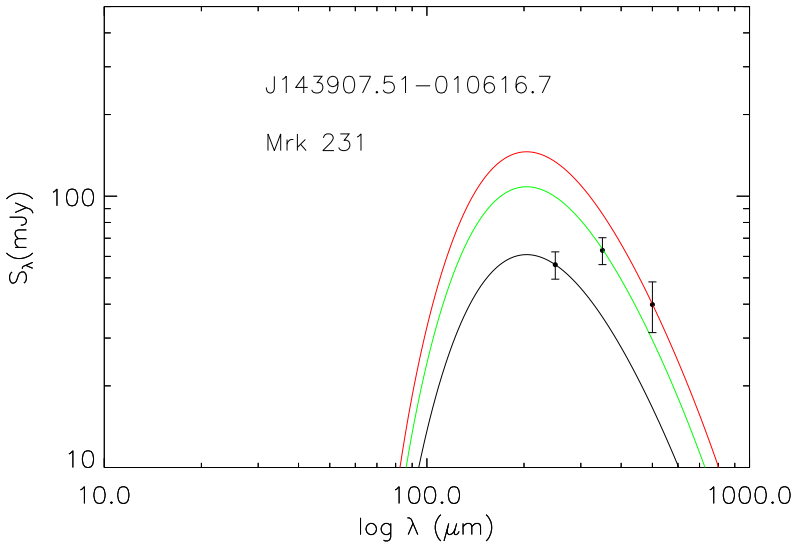
J143907.51−010616.7
Mrk 231
100
10
S_λ(mJy)
10.0
100.0
1000.0
log λ (μm)

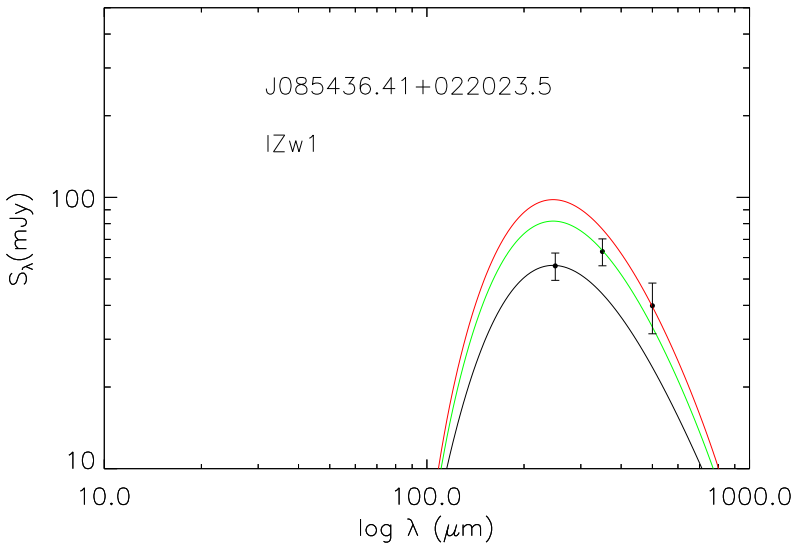
J085436.41+022023.5
IZw1
100
10
S_λ(mJy)
10.0
100.0
1000.0
log λ (μm)

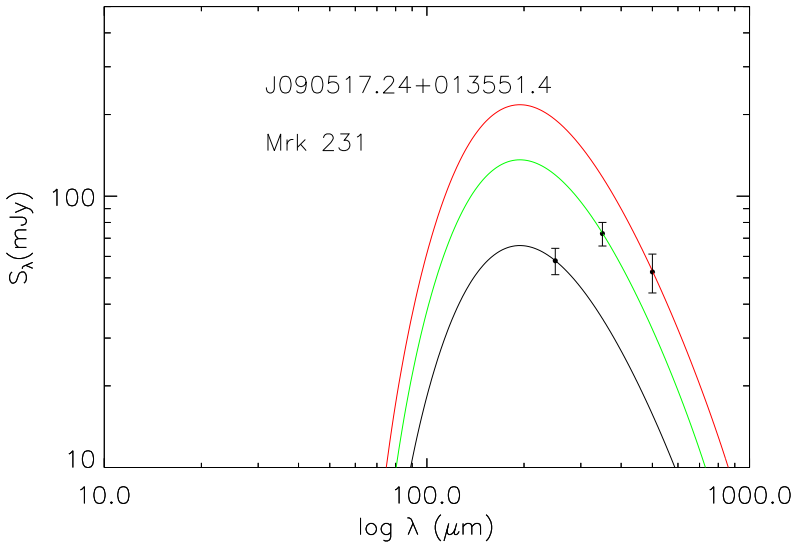
J090517.24+013551.4
Mrk 231
100
10
S_λ(mJy)
10.0
100.0
1000.0
log λ (μm)

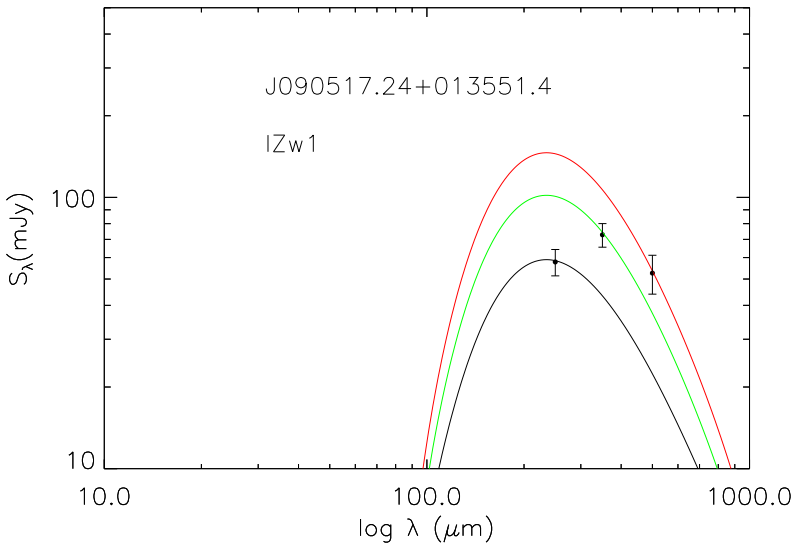
J090517.24+013551.4
IZw1
100
10
S_λ(mJy)
10.0
100.0
1000.0
log λ (μm)

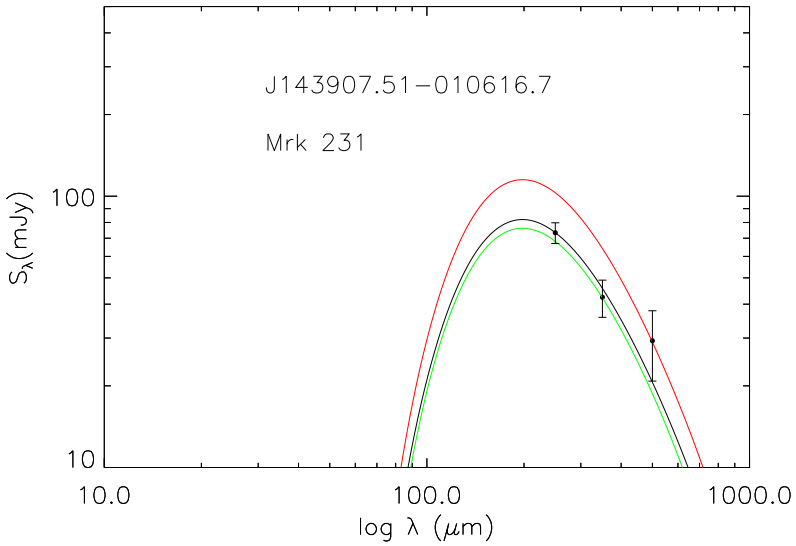
J143907.51−010616.7
Mrk 231
100
10
S_λ(mJy)
10.0
100.0
1000.0
log λ (μm)

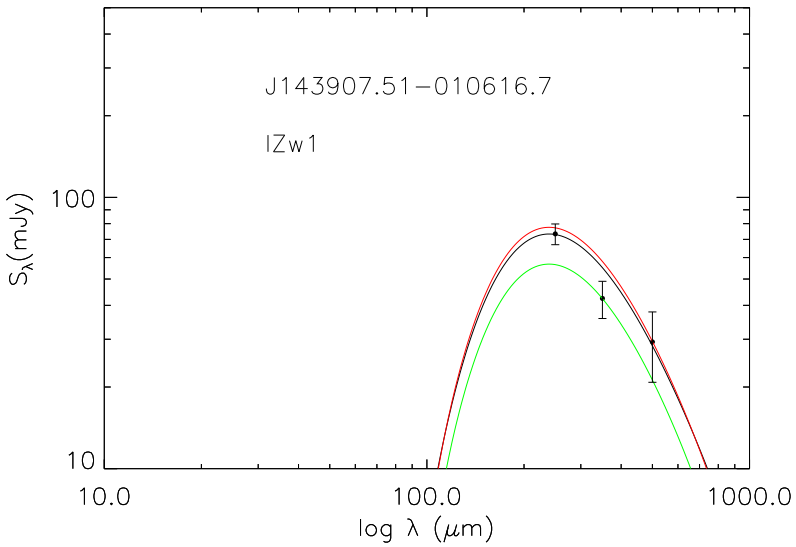
J143907.51−010616.7
IZw1
100
10
S_λ(mJy)
10.0
100.0
1000.0
log λ (μm)

.2 SCUBA–2 850 μm images

The following section is comprised of the reduced images for each AGN source at 450 and 850 μm (left and right panels in each figure respectively). On the first page is shown the 450 μm images for J030238.16+000203.4 (left panel) and and J100205.36+554257.9 (right panel), whose 850 μm observations are already included in the main body of the thesis. Each of the following observations has been overlaid with contours at the 3, 4, 5, 6, 7, 8, 10 and 12 σ level (in the case of J100205, these correspond to 3, 4, 5, 10, 20, 50, 100 σ). In white is marked the 3 arc minute 'nominal' noise region and the red circle in the 850 μm observation shows the area used to sample source counts in that field in Section 4.4.2. The name of each AGN on which the observation was centred can be found in the corner of each plot. In the case of 850 μm observations, the detected 5 σ sources within the field have also been identified by green circles.

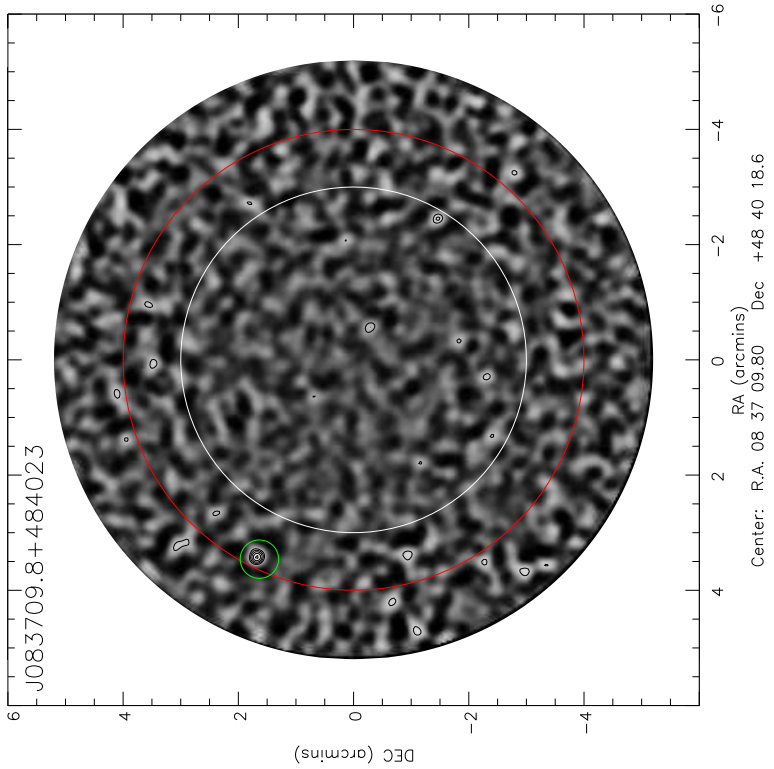
J083709.8+484023
DEC (arcmins)
RA (arcmins)
Center: R.A. 08 37 09.80 Dec +48 40 18.6

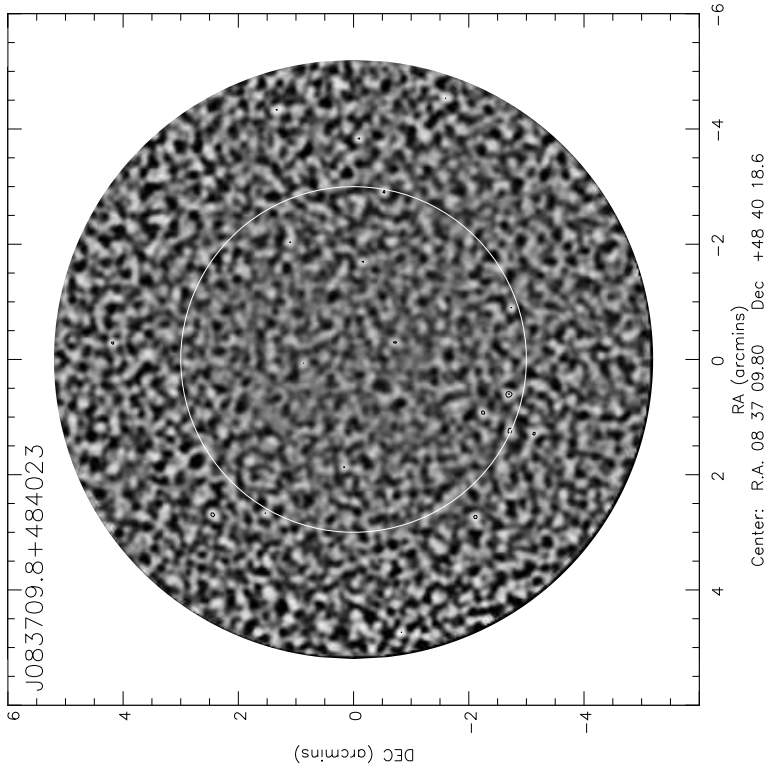
J083709.8+484023
DEC (arcmins)
RA (arcmins)
Center: R.A. 08 37 09.80 Dec +48 40 18.6

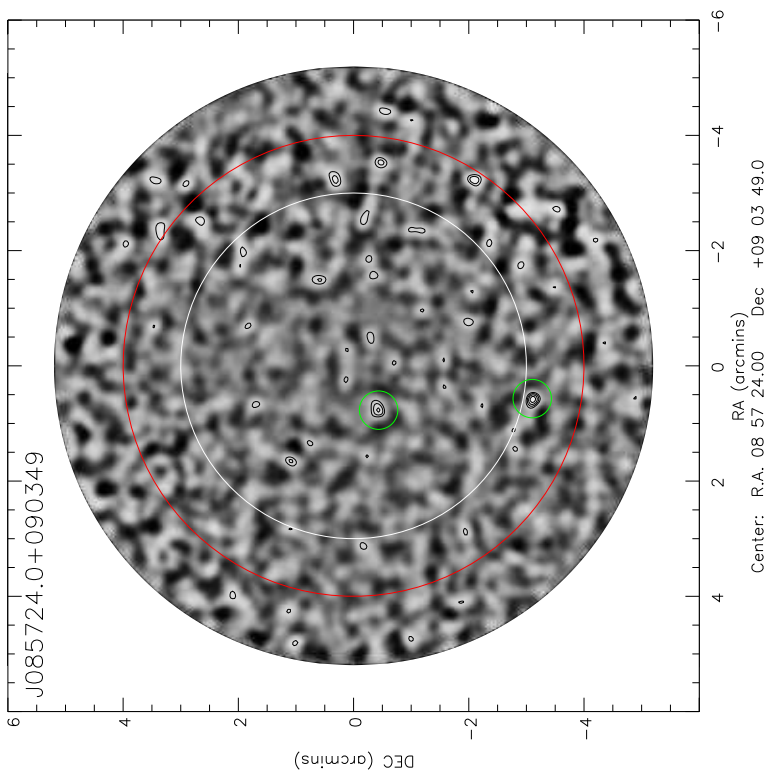
J085724.0+090349
DEC (arcmins)
RA (arcmins)
Center: R.A. 08 57 24.00 Dec +09 03 49.0

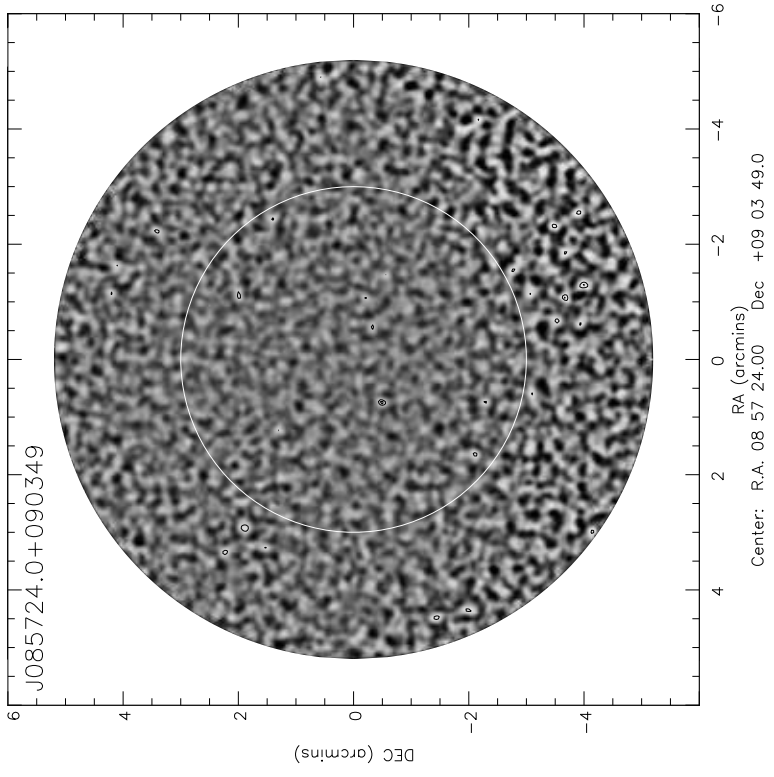
J085724.0+090349
DEC (arcmins)
RA (arcmins)
Center: R.A. 08 57 24.00 Dec +09 03 49.0

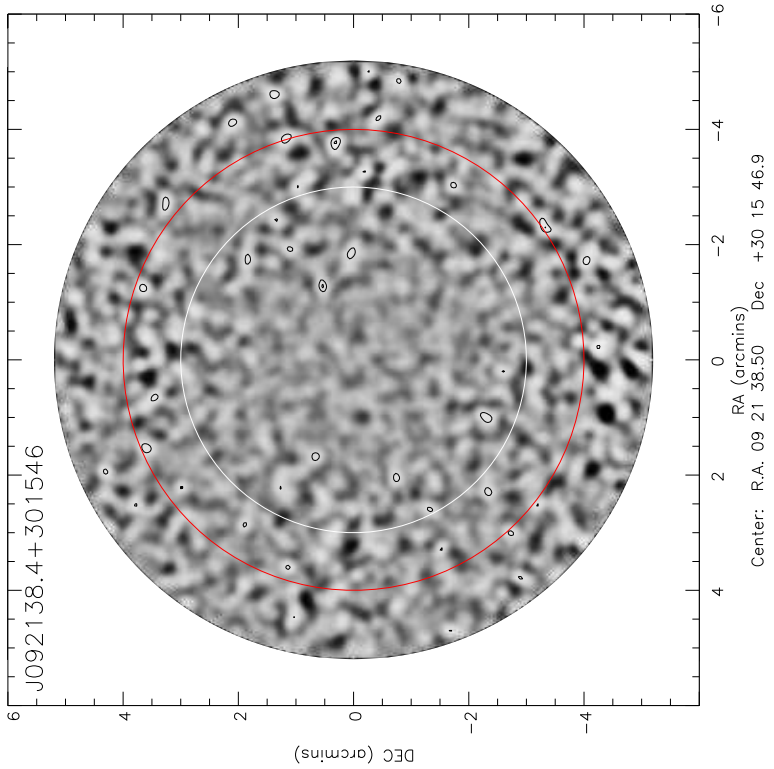
J092138.4+301546
DEC (arcmins)
RA (arcmins)
Center: R.A. 09 21 38.50 Dec +30 15 46.9

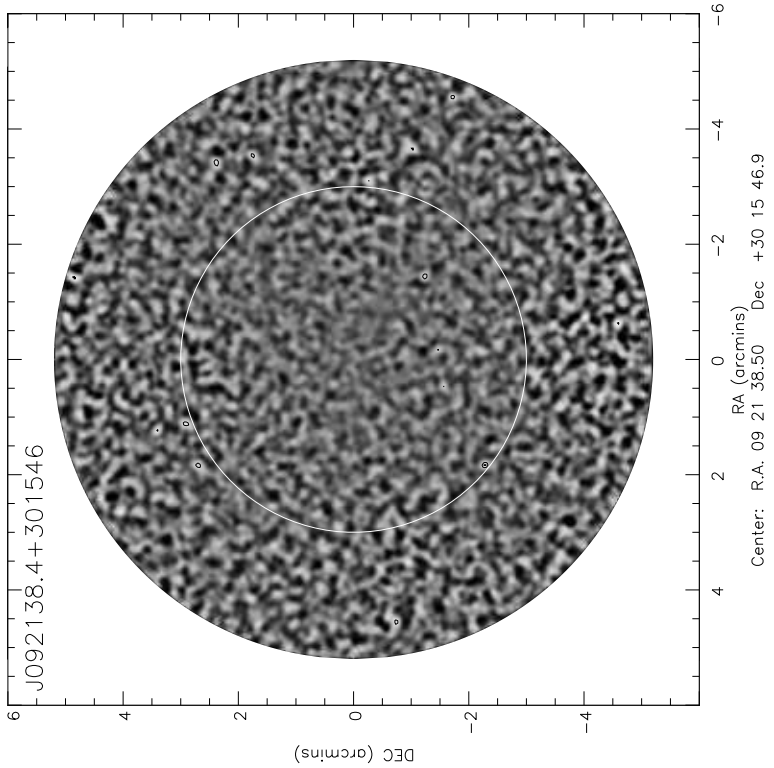
J092138.4+301546
DEC (arcmins)
RA (arcmins)
Center: R.A. 09 21 38.50 Dec +30 15 46.9

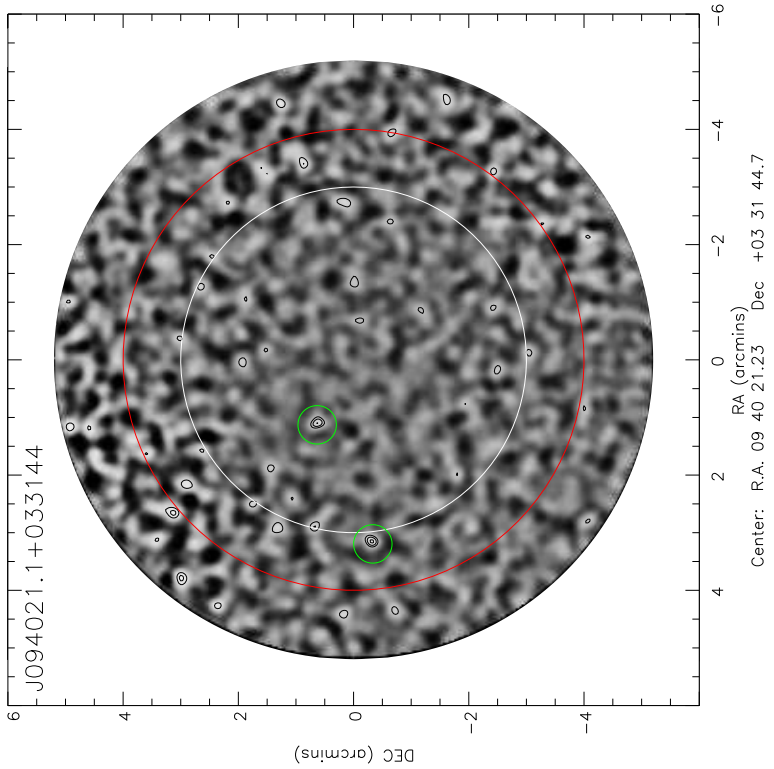
J094021.1+033144
DEC (arcmins)
RA (arcmins)
Center: R.A. 09 40 21.23 Dec +03 31 44.7

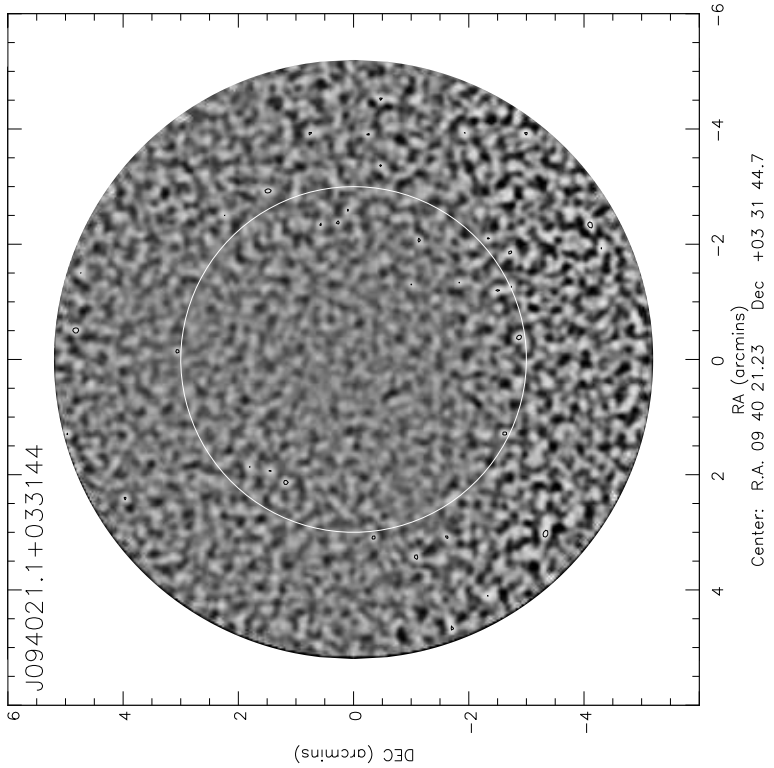
J094021.1+033144
DEC (arcmins)
RA (arcmins)
Center: R.A. 09 40 21.23 Dec +03 31 44.7

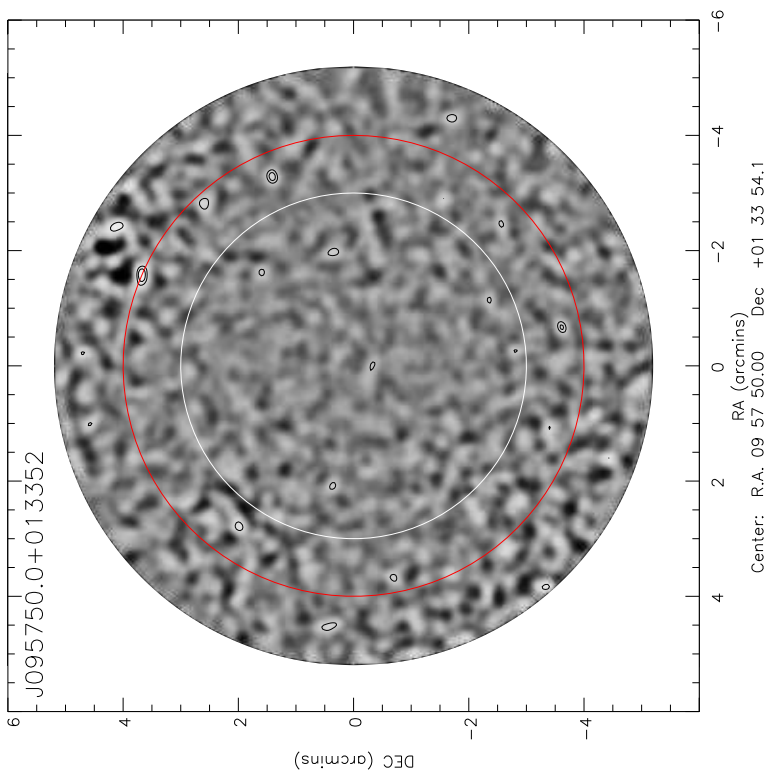
J095750.0+013352
DEC (arcmins)
RA (arcmins)
Center: R.A. 09 57 50.00 Dec +01 33 54.1

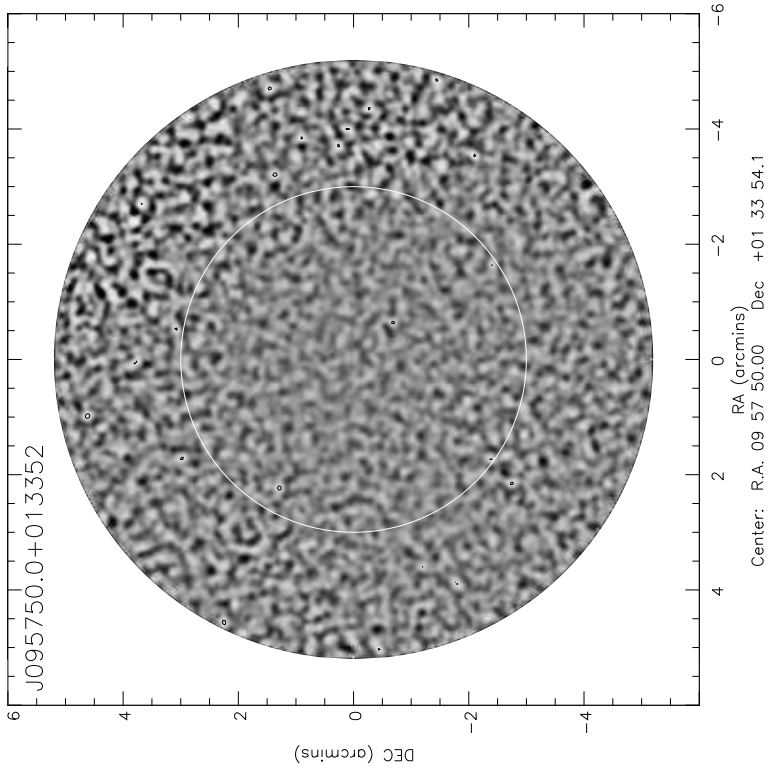
J095750.0+013352
DEC (arcmins)
RA (arcmins)
Center: R.A. 09 57 50.00 Dec +01 33 54.1

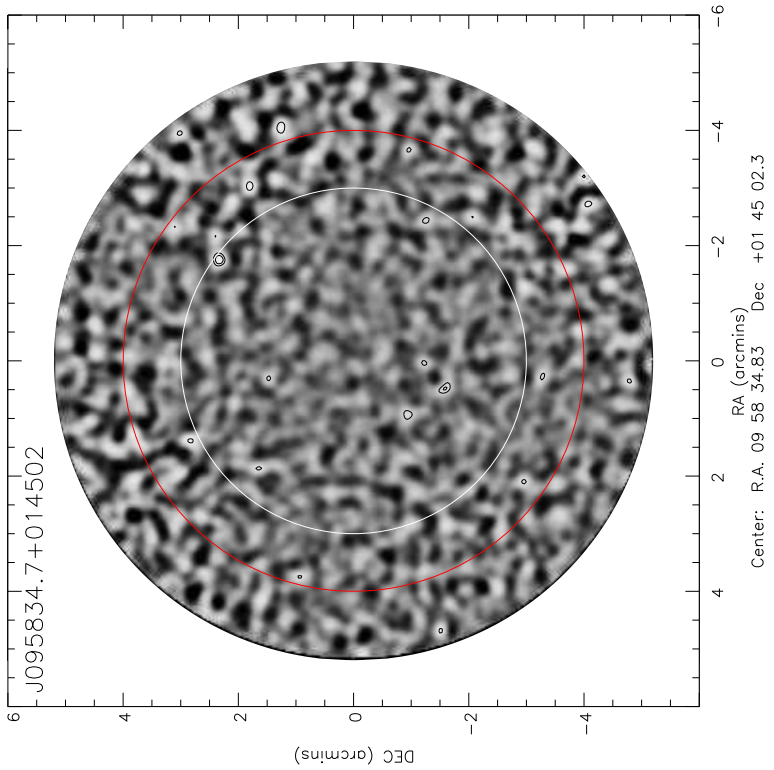
J095834.7+014502
DEC (arcmins)
RA (arcmins)
Center: R.A. 09 58 34.83 Dec +01 45 02.3

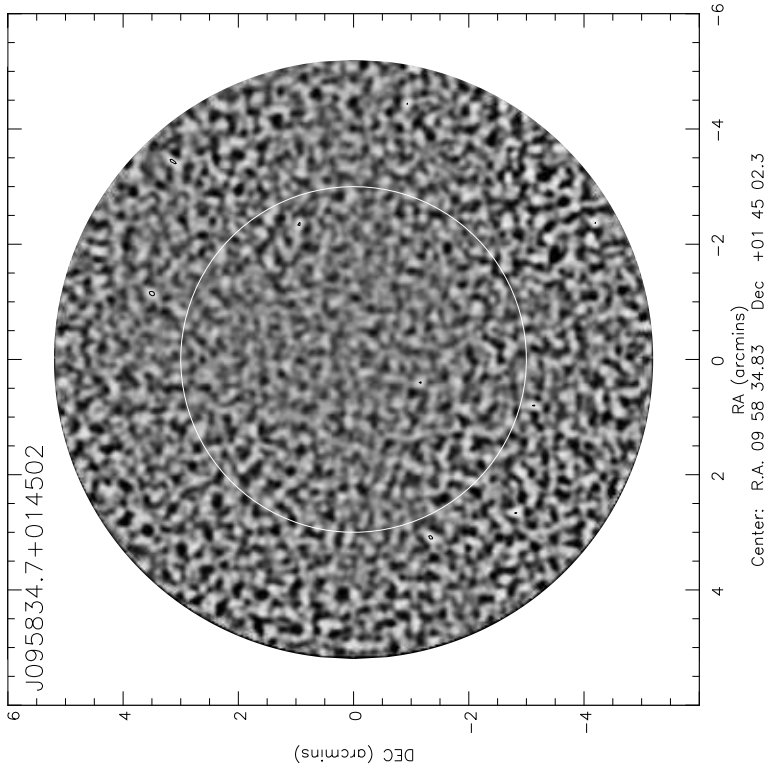
J095834.7+014502
DEC (arcmins)
RA (arcmins)
Center: R.A. 09 58 34.83 Dec +01 45 02.3

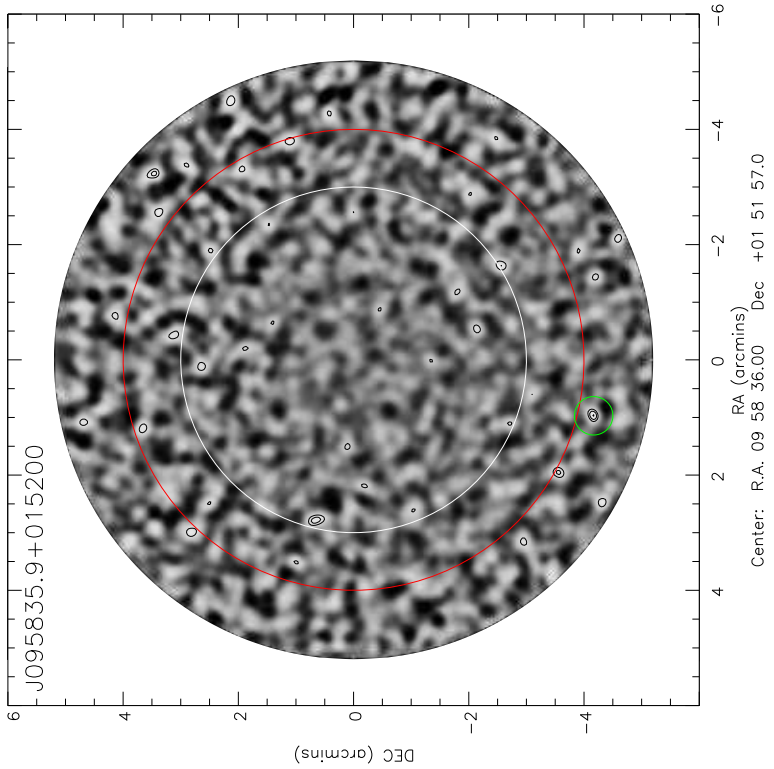
J095835.9+015200
DEC (arcmins)
RA (arcmins)
Center: R.A. 09 58 36.00 Dec +01 51 57.0

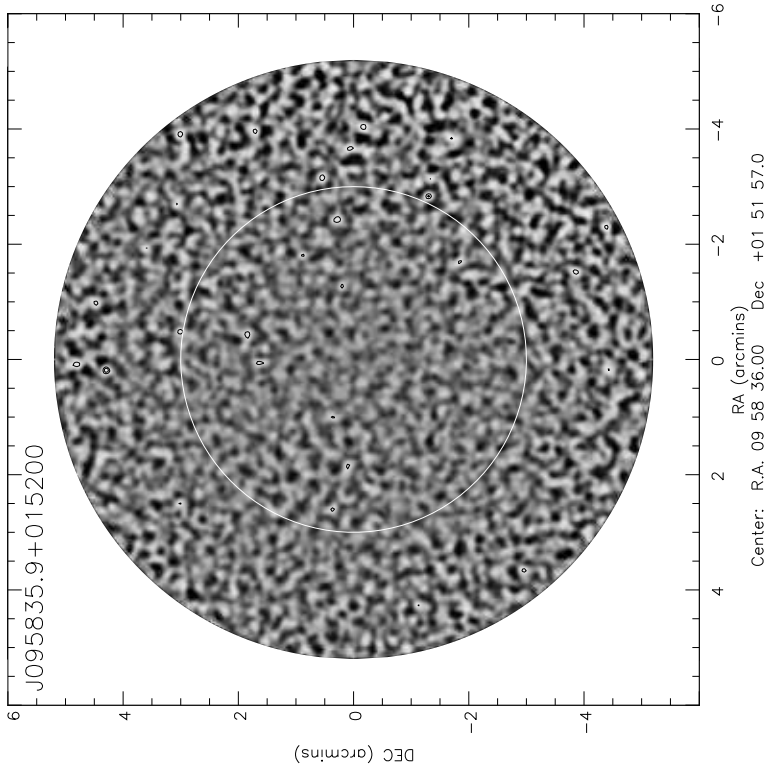
J095835.9+015200
DEC (arcmins)
RA (arcmins)
Center: R.A. 09 58 36.00 Dec +01 51 57.0

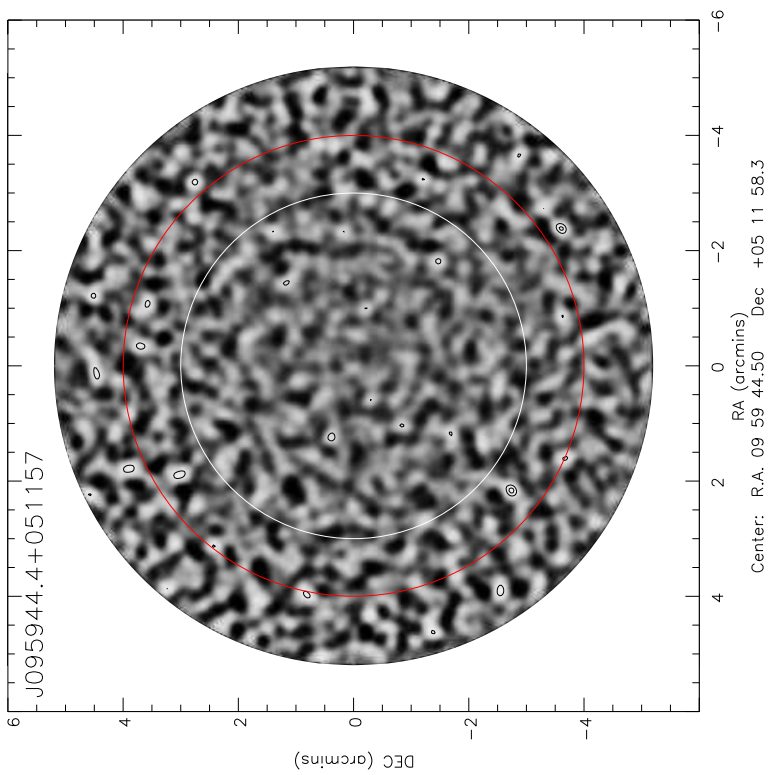
J095944.4+051157
DEC (arcmins)
RA (arcmins)
Center: R.A. 09 59 44.50 Dec +05 11 58.3

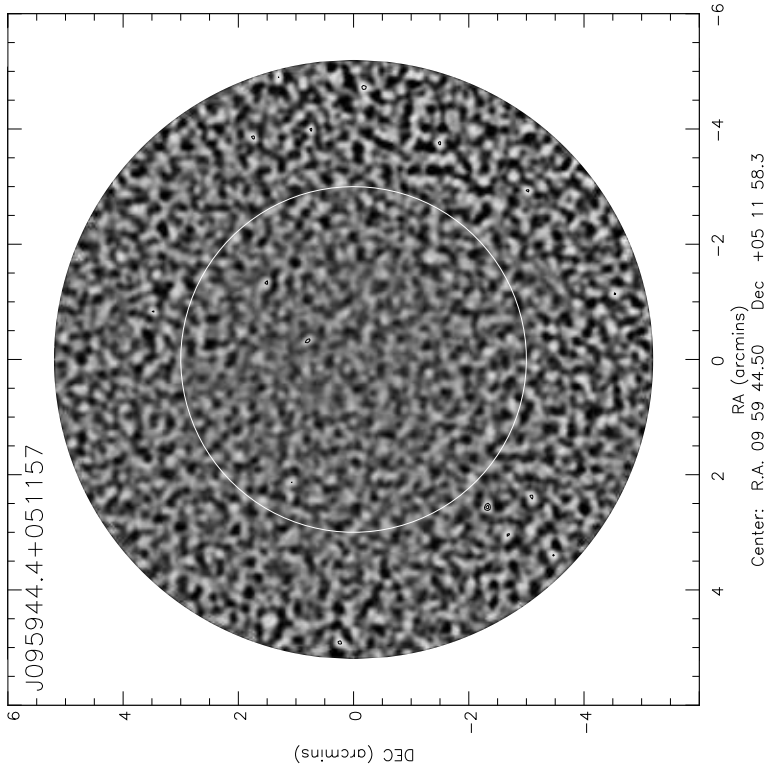
J095944.4+051157
DEC (arcmins)
RA (arcmins)
Center: R.A. 09 59 44.50 Dec +05 11 58.3

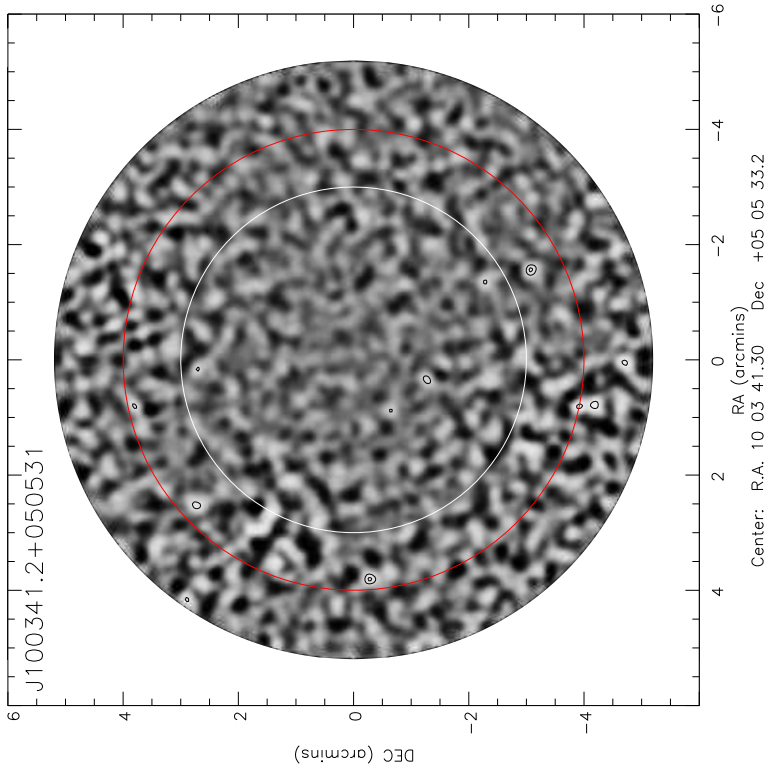
J100341.2+050531
DEC (arcmins)
RA (arcmins)
Center: R.A. 10 03 41.30 Dec +05 05 33.2

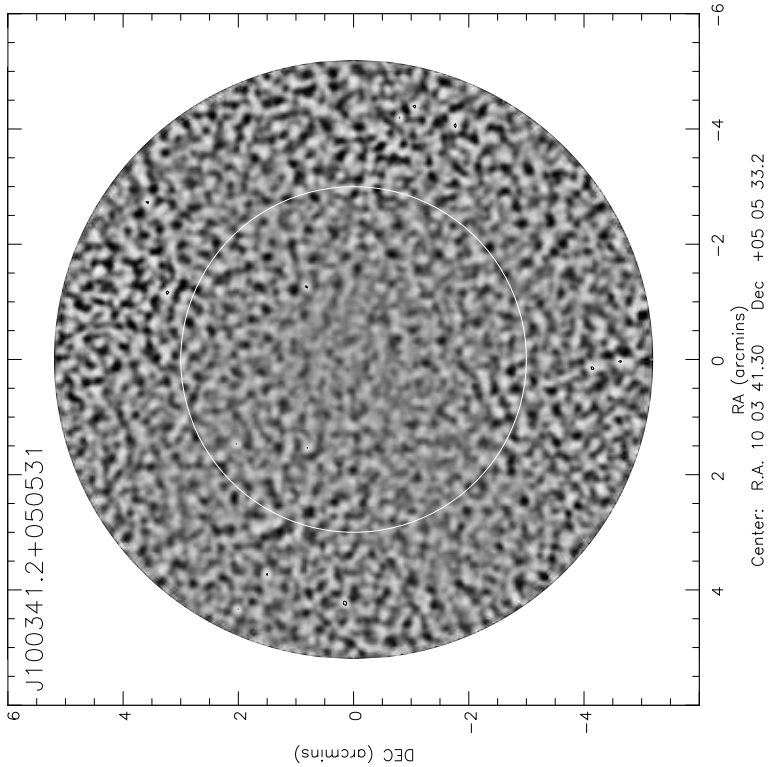
J100341.2+050531
DEC (arcmins)
RA (arcmins)
Center: R.A. 10 03 41.30 Dec +05 05 33.2

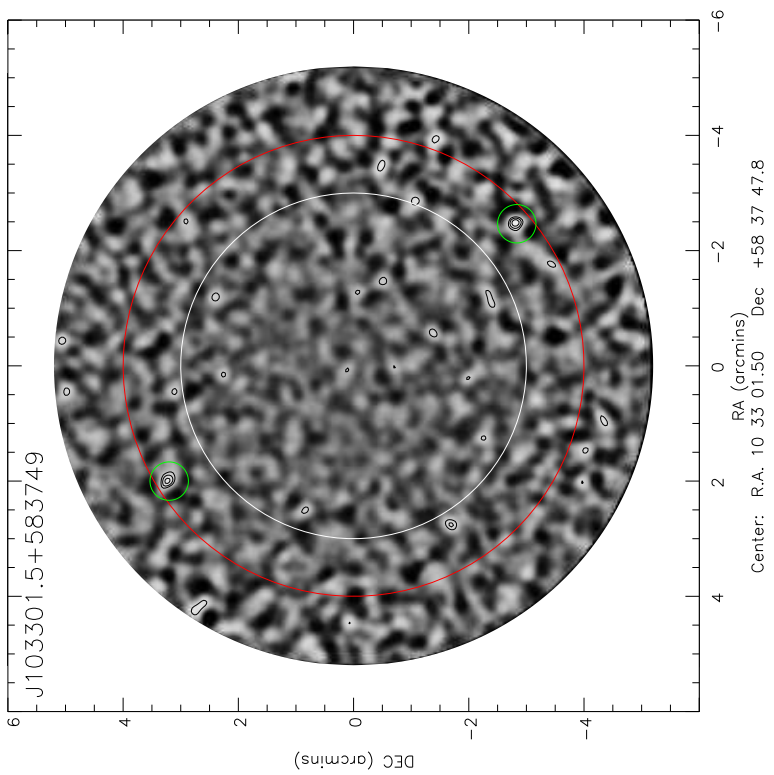
J103301.5+583749
DEC (arcmins)
RA (arcmins)
Center: R.A. 10 33 01.50 Dec +58 37 47.8

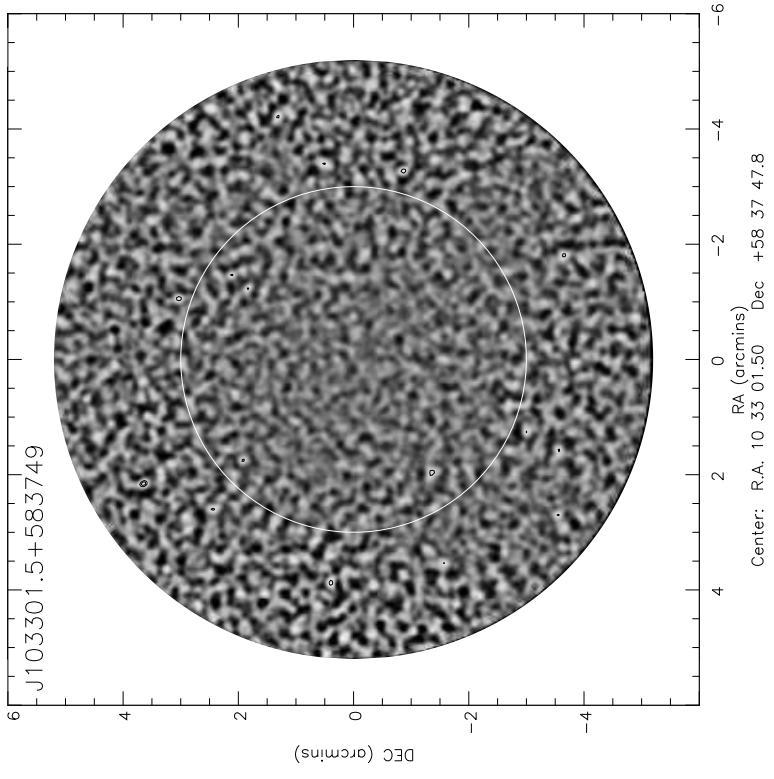
J103301.5+583749
DEC (arcmins)
RA (arcmins)
Center: R.A. 10 33 01.50 Dec +58 37 47.8

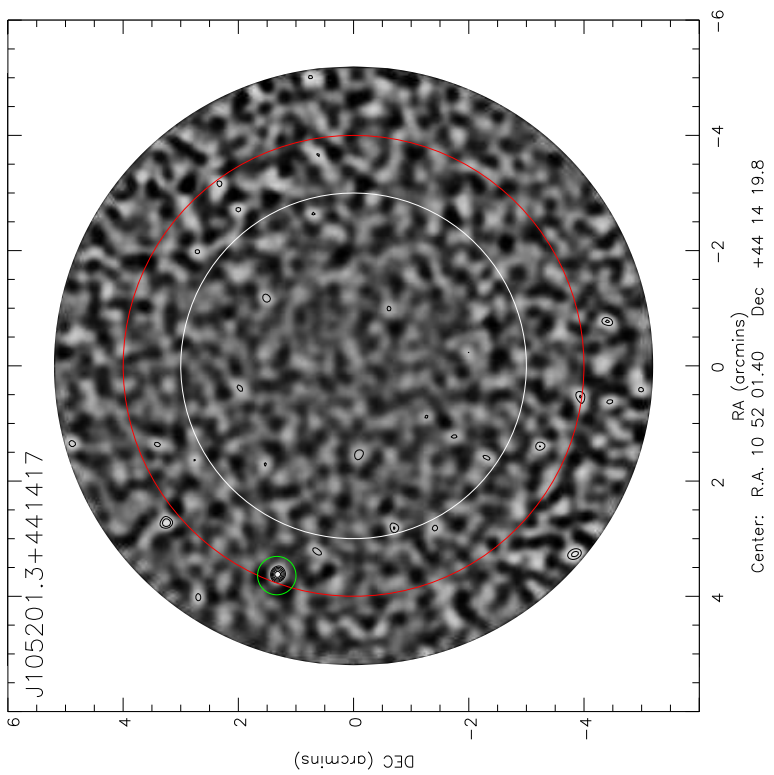
J105201.3+441417
DEC (arcmins)
RA (arcmins)
Center: R.A. 10 52 01.40 Dec +44 14 19.8

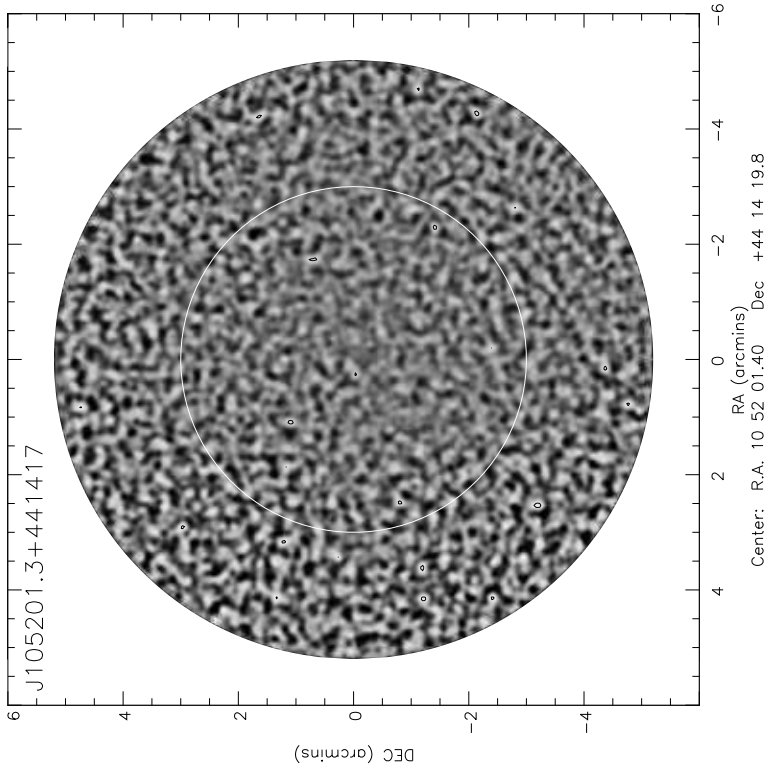
J105201.3+441417
DEC (arcmins)
RA (arcmins)
Center: R.A. 10 52 01.40 Dec +44 14 19.8

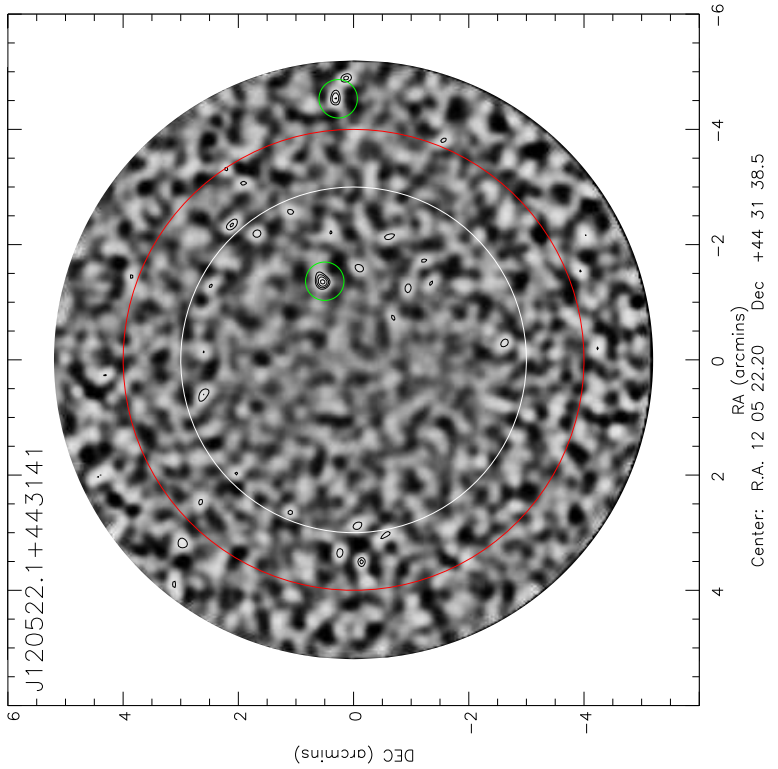
J120522.1+443141
DEC (arcmins)
RA (arcmins)
Center: R.A. 12 05 22.20 Dec +44 31 38.5

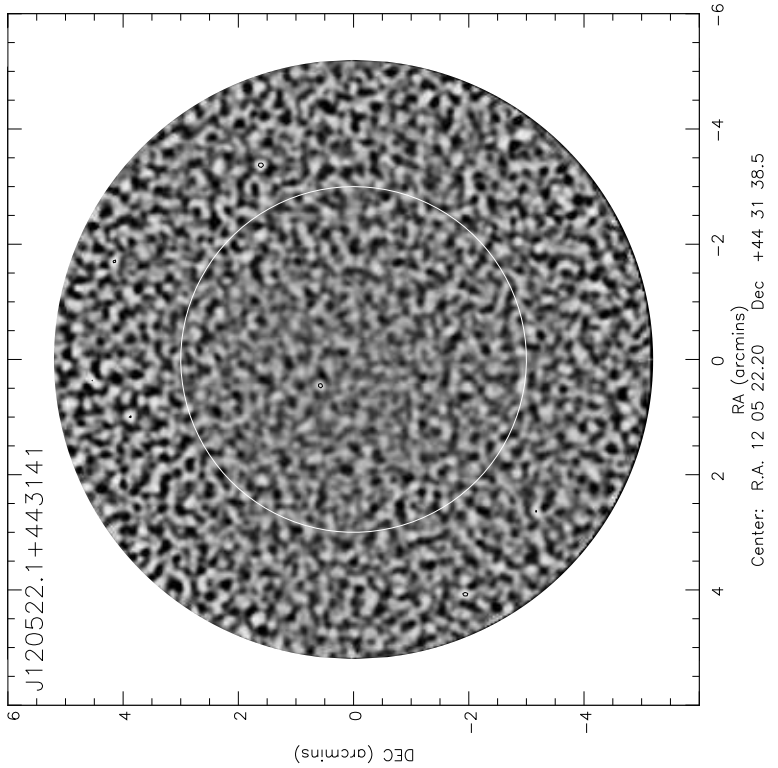
J120522.1+443141
DEC (arcmins)
RA (arcmins)
Center: R.A. 12 05 22.20 Dec +44 31 38.5

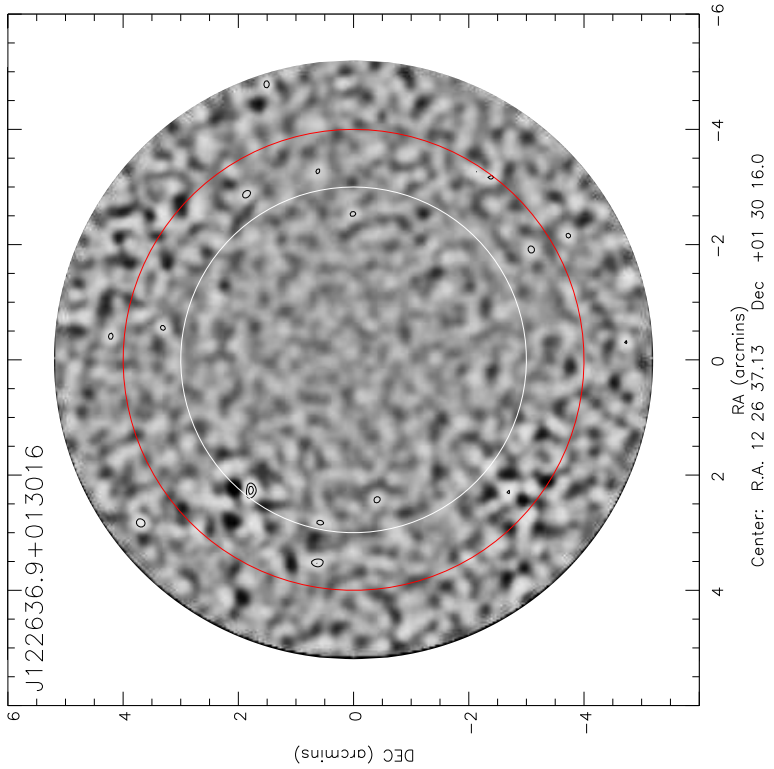
J122636.9+013016
DEC (arcmins)
RA (arcmins)
Center: R.A. 12 26 37.13 Dec +01 30 16.0

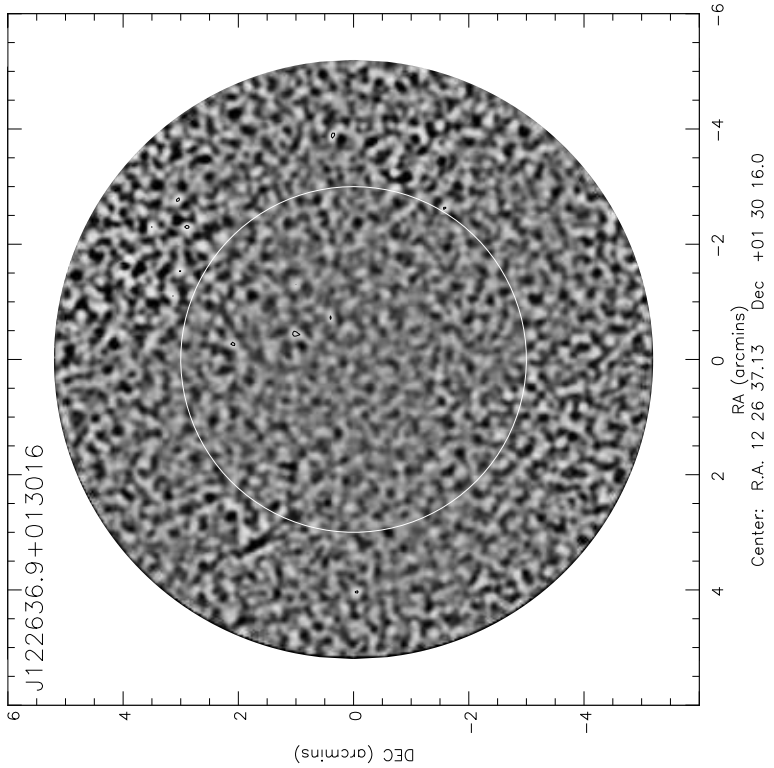
J122636.9+013016
DEC (arcmins)
RA (arcmins)
Center: R.A. 12 26 37.13 Dec +01 30 16.0

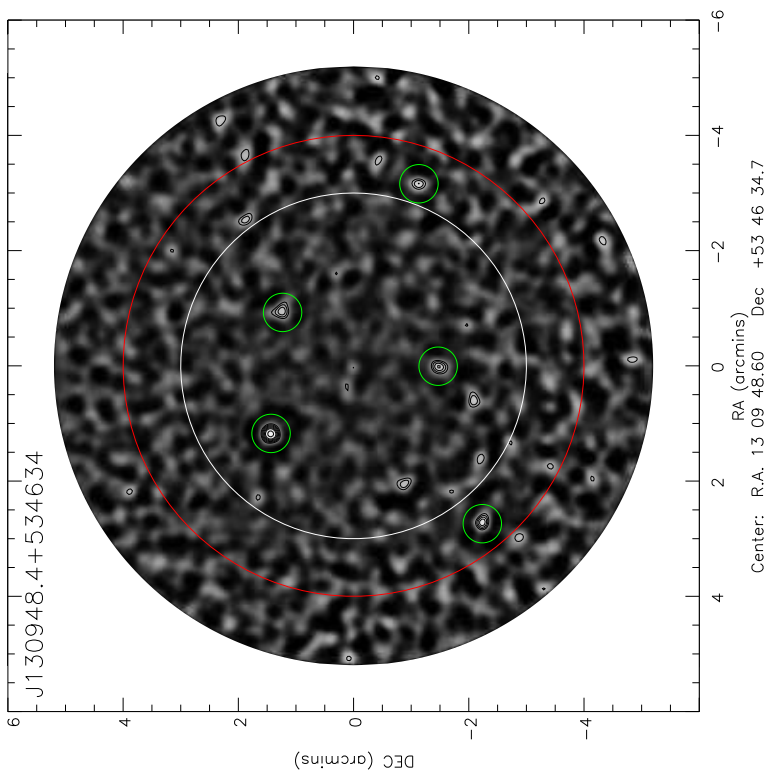
J130948.4+534634
DEC (arcmins)
RA (arcmins)
Center: R.A. 13 09 48.60 Dec +53 46 34.7

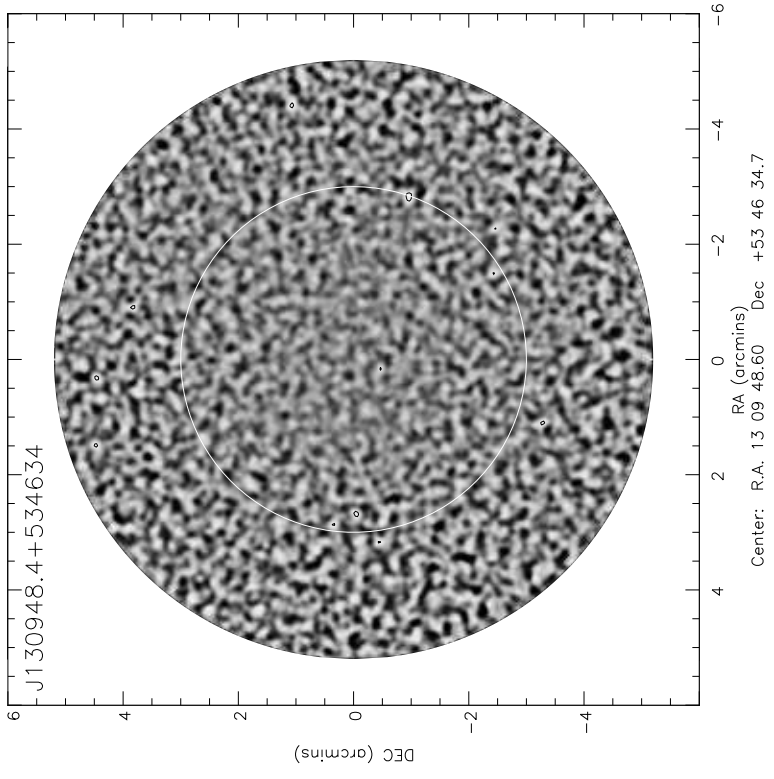
J130948.4+534634
DEC (arcmins)
RA (arcmins)
Center: R.A. 13 09 48.60 Dec +53 46 34.7

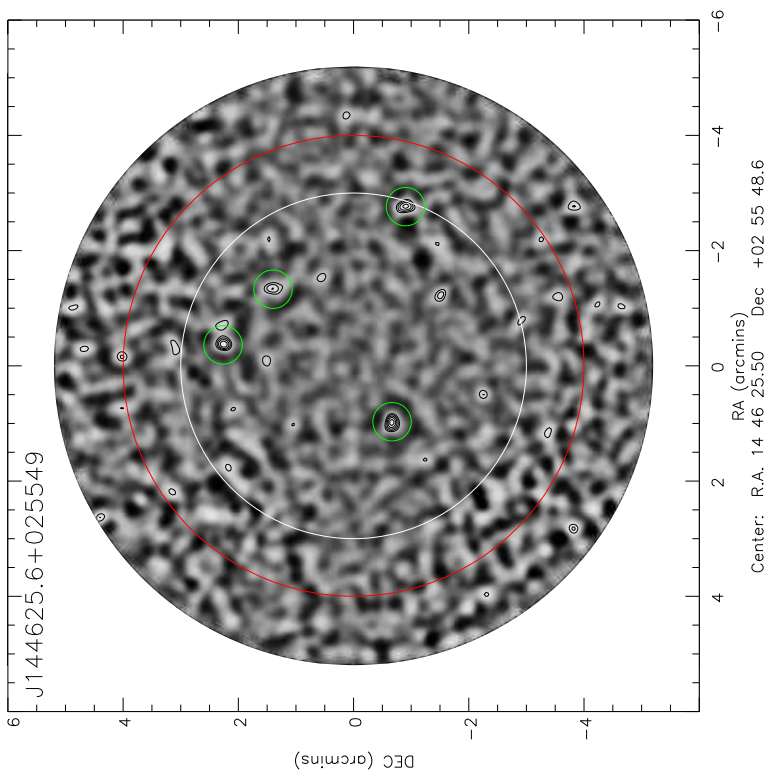
J144625.6+025549
DEC (arcmins)
RA (arcmins)
Center: R.A. 14 46 25.50 Dec +02 55 48.6

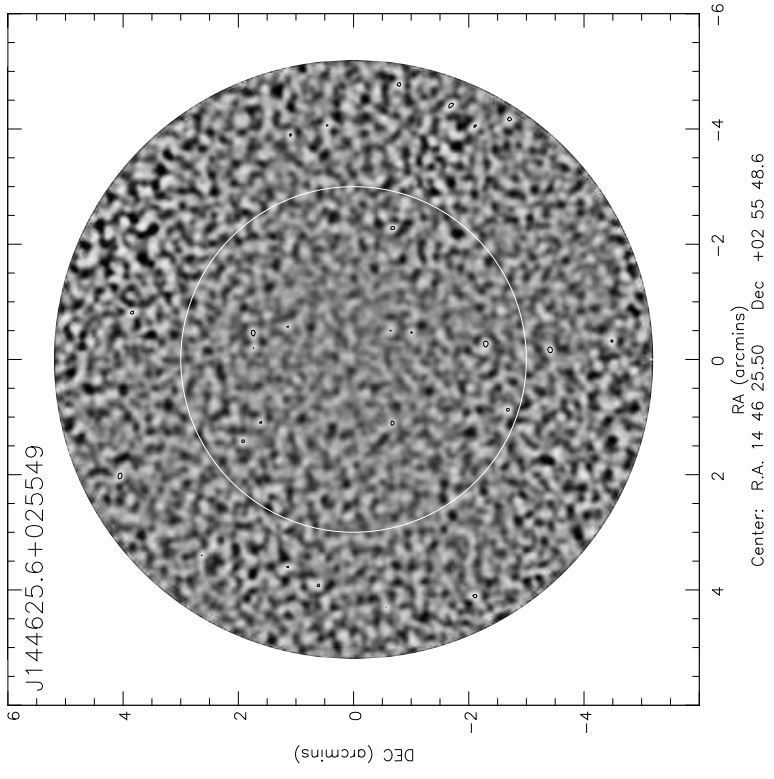
J144625.6+025549
DEC (arcmins)
RA (arcmins)
Center: R.A. 14 46 25.50 Dec +02 55 48.6

References

Abazajian K. et al., 2003, AJ, 126, 2081 47, 56

Adams T.F., 1977, ApJS, 33, 19 25

Antonucci R., Miller J.S., 1985, ApJ, 297, 621 7

Antonucci R. 1993, ARA&A, 31, 473 6, 98

Arav N. et al., 2001, ApJ, 561, 118 11

Baade W., Minkowski R., 1954, ApJ, 119, 206 2

Bahcall J.N., Schmidt M., Gunn J.E., 1969, ApJL, 157, L77 27

Barthel P.D., Arnaud K.A., 1996, MNRAS, 283, L45 29, 161

Becker R.H., White R.L., Helfand D.J., 1995, ApJ, 450, 559 98

Becker R.H., Gregg M.D., Hook I.M., McMahon R.G., White R.L., Helfand D.J., 1997, ApJL, 479, L93 10, 14

Becker R.H., White R.L., Gregg M.D., Brotherton M.S., Laurent-Muehleisen S.A., Arav N., 2000, ApJ, 538, 72 14

Beckmann V., Shrader C., 2012, in Proceedings of "An INTEGRAL view of the high-energy sky (the first 10 years)" - 9th INTEGRAL Workshop and celebration of the 10th anniversary of the launch (INTEGRAL 2012). 15-19 October 2012. Bibliotheque Nationale de France, Paris, France 6

Beelen A., et al., 2008, A&A, 485, 645 195, 196

Bekki K., 2009, MNRAS, 399, 2221 161

Bendo G.J., et al., 2003, AJ, 125, 2361 43

Bennett A.S., 1962, MmRAS, 68, 163 2

Best P.N., 2002, MNRAS, 336, 1293 30, 96, 140

Best P.N., Lehnert M.D., Miley G.K., Röttgering H.J.A., 2003, MNRAS, 280, 9 94, 127, 142, 143, 194

Best P.N., 2007a, NAR, 51, 168 24

Best P.N., 2007b, in Astronomical Society of the Pacific Conference Series, Vol. 379, Cosmic Frontiers, Metcalfe N., Shanks T., eds., p. 213 25

Béthermin M., Dole H., Beelen A., Aussel H., 2010, A&A, 512, A78 67, 68

Bird J., Martini P., Kaiser C., 2008, ApJ, 676, 147 204

Blain A.W., Smail I., Ivison R., Kneib J.P., Frayer D.T., 2002, Physics Reports, 369, 111 160, 199, 205, 207

Blandford R.D., Znajek R.L., 1977, MNRAS, 179, 433 29

Böhringer H., 2001, in Astronomische Gesellschaft Meeting Abstracts, Vol. 18, Astronomische Gesellschaft Meeting Abstracts, Schielicke E.R., ed., p. 122

Bolzonella M., Miralles J.M., Pelló R., 2000, A&A, 363, 476 136, 137, 212

Bonfield D.G et al., 2011, MNRAS, 416, 13 58, 142

Borguet B., Hutsemékers D., 2010, A&A, 515, A22 10

Borys C., Chapman S., Halpern M., Scott D., 2003, MNRAS, 344, 385 194, 197

Bournaud F., Duc P.A., Emsellem E., 2008, MNRAS, 389, L8 162

Bournaud F., Powell L.C., Chapon D., Teyssier R., 2011, in IAU Symposium, Vol, 271, IAU Sumposium, Brummel N.H., Brun A.S., Miesch M.S., Ponty Y., eds., p. 160 161

Bower R.G., Benson A.J., Malbon R., Helly J.C., Frenk C.S., Baugh C.M., Cole S., Lacey C.G., 2006, MNRAS, 370, 645 24

Brotherton M.S., Tran H.D., Becker R.H., Gregg M.D., Laurent-Muehleisen S.A., White R.L., 2001, ApJ, 546, 775 15

Brotherton M. S., De Breuck C., Schaefer J. J., 2006, MNRAS, 372, L58 15

Bruni G. et al., 2012, Journal of Physics Conference Series, 372, 012031 10

Bruzual G., Charlot S., 2003, MNRAS, 344, 1000 136, 137, 212

Burbidge G.R., 1961, Nature, 190, 1053 4

Burbidge E.M., Lynds C.R., Burbidge G.R., 1966, ApJ, 144, 447 5

Cao Orjales J.M., et al., 2012, MNRAS, 427, 1209 221

Chapin E.L., Berry D.S., Gibb A.G., Jenness T., Scott D., Tilanus R.P.J., Economou F., Holland W.S., 2013, MNRAS, 430, 2545 174, 213

Chartas G., Saez C., Brandt W.N., Giustini M., Garmire G.P., 2009, ApJ, 706, 644 10

Choi E., Ostriker J.P., Naab T., Johansson P.H., 2012, ApJ, 754, 125 207, 215

Churchill C.W., Schneider D.P., Schmidt M., Gunn J.E., 1999, AJ, 117, 2573 10

Ciotti L., Ostriker J.P., Proga D., 2010, ApJ, 717, 708 24

Clewley L., Jarvis M.J., 2004, MNRAS, 352, 909 153

Colless M. et al., 2001, MNRAS, 328, 1039 56

Condon J.J., Odell S.L., Puschell J.J., Stein W.A., 1981, ApJ, 246, 624 3

Condon J.J., Cotton W.D., Greisen E.W., Yin Q.F., Perley R.A., Taylor G.B., Broderick J.J., 1998, AJ, 115, 1693 98

Coppin K. et al., 2006, MNRAS, 372, 1621 116, 194, 195, 196, 205

Cowie L.L., Barger A.J., Hasinger G., 2012, ApJ, 748, 50 17

Croton D.J. et al., 2006, MNRAS, 365, 11 9, 24

Daddi E. et al. 2010, ApJ, 713, 686 162

Davies J.I. et al., 2010, A&A, 518, L48 104

De Breuck C. et al., 2004, A&A, 424, 1 197

de Vaucouleurs G., 1953, MNRAS, 113, 134 134

Debuhr J., Quataert E., Ma C.P., 2012, MNRAS, 420, 2221 25

Dekel A. et al., 2009, Nature, 457, 451 198

Dempsey J.T. et al., 2013, MNRAS, 430, 2534 171, 174

Devereux N.A., Young J.S., 1990, ApJ, 359, 42 43

Di Matteo T., Springel V., Hernquist L., 2005, Nature, 433, 604 25

Doherty et al., 2010, A&A, 509, A83 27

Dole H. et al., 2006, A&A, 451, 417 34, 35, 36, 65

Donoso E., Li C., Kauffmann G., Best P.N., Heckman T.M., 2010, MNRAS, 407, 1078 165

Driver S.P. et al., 2009, Astronomy and Geophysics, 50, 12 56
Astronomy and Geophysics Year 2009 Volume 50 Number 5 Pages 12-5

Dressler A., Richstone D.O., 1988, ApJ, 324, 701 4

Dupac X. et al., 2003, A&A, 404, L11 41

Eales S.A., 1985, MNRAS, 217, 149 98

Eales S. et al., 2010, PASP, 122, 499 i, 49, 53, 56, 103

Edge D.O., Shakeshaft J.R., McAdam W.B., Baldwin J.E., Archer S., 1959, MmRAS, 68, 37 2

Elbaz D., Cesarsky C.J., 2003, Science, 300, 270 162

Ellingson E., Yee H.K.C., Green R.F., 1991, ApJ, 371, 49 28

Fabian A.C., 1994, ARA&A, 32, 277 23

Fabian A.C., 1999, MNRAS, 308, L39 17

Falder J.T. et al., 2010, MNRAS, 405, 347 i, ii, 28, 30, 127, 128, 129, 130, 136, 137, 142, 143, 148, 149, 150, 153, 155, 157, 161, 162, 164, 165, 212, 219

Falder J.T. et al., 2011, ApJ, 735, 123 140, 143

Fan X., Carilli C.L., Keating B., 2006, ARA&A, 44, 415 49

Fanaroff B.L., Riley J.M., 1974, MNRAS, 167, 31P 22

Farrah D., Lacy M., Priddey R., Borys C., Afonso J., 2007, ApJ, 662, L59 90

Farrah D. et al., 2010, ApJ, 717, 868 91

Farrah D. et al., 2012, ApJ, 745, 178 91, 201, 211

Fath E.A., 1909, Lick Observatory Bulletin, 5, 71 1

Ferrarese L., Merritt D., 2000, ApJL, 539, L9 23, 215

Gabel J.R., Arav N., Kim T., 2006, ApJ, 646, 742 9, 26

Gaibler V., Khochfar S., Krause M., Silk J., 2012, MNRAS, 425, 438 26

Galametz A., Stern D., Stanford S.A., De Breuck C., Vernet J., Griffith R.L., Harrison F.A., 2010, A&A, 516, A101 27

Galametz A. et al., 2012, ApJ, 749, 169 27, 94

Gallagher S.C., Brandt W.N., Chartas G., Garmire G.P., 2007, ApJ, 567, 37 15, 90

Gallagher S.C., Brandt W.N., Chartas G., Priddey R., Garmire G.P., Sambruna R.M., 2007, ApJ, 644, 709 15, 90

Gallagher S.C., Hines D.C., Blaylock M., Priddey R.S., Brandt W.N., Egami E.E., 2007, ApJ, 665, 157 15, 17, 90, 93

Ganguly R., Brotherton M.S., 2008, ApJ, 672, 102 8, 9

Garofalo D., Evans D.A., Sambruna R.M., 2010, MNRAS, 406, 975 29, 30, 161

Gaspari M., Ruszkowski M., Sharma P., 2012, ApJ, 746, 94 161

Geach et al., 2013, MNRAS, 432, 53 50, 177

Gebhardt K. et al., 2000, ApJL, 539, L13 23, 216

Gendreau K.C. et al., 1995, PASJ, 47, L5 19

Genzel R., Cesarsky C.J., 2000, ARA&A, 38, 761 27, 37

Georgantopoulous I. et al., 1996, MNRAS, 280, 276 19

Gibson R.R. et al., 2009, ApJ, 692, 758 x, 55, 58, 63, 67, 87, 88, 91, 209

Gibson R.R., Brandt W.N., Gallagher S.C., Schneider D.P., 2009, ApJ, 696, 924 15, 86, 90

Gilli R., 2004, Advances in Space Research, 34, 2470 17, 19

Gilli R., Comastri A., Hasinger G., 2007, A&A, 463, 79 17, 18

Gnedin O.Y., 2003, ApJ, 582, 141 162, 163, 165, 220

Godfrey L.E.H. et al., 2012, ApJL, 758, L27 22

Graham J.R., Carico D.P., Matthews K., Neugebauer G., Soifer B.T., Wilson T.D., 1990, ApJL, 354, L5 199

Granato G.L., De Zotti G., Silva L., Bressan A., Danese L., 2004, ApJ, 600, 580 9

Green P.J., Mathur S., 1996, ApJ, 462, 637 15

Green P.J., Alcroft T.L., Mathur S., Wilkes B.J., Elvis M., ApJ, 538, 109 90

Greenstein J.L., Matthews T.A., 1963, AJ, 68, 279 2

Greenstein J.L., Schmidt M., 1964, ApJ, 140, 1 3, 5

Gregg M. D., Becker R. H., Brotherton M. S., Laurent-Muehleisen S. A., Lacy M., White R. L., 2000, ApJ, 544, 142 14

Gregg M.D., Becker R.H., de Vries W., 2006, ApJ, 641, 210 14, 16

Greve T.R., Stern D., Ivison R.J., De Breuck C., Kovács A., Bertoldi F., 2007, MNRAS, 382, 48 30

Griffin M.J. et al., 2010, A&A, 518, L3 54, 99, 102, 103

Gruber, D.E., 1992, The Hard X-Ray Background, The X-ray background, Barcons X., Fabian A.C., eds., p.44 19

Gruber D.E., Matteson J.L., Peterson L.E., Jung G.V., ApJ, 1999, 520, 124 19

Gultekin K. et al., 2009, ApJ, 698, 198 23, 216

Gwyn S.D.J., 2011, ArXiv e–prints 45 50

Hall P. B, Green R. F., 1998, ApJ, 507, 558 94

Hall P.B. et al., 2002, ApJS, 141, 267 11

Hall P.B., Anosov K., White R.L., Brandt W.N., Gregg M.D., Gibson R.R., Becker R.H., Schneider D.P., 2011, MNRAS, 411, 2653 16, 93

Hamann F., Barlow T., Cohen R.D., Junkkarinen V., Burbidge E.M., 1997, in Arav N., Shlosman I., Weymann R. J., eds, ASP Conf. Ser Vol. 128, Mass Ejection from Active Galactic Nuclei, Astron. Soc. Pac., San Francisco, p. 19 10

Hamann F., Ferland G., 1999, ARA&A, 37, 487 9, 26

Hardcastle M.J. et al., 2010, MNRAS, 409, 122 71

Harrison C.M. et al., 2012, ApJL, 760, L15 203

Hatziminaoglou E. et al., 2008, MNRAS, 386, 1252 131

Hatziminaoglou E., Fritz J., Jarrett T.H., 2009, MNRAS, 399, 1206 131

Hatziminaoglou E. et al., 2010, A&A, 518, L33 142

Hauser M.G., Dwek E., 2001, ARA&A, 39, 249 34

Hazard C., Mackey M.B., Shimmins A.J., 1963, Nature, 197, 1037 2

Heavens A., Panter B., Jimenez R., Dunlop J., 2004, Nature, 428, 625 23, 203

Hewett P.C., Foltz C.B., Chaffee F.H., 1995, 109, 1498 82

Hildebrand R.H., 1983, QJRAS, 24, 267 i, 75, 153, 199

Hill G.J., Rawlings S., 2003, NAR, 47, 373 98

Hlavacek-Larrondo J. et al., 2013, ApJ, 777, 163 28

Ho L.C., Kim M., 2009, ApJS, 184, 398 75

Holland W.S. et al., 1999, MNRAS, 303, 659 43, 166, 213

Holland W.S. et al., 2013, MNRAS, 430, 2513 46, 171, 174

Hoyle F., Fowler W.A., 1963, MNRAS, 125, 169 4

Hughes S.A., Blandford R.D., 2003, ApJL, 585, L101 30

Hutchings J.B., Crampton D., Morris S.L., Durand D., Steinbring E., 1999, AJ, 117, 1109 28, 95

Hutchings J.B., Scholz P., Bianchi L., 2009, AJ, 137, 3533 94

Irwin K.D., 1995, Applied Physics Letters, 66, 1998 47

Irwin M., 2010, UKIRT Newsletter, 26, 3533 106

Ivezić Ž et al., 2002, AJ, 124, 2364 21

Ivison R.J., Dunlop J.S., Smail I., Dey A., Liu M.C., Graham J.R., 2000, ApJ, 542, 27 27

Jaffe W. et al., 2004, Nature, 429, 47 8

Jahnke K., Macció A.V., 2011, ApJ, 734, 92 23

Jarvis M.J., et al., 2013, MNRAS, 428, 1281 50

Jenness T., Robson E.I., Stevens J.A., 2010, MNRAS, 401, 1240 174

Jenness T., Berry D., Chapin E., Economou F., Gibb A., Scott D., 2011, in Astronomical Society of the Pacific Conference Series, Vol. 442, Astronomical Data Analaysis Software and Systems XX, Evans I.N., Accomazzi A., Mink D.J., Rots A., eds., p.281 174, 213

Kauffmann G. et al., 2007, ApJS, 173, 357 24, 218

Keel W.C., White III R.E., Owen F.N., Ledlow M.J., 2006, AJ, 132, 2233 25

Kellermann K.I., Sramek R., Schmidt M., Shaffer D.B., Green R., 1989, AJ, 98, 1195 20

Kennicutt Jr., R.C., 1998, ARA&A, 36, 189 38, 39, 44, 80, 153

Kessler M.F. et al., 1996, A&A, 315, L27 42

Kessler M.F., 1999, in ESA Special Publication, Vol. 427, The Universe as Seen by ISO, Cox P., Kessler M., eds., p.23 42

Kinzer R.L., Jung G.V., Gruber D.E., Matteson J.L., Peterson L.E., 1997, ApJ, 475, 361 19

Knigge C., Scaringi S., Goad M.R., Cottis C.E., 2008, MNRAS, 386, 1426 14, 57

Knudsen K.K., van der Werf P.P., Kneib J.P., 2008, MNRAS, 384, 1611 194

Konigl A., Kartje J.F., 1994, ApJ, 434, 446 8

Kormendy J., 1988, ApJ, 325, 128 4

Kotilainen J.K., Falomo R., Labita M., Treves A., Uslenghi M., 2007, ApJ, 660, 1039 96

Kron R.G., 1980, ApJS, 43, 305 134

Kukula M.J., Dunlop J.S., McLure R.J., Miller L., Percival W.J., Baum S.A., O'Dea C.P., 2001, MNRAS, 326, 1533 96

Kushino M.J., Ishisaki Y., Morita U., Yamasaki N.Y., Ishida M., Ohashi T., Ueda Y., 2002, PASJ, 54, 327 19

Kwok S., Bignell R.C., 1984, ApJ, 276, 544 174

Lacy M. et al., 2004, ApJS, 154, 166 131

Lagache G., Puget J.L., Gispert R., 1999, Ap&SS, 269, 263 34

Lagache G., Puget J.L., Dole H., 2005, ARA&A, 43, 727 40

Laing R.A., Riley J.M., Longair M.S., 1983, MNRAS, 204, 151 98

Le Floc'h E. et al., 2007, ApJL, 660, L65 159

Leitherer C., Heckman T.M., 1995, ApJS, 96, 9 38

Luo B. et al., 2013, ApJ, 772, 153 10, 11

Lumb D.H., Warwick R.S., Page M., De Luca A., 2002, A&A, 389, 93 19

Lynden-Bell D., 1969, Nature, 223, 690 4

Lynden-Bell D., 1978, Phys. Scr, 17, 185 4

Lynds C.R., 1967a, ApJ, 147, 396 5, 10

Lynds C.R., 1967b, ApJ, 147, 837 10

Madau P., Pozzetti L., Dickinson M., 1998, ApJ, 498, 106 23

Maddox S.J. et al., 2010, A&A, 518, L11 64

Magnelli B., Elbaz D., Chary R.R., Dickinson M., Le Borgne D., Frayer D.T., Wilmer C.N.A., 2009, A&A, 496, 57 159

Magnelli B. et al., 2010, A&A, 518, L28 204

Magnelli B. et al., 2012, A&A, 539, A155 204

Magorrian J. et al., 1998, AJ, 115, 2285 23

Malkan M.A., 1983, ApJ, 268, 582 4

Mann H.B., Whitney D.R., 1947, AoMS, 18, 50 86

Matthews T.A., Sandage A., 1962, PASP, 74, 406 2

Matthews T.A., Morgan W.W., Schmidt M., 1964, ApJ, 140, 35 25

Mauduit J.C. et al., 2012, PASP, 124, 714 128

Mayo J.H., Vernet J., De Breuck C., Galametz A., Seymour N., Stern D., 2012, A&A, 539, 33 27, 29, 94

McCarthy I.G. et al., 2010, MNRAS, 406, 822 24, 26

McLlure R.J., Dunlop J.S., 2001, MNRAS, 321, 515 28, 95

McNamara B.R. et al., 2000, ApJL, 534, L135 28

McNamara B.R., Nulsen P.E.J., 2007, ARA&A, 45, 117 23

McNamara B.R., Rohanizadegan M., Nulsen P.E.J., 2011, ApJ, 727, 39 29, 161

Merloni A., Rudnick G., Di Matteo T., 2004, MNRAS, 354, L37 24

Miller J.M. et al., 2006, ApJ, 646, 394 10

Miller B.P., Brandt W.N., Gibson R.R., Garmire G.P., Shemmer O., 2009, ApJ, 702, 911 15

Moderski R., Sikora M., Lasota J.P., 1998, MNRAS, 301, 142 29, 161

Montenegro-Montes F. M., Mack K.-H., Vigotti M., Benn C. R., Carballo R., Gonzlez-Serrano J. I., Holt J., Jimnez-Lujn F., 2008, MNRAS, 388, 1853 10

Montenegro-Montes F. M., Mack K.-H., Benn C. R., Carballo R., Gonzlez-Serrano J. I., Holt J., Jimnez-Lujn F., 2009, AN, 330, 157 10

Murphy E.J., Chary R.R., Dickinson M., Pope A., Frayer D.T., Lin L., 2011, ApJ, 732, 126 38

Murray N., Chang J., Grossman S.A., Voit G.M., 1994, in Bulletin of the American Astronomical Society, Vol. 26, American Astronomical Society Meeting Abstracts, p.1369 216

Murray N., Chang J., Grossman S.A., Voit G.M., 1995, ApJ, 451, 498 10

Neugebauer G. et al., 1984, ApJL, 278, L1 41

Newburg H.J., Yanny B., 1997, ApJS, 113, 89 57

Nguyen H.T. et al., 2010, A&A, 518, L5 38

Nikutta R., Elitzur M., Lacy M., 2009, ApJ, 707, 1550 8

Nulsen P.E.J., Fabian A.C., 2000, MNRAS, 311, 346 17

O'Dowd M., Urry C.M., Scarpa R., 2002, ApJ, 580, 96 25

Oliver S.J et al., 2012, MNRAS, 424, 1614 49, 104

Ott S., 2010, in Astronomical Society of the Pacific Conference Series, Vol. 434, Astronomical Data Analysis Software and Systems XIX, Mizumoto Y., Morita K.I., Ohishi M., eds., p.139 103

Page M.J., Mittaz J.P.D., Carrera F.J., MNRAS, 318, 1073 169

Page M.J., Mittaz J.P.D., Carrera F.J., 2001, MNRAS, 325, 575 18, 169

Page M.J., Stevens J.A., Mittaz J.P.D., Carrera F.J., 2001, Science, 294, 2516 166

Page M.J., Stevens J.A., Ivison R.J., Carrera F.J., 2004, ApJL, 611, L85 18, 89, 166, 189, 201, 206, 208, 213, 216, 219

Page M.J., Carrera F.J., Stevens J.A., Ebrero J., Blustin A.J., 2011, MNRAS, 416, 2792 89, 167, 201, 202, 207, 213, 216, 218

Page M.J. et al., 2012, Nature, 485, 213 202, 207, 214

Papovich C., 2008, ApJ, 676, 206 140

Pâris I. et al., 2012, A&A, 548, A66 49, 129

Pascale E. et al., 2008, ApJ, 681, 400 47

Pascale E. et al., 2011, MNRAS, 415, 911 38, 54

Peacock J.A., 1983, MNRAS, 202, 615 63

Peterson J.R., Kahn S.M., Paerels F.B.S., Kaastra J.S., Tamura T., Bleeker J.A.M., Ferrigno C., Jernigan J.G., 2003, ApJ, 590, 207 23

Peterson J.R., Fabian A.C., 2006, Physics Reports, 427, 1 23

Pilbratt G.L. et al., 2010, A&A, 518, L1 44, 53, 99, 116, 121

Poglitsch A. et al., 2010, A&A, 518, L2 54, 99

Postman M. et al., 2005, ApJ, 623, 721 ii, 163, 165, 213, 220

Priddey R.S., McMahon R.G., 2001, MNRAS, 324, L17 169

Priddey R.S., Gallagher S.C., Isaak K.G., Sharp R.G., McMahon R.G., Butner H.M., 2007, MNRAS, 374, 867 82, 85, 86, 87, 89, 90, 92, 93, 210, 217

Proga D., Stone J.M., Kallmann T.R., 2000, ApJ, 543, 686 10, 16

Puget J.L., Abergel A., Bernard J.P., Boulanger F., Burton W.B., Desert F.X., Hartmann D., 1996, A&A, 308, L5 34

Rawlings S., Jarvis M. J., 2004, MNRAS, 355, L9 21, 25

Reichard T.A. et al., 2003a, AJ, 125, 1711 11, 13, 16, 57

Reichard T.A. et al., 2003b, AJ, 126, 2594 90

Rengelink R.B., Tang Y., de Bruyn A.G., Miley G.K., Bremer M.N., Roettgering H.J.A., Bremer M.A.R., 1997, A&AS, 124, 259 98

Renzini A., 2006, ARA&A, 44, 141 23

Reynolds C., Punsly B., Kharb P., O'Dea C., Wrobel J., 2009, ApJ, 706, 851 74

Richards G.T. et al., 2002, 123, 2945 57

Rieke G.H. et al., 2004, ApJS, 154, 25 42, 43

Rigby E.E. et al., 2011, MNRAS, 415, 2336 38, 54, 61, 64, 104, 106, 107, 110, 116, 121

Rigby E.E. et al., 2014, MNRAS, 437, 1882 197

Rosario D.J. et al., 2013, ApJ, 771, 63 25

Roseboom I.G. et al., 2010, MNRAS, 409, 48 38

Sadler E.M. et al., 2007, MNRAS, 381, 211 153

Saez C., Brandt W.N., Gallagher S.C., Bauer F.E., Garmire G.P., 2012, ApJ, 759, 42 16

Salpeter E.E., 1964, ApJ, 140, 796 4

Sandage A., 1965, ApJ, 141, 1560 3

Sanders D.B., Soifer B.T., Elias J.H., Neugebauer G., Matthews K., 1988, ApJL, 328, L35 161

Sanders J.S., Fabian A.C., 2008, MNRAS, 390, L93 28

Savage R. S., Oliver S., 2007, ApJ, 661, 1339 109

Scaringi S., Cottis C.E., Knigge C., Goad M.R., 2009, MNRAS, 399, 2231 14, 15

Schechter P. 1976, ApJ, 203, 297 195

Schmidt M., 1963, Nature, 197, 1040 2

Schneider D.P. et al., 2005, AJ, 130, 367 13, 49

Schneider D.P. et al., 2007, AJ, 134, 102 55, 67, 87, 98, 99, 168

Schneider D.P. et al. 2010, AJ, 139, 2360 129

Scott S.E., Dunlop J.S., Serjeant S., 2006, MNRAS, 370, 1057 194, 197

Seyfert C.K., 1943, ApJ, 97, 28 1

Sijacki D., Springel V., Di Matteo T., Hernquist L., 2007, MNRAS, 380, 877 24

Silk J., Rees M.J., 1998, A&A, 331, L1 25

Sinha M., Holley–Bockelmann K., 2012, ApJ, 751, 17 162, 165

Smail I., Ivison R.J., Blain A.W., 1997, ApJ, 490, L5 160

Smith H.E., Lonsdale C.J., Lonsdale C.J., Diamond P.J., 1998, in Bulletin of the American Astronomical Society, Vol. 30, American Astronomical Society Meeting Abstracts #192, p.833 74

Smith R.J., Boyle B.J., Maddox S.J., 2000, MNRAS, 313, 252 127

Smith G.P., Treu T., Ellis R.S., Moran S.M., Dressler A., 2005, ApJ, 620, 78 ii, 163, 165, 213

Smith D.J.B. et al., 2011, MNRAS, 416, 857 54, 64

Smith A.J. et al., 2012, MNRAS, 419, 377 38, 109, 116, 121, 126

Smith D.J.B. et al., 2013, MNRAS, 436, 2435 54, 112, 169

Soifer B.T., Sanders D.B., Madore B.F., Neugebauer G., Danielson G.E., Elias J.H., Lonsdale C.J., Rice W.L., 1987, ApJ, 320, 238 42, 216

Soifer B.T., Neugebauer G., 1991, AJ, 101, 354 35

Sprayberry D., Foltz C.B., 1992, ApJ, 390, 39 13, 15

Springel V., Di Matteo T., Hernquist L., 2005a, ApJ, 620, L79 26

Sramek R.A., Weedman D.W., 1980, ApJ, 238, 435 3

Stevens J.A. et al., 2003, MNRAS, 342, 249 27, 30, 94, 160

Stevens J.A., Page M.J., Ivison R.J., Smail I., Carrera F.J., 2004, ApJL, 604, L17 197

Stevens J.A., Page M.J., Ivison R.J., Carrera F.J., Mittaz J.P.D., Smail I., McHardy I.M., 2005, MNRAS, 360, 610 ii, 18, 166, 193, 201, 213

Stevens J.A., Jarvis M.J., Coppin K.E.K., Page M.J., Greve T.R., Carrera F.J., Ivison R.J., 2010, MNRAS, 405, 2623 30, 94, 160, 166, 167, 195, 196, 197, 201, 207, 213

Stocke J.T., Morris S.L., Weymann R.J., Foltz C.B., 1992, ApJ, 396, 487 14

Streblyanska A., Barcons X., Carrera F.J., Gil-Merino R., 2010, A&A, 515, 2 16, 90

Sunyaev R.A., Zeldovich Y.B., 1970, Ap&SS, 7, 20 35

Swinbank M. et al., 2014, MNRAS, 438, 1267 204

Swinyard B.M. et al., 2010, A&A, 518, L4 103

Tacconi L.J. et al., 2008, ApJ, 680, 246 204

Tacconi L.J. et al., 2010, Nature, 463, 781 162

Taylor M.B., 2005, in Astronomical Society of the Pacific Conference Series, Vol. 347, Astronomical Data Analysis Software and Systems XIV, Shopbell P., Britton M., Ebert R., eds., p.29 56

Tchekhovskoy A., Narayan R., McKinney J.C., 2010, ApJ, 711, 50 29, 161

Thompson T.A., Quataert E., Murray N., 2009, MNRAS, 397, 1410 20

Tolea A., Krolik J.H., Tsvetanov Z., 2002, ApJL, 578, L31 13

Tozzi P. et al., 2001, ApJ, 562, 42 19

Trump J.R. et al., 2006, ApJS, 165, 1 13

Ueda Y., Akiyama M., Hasinger G., MIyaji T., Watson M.G., 2014, ApJ, 786, 104 18

Urrutia T., Becker R.H., White R.L., Glikman E., Lacy M., Hodge J., Gregg M.D., 2009, ApJ, 698, 1095 90, 91

Urry C.M., Padovani P., 1995, PASP, 107, 803 6

Vecchi A., Molendi S., Guainazzi M., Fiore F., Parmar A.N., 1999, A&A, 349, L73 19

Veilleux S. et al., 2009, ApJ, 701, 587 75

Venemans B.P. et al., 2007, A&A, 461, 823 27, 197

Vivek et al., 2014, MNRAS, 440, 799 10, 93

Volonteri M., Sikora M., Lasota J.P, 2007, ApJ, 667, 704

Warwick R.S., Roberts T.P., 1998, AN, 319, 59 19

Waskett T.J., Sibthorpe B., Griffin M.J., Chanial P.F., 2007, MNRAS, 381, 1583 110

Watson M.G. et al., 2009, A&A, 493, 339 168

Webster B.L., Murdin P., 1972, Nature, 235, 37 4

Weiß A. et al., 2009, ApJ, 707, 1201 195, 197, 205

Werner M.W. et al., 2004, ApJS, 154, 1 42

Weymann R.J., Morris S.L., Foltz C.B., Hewett P.C., 1991, ApJ, 373, 23 9, 11, 13

Wiita P.J., 2004, Ap&SS, 293, 235 25

Willott C.J., et al., 1998, in Astrophysics and Space Science Library, Vol. 226, Observational Cosmology with the New Radio Surveys, Bremer M.N., Jackson N., Perez-Fournon I., eds., p.209 98

Willott C.J., Rawlings S., Grimes J.A., 2003, ApJ, 598, 909 90, 92, 93, 217

Wilson A.S., Colbert E.J.M., 1995, ApJ, 438, 62 29, 161

Wold M., Lacy M., Lilje P.B., Serjeant S., 2001, MNRAS, 323, 231 28, 95

Woltjer L., 1959, ApJ, 130, 38 3

Worsley M.A., Fabian A.C., Barcons X., Mateos S., Hasinger G., Brunner H., 2004, MNRAS, 352, L28 17

Worsley M.A. et al., 2005, MNRAS, 357, 1281 17

Wright E.L. et al., 2010, AJ, 140, 1868 44

Wylezalek D. et al., 2013, MNRAS, 428, 3206 27

Yee H.K.C., Green R.F., 1984, ApJ, 280, 79 28, 95

Yee H.K.C., Green R.F., 1987, ApJ, 319, 28 28, 95

Zel'dovich Y.B., Novikov I.D., 1965, Soviet Physics Doklady, 9, 834 4